An Introduction to Atmospheric Gravity Waves

Carmen J. Nappo

INTERNATIONAL GEOPHYSICS SERIES, VOLUME 85

An Introduction to Atmospheric Gravity Waves

This is Volume 85 in the
INTERNATIONAL GEOPHYSICS SERIES
A series of monographs and textbooks
Edited by RENATA DMOWSKA, JAMES R. HOLTON AND
H. THOMAS ROSSBY

A complete list of books in this series appears at the end of this volume.

An Introduction to Atmospheric Gravity Waves

Carmen J. Nappo

National Oceanic and Atmospheric Administration
Air Resources Laboratory
Atmospheric Turbulence and Diffusion Division
Oak Ridge, Tennessee

ACADEMIC PRESS
An imprint of Elsevier Science

Amsterdam Boston London New York Oxford Paris
San Diego San Francisco Singapore Sydney Tokyo

This book is printed on acid-free paper. ♾

Academic Press
An Elsevier Science Imprint
525 B Street, Suite 1900, San Diego, California 92101-4495, USA
http://www.academicpress.com

Academic Press
84 Theobalds Road, London WC1X 8RR, UK
http://www.academicpress.com

Library of Congress Catalog Card Number: 2002101285

International Standard Book Number: 0-12-514082-7
International Standard Book Number: 0-12-514083-5 (CD-ROM)

PRINTED IN THE UNITED STATES OF AMERICA
02 03 04 05 06 07 MM 9 8 7 6 5 4 3 2 1

Disclaimer

The opinions expressed in this book are those of the author, and do not represent official positions or policies of the United States Government or any of its departments or agencies.

Acknowledgments

I wish to thank Professor George Chimonas, Georgia Institute of Technology, Atlanta, GA; Dr. Branko Grisogono, Stockholm University, Stockholm, Sweden, and Professor Hey-Yeong Chun, Yonsei University, Seoul, Korea for their manuscript reviews and their many fine recommendations. I wish also to thank Professor Michael Tjernström, Stockholm University, Stockholm, Sweden for giving me the opportunity to test the material in this book on a graduate class, and to compile a first draft of the text. Special thanks goes to the participants of that class, *i.e.*, Babatunde Abiodun, Ulf Andrae, Jenny Brandefelt, Nedjelika Brzovic, Igor Esau, Pia Hultgren, Kairi Kasemets, Xiaoli Gou-Larsen, Oskar Parmhed, Marc Salzman, Stefan Söderberg, and Admir Taragino. Their many questions and suggestions contributed greatly to this book.

This book is dedicated to my wife Joan MacReynolds.
Her support and constant enthusiasm made it possible.

This Page Intentionally Left Blank

Contents

3

Terrain-Generated Gravity Waves

4

Ducted Gravity Waves

5

Gravity Wave Energetics

6

Waves and Turbulence

7

The Parameterization of Wave Stress

8

Observational Techniques

9

Data Analyses and Numerical Methods

APPENDIX A

THE HYDROSTATIC ATMOSPHERE

APPENDIX B

COMPUTER CODES AND DATA ON CD-ROM

This Page Intentionally Left Blank

Foreword

Internal gravity waves are now a part of mainstream meteorology. Calculations of the atmospheric budgets, whether at the largest scales of the general circulation or the smaller scales of surface turbulence, routinely include contributions from wave transport and mixing. Waves were not always paid such respect: I recall conferences where an eminent proponent of waves and their effects in the middle atmosphere (C.O.H) would be confronted by colleagues who disputed the very existence of internal gravity waves. But the success of models in which stresses from breaking waves drive the middle-atmosphere circulation have made wave-skeptics an endangered species. Most atmospheric scientists now recognize the need to evaluate the function of waves in each dynamical situation.

There are many dynamical situations. The different layers of the atmosphere are often studied in isolation: the boundary-layer meteorologist might spend an entire career investigating the few-hundred meters nearest the ground, the aeronomist might be unconcerned with anything below 80 kilometers, while between these extremes various subspecies of meteorologist populate niches with their own jargon and journals. In contrast, internal gravity waves cover all the bases. Some waves travel from surface sources to the outer reaches of the atmosphere while others couple the synoptic scales to the scales of dissipative turbulence. Wave effects discovered at one scale or height provide clues to the dynamics in other regimes; and atmospheric scientists find themselves working with wave systems that have direct counterparts in the ocean sciences. Thus there is a constant exchange of ideas between people working in seemingly diverse areas, an unusual but stimulating state of affairs in this age of specialization.

But of course some problems are closer to solution than others. It is possible that waves control the location and timing of significant weather events, but

evaluating such possibilities and using the information in actual forecasts is a formidable challenge. Even the casual observer is aware how unpredictable the weather can be. Some even find comfort in this reminder that nature does not conform to civilization's nine-to-five humdrum routine. However, if the casual observer optimistically suggests that "the experts know what is going on" he is, like most optimists, sadly mistaken. The true expert is quite certain that he does not know what is going on. Richardson, one of the acknowledged giants of meteorology, asked "Does the wind possess a velocity?," and then proceeded to undermine this basic concept of dynamic meteorology. Perhaps Richardson was being mischievous, but it is worth bearing in mind that the real atmosphere bears only a tenuous relationship to the ideal flows that the theoretician can handle, or to the large numerical models that grind their predetermined route through the latest supercomputers.

The current task then is not to predict the behavior of the atmosphere, but to extract knowledge from the problems that current resources can handle. It must be left to future generations to synthesize such knowledge into predictions—or, more likely, to quantify the limits and cost-benefits of predictions. Given this situation, today's investigator needs to identify worthwhile problems that can be profitably investigated with the available experimental techniques and the available funding. Waves provide such problems. As an example, the saturation and breaking of waves presents a first-class scientific problem whose nonlinear features may soon be resolvable with remote-sensing systems. The social concerns about the ozone layer, the Earth's climate and boundary-layer air quality, all problems that involve wave transports and mixing, generate financial support for such work.

It is timely to have a book that introduces the reader to current themes in atmospheric waves. Famous persons from previous eras—Rayleigh, Taylor, Richardson, v. Karmen, and Kolmogoroff—have made contributions to the problems that are discussed, but the problems are still largely unsolved. The optimistic student beginning a career may find inspiration in this.

George Chimonas
Atlanta, Georgia
May, 2002

Preface

Virtually the whole theory of linear atmospheric gravity waves can be found in the six pages of Colin Hines' 1965 article entitled, "Atmospheric Gravity Waves: A New Toy for the Wave Theorist" from the journal *Radio Science*. However, learning about gravity waves by reading this paper is equivalent to learning to swim by jumping into the middle of an ocean. Similar analogies can be made concerning some of the textbooks on the subject. In these cases, instead of an ocean, one jumps into the middle of a lake. It is with this in mind, that I set about writing an introduction to gravity waves which I hope will, at most, place the student into a pool of water only neck-deep.

The aim of this monograph is to present the reader with a background necessary to tackle advanced texts and scientific articles. In addition to the theoretical treatments which are a necessary part of the study of waves, I have included chapters on practical issues such as observation techniques, data analyses, numerical parameterizations of wave effects, and numerical models of gravity waves. These chapters should be of interest to observationalists and numerical modelers. However, the discussions of these issues are neither comprehensive nor complete. Indeed, a book could be written on each of them.

I have tried to make the theoretical discussions as simple as possible and to concentrate on physical insight rather than mathematical rigor. However, I recognize that waves are fundamentally a mathematical concept and construct. Some chapters are more mathematically concentrated than others. To ease the problem inherent in mathematical developments, I have tried to include many intermediary steps, and have tried to avoid expressions such as "it can be shown. . ." or "it follows that. . .," etc. In some cases, the mathematical developments may not be essential, and one could say that the means do not justify the ends. Because I come from the old school of physics, I feel compelled to justify conclusions. One can

consider these developments "cultural enhancements," but what really matters are the final results.

Chapter 1 presents a brief description of the types of gravity waves observed in the atmosphere and their related sources. The basics of wave mechanics is introduced. Topics include wavenumbers, wavelengths, wave vectors, angular frequency, wave period, wave phase, wave fronts, wave dispersion, phase velocity, wave packets, group velocity, buoyancy, static stability, slant-wise static stability, and the Boussinesq approximation.

Chapter 2 introduces the basic mathematics and physics required for understanding gravity waves. The equation for linear gravity waves, the Taylor–Goldstein equation, is developed from basic principles, and solutions are discussed for idealized cases. Expressions are developed for wave dispersion and group velocities. Propagating and evanescent waves are defined and discussed.

The important topic of terrain-generated gravity waves is introduced in Chapter 3. Wave fields above two-dimensional surface corrugations and ridges, and three-dimensional mountains are examined as well as wave stress and its vertical variation.

Chapter 4 deals with wave ducting. We shall see that a gravity wave can become trapped between the ground surface and some upper level where wave reflections occur. Under these conditions, the waves can travel long distances with relatively little attenuation.

Chapter 5, perhaps the most mathematical chapter in this book, deals with wave energetics. We shall examine the vertical variations of wave energy and wave stress, and introduce the concept of wave action. Wave encounter with critical levels where the wave speed equals the local wind speed are treated in detail.

In Chapter 6, the important topic of wave-turbulence interactions is introduced. Indeed, if it were not for the ability of gravity waves to generate turbulence and thus modify the background flow, there would not be much interest in their study. Waves and turbulence are often observed to exist simultaneously. Mechanisms leading to wave instability, wave breaking, and the resulting generation of turbulence are examined in this chapter.

In Chapter 7, much of what has been learned from the previous chapters is used to develop parameterizations of wave stress for use in numerical models. The subject of wave saturation that describes the process of wave breaking in terms of wave amplitudes is introduced. Several parameterization schemes to account for wave saturation in numerical models are described.

Chapter 8 reviews the many techniques for observing the meteorological perturbations produced by gravity waves. It is only through these observations that the existence of gravity waves can be inferred.

Chapter 9 describes numerical techniques for analyzing data for wave content, *i.e.*, phase speed, propagation direction, wavelengths, etc. These techniques include correlations between pressure and wind speed perturbations, analysis of phase lag between wave observation stations, wavelet analysis, and beamsteering.

Also included in Chapter 9, are discussions of numerical models for terrain-generated and ducted gravity waves.

The CD accompanying this book contains FORTRAN 77 computer models for terrain-generated gravity waves and ducted gravity waves. Also included on the CD are computer codes for wavelet analysis, beamsteering, and a 24-hour record of surface pressure perturbation data observed at six microbarograph stations. These codes and data sets are provided as a learning tool and are described in Appendix B. The reader is encouraged to "play" with these programs, and to modify or rewrite them in more modern languages.

Many fine textbooks and monographs on gravity waves exist including, for example:

Baines, P. G. *Topographic Effects in Stratified Flows*, 1995. New York: Cambridge University Press.

Eckart, C. *Hydrodynamics of Oceans and Atmospheres*, 1960. New York: Pergamon Press.

Gill, A. E. *Atmosphere-Ocean Dynamics*, 662 pp., 1982. San Diego: Academic Press.

Gossard, E. E. and Hooke, W. H. *Waves in the Atmosphere*, 456 pp., 1975. San Diego: Academic Press.

Hines, C. O. Atmospheric gravity waves: A new toy for the wave theorist. *Radio Sci.* **69D**:375–380.

Hines, C. O. *The Upper Atmosphere in Motion*, 1974. Washington, D.C.: American Geophysical Union.

Lighthill, M. J. *Waves in Fluids*, 504 pp., 1978. New York: Cambridge University Press.

Phillips, O. O. *The Dynamics of the Upper Ocean*, 336 pp., 1977. New York: Cambridge University Press.

Smith, R. B. On severe downslope winds. *J. Atmos. Sci.* **42**:2597–2603, 1985.

Tolstoy, I. The theory of waves in stratified fluids including the effects of gravity wave rotation. *Rev. Mod. Phys.* **35(1)**:207–230, 1963.

These resources, and the references contained therein, should be consulted for more detailed and comprehensive expositions than are given in this monograph.

Carmen J. Nappo
Oak Ridge, Tennessee

This Page Intentionally Left Blank

1

FUNDAMENTALS

In this chapter, the stage is set for what is to follow. We first give a perspective of the types of gravity waves we shall study and describe how these waves permeate the atmosphere on almost all scales of motion. Next, we present fundamentals of wave theory which are necessary for future discussions. This presentation is not complete, but should be sufficient to give the reader a working knowledge of the mechanics of waves. We shall try to look for physical meanings rather than mathematical expressions. We shall also discuss the property of the atmosphere necessary for gravity wave propagation, *i.e.*, buoyancy.

1.1 INTRODUCTION

A stably stratified fluid is one in which the fluid density increases with depth. A characteristic of a stably stratified fluid is the ability to support and propagate wave motions. Except for a relatively thin layer in contact with the Earth's surface, *i.e.*, the *planetary boundary layer*, the atmosphere is almost always stably stratified, and it is reasonable to assume that it always contains gravity waves. If it were possible to see these waves and to greatly speed up their motions, we would see a wide variety of wave shapes moving in many directions. Hines (1974) presents a "surrealistic" representation of these waves, which is reproduced in Fig. 1.1. Most of the waves move diagonally upward or downward across our field of view, but some move horizontally. Some waves extend through our whole field of view.

FIGURE 1.1 A surrealistic representation of atmospheric gravity waves. (From *The Upper Atmosphere in Motion*, C.O. Hines, Am. Geophys. Union, Washington, DC, 1974, p. 194.)

Some waves appear stationary as if frozen in space. We see waves moving upward, much like writhing snakes with their "wiggles" rapidly increasing in frequency and magnitude, and then suddenly being reflected downward. Some of these waves are not reflected, but instead seem to break apart into countless smaller waves which gradually fade from view. We also see waves that follow curved paths or are partially reflected and partially transmitted. Indeed, it is a view of unending variety and action, but also a view of immeasurable complexity and puzzlement.

We cannot see atmospheric gravity waves. We can only see the effects of the waves on the atmosphere. Figure 1.2 is a "picture" of gravity waves in the planetary boundary layer obtained by an upward-looking sodar. Sodar (see Chapter 8 for a description) is similar to radar except that sound is used instead of radio frequencies. The upward-moving sound waves are partially reflected downward by thin layers of atmospheric turbulence. These reflected waves are detected by the sodar and are represented by the dark bands in Fig. 1.2. These layers of turbulence are perturbed by gravity waves, thus revealing the wave's presence. In some cases, the waves break down and generate the turbulence. We see a wide range of wave frequencies, and in many cases we see high-frequency waves superimposed on lower frequency waves. Some waves last only a few minutes, while others persist for hours. Some waves appear to ascend or descend with time, and some seem to intermittently appear and disappear. Some waves have large amplitudes, while others are barely noticeable. The complicated images depicted in Fig. 1.2 represent

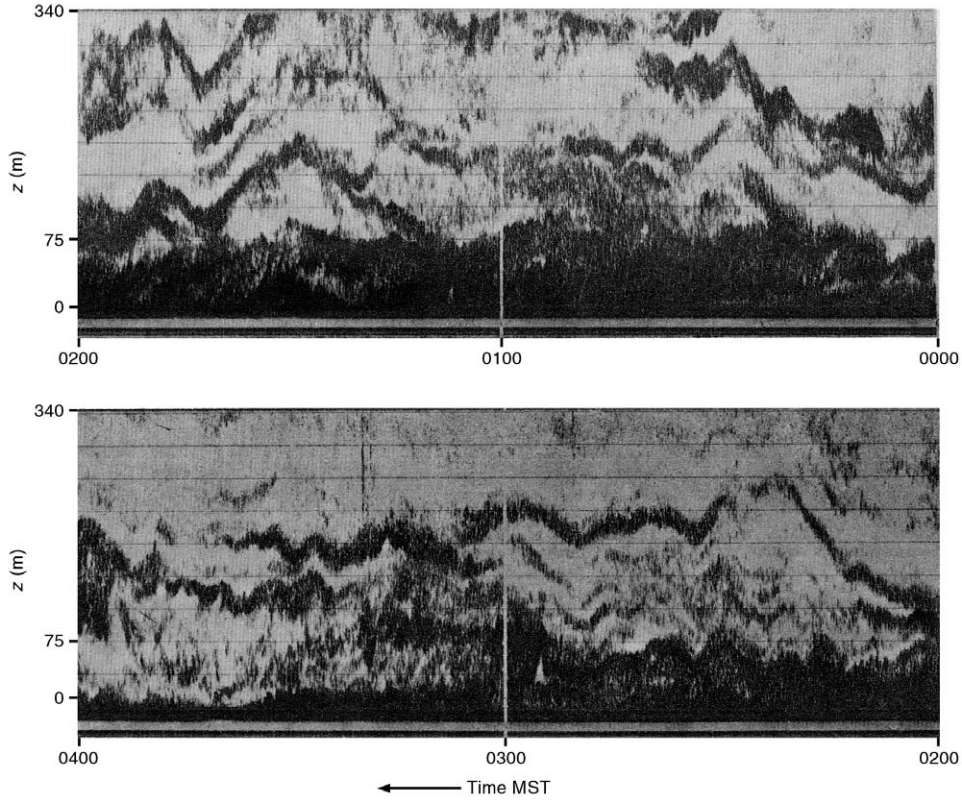

FIGURE 1.2 Sodar images of gravity waves in the planetary boundary layer. (From *Studies in Nocturnal Stable Layers at BAO*, R.L. Zamora, National Atmospheric and Oceanic Administration, NOAA/ERL, Boulder, CO, 1983, p. 109.)

some of the fundamental characteristics and physics of atmospheric gravity waves. But however interesting the physics of these waves may be, unless the waves have an effect on the atmosphere there is little reason for their study.

Although the characteristics of waves in stratified fluids had been known for many years, they remained a somewhat esoteric subject until Hines (1960) used gravity wave theory to explain the origins of turbulence observed in the ionosphere. Hines (1989a) gives a historical perspective of this work, and the reader is encouraged to peruse this article. However, we must not overlook the early work on gravity waves done, for example, by Queney (1948), Scorer (1949), Gossard and Munk (1954), Palm (1955), and Sawyer (1959). The introduction of gravity wave theory into the field of meteorology initiated an avalanche of interest in the applications of the theory to atmospheric physics. Today, it is recognized that gravity waves are essential parts of the dynamics of the atmosphere on all meteorological scales. On the largest atmospheric scale, the studies, for example, by Lindzen (1981) and Holton (1982) examined the effects of gravity waves on the upper atmosphere and the general circulation (see Fritts, 1984 for a review of these and other studies). On the mesoscale, studies by Uccellini (1975), Stobie, Einaudi, and Uccellini (1983), Uccellini and Kock (1987), and Chimonas and Nappo (1987) examined the interactions between gravity waves and thunderstorms. Studies by Lilly and Kennedy (1973), Clark and Peltier (1977), and Smith (1985) examined the generation of gravity waves by mountains and the severe downslope winds these waves can produce. On the microscale, studies by Chimonas (1972), Einaudi and Finnigan (1981), and Fua *et al.* (1982) examined the interactions between gravity waves and turbulence in the stable planetary boundary layer; and Hines (1988), Chimonas and Nappo (1989), and Nappo and Chimonas (1992) examined the interactions of gravity waves generated by small-scale terrain features with the mean boundary-layer flow to produce turbulence in the upper regions of the stable planetary boundary layer. The study of gravity waves and their effects on turbulence in the nighttime boundary layer was a primary goal of the CASES-99 field campaign conducted in the planes of south-central Kansas (Poulos *et al.*, 2001) and the VTMX field campaign in the Salt Lake City basin in Utah (Doran, Fast, and Horel, 2001). Figure 1.3 shows plots of vertical velocity observed by aircraft flights on October 14, 1999, during the CASES-99 campaign. The wavelike structures and turbulence seen between about 300 and 700 m AGL are typical. Lee *et al.* (1997) examined gravity waves within and above a boreal forest canopy. These types of waves, shown in Fig. 1.4, are a common feature of the nighttime flow above forests.

Almost all of the theoretical studies of gravity waves to date have been done using the linear theory. One reason for this is that a clear understanding of waves is attainable under the simplifications of a linear theory. The linearization process eliminates the interactions of waves with waves and the resultant transfers of energy. The process partitions the meteorological variables into slowly varying or stationary background parts and small first-order perturbations, which we take to be due to waves. In the middle and upper atmospheres, the background flows

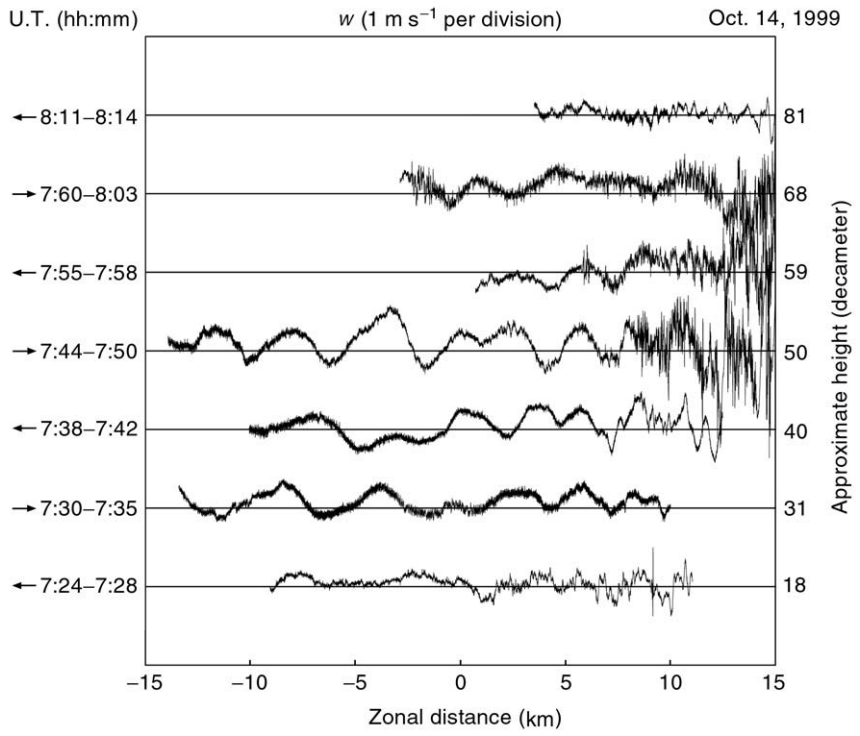

FIGURE 1.3 Vertical velocity recorded by the University of Wyoming King-Air B200 research aircraft on October 14, 1999, during the CASES-99 field campaign. The flights were in the east–west direction at various heights. The arrows on the left indicate the flight direction, and the time marks indicate the beginning and ending of data recording.

often approach these conditions, but in the troposphere and especially in the stable planetary boundary layer these constraints may not be strictly applicable. In the middle and upper atmospheres, gravity waves appear to be nearly monochromatic, *i.e.*, composed of a single frequency, and so wave–wave interactions there may not be important. However, in the troposphere where many different wave frequencies can exit, wave–wave interactions may be important. Yet in spite of these limitations, the linear theory is still a useful tool for understanding and making first-order analyses of observations.

An important property of waves is their ability to transport energy. Gravity waves transport energy away from the disturbances that generate them (mountains, hills, thunderstorms, velocity jets, large explosions, *etc.*) and act to distribute this energy throughout the atmosphere. The distribution of energy is more rapidly done by waves than by the mean flow. Wave transport and subsequent deposition of energy are an important component of the atmospheric dynamics. It is now recognized that turbulence in the nighttime atmospheric boundary layer and clear air turbulence (CAT) is due to breaking gravity waves. The roles of gravity waves

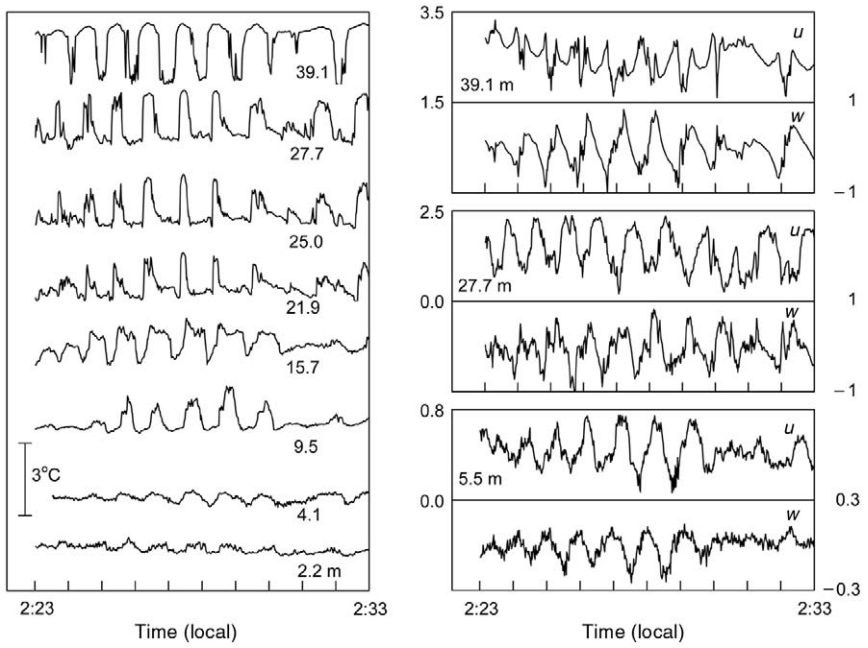

FIGURE 1.4 Ten-minute time series of temperatures (°C) and wind speeds ($m\,s^{-1}$) observed on July 13, 1994, in a boreal aspen forest. Canopy height was 21 m. Measurement heights are listed: u is the horizontal wind speed, and w is the vertical wind speed. (From "Observation of gravity waves in a boreal forest," X. Lee *et al.*, *Boundary-Layer Meteorol.* **84**: 388, 1997.)

in meteorology are continually being studied and expanded. Almost every issue of the *Journal of Atmospheric Science*, *Quarterly Journal of the Royal Meteorological Society*, *Monthly Weather Review*, *Journal of Geophysical Research*, *Tellus*, *Boundary-Layer Meteorology*, etc. contain articles about gravity waves. Considering the wide spectrum of the time and space scales of gravity waves and the complex interactions of these waves with themselves and the mean flow, we expect interest in gravity waves to increase in the future.

1.2 SOME WAVE MECHANICS

In this section, we define the space and time scales needed to describe waves. But first, let us be clear about what we mean by "wave." A wave is the result of harmonic oscillations of fluid particles. The apparent movement of a wave is due to the phase difference in these oscillations between adjacent particles. These oscillations or orbits occur on planes which are perpendicular to the apparent direction of the wave motion. We have all seen waves on water, but we will not discuss waves we see during storms, such as those rendered in Fig. 1.5. Instead, we limit our attention to waves which are similar to waves on a gentle sea or lake,

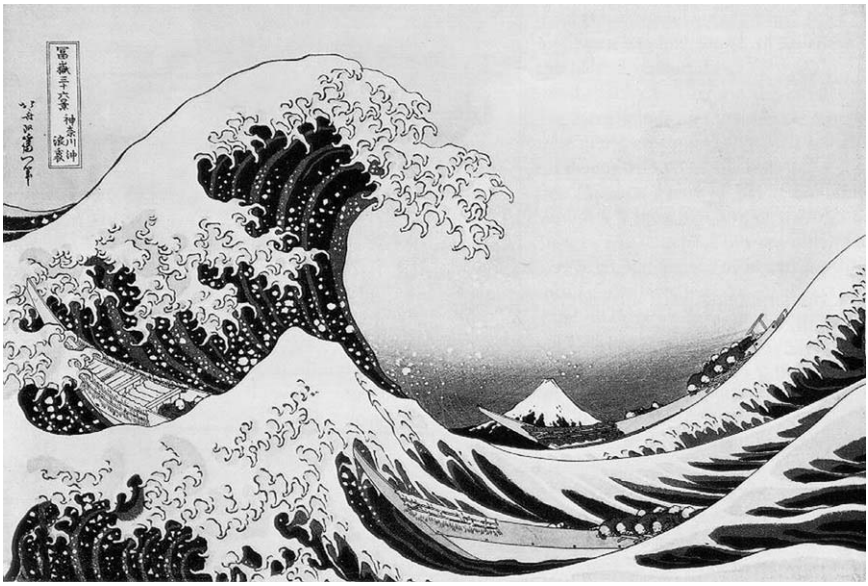

FIGURE 1.5 "The Great Wave" by Hokusai (1760–1849) is an example of a nonlinear wave. These types of waves will not be discussed in this book.

FIGURE 1.6 Two-dimensional waves on a calm sea.

as illustrated in Fig. 1.6. We must distinguish right off between wave and waves. If we consider a sine wave or a breaking wave or a solitary wave, then we are comfortable with the singular term, wave. We know what we are talking about. However, we often hear and use the plural in phrases such as "gravity waves," "Kelvin–Helmholtz waves," "unstable waves," *etc*. Sometimes the meanings of

FIGURE 1.7 A lenticular cloud produced by a three-dimensional wave over a mountain. (Photo by Paul Field, Met Office, UK.)

these phrases are clear, but often they are rhetorical. Consider for a moment fish. In English, "fish" is the proper plural when applied to several members of the same species; however, "fishes" is the proper plural when applied to several species. In an analogous way, we shall use wave to mean a singular event such as depicted in Fig. 1.1 or a continuous wave such as a sine wave, and we shall use waves to mean ensembles of singular waves or several sine waves with different periods. We will also sometimes use the term "*wave train*" or "*plane waves*" (Hines, 1955[1]) to describe a series of repeating motions such as shown in Fig. 1.2. Continuing our discussion, we see that the waves shown in Fig. 1.2 appear as long parallel lines with peaks, which are called *crests*, and valleys, which are called *troughs*. These types of waves are *two-dimensional* waves because the shapes of the waves change only with height and width, but not with length. Waves at the beach are good examples of two-dimensional waves. A two-dimensional wave is sometimes called a *plane wave*. A *three-dimensional wave* changes shape in three dimensions. An example of a three-dimensional wave is the linticular cloud shown in Fig. 1.7. These types of clouds are often seen above mountains. Another example of a three-dimensional wave is the ring wave on the surface of a calm pond after a stone is dropped into it. In the atmosphere or the oceans, three-dimensional waves are spherical, not unlike the layers of an onion. In this book, we shall study mostly two-dimensional waves; however, in many cases what we learn from two-dimensional waves can be easily extended to three dimensions.

The waves shown in Figs. 1.1 and 1.2 appear on the surface of the water; however, the motions of the fluid particles which create the wave extend throughout

[1] See also p. 233 of Hines (1974) for a precise definition of plane waves.

the fluid. Thus, we can speak of a *wave field* which permeates the fluid much as an electromagnetic field permeates space. In the absence of boundaries where wave reflections occur, the wave field will exist everywhere; however, in some regions wave amplitudes may be vanishingly small.

1.2.1 FRAMES OF REFERENCE

Because waves move in a medium which can also be moving, confusion can arise if we are not clear as to the frame of reference of observations or theoretical analysis. In a *Lagrangian* reference frame, fluid motions are observed in a coordinate system moving with the flow. In this frame, some waves would be moving faster than the observer and some waves would be moving slower. Thus, waves would appear to be always moving horizontally away from the observer. Most atmospheric observations, including waves, are made in a coordinate system fixed to the Earth. A reference frame that is stationary realtive to the flow is called an *Eulerian* reference frame. Observations in Lagrangian and Eulerian reference frames are related through appropriate mathematical transformations along with the constraint that the physics in both frames must be identical. However, it often happens that the descriptions of certain motions are more conceptual and more easily described in one frame rather than another. In this book, we shall use the Eulerian reference and thereby relate wave motions to a stationary observer. Exceptions to this general rule will be noted.

1.2.2 WAVE SCALES

We shall use a Cartesian coordinate system (x, y, z) with x and y in the horizontal plane and z in the vertical direction. The coordinates have unit vectors $(\hat{x}, \hat{y}, \hat{z})$. Unless otherwise noted, the horizontal directions of wave motion will be along the x-axis. The *wavelength* ℓ is the distance between successive crests of a wave, as illustrated in Fig. 1.8. In this book, we shall consider only waves with horizontal wavelengths less than 1000 km so that the effects of the effects of the Earth's curvature can be neglected (Hines, 1968). Accordingly, we can consider horizontal planes as being flat. The mathematical description of a wave involves trigonometric functions, for example, $\sin(2\pi x/\ell)$, *etc*., and it is convenient to define the *wavenumber* as

$$\kappa = \frac{2\pi}{\ell} \,. \tag{1.1}$$

We can think of the wavenumber as 2π times the number of wave oscillations per unit length, or wavelength per unit radian. The wavenumber is a fundamental property of a wave. We label the wavenumbers in the x-, y-, and z-directions as k, l, and m, respectively. These wavenumbers are defined as

$$k = \frac{2\pi}{\lambda_x} \qquad l = \frac{2\pi}{\lambda_y} \qquad m = \frac{2\pi}{\lambda_z} \,, \tag{1.2}$$

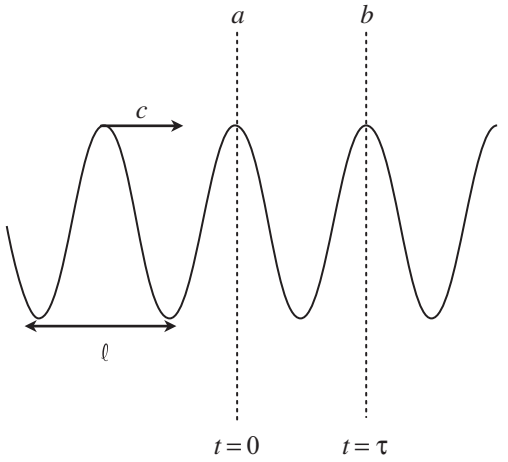

FIGURE 1.8 A wave with wavelength ℓ moves to the right with speed c. The wave crest moves from point a to b in time τ, which is the period of oscillation of the wave as seen by a stationary observer.

where λ_x, λ_y, and λ_z are the wavelengths of the wave in the x-, y-, and z-directions, respectively. The *wave vector*, $\vec{\kappa}$, defines the direction of wave propagation and is given by

$$\vec{\kappa} = k\hat{x} + l\hat{y} + m\hat{z}\,. \tag{1.3}$$

The *wave period*, τ, is the time required for the fluid particles to make one oscillation. If the wave is moving, then the wave period is the time required for successive wave crests to pass a stationary observer, as illustrated in Fig. 1.8. For waves with periods less than a few hours, the effects of the Earth's rotation (the Coriolis force, see Appendix A) can be ignored. The *wave frequency*, ω, is 2π times the number of wave oscillations per unit time, *i.e.*,

$$\omega = \frac{2\pi}{\tau}\,. \tag{1.4}$$

1.2.3 WAVE PHASE AND WAVE SPEED

Let $A\cos(kx - \omega t)$ describe a wave with amplitude A, wavenumber k, and frequency ω. As we shall see, the minus sign indicates a wave moving in the positive x-direction. A single oscillation of the wave either in space or time is a *cycle* of 2π radians or 360°. Each point in the cycle is a *phase point*. If the wave cycle is represented in *polar coordinates*, as illustrated in Fig. 1.9, then the wave phase, ϕ, is represented by the positive angle between the radius vector and the horizontal axis which corresponds to $\phi = 0$. Thus, the wave phase is often referred to as the *phase angle*, *i.e.*, $\phi = kx - \omega t$. In the two-dimensional case,

$$\phi = \vec{\kappa} \cdot \vec{r} - \omega t = kx + mz - \omega t\,, \tag{1.5}$$

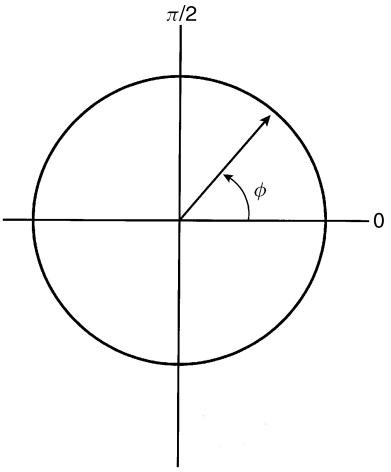

FIGURE 1.9 An illustration of phase angle in polar coordinates.

where $\vec{r}$ is the radius vector defined by

$$\vec{r} = x\hat{x} + z\hat{z}\,. \tag{1.6}$$

Consider now a wave described by

$$f(x, z, t) = \Re A e^{i\phi} = A\cos(kx + mz - \omega t)\,, \tag{1.7}$$

where $\Re$ indicates the real part of the complex number.[2] From (1.7) we see that at a fixed point in space, the function f oscillates with angular frequency ω, and at any instant of time f will have a wave structure of the form $\cos(kx + mz)$. The lines of constant ϕ determine the spatial orientation of the *wave fronts* or crests as represented by the dashed lines in Fig. 1.10. The equation for the family of wave fronts is

$$\phi(x, z) = kx + mz = \text{constant}\,. \tag{1.8}$$

If the z-component of the wave vector, m, goes to zero, then the vertical wavelength, $\lambda_z \to \infty$, and the wave fronts become parallel to the z-axis. Likewise, if $k \to 0$, then the horizontal wavelength, $\lambda_x \to \infty$, and the wave fronts become parallel to the x-axis. From (1.8), we can write

$$z_\phi = -\frac{k}{m}x + \text{constant}\,, \tag{1.9}$$

[2] We shall use mostly exponential notation in describing waves. Since this results in complex numbers, we must select at the very end of an analysis the real parts of the numbers in order to get physically meaningful results.

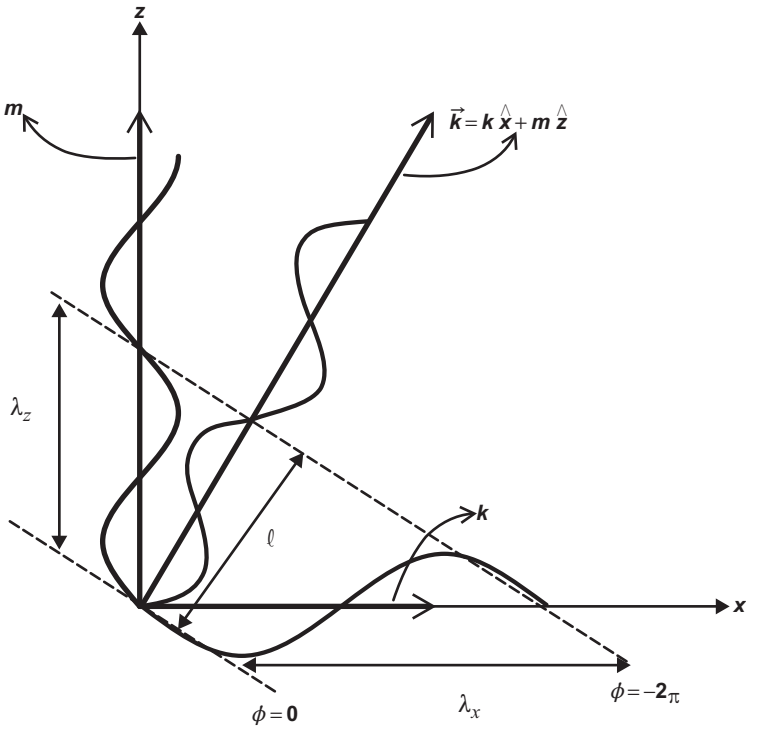

FIGURE 1.10 An illustration of wave fronts and wave vectors for a two-dimensional wave. The wave fronts are perpendicular to the wave vector. The negative values of phase angle ϕ indicate that these wave fronts passed a stationary observer earlier than the following fronts.

where z_ϕ is the height of a line of constant phase. We can define a *phase vector* as

$$\vec{\phi} = x\hat{x} + z_\phi \hat{z}\,. \tag{1.10}$$

Then, using (1.9) in (1.10) gives

$$\vec{\phi} = x\left(\hat{x} - \frac{k}{m}\hat{z}\right)\,. \tag{1.11}$$

It follows that

$$\vec{\kappa} \cdot \vec{\phi} = (k\hat{x} + m\hat{z}) \cdot x\left(\hat{x} - \frac{k}{m}\hat{z}\right) = 0\,, \tag{1.12}$$

and we see that the wave vector is perpendicular to the wave fronts, as illustrated in Fig. 1.10. The magnitude of the wave vector is

$$|\vec{\kappa}|^2 = k^2 + m^2\,, \tag{1.13}$$

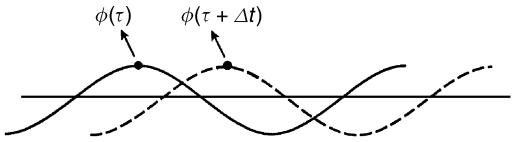

FIGURE 1.11 A wave moving in the x–z plane seen at times τ and $\tau + \Delta t$.

FIGURE 1.12 A surfer riding a wave at a point of constant wave phase. The surfer is moving at the phase speed of the wave.

where we have rotated the coordinate axis so that the x-axis is in the direction of horizontal wave propagation. It follows from (1.13) that

$$\left(\frac{1}{\ell}\right)^2 = \left(\frac{1}{\lambda_x}\right)^2 + \left(\frac{1}{\lambda_z}\right)^2 . \tag{1.14}$$

It is clear from (1.14) that ℓ must be less than either λ_x or λ_z.

To determine the wave speed, we pick a point on the wave, for example, a wave crest, and follow it along the direction of wave propagation, as illustrated in Fig. 1.11 which shows the wave at times τ and $\tau + \Delta t$. The *phase velocity*, c, of the wave is the speed at which a point of constant phase moves in the direction of wave propagation. It is important to keep in mind that we are talking about the speed of a disturbance (the wave) moving through a fluid, not the speed of the fluid. Figure 1.12 shows a surfer riding a wave at a point of constant wave phase. The surfer is moving at the wave phase speed. If we differentiate (1.5) holding ϕ constant, we get

$$\left.\frac{d\phi}{dt}\right|_{\phi} = \vec{\kappa} \cdot \frac{d\vec{r}}{dt} - \omega = 0 , \tag{1.15}$$

and, consequently,

$$\frac{d|\vec{r}|}{dt} = c = \frac{\omega}{\kappa} = \frac{\omega}{\sqrt{k^2 + m^2}} . \tag{1.16}$$

In Fig. 1.10, we see that the components of the wave vector along the horizontal and vertical axes have wavenumbers less than κ and wavelengths greater than ℓ. The speed of the wave along the horizontal x-axis, c_x, is obtained by differentiating (1.5) with respect to t holding ϕ and z constant, *i.e.*,

$$\left.\frac{d\phi}{dt}\right|_{\phi,z} = k\frac{dx}{dt} - \omega = 0, \tag{1.17}$$

and then

$$c_x = \frac{\omega}{k}. \tag{1.18}$$

Likewise, the phase speed in the z-direction is

$$c_z = \frac{\omega}{m}. \tag{1.19}$$

Note also that if we multiply (1.14) by ω^2 and use (1.16) we get

$$\left(\frac{1}{c}\right)^2 = \left(\frac{1}{c_x}\right)^2 + \left(\frac{1}{c_z}\right)^2, \tag{1.20}$$

indicating that phase speed is not a vector.

In textbooks and the scientific literature, we will see references to either phase speed or phase velocity. For example, Gossard and Hooke (1975), Booker and Bretherton (1967), and Baines (1995) use "phase velocity," while Hines (1960), Lighthill (1978), and Gill (1982) use "phase speed." The distinction between the terms "speed" and "velocity" is trivial if we agree that in either case we are describing the speed of a wave in the direction of wave propagation.

1.2.4 GROUP VELOCITY

One of the most important and perhaps least appreciated concepts in gravity wave theory is *group velocity*. As we shall see, it is the group velocity that transports wave energy through space. In the real world, all waves must have a source, a point of creation. There are many sources of waves. These can be instantaneous at a point in space, for example, a nuclear explosion, or they can be continuous in time over extended space, for example, flow over a mountain range. However, in any and every case, the energy created by these disturbances must move away from the source. In the stably stratified atmosphere, gravity waves carry this energy away. In many books on gravity waves, the wave characteristics, *i.e.*, wavenumber, phase velocity, frequency, *etc*., are treated as if they are independent of wave energy. We have noted that expressions such as (1.7) imply a wave field everywhere in space, but this is an idealization. It is only when the origin of the wave and the transport

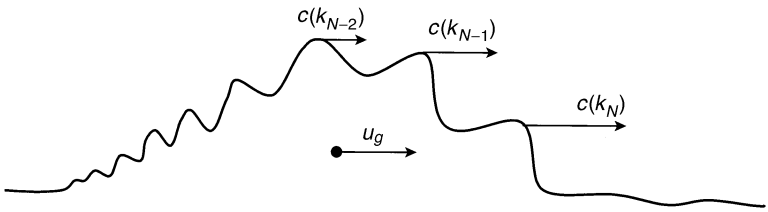

FIGURE 1.13 A ring wave on the surface of a calm pond moves with group velocity u_g, but the wavelets move with their individual phase speeds, c, which is a function of their wavenumbers, *i.e.*, $k_N, k_{N-1}, k_{N-1}, \ldots$.

of the wave energy is considered that the problem becomes realistic. Indeed, it is the energy transport that creates the wave. The wave does not create the energy transport. The speed and direction of energy transport is determined by the group velocity.

Following Lighthill (1978), imagine a stone thrown into a pond of still water. After the initial splash, we see a ring of water, a "ring wave," moving away from its center. If we could follow the wave and examine it closely, we would see that the surface of the wave is continually disturbed by a series of smaller waves or wavelets which propagate from the rear to the front of the larger wave. These wavelets were created when the stone struck the water surface. The energy of that initial disturbance was distributed over a wavenumber *spectrum* of waves. The wavelets at the rear will have shorter wavelengths than the ones at the front, as illustrated in Fig. 1.13. These wavelets act to manifest the larger wave, which in effect is a bundle or packet of waves referred to as a *wave packet*. Each wavelet is moving at phase $c(k)$, which is a function of its wavenumber k. The wavelets at the front have larger wavelengths than the waves at the rear and, therefore have greater phase speeds. However, it is clear that the wavelets are moving faster than wave packet which we observe to have speed u_g. The wavelets appear neither ahead nor behind the wave packet, and we conclude that they have no energy content. If they did, then we would be able to observe them as they moved ahead of the wave packet. Thus, the energy of the disturbance is contained in the wave packet which we can observe on the water's surface. But what is the speed of this packet?

To analyze this energy transport let us consider the simplest case: a wave packet composed of only two waves traveling in the positive x-direction. Let the waves have equal amplitudes, a, but slightly different frequencies, *i.e.*, $\omega + \delta\omega$, $\omega - \delta\omega$, and wavenumbers, *i.e.*, $k + \delta k$ and $k - \delta k$. The superposition of these waves is given by

$$\zeta = a\cos[(k+\delta k)x - (\omega+\delta\omega)t] + a\cos[(k-\delta k)x - (\omega-\delta\omega)t]\,. \quad (1.21)$$

With some trigonometry, (1.21) can be written as

$$\zeta = 2a\cos(\delta k x - \delta\omega t)\cos(kx - \omega t)\,. \quad (1.22)$$

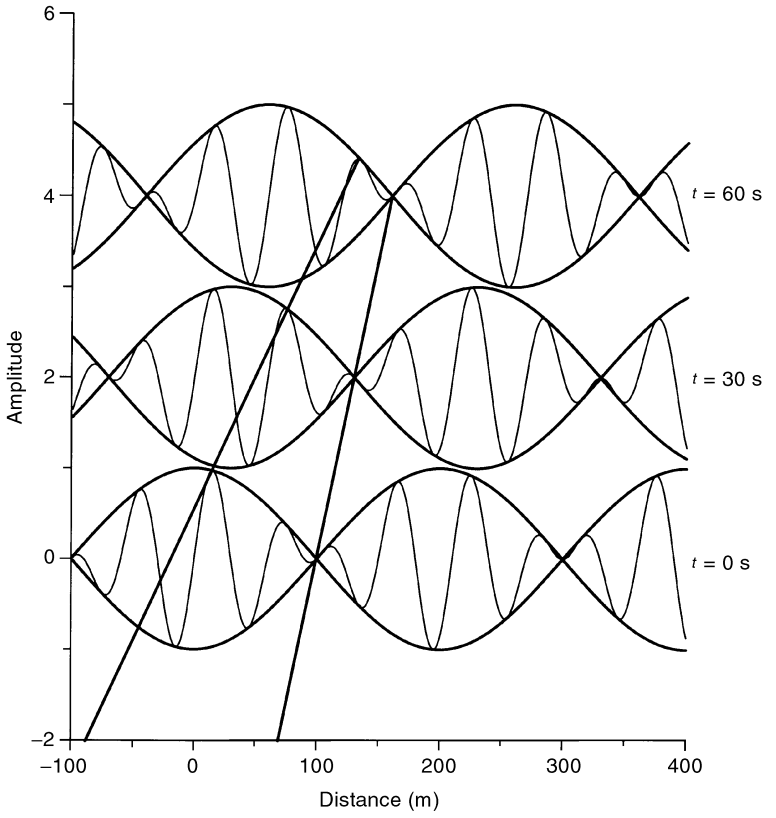

FIGURE 1.14 A modulated carrier wave at times 0, 30, and 60 s.

Figure 1.14 shows a graph of (1.22) at times $t = 0$, 30, and 60 s for the case $k = 2\pi/60\ \mathrm{m}^{-1}$, $\delta k = 2\pi/400\ \mathrm{m}^{-1}$, $\omega = 2\pi/10\ \mathrm{s}^{-1}$, and $\delta\omega = 2\pi/400\ \mathrm{s}^{-1}$. The two waves combine to form an amplitude-modulated carrier given by $\cos(kx - \omega t)$. The sloping lines in Fig. 1.14 connect the crests of the carrier wave and the node points of the wave packet at various times. The slopes of these lines are proportional to the speeds of the crests and the nodes, and it is clear that the carrier waves are moving faster than the packet. The amplitude modulation is given by $2a\cos(\delta k x - \delta\omega t)$. The phase velocity of the carrier wave is $\omega/k = 6\ \mathrm{m\ s}^{-1}$. Note that wave energy cannot pass through the *node* points of the carrier wave since the amplitude there is zero. The wave energy is trapped in the wave packet and is thereby constrained to move with the wave packet. The velocity of this packet is called the group velocity. In the same way that we developed an expression for the phase speed, we calculate the group velocity in the x-direction as

$$u_g = \frac{\delta\omega}{\delta k}\,. \tag{1.23}$$

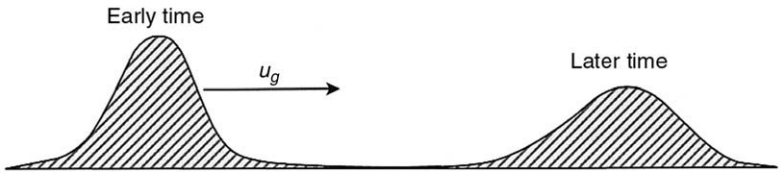

FIGURE 1.15 A cross-section of a ring wave seen at early and late times.

In the limit of small values of $\delta\omega$ and δk, (1.23) becomes

$$u_g = \frac{\partial \omega}{\partial k}\,. \tag{1.24}$$

Likewise, the group velocity in the vertical direction is

$$w_g = \frac{\partial \omega}{\partial m}\,. \tag{1.25}$$

The group velocity for the wave in Fig. 1.14 is $u_g = 1\ \mathrm{m\ s^{-1}}$.

1.2.5 WAVE DISPERSION

Phase speed is a function of wave frequency and wavenumber, *i.e.*, $c = \omega/k = \lambda_x/\tau$. For a given wave period, τ, long waves will travel faster than short waves, and this leads to *wave dispersion*. Recalling the example of a surface ring wave created by a stone thrown into a calm pond, we observe that initially the disturbance is sharply peaked, as illustrated in Fig. 1.15. As the ring expands, the width of the disturbance increases. This is because the waves that make up the disturbance are moving at different phase speeds. Because the long waves move faster than the short waves, the disturbance broadens. Note that the total energy of the wave packet remains constant, but disperses horizontally. The relation between phase speed and wavenumber is called the *dispersion relation*.

1.3 THE BUOYANT FORCE

The term gravity wave suggests that gravity is the restoring force acting on a fluid parcel which has been displaced from its equilibrium position. However, it is the fluid *buoyancy* rather than gravity that is acting. Consider an atmosphere at rest and an air parcel of mass m_p in equilibrium with its environment at height z_e. Let the parcel be displaced upward a small distance δz from z_e. We assume that during this displacement the air in the parcel does not mix with its surroundings

and that the process is adiabatic, *i.e.*, there is no net transfer of heat across the surface of the air parcel. The buoyant force, $\vec{F}_b$, acting on the fluid parcel is

$$\vec{F}_b = -g(m_p - m_a)\,\hat{z}\,, \tag{1.26}$$

where m_a is the mass of air displaced by the fluid parcel and g is the acceleration (positive upward) of gravity. From the second law of motion, we have

$$m_p \frac{d^2(\delta z)}{dt^2} = -g(m_p - m_a)\,. \tag{1.27}$$

The mass of each air parcel can be expressed as, for example,

$$m_p = \rho_p v_p\,, \tag{1.28}$$

where ρ_p and v_p are the density and volume of the air parcel, respectively. We assume that the volumes of the air parcel and the displaced air are equal and that the pressure in the air parcel is always equal to the environmental pressure. The *equation of state* for dry air is represented by the ideal gas law, *i.e.*,

$$p = \rho R T\,, \tag{1.29}$$

where R is the universal *gas constant*. For dry air, $R = 287\ \mathrm{J\,kg^{-1}\,K^{-1}}$. Using (1.29), (1.27) becomes

$$\frac{d^2(\delta z)}{dt^2} = -g\,\frac{\rho_p - \rho_a}{\rho_p} = -g\,\frac{T_a - T_p}{T_a}\,, \tag{1.30}$$

where ρ_a is the environmental air density and T_a and T_p are the environmental and parcel temperatures, respectively. We now expand T_a and T_p to first order, *i.e.*,

$$T_a(z_e + \delta z) = T_0 + \left.\frac{\partial T_a}{\partial z}\right|_{z_e} \delta z + \cdots \tag{1.31}$$

$$T_p(z_e + \delta z) = T_0 + \left.\frac{\partial T_p}{\partial z}\right|_{z_e} \delta z + \cdots\,, \tag{1.32}$$

where T_0 is the temperature at equilibrium height z_e. Using (1.31) and (1.32) in (1.30) and noting that the change of environmental temperature due to the vertical displacement is small, *i.e.*,

$$T_0 \gg \frac{\partial T_a}{\partial z}\,\delta z, \tag{1.33}$$

(1.30) becomes

$$\frac{d^2(\delta z)}{dt^2} = -\frac{g}{T_a}\left(\frac{\partial T_a}{\partial z} - \frac{\partial T_p}{\partial z}\right)\delta z\,. \tag{1.34}$$

As shown in Appendix A, $-\partial T_p/\partial z = g/c_p = \Gamma$, where c_p is the *specific heat capacity* at constant pressure and Γ is the *adiabatic lapse rate*. For dry air, $c_p = 1005\ \mathrm{J\,kg^{-1}\,K^{-1}}$ so that $\Gamma \approx -10\ \mathrm{K\,km^{-1}}$. We also set $\partial T_a/\partial z = \gamma_a$, *i.e.*, the *atmospheric temperature gradient*. Equation (1.34) can now be written as

$$\frac{d^2(\delta z)}{dt^2} = -\frac{g}{T_a}(\Gamma - \gamma_a)\,\delta z\,. \tag{1.35}$$

The *potential temperature* is discussed in Appendix A and is defined as

$$\theta = T_a\left(\frac{1000}{p}\right)^{R/c_p}\,. \tag{1.36}$$

The potential temperature is the temperature an air parcel would have if it were brought down adiabatically from a height where the pressure is p to a height where the pressure is 1000 mb, *i.e.*, the ground surface. It is straightforward to show that if the logarithmic derivative of (1.36) is taken and if use is made of (1.29) and the *hydrostatic approximation* (see Appendix A), *i.e.*,

$$\frac{\partial p}{\partial z} = -\rho g, \tag{1.37}$$

then

$$\frac{1}{\theta}\frac{\partial \theta}{\partial z} = \frac{1}{T_a}\left(\frac{\partial T_a}{\partial z} + \frac{g}{c_p}\right) = \frac{\Gamma - \gamma_a}{T_a}\,. \tag{1.38}$$

Using (1.38) in (1.35) gives the result

$$\frac{d^2(\delta z)}{dt^2} = -\frac{g}{\theta}\frac{\partial \theta}{\partial z}\,\delta z\,. \tag{1.39}$$

Equations (1.35) and (1.39) are examples of the equation for simple harmonic motion in the vertical direction. If the air parcel is displaced vertically and released, then its motion is described by

$$\delta z(t) = A\,e^{iNt} + B\,e^{-iNt}\,, \tag{1.40}$$

where

$$N = \sqrt{\frac{g}{\theta}\frac{\partial \theta}{\partial z}}\,. \tag{1.41}$$

If N is real, then it is the frequency of oscillation of the air parcel and is sometimes called the Brunt–Väisälä frequency. If N is imaginary, *i.e.*, $\partial\theta/\partial z < 0$, then

$$\delta z = A\, e^{-N_i t} + B\, e^{N_i t}, \tag{1.42}$$

where $N = iN_i$. Solution B in (1.42) represents unbounded growth of the displacement, *i.e.*, an *instability*. This type of instability is due to the thermal properties of the atmosphere and is refereed to as *convective instability*. Thus, we see that wave motion is possible only when the atmosphere is *stably stratified*, *i.e.*, $\partial\theta/\partial z > 0$; however, this does not mean that all gravity waves have frequency N. We shall see that the Brunt–Väisälä frequency represents the maximum frequency for vertically propagating gravity waves. In an *isothermal* atmosphere where $\partial T/\partial z = 0$, $N \approx 0.02\ \mathrm{s}^{-1}$, and the buoyancy period is about 5 min. Holton (1992) gives $N \approx 0.012\ \mathrm{s}^{-1}$ for average tropospheric conditions, so that the buoyancy period is about 8 min. In the nighttime PBL, $N \approx 0.2\ \mathrm{s}^{-1}$, and typical buoyancy periods are on the order of a minute.

The buoyant force described by (1.26) is restricted to vertical displacements of fluid parcels. Purely vertical displacements of air parcels due to waves occur only when the wave train is moving horizontally, for example, surface waves on water. However, gravity waves almost always propagate at an angle to the vertical, and so the fluid parcels will be displaced at an angle to the vertical. To examine this case, let δs be the displacement of a fluid parcel from its equilibrium position on a surface inclined an angle β to the horizontal, as shown in Fig. 1.16. As we shall see, air parcels displaced by a gravity wave oscillate along streamlines which are perpendicular to the path of the wave, and so we can consider the inclined surface to be a streamline. The buoyant force acting on the displaced air parcel is

$$\vec{F}_s = m_p \frac{d^2(\delta s)}{dt^2} = -g\, \sin\beta\, (m_p - m_a)\,, \tag{1.43}$$

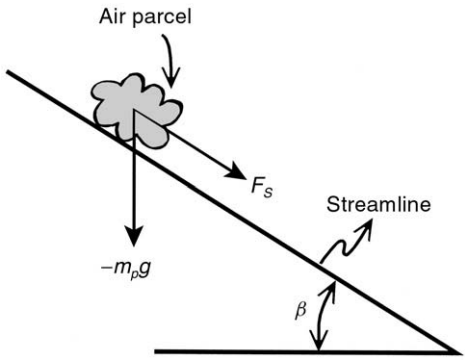

FIGURE 1.16 Air parcel displaced from equilibrium along an inclined plane.

where $-g \sin\beta$ is the component of gravity along s. Continuing as above, (1.30) takes the form

$$\frac{d^2(\delta s)}{dt^2} = -g \sin\beta \, \frac{T_a - T_p}{T_a}. \tag{1.44}$$

Expanding T_a and T_p in Taylor series in the s-direction and using these in (1.44) gives

$$\frac{d^2(\delta s)}{dt^2} = -\frac{g \sin\beta}{T_a} \left(\frac{\partial T_a}{\partial s} - \frac{\partial T_p}{\partial s} \right) \delta s. \tag{1.45}$$

The air parcel will warm or cool at the adiabatic lapse rate projected onto the streamline. Then (1.45) can be written as

$$\frac{d^2(\delta s)}{dt^2} = -\frac{g \sin\beta}{T_a} \left(\frac{\partial T_a}{\partial s} + \frac{g \sin\beta}{c_p} \right) \delta s. \tag{1.46}$$

Taking the derivative of the potential temperature (1.36) in the s-direction and again making use of the equation of state and the hydrostatic approximation, we get

$$\frac{1}{\theta} \frac{\partial \theta}{\partial s} = \frac{1}{T_a} \left(\frac{\partial T_a}{\partial s} + \frac{g \sin\beta}{c_p} \right). \tag{1.47}$$

However, since $\partial T_a / \partial s = (\partial T_a / \partial z) \sin\beta$, (1.47) becomes

$$\frac{1}{\theta} \frac{\partial \theta}{\partial s} = \frac{1}{T_a} \left(\frac{\partial T_a}{\partial z} + \frac{g}{c_p} \right) \sin\beta. \tag{1.48}$$

But this is identical to $(1/\theta)(\partial\theta/\partial z) \sin\beta$. Substituting this result into (1.46) gives

$$\frac{d^2(\delta s)}{dt^2} = -\frac{g}{\theta} \frac{\partial \theta}{\partial z} \sin^2\beta \, \delta s \,, \tag{1.49}$$

and the motion of the parcel along the s-direction is

$$\delta s(t) = A \, e^{iN't} + B \, e^{-iN't} \,, \tag{1.50}$$

where

$$N' = \left[\frac{g}{\theta} \frac{\partial \theta}{\partial z} \sin^2\beta \right]^{1/2} = N \sin\beta. \tag{1.51}$$

If $\beta = 0°$, then the motion is horizontal but not oscillatory since then $N' = 0$. We see that the range of buoyancy frequencies extends from 0 to N depending on the angle of propagation relative to the horizontal plane, β.

1.4 THE BOUSSINESQ APPROXIMATION

In the next chapter, we derive the equations for gravity waves from the Eulier equations of motion for an irrotational, frictionless atmosphere, *i.e.*,

$$\rho \frac{D\vec{U}}{Dt} = -\nabla p + \rho \vec{g}\,. \tag{1.52}$$

$$\frac{D\rho}{Dt} + \rho \nabla \cdot \vec{U} = 0 \tag{1.53}$$

$$\frac{DP}{Dt} - C_s^2 \frac{D\rho}{Dt} = 0, \tag{1.54}$$

where $C_S = (c_p/c_v)(p/\rho)$ is the speed of sound, c_v is the specific heat capacity for dry air at constant volume, and

$$\frac{D}{Dt} = \frac{\partial}{\partial t} + \vec{U} \cdot \nabla\,. \tag{1.55}$$

Equations (1.52)–(1.54) represent the conservation of momentum, the conservation of mass, and the conservation of thermal energy. From the thermal energy equation (1.54), we see that the density and pressure are related, and in general $\rho = f(p, T)$. However, in such an atmosphere, *acoustic* waves will exist as well as gravity waves, and this can lead to complications. It is through the *Boussinesq approximation* (see, for example, Spiegel and Veronis, 1960) that we can eliminate the acoustic waves.

Consider (1.52), and make the substitutions $\rho = \rho_0 + \rho_1$ and $p = p_0 + p_1$, where subscript 0 indicates a mean or background value and subscript 1 indicates a small departure from the mean state, *i.e.*, a *perturbation*. Then (1.52) becomes

$$(\rho_0 + \rho_1)\frac{D\vec{U}}{Dt} = -\nabla p_0 + \rho_0 \vec{g} - \nabla p_1 + \rho_1 \vec{g}\,. \tag{1.56}$$

We assume the background state is in hydrostatic equilibrium (1.37), so that (1.56) becomes

$$\left(1 + \frac{\rho_1}{\rho_0}\right)\frac{D\vec{U}}{Dt} = -\frac{1}{\rho_0}\nabla p_1 + \frac{\rho_1}{\rho_0}\vec{g}\,. \tag{1.57}$$

The Boussinesq approximation assumes that $|\rho_1/\rho_0| \ll 1$, and accordingly, fluctuations in density affect the buoyancy term much more then the inertial term. Thus, density fluctuations are considered only when they occur in combination with g.

The condition that $|\rho_1/\rho_0| \ll 1$ is satisfied when the vertical scale of the mean motions, λ_z, is much less than the isothermal *scale height* of the atmosphere (see Appendix A), *i.e.*,

$$\lambda_z \ll H_s = RT_0/g, \tag{1.58}$$

where H_s is the scale height of the isothermal atmosphere. To visualize this requirement, consider the vertical variation of density in an isothermal atmosphere, *i.e.*,

$$\rho = \rho_s \, e^{-z/H_s}, \tag{1.59}$$

where ρ_s is the density at the ground surface. Then

$$\frac{\partial \rho}{\partial z} = -\frac{\rho_s}{H_s} \, e^{-z/H_s} = -\frac{\rho}{H_s}. \tag{1.60}$$

If we replace the derivative in (1.60) by differentials, we can write

$$\frac{\delta \rho}{\rho} = -\frac{\delta z}{H_s}, \tag{1.61}$$

where $\delta\rho$ is a small change in density due to a small vertical displacement δz. Now, if we identify the small density change $\delta\rho$ with the density perturbation ρ_1, and if we identify the small vertical displacement δz with the scale of the wave motion λ_z, then we can write

$$\left| \frac{\rho_1}{\rho_0} \right| = \frac{\lambda_z}{H_s}. \tag{1.62}$$

We see from (1.62) that if $\lambda_z \ll H_s$, then $|\rho_1/\rho_0| \ll 1$.

As demonstrated by Spiegel and Veronis (1960), a result of the Boussinesq approximation is that the fluctuating changes in density due to local pressure variations are negligible. In this case, we can treat the fluid as being incompressible, and acoustic waves are eliminated. A consequence of the separation of the pressure and density changes is that as $c_s \to \infty$, *i.e.*, as the fluid becomes incompressible, (1.54) can be broken into two terms. Then the Eulier equations take the form

$$\frac{D\vec{U}}{Dt} = -\frac{1}{\rho_0} \nabla p + \frac{\rho_1}{\rho_0} \vec{g}. \tag{1.63}$$

$$\nabla \cdot \vec{U} = 0 \tag{1.64}$$

$$\frac{D\rho}{Dt} = 0. \tag{1.65}$$

Other results following the Boussinesq approximation, which are derived in Appendix A, are

$$\frac{1}{\theta_0}\frac{\partial \theta_0}{\partial z} = -\frac{1}{\rho_0}\frac{\partial \rho_0}{\partial z} \tag{1.66}$$

and

$$\frac{\theta_1}{\theta_0} = -\frac{\rho_1}{\rho_0}. \tag{1.67}$$

Note that because of (1.66) the Brunt–Väisälä frequency (1.41) can be written as

$$N^2 = -\frac{g}{\rho_0}\frac{\partial \rho_0}{\partial z}. \tag{1.68}$$

2

The Linear Theory

Almost all of what we know about the nature of atmospheric gravity waves is derived from the *linear theory*. From a computational consideration, the simplified equations describing linear systems are solved much more rapidly than nonlinear ones.[1] But perhaps more important is that linear systems are more comprehensible and understandable than non-linear systems. The recipe for linearization is simple. Some variable q is expanded into a *background state* q_0 and a *perturbation* q_1. The background state is usually assumed to be steady or slowly varying. We will also ignore the effects of the Earth's rotation and air viscosity. The perturbations are assumed much smaller than the background values, and it is assumed that the perturbations do not affect the background state. However, if the perturbations are small, then the products of the perturbations are also small and therefore are neglected. The mathematics is simplified if we assume the background state is steady and horizontally uniform. Thus, we can take the background flow to be the mean flow, but still varying vertically. The perturbations can be caused by several mechanisms including turbulence, density currents, thermal plumes, *etc.*; however, here we shall only consider perturbations that are due to gravity waves. Neglecting products of the wave perturbations negates the interactions of waves. The waves can add and subtract to form, for example, wave packets, but they cannot interact to form new waves or to destroy existing waves. Each wave of the packet behaves as if it were the only wave present. The accuracy and practical limitations of the linear theory were examined by Dörnbrack and Nappo (1997) by comparing the results of a linear wave model with a nonlinear, time-dependent, hydrodynamic numerical model (Dörnbrack, 1998). They concluded

[1] However, with ever-increasing computer speeds, this advantage is becoming less significant.

that essentially similar results are obtained from each model for the important wave parameters and dynamic effects.

The simplicity of the linear theory is not without cost. In the real atmosphere, waves interact with other waves as well as with turbulence which itself might have been produced by interactions between waves and the mean flow. Observations of gravity waves made, for example, by Gossard and Munk (1954); Caughey and Readings (1975); Bedard, Canavero, and Einaudi (1986); Koch and Golus (1988); Einaudi, Bedard, and Finnigan (1989); Hauf *et al.* (1996); and Lee and Barr (1998) show complex wave structures, with time-varying amplitudes and usually with several frequencies present. A single-frequency wave, *i.e.*, a *monochromatic* wave, with constant amplitude lasting more than several wave periods is essentially never observed in the lower troposphere. Applying linear analyses to observations of wave phenomena is often frustrating, as discussed by Hunt, Kaimal, and Gaynor (1985) and Finnigan (1988). For example, wave amplitudes often change with time; waves within the nighttime planetary boundary layer are often nonlinear because of the presence of the ground surface; and it is generally difficult to distinguish between gravity waves and turbulence (see, for example, Bretherton, 1969; Stewart, 1969). Yet in spite of these difficulties, the linear theory is still useful and provides a first-order estimate of most wave phenomena. Also, the simplicity of the linear theory gives an understandable picture of the wave processes and observations. Relatively few people can think and work in a nonlinear world.

2.1 THE TAYLOR–GOLDSTEIN EQUATION

The *Taylor–Goldstein* equation is the *wave equation* for linear gravity waves. We consider the two-dimensional Eulier equations for irrotational and inviscid flow. Under the Boussinesq approximation we have

$$\frac{\partial u}{\partial t} + u\frac{\partial u}{\partial x} + w\frac{\partial u}{\partial z} = -\frac{1}{\rho}\frac{\partial p}{\partial x} \tag{2.1}$$

$$\frac{\partial w}{\partial t} + u\frac{\partial w}{\partial x} + w\frac{\partial w}{\partial z} = -\frac{1}{\rho}\frac{\partial p}{\partial z} - g \tag{2.2}$$

$$\frac{\partial u}{\partial x} + \frac{\partial w}{\partial z} = 0 \tag{2.3}$$

$$\frac{\partial \rho}{\partial t} + u\frac{\partial \rho}{\partial x} + w\frac{\partial \rho}{\partial z} = 0\,. \tag{2.4}$$

Equation (2.1) is the equation for momentum in the x-direction. Equation (2.2) is the equation for momentum in the z-direction. Equation (2.3) is the mass continuity equation. From (1.54) we see that (2.4) represents the conservation of

thermal energy. We linearize the above equations according to

$$q(x, z, t) = q_0(z) + q_1(x, z, t)\,, \tag{2.5}$$

where $q_0(z)$ is a steady, horizontally uniform background value and $q_1(x, z, t)$ is a first-order perturbation. We also assume that the background flow is in hydrostatic balance, *i.e.*, (1.37). Then (2.1)–(2.4) become

$$\frac{\partial u_1}{\partial t} + u_0\frac{\partial u_1}{\partial x} + w_1\frac{du_0}{dz} = -\frac{1}{\rho_0}\frac{\partial p_1}{\partial x} \tag{2.6}$$

$$\frac{\partial w_1}{\partial t} + u_0\frac{\partial w_1}{\partial x} = -\frac{1}{\rho_0}\frac{\partial p_1}{\partial z} - \frac{\rho_1}{\rho_0}g \tag{2.7}$$

$$\frac{\partial u_1}{\partial x} + \frac{\partial w_1}{\partial z} = 0 \tag{2.8}$$

$$\frac{\partial \rho_1}{\partial t} + u_0\frac{\partial \rho_1}{\partial x} + w_1\frac{d\rho_0}{dz} = 0\,, \tag{2.9}$$

where ρ_0 is the background atmospheric density. At this point, we can either double Fourier transform (2.6)–(2.9) in x and t or we can assume wave-like solutions of the form

$$u_1(x, z, t) = \tilde{u}(z)e^{i(kx-\omega t)} \tag{2.10}$$

$$\rho_1(x, z, t) = \tilde{\rho}(z)e^{i(kx-\omega t)} \tag{2.11}$$

$$p_1(x, z, t) = \tilde{p}(z)e^{i(kx-\omega t)} \tag{2.12}$$

$$w_1(x, z, t) = \tilde{w}(z)e^{i(kx-\omega t)}\,. \tag{2.13}$$

In either case, (2.6)–(2.9) become

$$-i\omega\tilde{u} + iu_0k\tilde{u} + \tilde{w}\frac{du_0}{dz} = -\frac{i}{\rho_0}k\tilde{p} \tag{2.14}$$

$$-i\omega\tilde{w} + iu_0k\tilde{w} = -\frac{1}{\rho_0}\frac{d\tilde{p}}{dz} - \frac{\tilde{\rho}}{\rho_0}g \tag{2.15}$$

$$ik\tilde{u} + \frac{d\tilde{w}}{dz} = 0 \tag{2.16}$$

$$-i\omega\tilde{\rho} + iu_0k\tilde{\rho} + \tilde{w}\frac{d\rho_0}{dz} = 0. \tag{2.17}$$

Note that because $\tilde{p}_1$, $\tilde{w}_1$, *etc.* are functions only of z, we can write the derivatives as total rather than partial. We now define the *intrinsic frequency*, Ω, as the

frequency of a wave relative to the flow, *i.e.*, the frequency of a wave measured by an observer drifting with the fluid at speed u_0; therefore,

$$\Omega = \omega - u_0 k. \tag{2.18}$$

Note that ω is the wave frequency observed in a fixed coordinate system, for example, by a *microbarograph* or a *sodar* at the ground surface. Chimonas and Hines (1986) refer to Ω as the *Doppler-shifted* intrinsic wave frequency. The wind speed, u_0, in (2.18) is the component of the background wind in the direction of wave propagation. If we considered both horizontal directions, then

$$\Omega = \omega - u_0 k - v_0 l = \omega - \vec{v}_H \cdot \vec{\kappa}, \tag{2.19}$$

where $\vec{v}_H$ is the horizontal background wind vector. If we write (2.18) as

$$\omega = \Omega + u_0 k, \tag{2.20}$$

then the *apparent frequency*, ω, of the wave is larger than Ω if the wave is moving with the wind and smaller than Ω if the wave is moving against the wind. From (2.20) the apparent horizontal phase speed is

$$c_x = \frac{\Omega}{k} + u_0 = c_I + u_0\,, \tag{2.21}$$

where $c_I = \Omega/k$ is the intrinsic phase speed in the x-direction. In Chapter 4, we shall see that Ω plays an essential role in the trapping or ducting of gravity waves. Using (1.68) and (2.18), (2.14)–(2.17) become

$$i\Omega\tilde{u} - \tilde{w}\frac{du_0}{dz} = \frac{i}{\rho_0} k\tilde{p} \tag{2.22}$$

$$i\Omega\tilde{w} = \frac{1}{\rho_0}\frac{d\tilde{p}}{dz} + \frac{\tilde{\rho}}{\rho_0} g \tag{2.23}$$

$$ik\tilde{u} + \frac{d\tilde{w}}{dz} = 0 \tag{2.24}$$

$$i\Omega\tilde{\rho} + \tilde{w}\frac{\rho_0}{g} N^2 = 0\,. \tag{2.25}$$

Hines (1960) refers to (2.22)–(2.25) as the *polarization equations* because they give the relative phases and amplitudes of various wave quantities. Solving (2.22)–(2.25) for $\tilde{w}$ gives

$$\frac{d^2\tilde{w}}{dz^2} + \frac{1}{\rho_0}\frac{d\rho_0}{dz}\frac{d\tilde{w}}{dz} + \left[\frac{k^2N^2}{\Omega^2} + \frac{k}{\Omega}\frac{d^2u_0}{dz^2} + \frac{k}{\Omega}\frac{1}{\rho_0}\frac{d\rho_0}{dz}\frac{du_0}{dz} - k^2\right]\tilde{w} = 0. \tag{2.26}$$

The second term in (2.26) represents the effects of changing atmospheric density on wave amplitude. We can remove this height dependence of the base-state density by assuming an exponentially decreasing atmospheric density of the form given by (1.59). Then (2.26) becomes

$$\frac{d^2\tilde{w}}{dz^2} - \frac{1}{H_s}\frac{d\tilde{w}}{dz} + \left[\frac{k^2N^2}{\Omega^2} + \frac{k}{\Omega}\frac{d^2u_0}{dz^2} - \frac{k}{\Omega}\frac{1}{H_s}\frac{du_0}{dz} - k^2\right]\tilde{w} = 0\,. \tag{2.27}$$

We can simplify this equation by defining a new variable, $\hat{w}$, by

$$\tilde{w} = e^{\int (1/2H_s)\,dz}\,\hat{w} = e^{z/2H_s}\,\hat{w}\,. \tag{2.28}$$

Substitution of (2.28) into (2.27) leads to the Taylor–Goldstein equation (Taylor, 1931; Goldstein, 1931)

$$\frac{d^2\hat{w}}{dz^2} + \left[\frac{k^2N^2}{\Omega^2} + \frac{k}{\Omega}\frac{d^2u_0}{dz^2} - k^2 - \frac{k}{\Omega}\frac{1}{H_s}\frac{du_0}{dz} - \frac{1}{4H_s^2}\right]\hat{w} = 0\,. \tag{2.29}$$

Note that if (1.60) and (2.28) are used in (2.22), one gets

$$i\Omega\tilde{u}e^{-z/2H_s} - \frac{du_0}{dz}\hat{w} = \frac{ik}{\rho_s}\tilde{p}e^{z/2H_s}\,. \tag{2.30}$$

To have a consistent notation, we must define new variables for $\tilde{u}$ and $\tilde{p}$, *i.e.*,

$$\tilde{u} = e^{z/2H_s}\hat{u} \tag{2.31}$$

$$\tilde{p} = e^{-z/2H_s}\hat{p}\,. \tag{2.32}$$

Likewise, using (1.60) and (2.28) in (2.25) leads to

$$\tilde{\rho} = e^{-z/2H_s}\hat{\rho}\,. \tag{2.33}$$

We can write (2.29) in a more compact form by representing the derivative by primes and using (2.20). The Taylor–Goldstein equation then takes the form

$$\frac{d^2\hat{w}}{dz^2} + \left[\frac{N^2}{(c-u_0)^2} + \frac{u_0''}{(c-u_0)} - \frac{1}{H_s}\frac{u_0'}{(c-u_0)} - \frac{1}{4H_s^2} - k^2\right]\hat{w} = 0\,, \tag{2.34}$$

where, for simplicity, we have replaced the c_x notation by c.[2] The first term on the left in the brackets is called the *buoyancy* term, the second term is called the *curvature* term, and the third term is called the *shear* term. The fourth term

[2] Note that in the future c will be used to mean c_x unless otherwise stated.

does not have a special name and is usually taken to be small below the tropopause. The last term in the brackets can be called the *nonhydrostatic* term. If the vertical perturbations are in hydrostatic balance, *i.e.*,

$$\frac{\partial p_1}{\partial z} = -\rho_1 g \,, \tag{2.35}$$

then this term will not appear in (2.34).

Analytic series solutions of (2.34) are possible, and in some cases solutions in terms of special functions (for example, Bessel functions) are known; however, solutions in terms of plane waves require the bracketed term in (2.34) to be constant. These plane wave solutions will have the form

$$w_1(x, z, t) = \hat{w}(z)\, e^{z/2H_s}\, e^{i(kx-\omega t)} \,. \tag{2.36}$$

However, using (1.59), an alternate form is

$$w_1(x, z, t) = \hat{w}(z) \left(\frac{\rho_s}{\rho_0(z)}\right)^{1/2} e^{i(kx-\omega t)} \,. \tag{2.37}$$

From (2.37) we see that if the wave propagates upward, then the background air density seen by the wave, ρ_0, decreases. But from (2.37), this means that the wave amplitude, w_1, increases with height. It will be shown in Chapter 3 that associated with a vertically propagating gravity wave is a vertical flux of horizontal momentum or *wave stress* given by

$$\tau(z) = -\rho_0 \overline{u_1 w_1} \,, \tag{2.38}$$

where the overline indicates a horizontal average which is usually over a wavelength if the wave is nearly monochromatic. It will be shown in Chapter 5 that in the absence of wave dissipation this momentum flux is constant. But if ρ_0 decreases with height, then the momentum being transported upward will also decrease. The only way the momentum can be constant is for $\overline{u_1 w_1}$ to increase in such a way as to balance the decrease in density. The factor $(\rho_s/\rho_0)^{1/2}$ accounts for this increase. An analogous effect causes the "crack" of a bullwhip. The thickness of a bullwhip decreases from about 4 cm at the handle to about 0.1 cm at the end. The decrease in linear density causes the amplitude of the wave initiated near the handle to grow as the wave moves down the whip. By the time the impulse reaches the end of the whip, the perturbation velocity of the whip end exceeds the speed of sound, causing the loud crack sound.

2.2 A SIMPLE SOLUTION

We begin our examination of the solutions of the Taylor–Goldstein equation (2.34) with the simple case of constant background stratification, N, and wavelength much less than H_s.

2.2.1 NO BACKGROUND WIND SPEED

In the case of no background wind speed, (2.34) becomes

$$\frac{d^2\hat{w}}{dz^2} + \left[\frac{k^2N^2}{\omega^2} - k^2\right]\hat{w} = 0\,. \tag{2.39}$$

The general solution is

$$\hat{w}(z) = Ae^{imz} + Be^{-imz}\,, \tag{2.40}$$

where the vertical wavenumber m is given by

$$m^2 = k^2\left[\frac{N^2}{\omega^2} - 1\right]. \tag{2.41}$$

Solving (2.41) for ω gives the *dispersion relation*

$$\omega = \pm\frac{kN}{(k^2+m^2)^{1/2}}\,. \tag{2.42}$$

The dispersion relation is perhaps the most important element in the linear wave theory because it relates the angular frequency of the wave to the wave structure and the physical characteristics of the atmosphere. The dispersion relation fixes all the variables of the wave field, *i.e.*, k, m, and ω. We cannot arbitrarily assign values to these variables. Each set of values is unique for a given atmospheric condition, *i.e.*, they are *eigenvalues* (see, for example, Bender and Orzag, 1999). Consider the negative branch of (2.42), then

$$\omega = ck = -\frac{kN}{(k^2+m^2)^{1/2}}\,, \tag{2.43}$$

which tells us that the horizontal phase velocity, c, is negative, and thus, the wave must be traveling in the negative x-direction. But if the wave is traveling in the negative x-direction, then $k < 0$ so that $\omega > 0$. Thus, if we keep to this convention, then $\omega > 0$ for all conditions.

The general solution of (2.39) in physical space is

$$w_1(x, z, t) = A\, e^{z/2H_s}\, e^{i(kx+mz-\omega t)} + B\, e^{z/2H_s}\, e^{i(kx-mz-\omega t)}\,. \tag{2.44}$$

The A solution represents the positive branch of (2.41), and the B solution represents the negative branch. Following the discussions in Chapter 1, Section 1.2, we see that for the A solution the phase speed in the z-direction is

$$c_z = \frac{\omega}{m}\,. \tag{2.45}$$

The slope of lines of constant phase (1.8) in the x-z plane is

$$\frac{dz}{dx} = -\frac{k}{m}\,. \tag{2.46}$$

For the B solution, these quantities are

$$c_z = -\frac{\omega}{m} \tag{2.47}$$

and

$$\frac{dz}{dx} = \frac{k}{m}\,. \tag{2.48}$$

The wave vectors and wave fronts for these cases are illustrated in Fig. 2.1. From the dispersion relation (2.42), we see that

$$\omega = \frac{kN}{(k^2+m^2)^{1/2}} = N\cos\beta, \tag{2.49}$$

where β is the angle the wave vector makes with the horizontal, as illustrated in Fig. 2.1. Several important aspects of wave propagation are implied by this simple result. For example, if N changes with height, then waves of constant frequency propagate along curved paths.[3] The wave frequency cannot be greater than N. When $\omega = N$, then $\beta = 0$, the wave propagates horizontally, and fluid particles oscillate vertically. When ω/N is very small, corresponding to strong stratification or low-frequency waves, β approaches $\pi/2$, the wave propagates almost vertically, and the fluid particles oscillate almost horizontally. We see that the spectrum of gravity wave frequencies is constrained between these two limits.

It is of interest to consider for a moment this upper limit of wave frequency. What physical process limits ω to values less than N? As angle β approaches zero, the wave fronts become increasingly vertical, and the fluid particles oscillate in

[3] Strictly speaking, the general solution (2.40) holds only when N and u_0 are constant, but we can use these results to approximate the behavior of smoothly varying N.

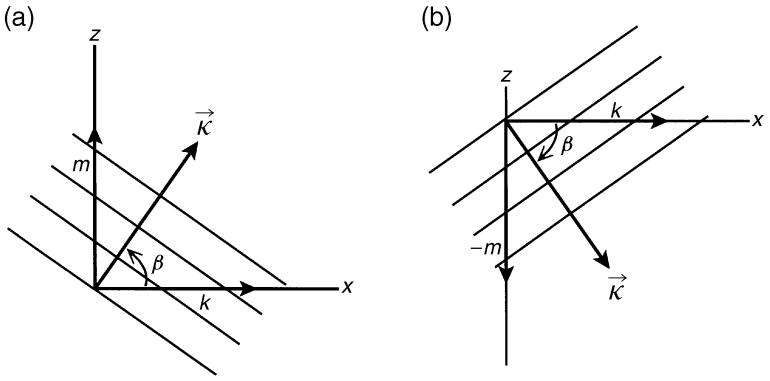

FIGURE 2.1 Wave vectors and wave fronts for an upward-propagating wave (a) and a downward-propagating wave (b).

increasingly vertically oriented planes. In Chapter 1, we saw that the frequency of oscillation of a vertically displaced parcel in a stably stratified fluid is N. This is the resonant frequency of the fluid, and even though one could imagine some process that would force a vertical vibration at a frequency greater than N, this vibration would not be supported by the fluid buoyancy, and the amplitude of the oscillation would decay rapidly with distance from the forcing point. Thus, the maximum frequency for gravity waves is N; however, a wide spectrum of wave frequencies exists below this value. It is sometimes erroneously assumed that gravity waves have frequency equal only to N. Clearly, this is not correct.

Let us now consider the group velocities for this case. Using (1.24) and (1.26), we have

$$u_g = \frac{Nm^2}{(k^2 + m^2)^{3/2}} \tag{2.50}$$

and

$$w_g = -\frac{Nmk}{(k^2 + m^2)^{3/2}}\,. \tag{2.51}$$

An interesting and paradoxical result is that the vertical phase velocity, c_z, and the vertical group velocity, w_g, are always of opposite signs. To see this more clearly, use (2.45) and (2.49) in (2.51) to get

$$w_g = -c_z \sin^2 \beta\,. \tag{2.52}$$

Because $\sin^2 \beta$ is always positive, c_z and w_g must be of opposite signs. Recall that the group velocity represents the speed of wave energy propagation, and so from (2.52) we see that if the wave fronts are propagating upward, then the wave energy must be propagating downward. Hines (1989a) describes a film made with Dave Fultz of the University of Chicago in 1967.

This film exhibited a laboratory tank simulation in which water having a height-varying salinity modeled the atmosphere's height-varying density. A rocking paddle at the top of the tank acted as the source of waves and so produced a downward energy flow. It was seen to be producing ripples of phase that progressed downward—in complete accord with normal experience but in complete contradiction of my accompanying patter on gravity waves! Or so it seemed, until a burnt-out match appeared on the screen, collected smoke from thin air, burst spontaneously into flame, and then was struck back into its pristine, virginal state. This entropy experiment was then repeated, but with time now progressing and the phase ripples ascending toward the source, as advertised.

In Chapter 5, we shall discuss the transports of energy by waves, and it is in this context that the $c_z - w_g$ paradox is resolved.

Consider now a downward-propagating wave, but with upward-propagating wave energy. Then

$$\vec{k} = k\hat{x} - m\hat{z}\,, \tag{2.53}$$

and

$$\vec{v_g} = \frac{Nm}{(k^2 + m^2)^{1/2}}(m\hat{x} + k\hat{z})\,. \tag{2.54}$$

Then

$$\vec{v_g} \cdot \vec{k} = \frac{Nm}{(k^2 + m^2)^{1/2}}(km - mk) = 0\,, \tag{2.55}$$

and we see that the flux of wave energy is perpendicular to the wave vector and parallel to the wave fronts, as illustrated in Fig. 2.2. From the continuity equation (2.16), and using the B solution of (2.42), we have

$$u_1 = \frac{m}{k} w_1\,, \tag{2.56}$$

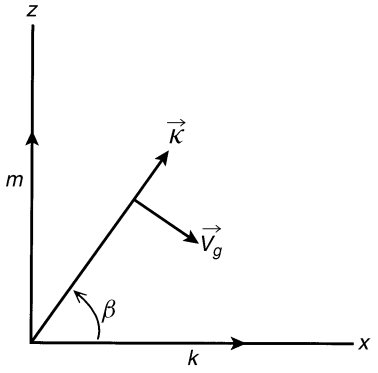

FIGURE 2.2 Relationship between phase velocity and group velocity for an internally propagating gravity wave. The flux of wave energy is in the direction of the group velocity vector.

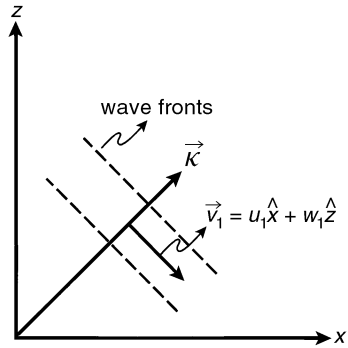

FIGURE 2.3 The motions of fluid particles are parallel to the wave fronts and perpendicular to the wave vector.

or, equivalently,

$$\frac{dx}{dz} = \frac{m}{k}\,. \tag{2.57}$$

Thus, fluid particles oscillate in planes parallel to the wave fronts and perpendicular to the wave vector, as illustrated in Fig. 2.3.

It is of interest to consider the *monochromatic* gravity wave. Such a wave is described by single horizontal and vertical wavenumbers, k and m, respectively. For the case of constant flow and stratification, the solution to the Taylor–Goldstein equation (2.39) has the form of (2.44). The dispersion relation can be used to fix ω and, consequently, the phase speeds. But does a monochromatic wave have a group velocity? From the definitions of group velocity, (1.24) and (1.26), it is clear that a monochromatic wave cannot have a group velocity because k, m, and ω are constants. However, one must wonder about the reality of a monochromatic wave. A monochromatic wave will extend indefinitely in space and time. This is the property of the Fourier transform or the wave-like solutions (2.10)–(2.13). The energy associated with such a wave will also be spread throughout space and time, and so the energy flux, which is proportional to the group velocity, will be zero. However, all "real" waves have a beginning and an ending. Real waves can neither extend nor persist indefinitely. To be generated, gravity waves require a disturbance to the stratification, and it is extremely unlikely that only a single wave will be excited. Indeed, a spectrum of waves will always be excited. The fact that waves have a beginning tells us that a spectrum of waves is required *a priori* so that at some point and at some time these waves can interact to cancel each other, thus making an ending. To be accurate, we should say "nearly monochromatic" rather than monochromatic.

From (2.41) we see that the vertical wavenumbers for the general solution to (2.39) are

$$m = \pm\, k \left[\frac{N^2}{\omega^2} - 1\right]^{1/2}\,. \tag{2.58}$$

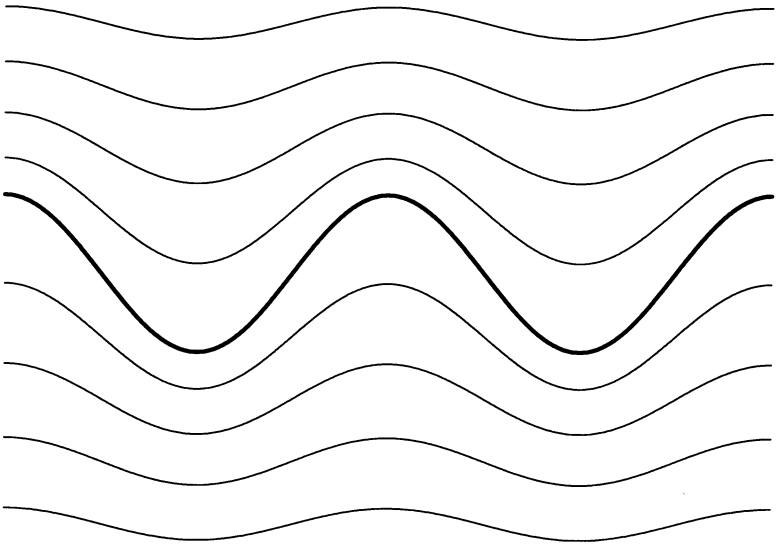

FIGURE 2.4 Evanescent wave generated at height z_L.

If $\omega < N$, then m is real, and the wave is said to be *propagating* or *internal*. If $\omega > N$, then m is imaginary, and the wave is said to be *evanescent* or *external*.[4] Consider the evanescent case $\omega > N$. Then we can write

$$m = \pm ik\left[1 - \frac{N^2}{\omega^2}\right]^{1/2} = \pm iq\,. \tag{2.59}$$

The general solution is then

$$w_1 = A\, e^{-q(z-z_L)}\, e^{i(kx-\omega t)} \qquad \text{for } z > z_L \tag{2.60}$$

$$= B\, e^{q(z-z_L)}\, e^{i(kx-\omega t)} \qquad \text{for } z < z_L, \tag{2.61}$$

where z_L is the height where the evanescent wave is created. Since we require the solutions to be bounded, we use solution A or B, depending on the sign of $z - z_L$. The waves then look like those illustrated in Fig. 2.4. Wave amplitude decreases exponentially with distance from the level of wave generation. Evanescent waves propagate only horizontally. It is possible for a wave to switch from propagating to evanescent if the stratification is changing with height. At the point where the wave switches, wave reflection occurs. Wave reflection will be discussed in Chapter 4.

[4] Gossard and Hooke (1975) in a section titled "Names and nonsense" express some well-established opinions about the use and misuse of nomenclature that has grown with the development of gravity wave theory. Accordingly, we shall refrain from using the terms "external" and "internal" in describing gravity waves and instead shall use "propagating" and "evanescent," which are more descriptive of the wave characteristics.

2.2.2 CONSTANT BACKGROUND WIND SPEED

We next consider the effect of a constant background wind on wave propagation. We are reminded that the wind speed, u_0, is the component of the background wind velocity in the direction of wave propagation. The Taylor–Goldstein equation is now

$$\frac{d^2\hat{w}}{dz^2} + \left[\frac{k^2N^2}{\Omega^2} - k^2\right]\hat{w} = 0\,. \tag{2.62}$$

The phase angle (1.7) is now given by

$$\phi = kx + mz - \Omega t. \tag{2.63}$$

The vertical wavenumber is

$$m = \pm\left[\frac{k^2N^2}{(\omega - u_0k)^2} - k^2\right]^{1/2}, \tag{2.64}$$

where we have used (2.18). Because of the background wind speed, we cannot *a priori* assign a branch to (2.64), since this would eventually determine the sign of the vertical group velocity. Indeed, we must not let the mathematics of the problem determine the physics of the problem. Rather, we must select the physics, and let the mathematics follow. Solving (2.64) for ω gives

$$\omega = u_0k \pm \left[\frac{N^2k^2}{m^2 + k^2}\right]^{1/2}. \tag{2.65}$$

The phase velocities are obtained by using (2.65) in (1.18) and (1.19). This gives

$$c = u_0 + \frac{N}{k}\cos\beta\,, \tag{2.66}$$

$$c_z = u_0\frac{k}{m} + \frac{N}{m}\cos\beta\,. \tag{2.67}$$

Using (2.65) in (1.24) and (1.26) gives the group velocity components as

$$u_g = u_0 + \frac{m^2}{N^2}\,(c - u_0)^3\,, \tag{2.68}$$

$$w_g = -\frac{km}{N^2}\,(c - u_0)^3\,. \tag{2.69}$$

To illustrate how the appropriate wavenumbers are selected, consider the case where u_g and w_g are both positive and $c > u_0$. Then, since k is positive, we see

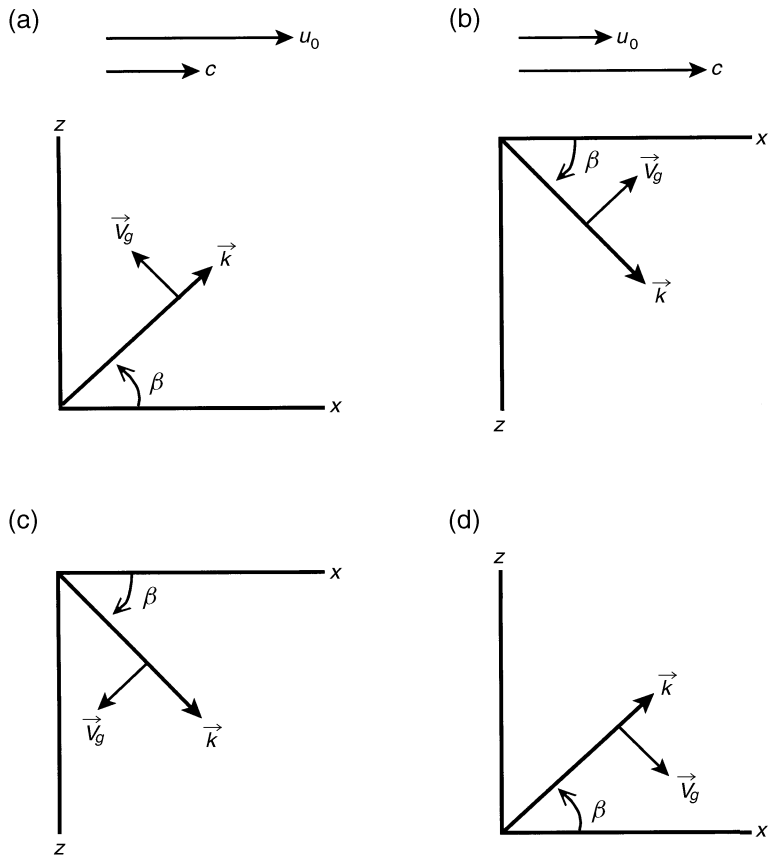

FIGURE 2.5 Wave vectors and group velocity vectors for (a) upward-propagating energy and wave speed less than background wind speed; (b) upward-propagating energy and wave speed greater than background wind speed; (c) same as (a) but with downward-propagating energy; and (d) same as (b) but with downward-propagating energy.

from (2.69) that $m < 0$. If $c < u_0$, then we must choose $m > 0$ if w_g is positive. Consider now the case where $u_g > 0$ and $w_g < 0$, *i.e.*, downward-propagating energy. Now we must take $m > 0$ when $c > 0$ and $m < 0$ when $c < 0$. These cases are illustrated in Fig. 2.5.

The background wind also affects the polarization equations. For example, consider (2.22) which relates the horizontal wind perturbation, $\tilde{u_1}$, to the pressure perturbation, $\tilde{p_1}$. For constant background wind, the equation is

$$\tilde{u_1} = \frac{\tilde{p_1}}{\rho_0(c - u_0)}. \tag{2.70}$$

Thus, if $c > u_0$, the pressure and wind speed perturbations are in phase, but if $c < u_0$, then the perturbations are 180° out of phase.

2.3 THE WKB METHOD

We have seen that the Taylor–Goldstein equation (2.34) has plane wave solutions only when the atmospheric variables are constant. However, one may ask if an approximate solution is possible when u_0 and N are slowly varying? Consider the equation

$$\frac{d^2\psi}{dz^2} + Q^2(z)\psi = 0\,. \tag{2.71}$$

The *WKB* method (see, for example, Pitteway and Hines, 1965; Einaudi and Hines, 1970; Laprise, 1993; Bender and Orzag, 1999) provides an approximate solution to (2.71) when $Q(z)$ is slowly changing. The WKB solution to (2.71) is

$$\psi(z) = \psi_0\, Q^{-1/2}\, e^{\pm i \int_0^z Q\, dz}\,, \tag{2.72}$$

where ψ_0 is a constant. Equation (2.72) satisfies the equation

$$\frac{d^2\psi}{dz^2} + Q^2(z)(1+d)\psi = 0\,, \tag{2.73}$$

where

$$d = \frac{1}{2Q^3}\frac{d^2Q}{dz^2} - \frac{3}{4Q^4}\left(\frac{dQ}{dz}\right)^2\,. \tag{2.74}$$

If $d \ll 1$, then (2.73) approaches (2.71), *i.e.*, the Taylor–Goldstein equation. Obviously, Q cannot equal zero since then $d \to \infty$. We shall see in Chapter 6 that when $Q = 0$ wave reflection occurs, and thus, the WKB solution does not allow wave reflection. If, however, Q becomes large and dQ/dz becomes small, then d becomes small. If Q is a vertical wavenumber, then large Q implies small vertical wavelength, and if dQ/dz is small, then the vertical scale of the background variables is small. Thus, if the WKB method is to apply, then the wave must appear to be propagating in a medium which is changing slowly relative to the vertical wavelength of the wave.

The WKB method is commonly used in wave studies on almost all atmospheric scales except the boundary layer and the lower troposphere where background wind speed and stratification can change significantly over a vertical wavelength. In many applications, the WKB approximation is combined with the assumption that the wave perturbations are in hydrostatic equilibrium. When this assumption is made, the Taylor–Goldstein equation takes the form

$$\frac{d^2\hat{w}}{dz^2} + \frac{N^2}{(c-u_0)^2}\hat{w} = 0. \tag{2.75}$$

2.4 ENERGETICS

A characteristic of all waves is the ability to transport energy. Indeed, if not for this property the study of wave phenomena would be little more than a mathematical curiosity. However, on all atmospheric scales of motion waves exist and transport energy. In this section, we introduce the concepts of wave kinetic and potential energy. The subject of energy transport by waves will be taken up in Chapter 5. We consider here the two-dimensional case with constant wind and stratification.

We begin by multiplying (2.6) by u_1 and (2.7) by w_1 and adding the two equations to get

$$\frac{D}{Dt}\left[\frac{1}{2}\rho_0\left(u_1^2+w_1^2\right)\right]+u_1\frac{\partial p_1}{\partial x}+w_1\frac{\partial p_1}{\partial z}+\rho_1 g w_1=-\rho_0 u_1 w_1\frac{du_0}{dz}\,, \quad (2.76)$$

where the total derivative is

$$\frac{D}{Dt}=\frac{\partial}{\partial t}+u_0\frac{\partial}{\partial x}\,. \quad (2.77)$$

We can write

$$u_1\frac{\partial p_1}{\partial x}+w_1\frac{\partial p_1}{\partial z}=\frac{\partial}{\partial x}(u_1p_1)+\frac{\partial}{\partial z}(w_1p_1)-p_1\left(\frac{\partial u_1}{\partial x}+\frac{\partial w_1}{\partial z}\right), \quad (2.78)$$

and using this and the continuity equation (2.8) in (2.76) gives, after some rearrangement of terms, the equation for the total perturbation energy per unit volume:

$$\frac{D}{Dt}\left[\frac{1}{2}\rho_0\left(u_1^2+w_1^2\right)\right]+\rho_1 g w_1=-\frac{\partial}{\partial x}(u_1p_1)-\frac{\partial}{\partial z}(w_1p_1)-\rho_0 u_1 w_1\frac{du_0}{dz}\,. \quad (2.79)$$

If we define ζ_1 as the vertical displacement of an air parcel from its equilibrium position, then $w_1 = D\zeta_1/Dt$, and from (2.9) the perturbation density, ρ_1, is

$$\rho_1=-\frac{d\rho_0}{dz}\,\zeta_1\,. \quad (2.80)$$

Note that because $d\rho_0/dz < 0$, an upward displacement of the air results in a positive density perturbation, *etc.* Using (1.68) and (2.80) in (2.9) results in

$$\rho_1 g w_1=\frac{D}{Dt}\left(\frac{1}{2}\rho_0 N^2\zeta_1^2\right), \quad (2.81)$$

where we have assumed that ρ_0 and N are constants. Then (2.79) becomes

$$\frac{D}{Dt}\left[\frac{1}{2}\rho_0\left(u_1^2+w_1^2\right)+\frac{1}{2}\rho_0 N^2\zeta_1^2\right]=-\frac{\partial}{\partial x}(u_1p_1)-\frac{\partial}{\partial z}(w_1p_1)-\rho_0u_1w_1\frac{du_0}{dz}\,. \tag{2.82}$$

The first term in brackets on the left-hand side of (2.82) is the total rate of change of the *perturbation kinetic energy*, and the second term is the total rate of change of *perturbation potential energy*. To verify this latter statement, consider the gravitational potential energy (PE) gained by a fluid parcel when it is displaced vertically a distance ζ_1 by the wave, *i.e.*,

$$PE=-\int_0^{\zeta_1}F_b\,dz\,, \tag{2.83}$$

where F_b is the buoyant force per unit volume exerted on the air parcel. From (1.39) and using (1.68), the buoyant force per unit volume is

$$F_b=g\frac{d\rho_0}{dz}z\,. \tag{2.84}$$

Using (2.84) in (2.83) and integrating gives the desired result, *i.e.*,

$$PE=-\frac{1}{2}g\frac{d\rho_0}{dz}\zeta_1^2=\frac{1}{2}\rho_0N^2\zeta_1^2\,. \tag{2.85}$$

The equation for the total perturbation energy per unit volume is

$$\frac{DE}{Dt}+\frac{\partial}{\partial x}(u_1p_1)+\frac{\partial}{\partial z}(w_1p_1)=-\rho_0u_1w_1\frac{du_0}{dz}\,, \tag{2.86}$$

where

$$E=\frac{1}{2}\rho_0\left(u_1^2+w_1^2+N^2\zeta_1^2\right). \tag{2.87}$$

The second and third terms on the left-hand side of (2.86) represent the divergences of the fluxes of wave energy in the horizontal and vertical directions, respectively. The right-hand side represents another flux term which we shall see involves the wave stress and the background wind shear.

An examination of the units of the terms u_1p_1 and w_1p_1 in (2.86) shows that these represent fluxes of wave energy in the x- and z-directions, respectively. To see this, consider Fig. 2.6 which illustrates the horizontal displacement δx of a surface of unit area A by the wave perturbation velocity u_1 against a force f_1 due to the pressure perturbation. Then

$$u_1p_1\approx\frac{f_1\delta x}{A\delta t}=\frac{\delta W}{A\delta t}\,, \tag{2.88}$$

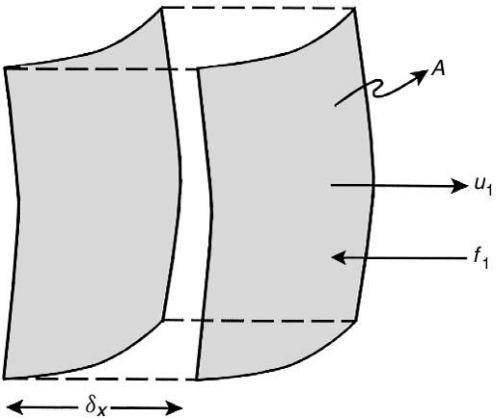

FIGURE 2.6 Horizontal displacement δ_x of a unit surface area by the horizontal wave perturbation velocity u_1.

where δW is the differential work done by the wave, and $u_1 p_1$ is the work done per unit area per unit time, but this is the horizontal flux of wave energy in the x-direction. The same analysis applies to the vertical term, $w_1 p_1$.

In the absence of a background wind, (2.86) becomes

$$\frac{\partial E}{\partial t} + \frac{\partial}{\partial x}(u_1 p_1) + \frac{\partial}{\partial z}(w_1 p_1) = 0\,, \tag{2.89}$$

and we see that the wave energy per unit volume is a conserved quantity, *i.e.*, the total rate of change of E is equal to the local divergence of the energy flux.

Because the wave energy is periodic in space and time, it is more useful to discuss spatially averaged values rather than local values. Because we are considering linear waves, an average over a large distance is essentially the same as an average over a single wavelength. Then, considering for the moment all three spatial dimensions, we can write

$$\overline{E} = \frac{1}{2}\rho_0 \left(\overline{u_1^2 + v_1^2 + w_1^2}\right) + \frac{1}{2}\rho_0 N^2 \overline{\zeta_1^2}\,, \tag{2.90}$$

where the overbars indicate time averaging. Now let us assume that there is a gravity wave with amplitude a_1, *i.e.*,

$$w_1 = a_1 \cos(\phi)\,, \tag{2.91}$$

where $\phi = kx + ly + mz - \omega t$. The polarization equations for u_1 and v_1, are

$$u_1 = -\frac{k}{k^2 + l^2} m a_1 \cos\phi \tag{2.92}$$

$$v_1 = -\frac{l}{k^2 + l^2} m a_1 \cos\phi, \tag{2.93}$$

where l is the wavenumber in the y-direction. Averaging the wave kinetic energy (KE) over 2π radians and using (2.91)–(2.93) gives

$$\overline{KE} = \frac{1}{2}\rho_0 \left(\overline{u_1^2 + v_1^2 + w_1^2}\right) = \frac{1}{4}\rho_0 \left(\frac{k^2 + l^2 + m^2}{k^2 + l^2}\right) a_1^2 = \frac{1}{4}\rho_0 \frac{a_1^2}{\cos^2\beta}, \tag{2.94}$$

where β is the angle the wave vector κ makes with the x–y plane, as illustrated in Fig. 2.7. The vertical displacement, ζ_1, appearing in the expression for the potential energy in (2.85) is related to w_1 by

$$\zeta_1 = \int w_1 \, dt = \frac{a_1}{\omega} \sin\phi \, . \tag{2.95}$$

Then using (2.95) in (2.85) and averaging over 2π and using (2.49) gives

$$\overline{PE} = \frac{1}{4}\rho_0 \frac{a_1^2}{\cos^2\beta} \, . \tag{2.96}$$

We see that the average kinetic and potential energies are equal, but this should not come as a surprise. As with all simple harmonic motions, for example, a pendulum

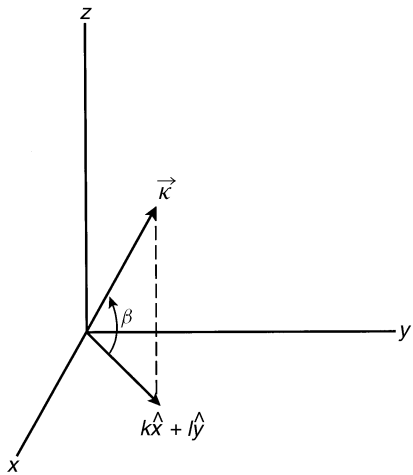

FIGURE 2.7 Projection of the three-dimensional wave vector onto the horizontal plane.

or a weighted spring, the kinetic and potential energies are equal but of opposite phases. When KE is at its maximum value, PE is at its minimum value, *etc.* When we calculate the average energies over a cycle, the results must be equal. Adding $\overline{KE}$ and $\overline{PE}$ gives the mean perturbation energy per unit volume as

$$\overline{E} = \frac{1}{2}\rho_0 \frac{a_1^2}{\cos^2\beta}\,. \tag{2.97}$$

The flux of wave energy across the surface bounding a volume of fluid is obtained by averaging the flux terms in (2.86) over a wavelength to get the *energy flux density vector*

$$\vec{F} = \overline{p_1 \vec{V}_1} = \frac{1}{2}\,\Re\big(p_1 \vec{V}_1^*\big)\,, \tag{2.98}$$

where $\vec{V}_1 = u_1\hat{x} + v_1\hat{z}$. Solving for p_1 using polarization equations (2.22) and (2.23) and using (2.91) and (2.92), the energy flux density vector is

$$\vec{F} = \frac{1}{2}\frac{\rho_0 \omega m^2 a_1^2}{k^3}\hat{x} - \frac{1}{2}\frac{\rho_0 \omega m a_1^2}{k^2}\hat{z}\,. \tag{2.99}$$

For the two-dimensional wave, $k = \kappa\cos\beta$. Using this and (2.49) in (2.99) gives

$$\vec{F} = \frac{1}{2}\rho_0 \frac{a_1^2}{\cos^2\beta}\left[\frac{Nm^2}{(k^2+m^2)^{3/2}}\hat{x} - \frac{Nkm}{(k^2+m^2)^{3/2}}\hat{z}\right]. \tag{2.100}$$

Using (2.50), (2.51), and (2.97) in (2.100) gives

$$\vec{F} = \overline{E}(u_g\hat{x} + w_g\hat{z}) = \overline{E}\vec{v}_g\,. \tag{2.101}$$

Equation (2.101) is an important result; it tells us that the flux of wave energy is in the direction of the group velocity. Using (2.101), we can write (2.89) as

$$\frac{\partial \overline{E}}{\partial t} + \nabla\cdot\overline{E}\vec{v}_g = 0\,. \tag{2.102}$$

In the absence of a background wind and assuming that uniform thermal stratification k and m will be constants, we can write (2.102) as

$$\frac{\partial \overline{E}}{\partial t} + \vec{v}_g\cdot\nabla\overline{E} = 0\,. \tag{2.103}$$

Thus, we see that wave perturbation energy is constant in the special case of calm winds and constant Brunt–Väisälä frequency.

In the general case, when the background flow is neither calm nor uniform, the equation for the mean wave energy is, after time averaging (2.86),

$$\frac{D\overline{E}}{Dt} + \frac{\partial}{\partial x}(\overline{u_1 p_1}) + \frac{\partial}{\partial z}(\overline{w_1 p_1}) = -\rho_0 \overline{u_1 w_1} \frac{du_0}{d} \,. \tag{2.104}$$

The term on the right-hand side of (2.104) is of interest. In the turbulence theory, the term $-\rho_0 \overline{u'w'} du_0/dz$, where u' and w' are turbulence quantities, represents the production of turbulence kinetic energy. This production is due to the work done by the Reynolds stress ($-\rho_0 \overline{u'w'}$) against the mean rate of strain (du_0/dz). It is always positive. However, such an interpretation of the right-hand side of (2.104) is not apparent. Indeed, if the wave stress $-\rho_0 \overline{u_1 w_1}$ and the mean-wind shear (du_0/dz) are of the same sign, then it would appear that the wave energy will increase; however, it is not clear where this increased energy originates. Since we have assumed *a priori* that the background flow is steady, the energy cannot originate there. If the wave stress and wind shear have opposite signs, then it would appear that the wave energy will decrease. But then where does this energy go? The problem is that our analysis of wave energy is only to first order. If we went to second order, then terms such as $u_1(\partial/\partial z)(u_0 u_1)$, $w_1(\partial/\partial z)(u_0 u_1)$, *etc.* would appear, and these would more clearly define the energy transfer process.

This Page Intentionally Left Blank

3

Terrain-Generated Gravity Waves

3.1 INTRODUCTION

The linearized equations of motion predict that the vertical displacement of a stably stratified flow almost always leads to the generation of gravity waves. This is especially true when the flow is over terrain obstacles such as ridges, hills, and mountains; however, terrain depressions such as canyons, basins, and valleys can also generate gravity waves. Terrain-generated gravity waves have been studied and modeled more than any other kind of gravity wave. Several reasons account for this interest. Large terrain features such as mountain ranges create waves that transport energy and mean-flow horizontal momentum away from the lower atmosphere toward the middle and upper atmosphere where the energy and momentum are deposited. It is now recognized that this deposition of energy and momentum is an essential component of the global circulation. Almost all terrain features generate waves, and the spectrum of these waves is as wide as the

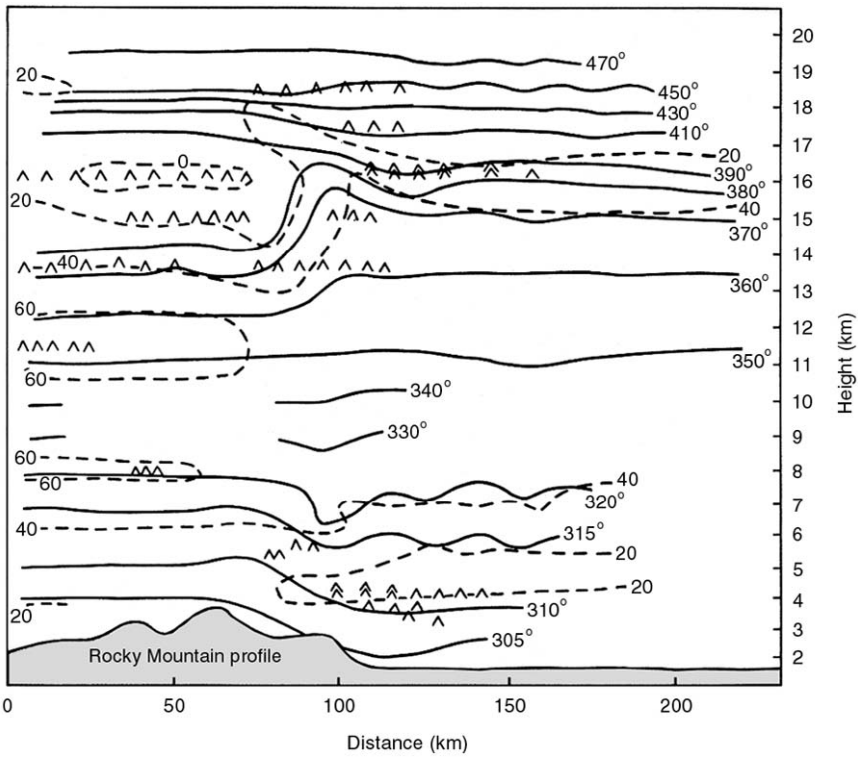

FIGURE 3.1 Waves and turbulence over the Continental Divide in Colorado on February 17, 1970: potential temperature (solid lines, K) and westerly wind component (dashed lines, m s^{-1}). ^ indicates light turbulence, and ⩓ indicates severe turbulence. (From "Observations of mountain-induced turbulence," D.R. Lily, *J. Geophys. Res.* **76**: 6587, 1971.)

spectrum of terrain widths. The amplitudes of terrain-generated gravity waves are proportional to the amplitudes of the wave-generating terrain. This is a significant point because the amplitudes of "ordinary" gravity waves are arbitrary constants. Terrain-generated waves are stationary relative to the ground surface, and they do not experience dispersion. All the waves have the same phase velocity, which is zero. Thus, standing waves, resulting from the superposition of many waves of relatively small amplitudes, can develop above the terrain obstacle, as shown in Fig. 3.1. Under certain conditions, the amplitudes of terrain-generated waves can grow as they move upward and eventually break much like waves at the beach. These breakdowns result in outbreaks of turbulence, more commonly known as *clear air turbulence*, as shown in Fig. 3.1.

To a stationary observer, terrain-generated gravity waves are fixed in space, *i.e.*, they appear to be attached to the terrain feature generating the wave. However, this is the picture in the Eulerian reference frame. Relative to the background flow, the wave must be propagating upwind at the same speed as the wind,

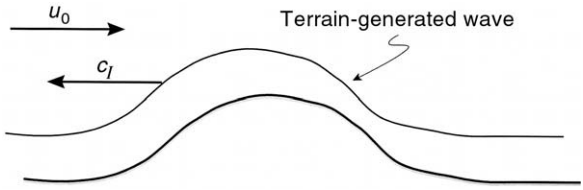

FIGURE 3.2 The intrinsic phase speed, c_I, of a terrain-generated wave is equal to the background wind speed, u_0, but in the opposite direction. To a stationary observer, the wave is stationary.

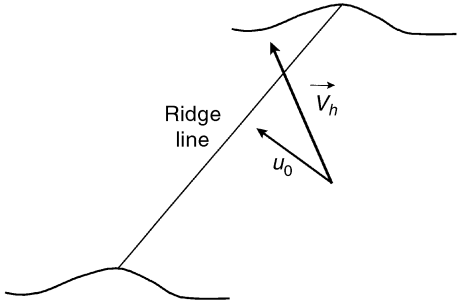

FIGURE 3.3 Gravity waves are generated only by the component of the background wind, u_0, directed perpendicular to the ridge line.

i.e., $c_I = -u_0$, where c_I is the intrinsic phase speed. These velocities are illustrated in Fig. 3.2. Note that u_0 is now the component of the background wind directed over the surface obstacle. If the flow is over a two-dimensional object, for example, a ridge or a series of parallel ridges, then u_0 is the component of the background wind perpendicular to the ridge line, as illustrated in Fig. 3.3. If the background wind is parallel to the ridge line, then $u_0 = 0$ and waves will not be generated. In this chapter, we shall always take u_0 to the component of the background wind directed perpendicular to the obstacle.

Because the wave is stationary relative to the ground surface, $\omega = 0$, and Ω is then

$$\Omega = \omega - ku_0 = -ku_0 \,. \tag{3.1}$$

The intrinsic phase speed is Ω/k, so

$$c_I = \frac{\Omega}{k} = \frac{-ku_0}{k} = -u_0 \,. \tag{3.2}$$

Because the wave vector is in the direction of wave propagation, the sign of the horizontal wavenumber must be given by

$$k = -|k| sgn\,(u_0), \tag{3.3}$$

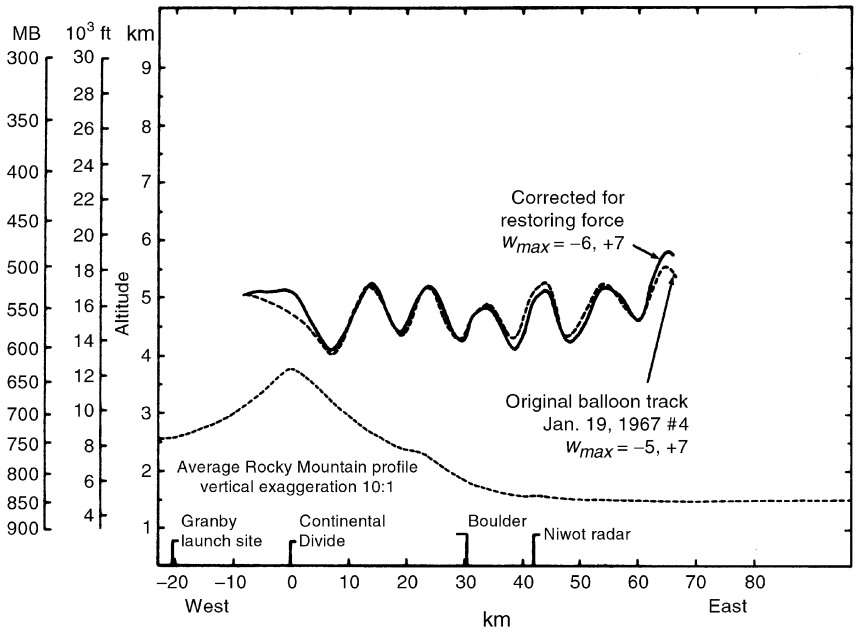

FIGURE 3.4 Illustrated are lee waves downwind of the Continental Divide determined by constant volume balloon flights on January 19, 1967. Sometimes the crests of the waves are marked by standing clouds. (Modified from "The dynamic structure of Lee wave flow as obtained from balloon and air plane observations," I. Vergeiner and D.K. Lilly, *Mon. Weather Rev.* **98**: 220–238, 1970.)

where $sgn(u_0)$ is the sign of u_0. If the wave appears stationary, then it must be propagating against the wind and at the same speed of the wind. If the wind speed changes with height, then the wave speed must also change. This opens the question of what happens to the wave if $u_0 \rightarrow 0$? As we shall see in Chapter 5, the wave is essentially absorbed into the mean flow.

Two types of terrain-generated gravity waves exist: *lee waves* and *mountain waves*. The lee wave, as its name implies, extends downwind from the generating obstacle. The wave is trapped between the ground surface and an upper level where wave reflection occurs and is characterized by a single horizontal wavenumber. Lee waves propagate only horizontally and can extend many wavelengths downwind from the obstacle that generates it, as illustrated in Fig. 3.4. Lee waves are, at times, marked by somewhat evenly spaced bands of clouds extending downwind from mountains and ridges. Because lee waves are trapped in a layer in contact with the ground surface, their influence on the atmosphere above this layer is negligible. We will not treat lee waves in this book. Comprehensive discussions can be found, for example, in Scorer (1949), Turner (1973), Beer (1974), Gossard and Hooke (1975), Scorer (1978), Smith (1979), Gill (1982), and Baines (1995).

3.2 UNIFORM FLOW OVER A SURFACE CORRUGATION

The simplest mountain wave problem is the case of uniform two-dimensional flow with constant Brunt–Väisälä frequency over a surface corrugation. We have seen that the mountain waves move against the background flow. Because the waves are generated at the ground, the waves must carry energy upward. Thus, the horizontal group velocity must be negative and the vertical group velocity must be positive. The phase fronts are parallel to the group velocity vector, and so they must tilt upstream, as illustrated in Fig. 3.5. Because the vertical group velocity must be positive and k must be negative (because $u_0 > 0$), we see from (2.69) that the vertical wavenumber, m, must be negative, *i.e.*, the wave fronts must be moving downward. Let the surface height be given by

$$h(x) = H\, e^{ik_s x}\,, \tag{3.4}$$

where H is the amplitude of corrugation, and

$$k_s = \frac{2\pi}{\lambda_s}\,, \tag{3.5}$$

where λ_s is the wavelength of the corrugation. For constant background wind and stratification, the Taylor–Goldstein equation (2.29) along with (3.1) takes the form

$$\frac{d^2\hat{w}}{dz^2} + \left[\frac{N^2}{u_0^2} - k^2\right]\hat{w} = 0\,, \tag{3.6}$$

and we define the Fourier transform as

$$\hat{w}(k, z) = \int_{-\infty}^{+\infty} w_1(x, z)\, e^{-ikx}\, dx\,. \tag{3.7}$$

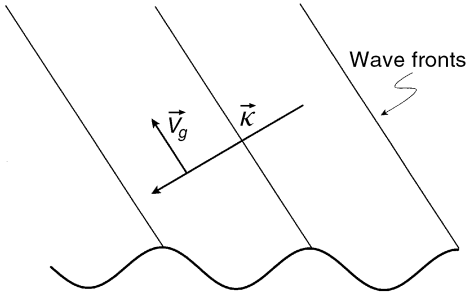

FIGURE 3.5 Wave fronts, wave vector (κ), and group velocity vector (V_g) over a surface corrugation. The transport of wave energy determines the tilt of the wave fronts.

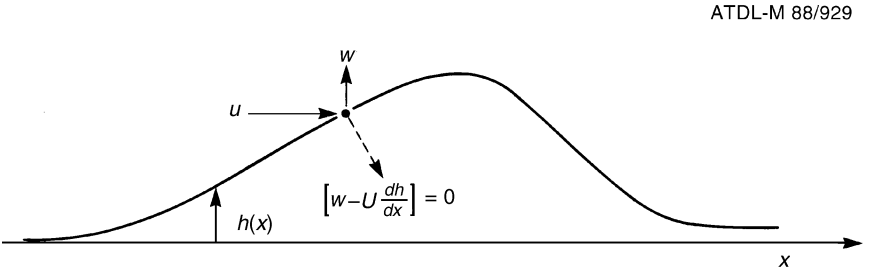

FIGURE 3.6 The flow component normal to a streamline must be zero. This condition provides the boundary condition at the ground surface.

When $N^2/u_0^2 > k^2$, the desired solution of (3.6) is

$$\hat{w}(k, z) = A\, e^{-imz}\,, \tag{3.8}$$

with

$$m^2 = \frac{N^2}{u_0^2} - k^2\,. \tag{3.9}$$

We must now select the proper boundary conditions. At the upper boundary we use the so-called *radiation condition*, *i.e.*, only upward-propagating wave energy is allowed. Thus, above the upper boundary wave reflections do not occur. Because we have assumed upward-propagating wave energy and chosen m accordingly, (3.8) satisfies the radiation condition. To evaluate A we use the bottom boundary condition. Because the background flow is frictionless and irrotational, the ground surface is a streamline, and the component of the flow normal to a streamline must be zero, *i.e.*,

$$\vec{V} \cdot \vec{n} = 0\,, \tag{3.10}$$

where $\vec{V}$ is the flow velocity and $\vec{n}$ is the unit normal to the streamline. Figure 3.6 illustrates these vectors. The equation for the surface streamline is

$$\phi = z - h(x)\,. \tag{3.11}$$

In the linear theory, it is assumed that $h(x)$ is a first-order perturbation, *i.e.*, is small. If this is not the case, then $h(x)$ would have to be written as $h(x, z)$, and the lower boundary condition would be nonlinear.[1] The unit vector normal to the streamline is

$$\vec{n} = \frac{\nabla\phi}{|\nabla\phi|} = \frac{-(dh/dx)\hat{x} + \hat{z}}{|\nabla\phi|}\,. \tag{3.12}$$

[1] Smith (1977) discusses the effects of nonlinear boundary conditions on the wave structure. One effect of the nonlinearity is enhanced steeping of gravity waves with height, which can lead to wave breakdown.

Using (3.12) in (3.10) gives

$$\vec{V} \cdot \vec{n} = [(u_0 + u_1)\hat{x} + w_1\hat{z}] \cdot \left(-\frac{dh}{dx}\hat{x} + \hat{z} \right) = 0 \,. \tag{3.13}$$

Solving for w_1 gives the *linear boundary condition* as

$$w_1(x, 0) = u_0 \frac{dh}{dx} \,. \tag{3.14}$$

Note that since both u_1 and dh/dx are first-order terms, their products are dropped in (3.14). In order to use the bottom boundary condition, (3.14) must be Fourier transformed. We select the Fourier transform pair as

$$h(x) = \frac{1}{2\pi} \int_{-\infty}^{+\infty} \hat{h}(k)\, e^{ikx}\, dk \tag{3.15}$$

$$\hat{h}(k) = \int_{-\infty}^{+\infty} h(x)\, e^{-ikx}\, dx \,. \tag{3.16}$$

Using (3.4) in (3.14) and taking the Fourier transform gives

$$\hat{w}(k, 0) = iu_0 k \int_{-\infty}^{+\infty} H e^{-i(k-k_s)x}\, dx \tag{3.17}$$

for the bottom boundary condition. We now introduce the *Dirac delta function* (see, for example, Bender and Orzag, 1999) defined as

$$\delta(x) = \frac{1}{2\pi} \int_{-\infty}^{+\infty} e^{-ixy}\, dy \,, \tag{3.18}$$

with the property that

$$\int_{-\infty}^{+\infty} \delta(x)\, dx = 1 \,. \tag{3.19}$$

The delta function is sometimes called the *sifting function* because of its ability to select a particular value from a continuous distribution of values, *i.e.*,

$$f(y) = \int_{-\infty}^{+\infty} f(x)\delta(x - y)\, dx \,. \tag{3.20}$$

Recognizing the delta function in (3.17), the value of A in (3.8) becomes

$$A = \hat{w}(k, 0) = i2\pi u_0 k H \delta(k - k_s) \,, \tag{3.21}$$

so that

$$\hat{w}(k, z) = i2\pi u_0 k H \, e^{-imz} \delta(k - k_s) \, . \tag{3.22}$$

To get the solution in physical space, we must take the inverse Fourier transform, *i.e.*,

$$w_1(x, z) = i u_0 H \int_{-\infty}^{+\infty} k e^{-imz} \, e^{ikx} \, \delta(k - k_s) \, dk \, . \tag{3.23}$$

The integration of (3.23) is straightforward. Using (3.20) and (3.3) and selecting $u_0 > 0$ gives

$$w_1(x, z) = -i u_0 H k_s \, e^{-i(k_s x + m_s z)} \, , \tag{3.24}$$

where the vertical wavenumber is

$$m_s = \left(\frac{N^2}{u_0^2} - k_s^2 \right)^{1/2} \, . \tag{3.25}$$

The sifting property of the delta function selects only that wavenumber that is in resonance with the forcing wavenumber at the ground surface, k_s; all other waves have zero amplitude. Using (3.24) in polarization equations (2.22), (2.24), and (2.25) plus (1.67) gives

$$p_1(x, z) = i\rho_0 u_0^2 H m_s \, e^{-i(k_s x + m_s z)} \tag{3.26}$$

$$u_1(x, z) = i u_0 H m_s \, e^{-i(k_s x + m_s z)} \tag{3.27}$$

$$\theta_1(x, z) = H \frac{d\theta_0}{dz} \, e^{-i(k_s x + m_s z)} \, . \tag{3.28}$$

The real parts of (3.24) and (3.26)–(3.28) are

$$w_1(x, z) = -u_0 H k_s \sin(k_s x + m_s z) \tag{3.29}$$

$$p_1(x, z) = \rho_0 u_0^2 H m_s \sin(k_s x + m_s z) \tag{3.30}$$

$$u_1(x, z) = u_0 H m_s \sin(k_s x + m_s z) \tag{3.31}$$

$$\theta_1(x, z) = H \frac{d\theta_0}{dz} \cos(k_s x + m_s z) \, . \tag{3.32}$$

Figure 3.7 illustrates the variations of wave perturbation pressure, wind speeds, and potential temperature along the surface corrugation for positive background wind. Along the windward side of the hill, the horizontal wind speed is reduced and the pressure is increased. On the lee side of the hill, the reverse is true. The pressure

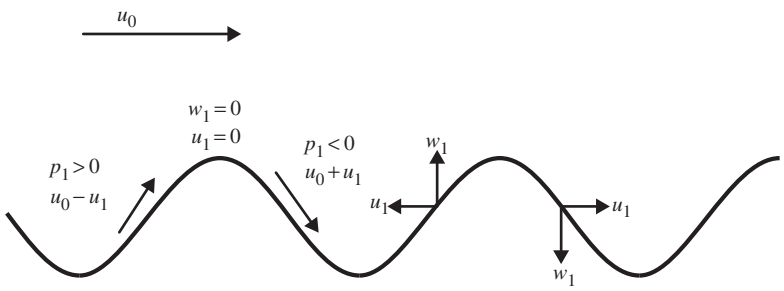

FIGURE 3.7 Variations of wave perturbation quantities along a surface corrugation.

difference across the hill causes an acceleration of the downslope flow. As we shall see in Chapter 4, mountain waves can sometimes produce extreme downslope winds such as those recorded near Boulder, CO [see, for example, Lilly (1978), Peltier and Calrk (1979), Durran (1986)].

The perturbation continuity equation (2.8) allows us to define a first-order vertical *streamline displacement*, $\zeta_1(x, z)$, of the flow streamlines, *i.e.*,

$$w_1(x, z) = u_0 \frac{\partial \zeta_1(x, z)}{\partial x} . \tag{3.33}$$

Comparing (3.33) with (3.14), we see that $\zeta_1(x, 0)$ represents the surface topography. Figure 3.8 shows the streamline displacements over two cycles of a surface corrugation for the case where $H = 50$ m, $\lambda_s = 2000$ m, $u_0 = 4$ m s^{-1}, and $N = 0.023$ s^{-1}. For these values, the vertical wavelength is $\lambda_z = 1320$ m. We see in Fig. 3.8 that the horizontal phase of the terrain shape is repeated at $z = \lambda_z$, as indicated by the thick line at that height. The inverse of the terrain shape, *i.e.*, where the wave is 180° out of phase with the surface terrain, is seen at $z = \lambda_z/2$. The up wind tilt of the wave fronts is clearly seen in Fig. 3.8.

When

$$\frac{N}{u_0} < k_s , \tag{3.34}$$

the waves are evanescent and the solution is

$$w_1(x, z) = -u_0 H k_s \, e^{-qz} \sin(k_s x) , \tag{3.35}$$

where q is given by (2.59). Figure 3.9 illustrates the wave streamlines for the evanescent case. Here u_0, N, and H are as in Fig. 3.8, but now $\lambda_s = 1000$ m. Note that now the wave amplitude decreases exponentially with height and the wave fronts are vertical. The wave perturbation quantities are symmetrically distributed with respect to the crests at the ground surface, and as we shall see in the next section a net or average wave stress is not exerted on the terrain. Evanescent waves

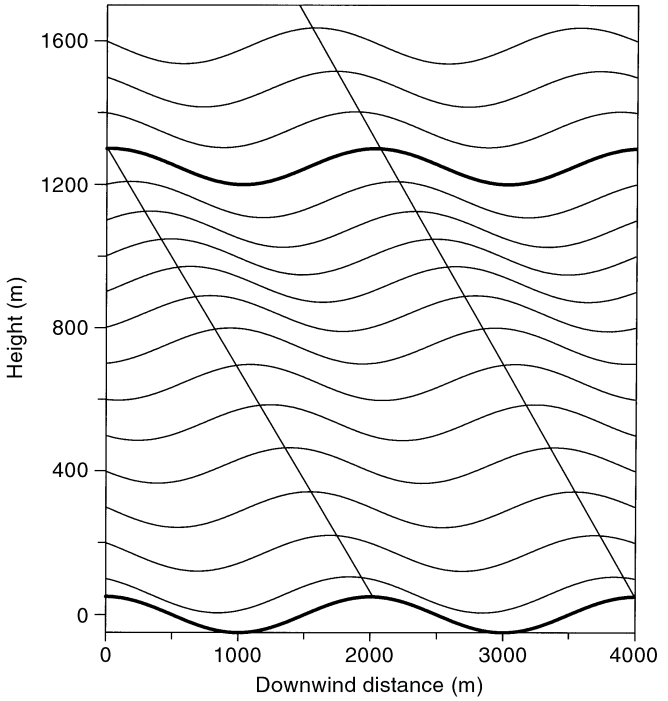

FIGURE 3.8 Streamline displacements over a surface corrugation with $H = 50$ m and wavelength $\lambda_s = 2000$ m. $N = 0.023\ \mathrm{s}^{-1}$ and $u_0 = 4\ \mathrm{m\ s}^{-1}$.

occur when u_0 is large, or N is small, or when λ_s is small. If u_0 is too large, then the frequency of the forced vertical oscillations of the air parcels as they pass over the surface corrugation will be greater than the resonant frequency of the atmosphere, N. As we have seen in Chapter 2, when a stably stratified flow is forced to oscillate at a frequency greater than its natural frequency, only evanescent waves are produced.

3.2.1 PHASE SPEED AND GROUP VELOCITY OVER A SURFACE CORRUGATION

We have seen that the physics of the problem has fixed the directions of the wave vectors so that $k < 0$ and $m < 0$. Using (3.1), we can write (3.6) as

$$\frac{d^2\hat{w}}{dz^2} + \left[\frac{k^2N^2}{\Omega^2} - k^2\right]\hat{w} = 0\,. \tag{3.36}$$

For constant N and u_0, the dispersion relation is

$$\Omega = \pm\frac{kN}{(k^2+m^2)^{1/2}}. \tag{3.37}$$

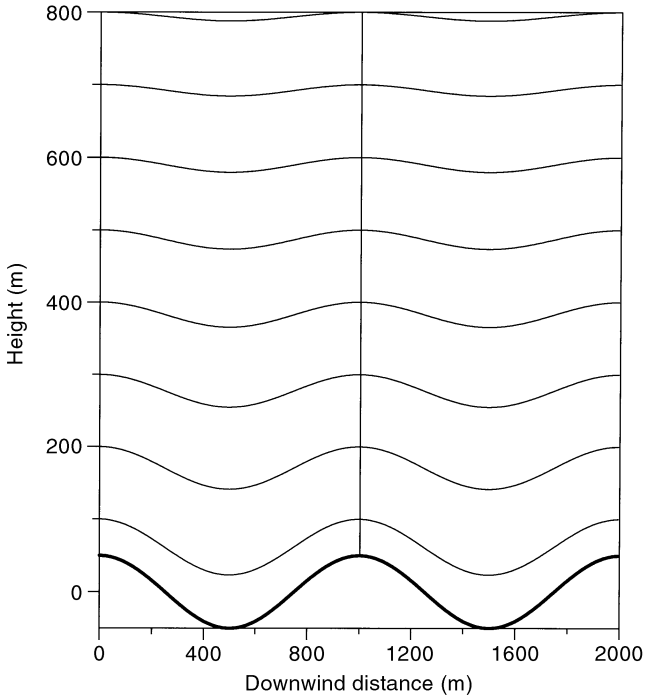

FIGURE 3.9 Evanescent mountain waves over a surface corrugation. The values are the same as in Fig. 3.8, but now $\lambda_s = 1000$ m. Note that now the wave fronts are vertical.

To determine the proper branch for Ω, we calculate the horizontal phase speed in the terrain-attached reference frame. Using (3.1) and (3.37), we get

$$c = \frac{\omega}{k} = u_0 \pm \frac{N}{(k^2 + m^2)^{1/2}} = u_0 \pm u_0. \tag{3.38}$$

Because we require $c = 0$, we must take the negative branch in (3.37). The vertical phase speed is then

$$c_z = \frac{\omega}{m} = u_0 \frac{k}{m} - \frac{N}{(k^2 + m^2)^{1/2}} = 0\,, \tag{3.39}$$

and we see that in the reference frame attached to the mountain, the wave fronts appear stationary. However, relative to the flow the phase speeds are $c = -u_0$ and $c_z = -u_0 k/m$, *i.e.*, the wave fronts appear to be moving downward and upstream, as shown in Fig. 3.5.

The horizontal group velocity in the terrain-attached reference frame is, using (3.1),

$$u_g = \frac{\partial \omega}{\partial k} = u_0 + \frac{\partial \Omega}{\partial k} . \tag{3.40}$$

Using the negative branch of (3.37) and recalling that $\Omega = -u_0 k$, we find

$$u_g = u_0 \frac{k^2}{k^2 + m^2} . \tag{3.41}$$

In a similar way, the vertical group velocity is

$$w_g = u_0 \frac{km}{k^2 + m^2} . \tag{3.42}$$

We see that energy is being transported upward and downstream; however, relative to the moving air,

$$u_g = \frac{\partial \Omega}{\partial k} = -u_0 \frac{m^2}{k^2 + m^2} , \tag{3.43}$$

but w_g is unchanged. In this frame, wave energy is being transported upward and upstream, as shown in Fig. 3.5.

3.2.2 ENERGY FLUX OVER A SURFACE CORRUGATION

We can calculate the vertical flux of energy density over the surface corrugation using (3.24)–(3.26) in (2.98) to get

$$F_z = 0.5 \Re \left(p_1 w_1^* \right) = 0.5 \rho_0 u_0^3 H^2 k_s m_s . \tag{3.44}$$

For the values of u_0, N, H, and λ_s used for the case shown in Fig. 3.8, $F_z = 1.5$ W m^{-2}. For comparison, the *solar irradiance*, which is the flux of solar radiation passing through a plane normal to the solar beam at the top of the atmosphere, is approximately 1367 W m^{-2} (Garratt, 1992). We see that the flux of energy density associated with terrain-generated waves is very small compared with the solar irradiance; however, this terrain-generated energy flux can have a large impact on the upper atmospheric. Hines (1960) proposed that gravity waves observed at meteor heights above 80 km have energy fluxes on the order of 10^{-3} W m^{-2}. Gossard (1962) showed that a flux of 10^{-1} W m^{-2} out of the troposphere is not uncommon. Hines (1963) concluded that the troposphere was a major source of these waves. These gravity waves can be generated by storm systems as well as by terrain.

3.3 THE TWO-DIMENSIONAL RIDGE

We now consider the case of flow over an isolated two-dimensional ridge. We use the word *ridge* instead of *mountain* because the former implies a large cross-wind extent, *i.e.*, two-dimensionality, while the latter implies a finite cross-wind extend, *i.e.*, three-dimensionality. The most often used ridge shapes are the *bell-shaped*[2] ridge given by

$$h(x) = \frac{Hb^2}{x^2 + b^2} \tag{3.45}$$

and the *Gaussian-shaped* ridge given by

$$h(x) = H\, e^{-x^2/b^2}\,, \tag{3.46}$$

where H is the maximum ridge height. In (3.45) b is the half-width of the bell-shaped ridge, and in (3.46) $0.83b$ is the half-width of the Gaussian ridge. The bell-shaped ridge has been used, for example, by Queney (1948); Smith (1976); and Grisogono, Pryor, and Keislar (1993). The Gaussian-shaped ridge has been used, for example, by Hines (1989b), Nappo and Chimonas (1992), and Grisogono (1994). Here we shall use the Gaussian ridge.

The solution to (3.6) requires the Fourier transform of the bottom boundary condition (3.14), which is given by

$$\hat{w}(k, 0) = iu_0 k\hat{h}(k)\,. \tag{3.47}$$

Assuming a horizontally infinite domain, the Fourier transform of (3.46) is

$$\hat{h}(k) = Hb\sqrt{\pi}\, e^{-(kb/2)^2}\,. \tag{3.48}$$

Using (3.48) in (3.47) gives the linear lower boundary condition

$$\hat{w}(k, 0) = iku_0 Hb\sqrt{\pi}\, e^{-k^2b^2/4}\,. \tag{3.49}$$

Note that when the background wind is not vertically uniform, then u_0 in (3.49) must be replaced by $u_0(z = 0)$. However, this can be problematic when modeling real-flow situations, since then $u_0(0) = 0$.

Unlike the waves over a surface corrugation which can be described by a single horizontal wavenumber, the isolated ridge must be represented by a spectrum of wavenumbers. The Taylor–Goldstein equation must be solved for each wave. These waves will destructively interfere everywhere except above the ridge where they combine to form a standing wave. These standing disturbances resemble those

[2] Also known as the Witch-of-Agnesi.

generated by water flowing over rocks in a briskly running stream. Unlike the surface corrugation case, we can neither draw nor visualize the wave vectors and the group velocity vectors. However, the fundamental physics remains unchanged. With this in mind, we proceed with our analysis.

It is convenient to introduce a shape function, $\Phi(k, z)$, such that

$$\hat{w} = \hat{w}(k, 0)\frac{\Phi(k, z)}{\Phi(k, 0)}\,. \tag{3.50}$$

The Taylor–Goldstein equation then has the form

$$\frac{d^2\Phi}{dz^2} + \left[\frac{N^2}{u_0^2} - \frac{u_0''}{u_0} - k^2\right]\Phi = 0\,, \tag{3.51}$$

where primes indicate vertical derivatives. For the case of constant flow and stratification, and imposing the radiation condition at the upper boundary, the solution of (3.6) for a particular wavenumber, k, is

$$\hat{w}(k, z) = \hat{w}(k, 0)\, e^{-imz}\,, \tag{3.52}$$

where

$$m = \left[\frac{N^2}{u_0^2} - k^2\right]^{1/2}\,. \tag{3.53}$$

The solution in physical space is obtained by summing the contributions of the waves given by (3.52), and this is achieved by taking the inverse Fourier transform of (3.52). Thus,

$$w_1(x, z) = \frac{1}{2\pi}\int_{-\infty}^{+\infty}[\hat{w}(k, 0)e^{-imz}]\, e^{ikx}dk\,, \tag{3.54}$$

which can be written as

$$w_1(x, z) = \frac{1}{\pi}\Re\int_0^{+\infty}\hat{w}(k, 0)\, e^{i(kx-mz)}\, dk\,. \tag{3.55}$$

If $u_0 > 0$, we must use negative horizontal wavenumbers so that

$$w_1(x, z) = \frac{1}{\pi}\Re\int_0^{+\infty}\hat{w}(-k, 0)\, e^{-i(kx+mz)}\, dk\,. \tag{3.56}$$

Distinguishing between propagating and evanescent waves, we can split the integral in (3.56) into two parts, *i.e.*,

$$w_1(x,z) = -\frac{u_0 Hb}{\sqrt{\pi}}\left[\int_0^{k_c} e^{-(kb/2)^2} k\sin(kx+mz)\,dk + \int_{k_c}^{+\infty} e^{-(kb/2)^2} e^{-qz} k\sin(kx)\,dk\right], \tag{3.57}$$

where q is given by (2.59) and $k_c = N/u_0$ is the *cut-off wavenumber* for propagating waves. The first integral in (3.57) represents the contributions to the vertical velocity by the propagating waves, and the second integral represents the contributions by the evanescent waves. If we compare the first integral of (3.57) with (3.29) and the second integral of (3.57) with (3.35), we can write

$$w_1(x,z) = \frac{Hb}{\sqrt{\pi}}\left[\int_0^{k_c} e^{-(kb/2)^2} w_P\,dk + \int_{k_c}^{\infty} e^{-(kb/2)^2} w_E\,dk\right], \tag{3.58}$$

where w_P is the vertical velocity due to propagating waves over a surface corrugation (3.29) and w_E is the vertical velocity due to evanescent waves over the same surface. We see that the flow disturbance over an isolated Gaussian-shaped ridge is the Gaussian-weighted sum of the disturbances due to a spectrum of corrugated surfaces each with unit amplitude. This is the essence of the linear theory. Each wave contributes independently to the perturbation variables.

From (3.57) we see that the structure of the mountain waves is strongly influenced by the term $kb\exp[-(kb/2)^2]$, which is plotted in Fig. 3.10. The maximum value occurs when $kb = \sqrt{2}$, *i.e.*, when the length of the excited wave is $\lambda_x \sim 4b$. This wavelength corresponds to about 98% of the width of the Gaussian-shaped ridge.[3] Thus, the strongest or most excited wave scales with the width of the ridge. From (3.51) we see that the wave is propagating if $L_s^2 > k^2$, where L_s is the *Scorer* parameter defined as

$$L_s^2 = \frac{N^2}{u_0^2} - \frac{u_0''}{u_0}. \tag{3.59}$$

The wave structure over an isolated ridge is determined by the relative magnitudes of L_s and b. If $L_s b \leq 1$, then the waves will be mostly evanescent with amplitudes decreasing with horizontal and vertical distance from the ridge. This case corresponds to combinations of narrow ridge width, weak stratification, and strong winds.[4] Figure 3.11 shows the wave field for the case $L_s b \approx 1$, with $u_0 = 10$ m s^{-1}, $N = 0.01$ s^{-1}, and $b = 1$ km. The waves stream downwind with amplitudes decreasing with distance from the ridge, but the rate of decrease

[3] A similar result is obtained for the bell-shaped ridge.

[4] In almost all cases, the curvature term in (3.59) is not significant.

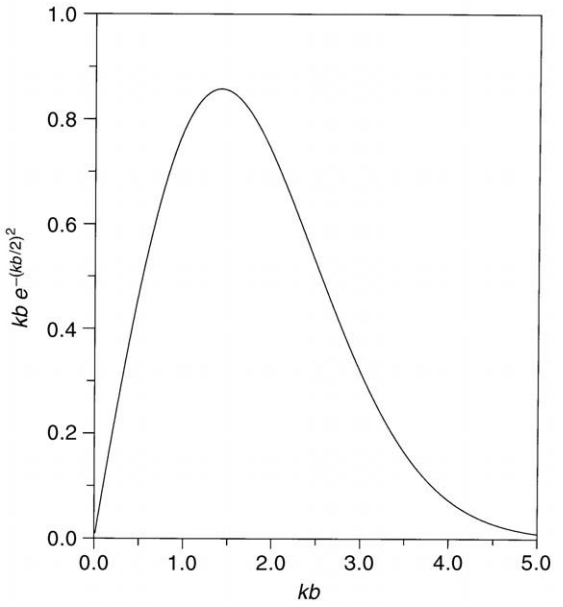

FIGURE 3.10 Response function, $kb \exp\{-(kb/2)^2\}$, plotted as a function of the dimensionless wavenumber kb.

is not great. Energy transport is vertical and downwind. The crests downwind of the ridge suggest the possibility of wave clouds often observed in mountainous regions. Figure 3.12 shows the wave field when $L_s b > 1$, which corresponds to combinations of wide ridge, strong stratification, and weak winds. In this case, L_s is as in Fig. 3.11, but now $b = 10$ km. The waves are aligned directly above the ridge, and the energy transport is vertical. The vertical wavelength is seen to be a bit less than 650 m, which is the height where the ridge shape is reproduced. If we set $\lambda_z = 2\pi u_0/N$, then $\lambda_z \approx 630$ km, and we see that that the vertical wavenumber is essentially independent of the horizontal wavenumber since the latter is very small. Indeed, this is also the reason for the vertical transport of wave energy. These waves are said to be *hydrostatic*, since if we assume that the wave perturbations are in hydrostatic balance, then it develops that $m = L_s$.

It is clear that as the width of the ridge increases, the wave field becomes increasingly hydrostatic. The time required for the flow to traverse the ridge shown in Fig. 3.12 is about 1 hour. Imagine now, instead of a single ridge, a mountain range, say with $b = 100$ km, *i.e.*, an effective width of about 400 km. An air parcel traveling at 10 m s^{-1} will require about 11 hours to traverse the range. Even if the winds are constant, on this time scale the Coriolis force due to the Earth's rotation will be effective. In the Northern Hemisphere, the Coriolis force will tend to accelerate the flow toward the right if looking downwind. If the flow is initially to the east, then while crossing the mountain range this component of the background wind speed will decrease, while the wind component to the south will increase.

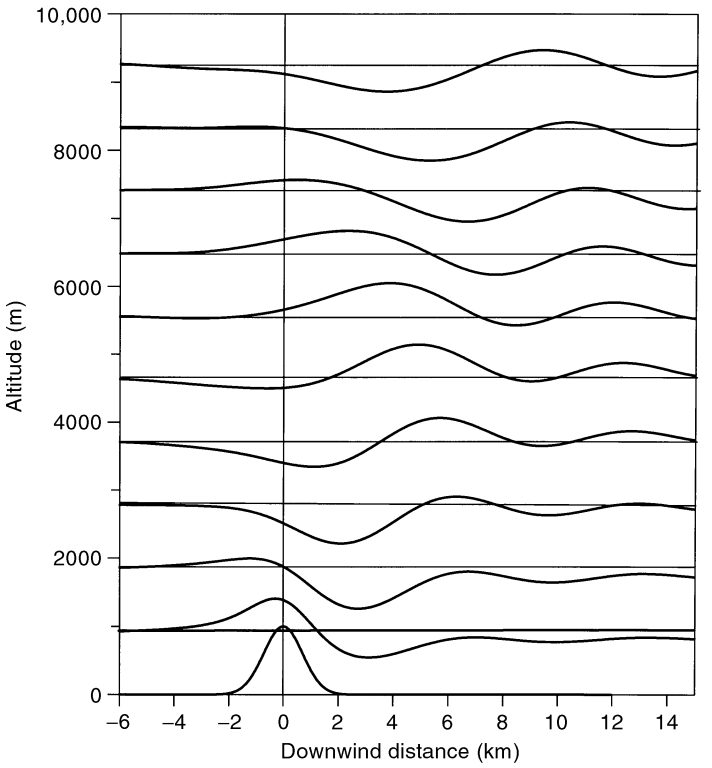

FIGURE 3.11 Wave field over a two-dimensional narrow ridge; $N = 0.01\ \mathrm{s}^{-1}$, $u_0 = 10\ \mathrm{m\,s}^{-1}$, and $b = 1$ km.

The problem is now three dimensional. If we include the Coriolis force, f, in the perturbation equations, then one gets (see, for example, Gill, 1982)

$$\frac{\partial^2}{\partial t^2}\left(\frac{\partial^2 w_1}{\partial z^2}+\frac{\partial^2 w_1}{\partial x^2}+\frac{\partial^2 w_1}{\partial y^2}\right)+f^2\frac{\partial^2 w_1}{\partial z^2}+N^2\left(\frac{\partial^2 w_1}{\partial x^2}+\frac{\partial^2 w_1}{\partial y^2}\right)=0, \quad (3.60)$$

where f is the *Coriolis parameter* equal to $2\Omega_E \sin \Phi_\mathrm{L}$, where Ω_E is the angular frequency of the Earth ($7.292 \times 10^{-5}\ \mathrm{s}^{-1}$) and Φ_L is the latitude. The waves described by (3.60) are called *inertia-gravity waves* because inertial forces have an influence. For midlatitudes, $f \approx 10^{-4}\ \mathrm{s}^{-1}$. If we assume wave solutions of the form $\exp[i(kx + ly + mz - \omega t)]$, then the dispersion relation for constant Brunt–Väisälä frequency is

$$\omega^2 = \frac{f^2 m^2 + N^2(k^2 + l^2)}{k^2 + l^2 + m^2}. \quad (3.61)$$

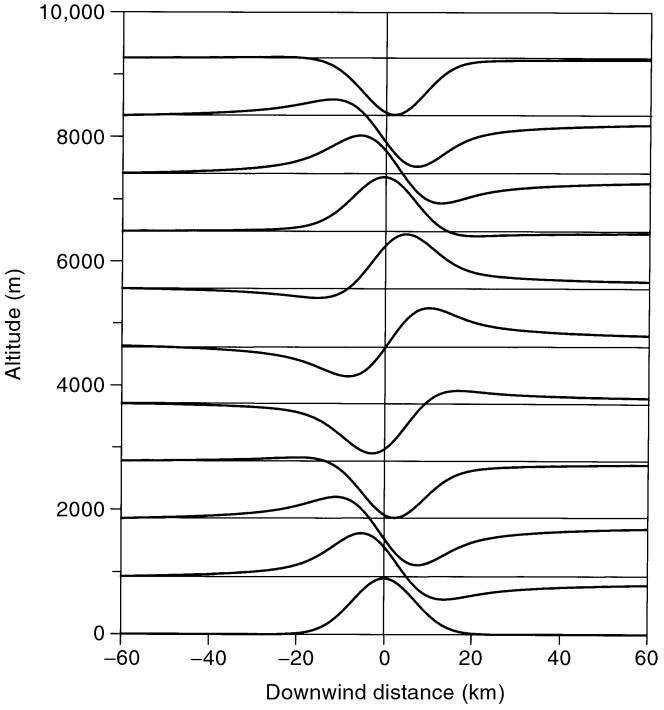

FIGURE 3.12 Same as Fig. 3.11, but now $b = 10$ km.

For constant wind and stratification, (3.51) becomes

$$\frac{d^2\Phi}{dz^2} + \left[\frac{k^2\left(N^2 - u_0^2k^2\right)}{u_0^2k^2 - f^2}\right]\Phi = 0\,. \tag{3.62}$$

Note that if f is small compared to u_0k, then (3.62) reduces to (3.51). If $b \approx$ 100 km, then the wavenumber of the most excited wave will be much less than L_s, so that (3.62) becomes

$$\frac{d^2\Phi}{dz^2} + \left[\frac{k^2N^2}{u_0^2k^2 - f^2}\right]\Phi = 0\,. \tag{3.63}$$

Figure 3.13 shows the wave field over a ridge with $b = 100$ km and background flow as in Fig. 3.12. The wave disturbances extend downwind with slowly changing amplitudes and increasing wavelengths. The vertical wavenumber is $m = kN(u_0^2k^2 - f^2)^{-1/2}$, and the angle, β, of the wave vector relative to the

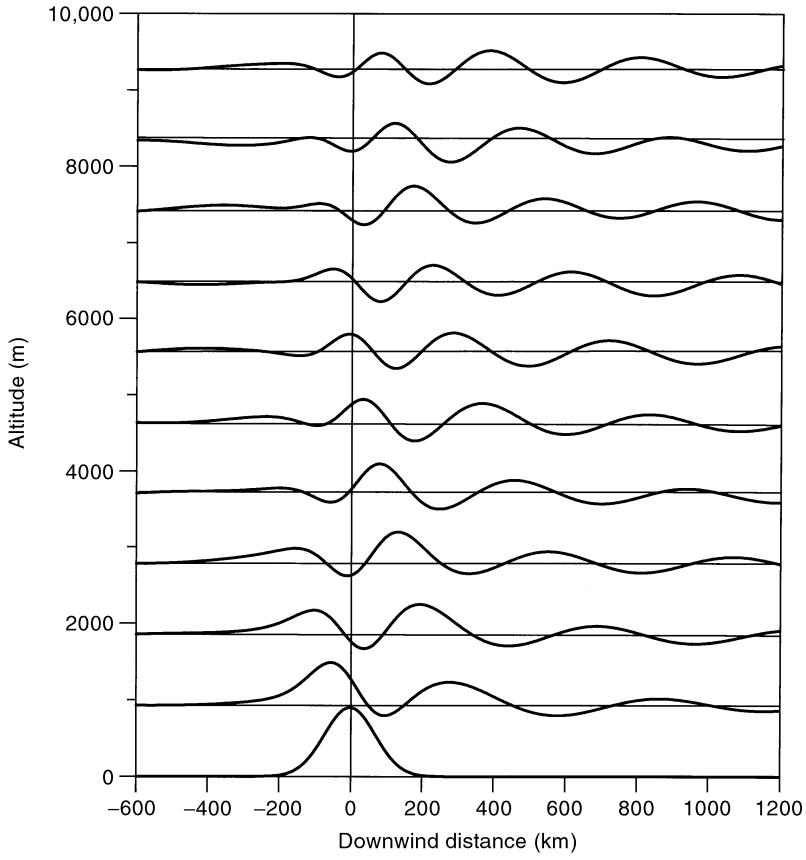

FIGURE 3.13 Same as Fig. 3.11, but now $b = 100$ km.

horizontal is

$$\beta = \tan^{-1}\left[\frac{N}{\left(u_0^2k^2 - f^2\right)^{1/2}}\right]. \tag{3.64}$$

From (3.64), we see that if k is large, then $\beta \to 0°$, and as k decreases $\beta \to 90°$. If $k < u_0/f$, then m is imaginary, and the waves are evanescent. For the case shown in Fig. 3.13, the critical horizontal wavelength is about 6.3 km. Thus, we see in Fig. 3.13 that the vertical transport of energy directly above the mountain range is accomplished by the short horizontal wavelengths, and the downwind transport of energy is accomplished by the longer wavelengths. This explains the observation in Fig. 3.13 that the horizontal wavelengths of the downwind disturbances decrease with increasing altitude. Perhaps one of the first observations

of a terrain-induced inertia-gravity wave,[5] shown in Fig. 3.14, was presented by Dörnbrack *et al.* (2001). The wave was observed on January 26, 2000, using an aircraft-mounted lidar to measure cloud aerosols in the stratosphere over the Scandinavian mountain range. The Scandinavian mountain ridge has sufficient width (∼300 km) to excite inertia-gravity waves. Comparison of Fig. 3.13 with Fig. 3.14 shows similar structures, and this illustrates the utility of the linear theory.

Figures similar to Figs. 3.11–3.13 appear in the classic paper by Queney (1948). His results were made using the bell-shaped ridge in (3.46). Comparing his results with Figs. 3.11 and 3.12 shows little difference, and this suggests that the linear theory for terrain-generated waves is not overly sensitive to the shape geometry.

3.4 THE THREE-DIMENSIONAL MOUNTAIN

Mountain waves over isolated terrain features have been extensively studied [see, for example, Blumen and McGregor, 1976; Smith, 1980; Hines, 1988; Kim and Mahrt, 1992; Baines, 1995; and references therein]. Because we have introduced the y-dimension into the problem, we must also include this dimension in the Eulier equations, (2.1)–(2.4). The Taylor–Goldstein equation now takes the form

$$\frac{d^2\hat{w}}{dz^2} + \left[\frac{(k^2+l^2)N^2}{(ku_0+lv_0)^2} - \frac{ku_0''+lv_0''}{ku_0+lv_0} - (k^2+l^2)\right]\hat{w} = 0\,, \tag{3.65}$$

where l and v_0 are the wavenumber and background wind speed in the y-direction, respectively. From the polarization equations, the horizontal perturbation velocities are

$$\hat{u}_1(k,l,z) = \frac{ik}{k^2+l^2}\left[\frac{l\hat{w}(lu_0' - kv_0')}{k(ku_0+lv_0)} + \frac{d\hat{w}}{dz}\right] \tag{3.66}$$

$$\hat{v}_1(k,l,z) = \frac{-il}{k^2+l^2}\left[\frac{k\hat{w}(lu_0' - kv_0')}{l(ku_0+lv_0)} - \frac{d\hat{w}}{dz}\right]. \tag{3.67}$$

Note that by setting $l = 0$ in (3.66) and (3.67), the solutions for the two-dimensional ridge are obtained. For a constant background wind, (3.65) reduces to

$$\frac{d^2\hat{w}}{dz^2} + \left[\frac{(\kappa_H^2)N^2}{(ku_0)^2 - (lv_0)^2} - \kappa_H^2\right]\hat{w} = 0\,, \tag{3.68}$$

[5] Inertia-gravity waves in the lower stratosphere have been observed, for example, by Allen and Vincent (1995); Vincent, Allen, and Eckermann (1997); and Guest *et al.* (2000).

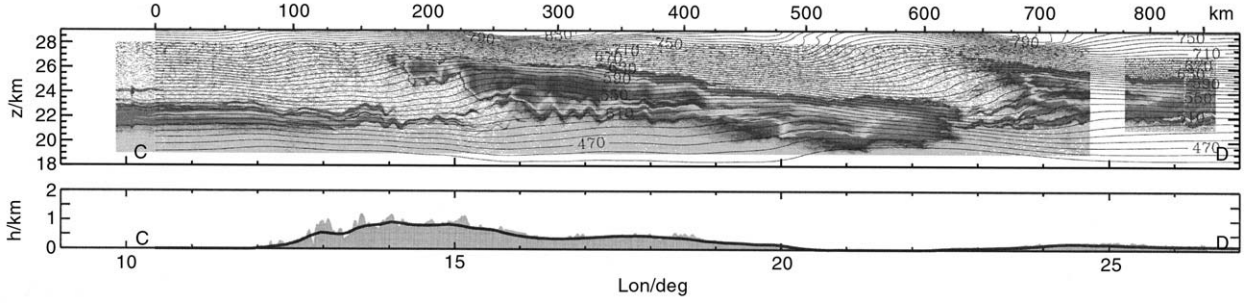

FIGURE 3.14 Top: Inertia-gravity wave observed over the Scandinavian mountain range on January 26, 2001. Bottom: Smoothed terrain profile beneath the flight track. (From "Evidence for inertia-gravity waves forming polar stratospheric clouds over Scandinavia," A.Dörnbrack *et al.*, *J. Geophys. Res.* submitted, 2001.)

where κ_H is the projection of the wave vector onto the horizontal plane. For this case, (3.66) and (3.67) reduce to

$$\hat{u}_1(k, l, z) = \frac{ik}{\kappa_H^2} \frac{d\hat{w}}{dz} \tag{3.69}$$

$$\hat{v}_1(k, l, z) = -\frac{il}{\kappa_H^2} \frac{d\hat{w}}{dz} . \tag{3.70}$$

The bottom boundary condition is

$$w_1(x, y, 0) = u_0 \frac{\partial h(x, y)}{\partial x} + v_0 \frac{\partial h(x, y)}{\partial y} , \tag{3.71}$$

with Fourier transform

$$\hat{w}(k, l, 0) = i(ku_0 + lv_0)\, \hat{h}(k, l) . \tag{3.72}$$

The most widely used mountain shapes are the three-dimensional, Gaussian-shaped mountain,

$$h(x, y) = He^{[(x/a)^2 + (y/b)^2]} , \tag{3.73}$$

where a and b are length scales in the x- and y-directions, respectively, and the three-dimensional, bell-shaped mountain,

$$h(x, y) = \frac{H}{((x^2/b^2) + (y^2/b^2) + 1)^{3/2}} . \tag{3.74}$$

If we assume horizontally symmetric hills, *i.e.*, $a = b$, then the two-dimensional Fourier transform of (3.73) is

$$\hat{h}(k, l) = Ha^2 \pi e^{-\kappa_H^2 \, a^2/4} , \tag{3.75}$$

and for (3.74) it is

$$\hat{h}(k, l) = \frac{1}{2\pi} \, ha^2 \, e^{-a\kappa_H} . \tag{3.76}$$

Figure 3.15 shows plane views of flow displacements over a three-dimensional, symmetric, bell-shaped mountain. Horizontal distances have been scaled by a, and vertical distances have been scaled by N/u_0, where $N = 0.01$ s^{-1} and $u_0 = 10$ m s^{-1}. Near the ground surface, the flow displacements are positive upwind of the mountain and negative downwind. This pattern changes with increasing height, so that eventually descending motion is upwind of the mountain and ascending motion is downwind. We see also a broadening and weakening with height of the

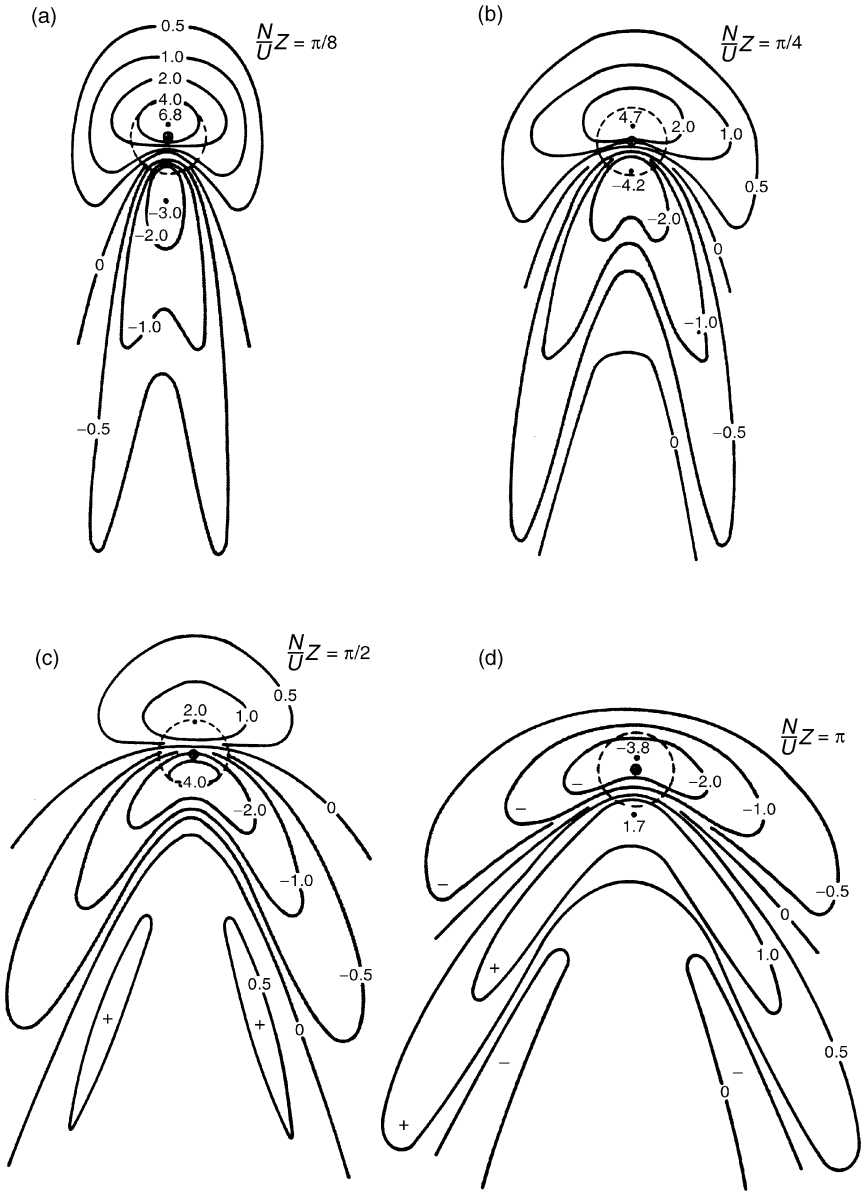

FIGURE 3.15 Streamline displacements over a three-dimensional, symmetric, bell-shaped mountain. (From "Linear theory of stratified hydrostatic flow past an isolated mountain," R.B. Smith, *Tellus*, **32**: 352, 1980.)

downstream displacement pattern. The results shown in Fig. 3.15 were obtained under the assumption that the wave perturbations were in *hydrostatic equilibrium*, which is valid when $Na/u_0 \gg 1$ (Smith, 1980). Under the hydrostatic assumption, and taking the background wind to be in the x-direction, *i.e.*, $v_0 = 0$, (3.68) takes the form

$$\frac{d^2\hat{w}}{dz^2} + \frac{\left(\kappa_H^2\right)N^2}{ku_0^2}\,\hat{w} = 0\,. \tag{3.77}$$

Because the mountain is the source of the waves, wave energy and stress must radiate horizontally and vertically away from the mountain. It is this radiation of wave energy that results in the broadening of the displacement field shown in Fig. 3.15. The transport of wave energy is done by the group velocities. Using the definition of the intrinsic frequency, (3.1), the vertical wavenumber for the plane wave solution to (3.77) is

$$m^2 = \frac{N^2\kappa_H^2}{\Omega^2}\,, \tag{3.78}$$

and the dispersion relation is

$$\Omega = \pm\frac{N\kappa_H}{m}\,. \tag{3.79}$$

Using arguments identical to those leading to (3.40), choosing the negative branch in (3.79), and noting that $\Omega = -ku_0$, the group velocity in the x-direction is

$$u_g = u_0\frac{l^2}{\kappa_H^2}\,. \tag{3.80}$$

In a similar manner, we find that

$$v_g = \frac{\partial\Omega}{\partial l} = -u_0\frac{kl}{\kappa_H^2} \tag{3.81}$$

and

$$w_g = \frac{\partial\Omega}{\partial m} = \frac{u_0^2\,k^2}{N\kappa_H}\,. \tag{3.82}$$

Smith (1980) points out that in the terrain-attached reference frame, wave energy moves away from the mountain along straight lines defined by

$$\frac{x}{z} = \frac{u_g}{w_g} \tag{3.83}$$

$$\frac{y}{z} = \frac{v_g}{w_g} \tag{3.84}$$

$$\frac{y}{x} = \frac{v_g}{u_g} \tag{3.85}$$

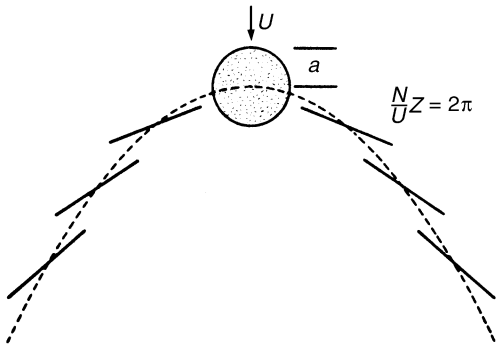

FIGURE 3.16 The parabola given by (3.87) along which the wave energy and stress above a three-dimensional hill is concentrated. (From "Linear theory of stratified hydrostatic flow past an isolated mountain," R.B. Smith, *Tellus*, **32**: 353, 1980.)

Using (3.85) with (3.80) and (3.81) gives

$$\frac{x}{y} = -\frac{k}{l}\,, \tag{3.86}$$

which describes a family of straight lines (phase lines) along which energy propagates horizontally away from the mountain which is the origin of the coordinates. Using (3.84) and (3.85) gives

$$y^2 = \frac{N}{u_0 \kappa_H}\, zx\,, \tag{3.87}$$

which describes a parabola along which the wave energy and stress are concentrated, as illustrated in Fig. 3.16. As z increases, the parabola widens. Figure 3.17 is similar to Fig. 3.16, but shows the direction and relative magnitude of the wave stress over a three-dimensional mountain. We see that the direction of the wave stress is always tangent to circles centered on the mountain.

3.5 GRAVITY WAVE DRAG

In the previous sections, we saw that gravity waves are stationary relative to the obstacle that generates them. In a sense, the waves are attached to the obstacle. However, if this is so, then the obstacle must in some way be exerting a force against the flow so that the waves remain stationary. This force takes the form of a *drag* or *stress* which must be exerted on the atmosphere by terrain obstacles. The effects of wave drag on the atmosphere are profound and important on all scales of flow. Indeed, Chapter 7 of this book is devoted to the parameterization of wave stress effects in numerical atmospheric flow models.

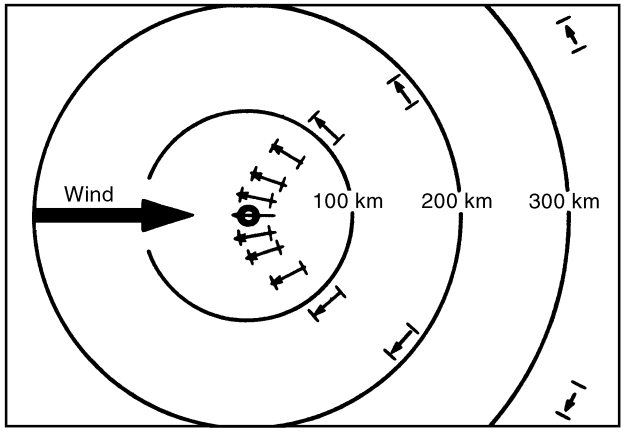

FIGURE 3.17 Direction and magnitude of wave stress above a three-dimensional mountain. (From "A modeling of atmospheric gravity waves and wave drag generated by isotropic and anisotropic terrain," C.O. Hines, *J. Atmos. Sci.*, **45**: 325, 1988.)

3.5.1 MATHEMATICAL DERIVATION

We begin by considering a steady, frictionless, nonrotating, and horizontally homogeneous background flow over an isolated two-dimensional ridge of arbitrary cross-section $h(x)$. Under the Boussinesq approximation, the linearized horizontal momentum equation is

$$u_0 \frac{\partial u_1}{\partial x} + w_1 \frac{du_0}{dz} + \frac{1}{\rho_0} \frac{\partial p_1}{\partial x} = 0 \,. \tag{3.88}$$

Because the terrain obstacle is isolated, $h(x) \to 0$ as $x \to \pm\infty$. Next, we multiply (3.88) by $h(x)$ and integrate over x to get

$$\int_{-\infty}^{+\infty} u_0 h \frac{\partial u_1}{\partial x} dx + \int_{-\infty}^{+\infty} w_1 h \frac{du_0}{dz} dx + \int_{-\infty}^{+\infty} \frac{h}{\rho_0} \frac{\partial p_1}{\partial x} dx = 0 \,. \tag{3.89}$$

Integrate the first integral by parts to get

$$I_1 = \int_{-\infty}^{+\infty} u_0 h \frac{\partial u_1}{\partial x} dx = - \int_{-\infty}^{+\infty} u_1 u_0 \frac{\partial h}{\partial x} \, dx \,. \tag{3.90}$$

Using (3.14), (3.90) becomes

$$I_1 = - \int_{-\infty}^{+\infty} u_1 w_1 \, dx \,, \tag{3.91}$$

where w_1 is the vertical perturbation velocity created by the obstacle. Using (3.14) in the second integral in (3.89) and noting that $h(x) \to 0$ as $x \to \pm\infty$ gives

$$I_2 = \frac{du_0}{dz}\int_{-\infty}^{+\infty} u_0 h \frac{dh}{dx}\,dx = -\frac{1}{4}\frac{du_0^2}{dz}\int_{-\infty}^{+\infty}\frac{dh^2}{dx}\,dx = 0\,. \tag{3.92}$$

Integrating the third integral in (3.89) by parts gives

$$I_3 = \int_{-\infty}^{+\infty}\frac{1}{\rho_0}h\frac{dp_1}{dx}\,dx = -\int_{-\infty}^{+\infty}\frac{p_1}{\rho_0}\frac{dh}{dx}\,dx\,. \tag{3.93}$$

Adding $I_1 + I_2 + I_3$ gives

$$-\int_{-\infty}^{+\infty}\rho_0 u_1 w_1\,dx = \int_{-\infty}^{+\infty} p_1\frac{dh}{dx}\,dx\,. \tag{3.94}$$

The right-hand side of (3.94) is the *form drag* per unit length of ridge exerted on the ridge by the flow, and the left-hand side is the drag per unit length of ridge exerted on the flow by the ridge, but this is simply a statement of Newton's third law. This response to the drag on the obstacle is transported upward by the gravity waves launched at the ground surface. If the ridge height and the pressure distribution are symmetric in x so that $h(x) = h(-x)$ and $p_1(x) = p_1(-x)$, then the form drag will be zero, and propagating gravity waves will not be launched; instead, the waves will be evanescent. In this case, the flow uniformly follows the terrain. If, however, $h(x)$ and $p_1(x)$ are asymmetric, then the waves will be propagating. If we divide (3.94) by some horizontal length scale, ℓ, then the *wave stress* over the length ℓ is

$$\tau(z) = -\frac{1}{\ell}\int_{-\ell/2}^{\ell/2}\rho_0 u_1 w_1\,dx = -\rho_0\overline{u_1 w_1}. \tag{3.95}$$

However, for this stress to be physically meaningful, ℓ must be defined in a meaningful way. Over a corrugated surface, we can take ℓ to be the wavelength of the corrugation. Over an isolated ridge, we can take ℓ as some scale of the ridge width. Recall that "stress" represents a flux of momentum across some surface. It is sometimes stated that wave stress is a vertical flux of wave momentum, but as discussed by McMintyre (1981) such a statement is not accurate. Gravity waves themselves do not posses a momentum. Instead, the flow perturbations created by the waves act to transport mean-flow horizontal momentum. From (3.29) and (3.31) we see that the vertical and horizontal velocity perturbations are of opposite sign, so that *cross-correlation* $\overline{u_1 w_1}$ is negative. This term may be interpreted as either the downward propagation of mean-flow positive momentum or the upward propagation of mean-flow negative momentum. Now consider for a moment a steady

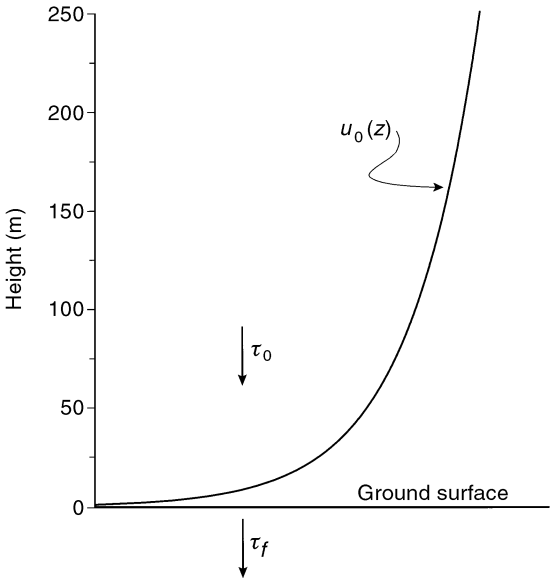

FIGURE 3.18 In the surface layer, a constant downward flux of momentum due to turbulence, τ_0, is required to balance the loss of momentum at the ground surface due to friction, τ_f.

surface-layer flow with $u_0(z)$ increasing with height above the ground surface. According to (Garratt, 1992)

$$u_0(z) = \frac{1}{k}\frac{\tau_0}{\rho}\,\ln(z - z_0)\,, \tag{3.96}$$

where k is the Von Karman constant, z_0 is the aerodynamic surface roughness (the effective height where $u_0 = 0$), and $\tau_0 = -\rho\overline{u'w'}$ is the surface stress due to turbulence. Then, as illustrated in Fig. 3.18, a constant downward flux of momentum, τ_0, is required to maintain the velocity profile and balance the momentum lost to friction at the ground surface, τ_f.

3.5.2 THE VARIATION OF WAVE STRESS WITH HEIGHT

We now consider a single wave and examine the stress associated with it. The vertical and horizontal velocity perturbations produced by the wave have constant magnitudes $\tilde{w}$ and $\tilde{u}$, respectively, and using (2.44) we can write

$$w(x, z, t) = \tilde{w}e^{z/2H_s}e^{i(kx+mz-\omega t)}\,. \tag{3.97}$$

Similarly, we can write

$$u(x, z, t) = \tilde{u}e^{z/2H_s}e^{i(kx+mz-\omega t)}\,. \tag{3.98}$$

From the continuity equation (2.8), we get

$$ik\tilde{u} + \left(im + \frac{1}{2H_s}\right)\tilde{w} = 0\,, \tag{3.99}$$

and hence

$$\tilde{u} = \left(-\frac{m}{k} + \frac{i}{2kH_s}\right)\tilde{w}\,. \tag{3.100}$$

Using (3.100) in (3.98) gives

$$u(x,z,t) = \left(-\frac{m}{k} + \frac{i}{2kH_s}\right)\tilde{w}e^{(z/2H_s)}e^{i(kx+mz-\omega t)}\,. \tag{3.101}$$

If we average the product of the real parts of u and w over one horizontal wavelength, λ_x, then the stress is given by

$$\tau(z) = -\frac{1}{\lambda_x}\int_0^{\lambda_x}\rho_0 \Re u\,\Re w\,dx = -0.5\Re(\rho_0 u w^*)\,. \tag{3.102}$$

Using (3.97) and (3.101) in (3.102) gives

$$\tau(z) = 0.5\rho_0\frac{m}{k}\tilde{w}^2 e^{(z/H_s)}\,. \tag{3.103}$$

Using (1.59) to eliminate ρ_0, (3.103) becomes

$$\tau(z) = 0.5\rho_s\frac{m}{k}\tilde{w}^2\,, \tag{3.104}$$

which is a constant. Hence, unless the wave breaks down or in some way dissipates, the stress associated with that wave is constant with height. Note also that this result does not require the background flow to be constant with height. Booker and Bretherton (1967) consider the wave stress to be an appropriate measure of wave magnitude. In Chapter 5, a more rigorous proof of the constancy of wave stress will be given.

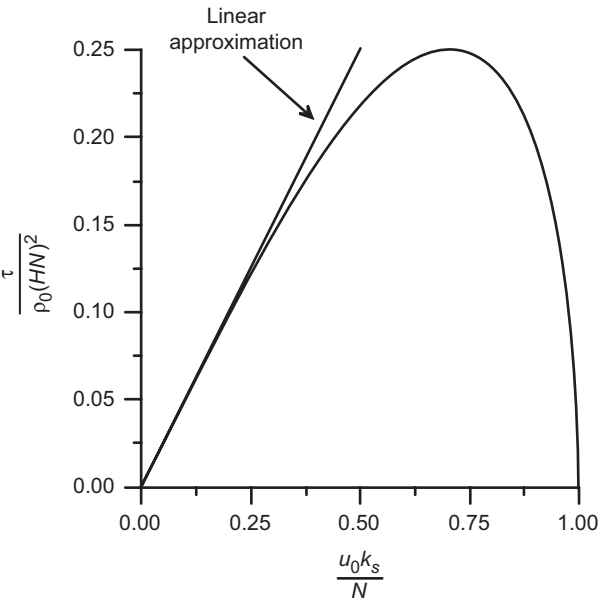

FIGURE 3.19 Nondimensional wave stress as a function of nondimensional wind speed over a surface corrugation. (From "Wave drag in the planetary boundary layer over complex terrain," G. Chimonas and C.J. Nappo, *Boundary-Layer Meteorol.*, **47**: 225, 1989.)

3.5.3 WAVE STRESS OVER A SURFACE CORRUGATION

Consider now the wave stress over a corrugated surface. Using (3.24) and (3.25) in (3.102) gives

$$\tau = \begin{cases} 0.5\rho_0(u_0 H)^2 k_s \left[\dfrac{N^2}{u_0^2} - k_s^2\right]^{1/2} & \text{if } \dfrac{N}{u_0} > k_s \\ 0 & \text{if } \dfrac{N}{u_0} \le k_s \end{cases} \tag{3.105}$$

Figure 3.19 shows a plot of dimensionless wave stress $(\tau/\rho_0(NH)^2)$ over a corrugated surface as a function of nondimensional background wind speed $u_0 k_s/N$. The maximum wave stress occurs when $u_0 k_s/N = 1/\sqrt{2}$. For small u_0, (3.105) takes the linear form

$$\tau = 0.5\rho_0 H^2 k_s N u_0 \,, \tag{3.106}$$

which is also plotted in Fig. 3.19. We can compare the magnitude of the wave stress with the *friction stress* at the ground surface if we let the friction stress, τ_f, be given by, for example, Gill (1982),

$$\tau_f = 0.5\rho_0 C_D u_0^2 \,, \tag{3.107}$$

where C_D is the *drag coefficient*. If we let τ_w be the wave stress, then

$$\frac{\tau_w}{\tau_f} = \frac{0.5\rho_0 k_s (u_0 H)^2 \left[(N^2/u_0^2) - k_s^2\right]^{1/2}}{0.5\rho_0 C_D u_0^2} . \tag{3.108}$$

For $C_D = 0.005$, which corresponds to lawn grass up to 1 cm high (Sutton, 1953), and $H/\lambda_s = 0.01$,

$$\frac{\tau_w}{\tau_f} \approx \left[\left(\frac{N}{u_0 k_s}\right)^2 - 1\right]^{1/2} . \tag{3.109}$$

If $u_0 < N/\sqrt{2}k_s$, then for this particular case $\tau_w/\tau_f > 1$, *i.e.*, the wave stress is greater than the surface friction stress. If, for example, $N = 0.03$ s^{-1}, $\lambda_s = 1000$ m, and $H = 10$ m, then for wind speeds less than 3 m s^{-1} the wave stress will be greater than the friction stress. This is a significant effect in the nighttime planetary boundary layer.

3.5.4 WAVE STRESS OVER AN ISOLATED RIDGE

We now consider the wave drag over an isolated two-dimensional ridge. The drag per unit length of ridge D/l is

$$\frac{D}{l} = -\int_{-\infty}^{\infty} \rho_0 u w \, dx . \tag{3.110}$$

Using the inverse Fourier transform, we write

$$w(x, z) = \frac{1}{2\pi} \int_{-\infty}^{\infty} \hat{w}(k, z) e^{ikx} \, dk \tag{3.111}$$

and

$$u(x, z) = \frac{1}{2\pi} \int_{-\infty}^{\infty} \hat{u}(k, z) e^{ikx} \, dk . \tag{3.112}$$

Using the continuity equation (2.24) in (3.112) we get

$$u(x, z) = \frac{1}{2\pi} \int_{-\infty}^{\infty} \frac{i}{k} \frac{d\hat{w}}{dz} e^{ikx} \, dk . \tag{3.113}$$

Then using (3.111) and (3.113) in (3.110) gives

$$\frac{D}{l} = -\frac{\rho_0}{4\pi^2}\int_{-\infty}^{\infty} dx \int_{-\infty}^{\infty} \hat{w}(k,z)e^{ikx}dk \int_{-\infty}^{\infty} \frac{i}{k'}\frac{d\hat{w}(k',z)}{dz}e^{ik'x}\,dk'$$

$$= -i\frac{\rho_0}{4\pi^2}\int_{-\infty}^{\infty} dk \int_{-\infty}^{\infty} dk'\hat{w}(k,z)\frac{d\hat{w}(k',z)}{dz}\frac{1}{k'}\int_{-\infty}^{\infty} e^{i(k+k')x}\,dx$$

$$= -i\frac{\rho_0}{2\pi}\int_{-\infty}^{\infty} dk \int_{-\infty}^{\infty} dk'\hat{w}(k,z)\frac{d\hat{w}(k',z)}{dz}\frac{1}{k'}\,\delta(k+k')\,. \tag{3.114}$$

Integration of (3.114) with respect to dk' gives

$$\frac{D}{l} = i\frac{\rho_0}{2\pi}\int_{-\infty}^{\infty} \hat{w}(k,z)\frac{d\hat{w}(-k,z)}{dz}\frac{1}{k}\,dk\,. \tag{3.115}$$

Since

$$\frac{d\hat{w}(-k,z)}{dz} = \frac{d\hat{w}^*(k,z)}{dz}\,, \tag{3.116}$$

we can write

$$\frac{D}{l} = \frac{\rho_0}{2\pi}\Im\int_{-\infty}^{\infty} \frac{1}{k}\hat{w}(k,z)\frac{d\hat{w}^*(k,z)}{dz}\,dk\,, \tag{3.117}$$

where $\Im$ is the imaginary part of the integral. If the isolated ridge is Gaussian shaped and if the background variables are constant, then we can use (3.49) and (3.52) in (3.117) to get

$$\frac{D}{l} = \rho_0(u_0H)^2\int_0^{k_c}[b^2e^{-(kb)^2/2}]\,k\left[\frac{N^2}{u_0^2}-k^2\right]^{1/2}dk\,. \tag{3.118}$$

Figure 3.20 shows a plot of dimensionless wave stress per unit length of ridge $(D/l)/[\rho_0 b(HN)^2]$ as a function of dimensionless wind speed $u_0/(Nb)$ for the case of flow over a Gaussian-shaped ridge. The curve is similar to that shown in Fig. 3.19; however, now the drag approaches zero asymptotically for large values of $u_0/(Nb)$. Numerical evaluation of (3.118) gives $0.34\,\rho_0 b(HN)^2$ for the maximum wave drag, which occurs at a wind speed of $0.54\,Nb$.

When the wind speed is small and the ridge is wide such that $Nb/u_0 \gg 1$, then (3.118) reduces to

$$D/\ell = \rho_0 u_0 H^2 b^2 N\int_0^{k_c} ke^{-k^2b^2/2}\,dk\,. \tag{3.119}$$

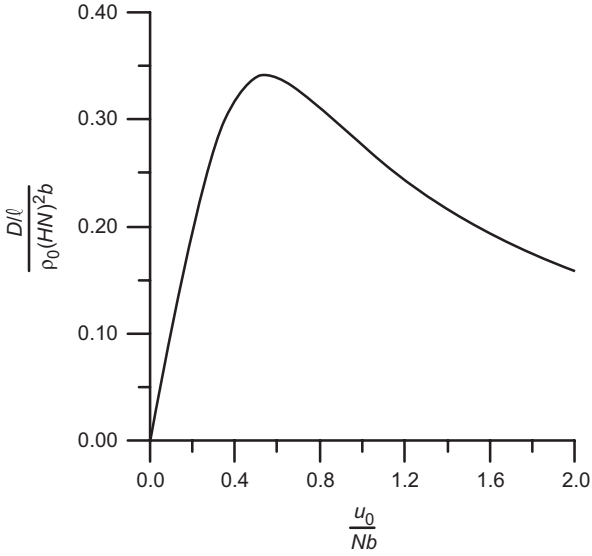

FIGURE 3.20 Same as Fig. 3.15, but for flow over a Gaussian-shaped ridge.

The integration is elementary, giving

$$D/\ell = \rho_0 u_0 H^2 N\left[1 - e^{-k^2 b^2/2}\right]. \tag{3.120}$$

Then because $k_c b = Nb/u_0 \gg 1$, (3.120) reduces further to

$$D/\ell = \rho_0 u_0 H^2 N\,. \tag{3.121}$$

We see that for low wind speed over wide ridges, the wave drag is linear in u_0 and independent of ridge width.

When the wind speed is high and the ridge is narrow such that $Nb/u_0 \ll 1$, only the very long wave lengths contribute to the integral in (3.118). In this case, the exponential term approaches unity and

$$D/\ell = \rho_0 (u_0 H b)^2 \frac{N}{u_0} \int_0^{k_c} k\, dk \tag{3.122}$$

and

$$D/\ell = 0.5\rho_0 (HNb)^2 \frac{N}{u_0}\,, \tag{3.123}$$

where we have used $k_c = N/u_0$. Thus, for high winds, the wave drag decreases as u_0^{-1}, as seen in Fig. 3.20. This behavior is the most significant difference between wave drag over a corrugated surface and over an isolated ridge.

If we divide both sides of (3.118) by $2b$, the result will be a wave stress, *i.e.*,

$$\tau_r = 0.5\rho_0(u_0H)^2 \int_0^{k_c} \left[kbe^{-(kb)^2/2}\right] \left[\frac{N^2}{u_0^2} - k^2\right]^{1/2} dk\,. \tag{3.124}$$

The relative contributions to τ_r by the dimensionless wavenumber kb are plotted in Fig. 3.10. The maximum contribution occurs when $kb = \sqrt{2}$. For scaling purposes, it may be sufficient to estimate the wave stress maximum over a ridge by setting $k = 1/b$ in (3.124). Then integration gives

$$\tau_r \approx 0.5\rho_0(u_0H)^2 \frac{1}{b} \left[\frac{N^2}{u_0^2} - \frac{1}{b}^2\right]^{1/2}, \tag{3.125}$$

which looks very much like the stress over a surface corrugation (3.105) if we replace k_s by $1/b$. We see that a surface corrugation and a two-dimensional ridge with approximately equal height and length scales will generate approximately equal values of wave stress. This presents a computational simplification since we can replace the integration over wavenumbers by a single term.

3.5.5 SECONDARY EFFECTS OF TERRAIN-INDUCED WAVE DRAG

The main effect of terrain-induced wave drag on the atmosphere is to reduce flow speeds. However, because the wave drag acts locally and in a given direction, secondary flow effects can be created. As discussed by Chimonas and Nappo (1989), one such effect created by the *directional selectivity* of wave drag is to turn the flow over complex terrain in a direction parallel to the surface contours. This process is illustrated in Fig. 3.21. The turbulent drag always acts against the flow, *i.e.*, opposite to the direction of the mean wind; however, the wave drag acts against the component of the mean wind normal to the terrain contours. This directional selectivity results in a tendency for the flow to follow the terrain contours rather than to go over the terrain, an effect which is enhanced by a stable stratification.

3.6 CONVECTIVELY GENERATED GRAVITY WAVES

This chapter has focused on the generation of gravity waves by vertical displacements of flow streamlines. We have seen that these types of waves can propagate into the stratosphere and higher atmosphere. However, another source of stratospheric gravity waves that is currently under active research is convection in the troposphere and the accompanying release of latent heat. Indeed, the field is so

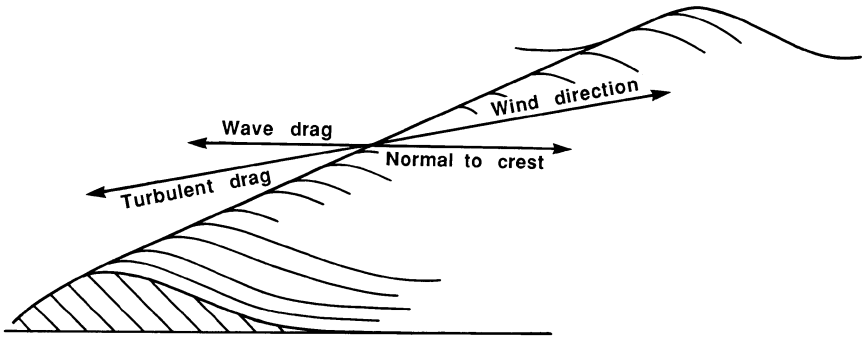

FIGURE 3.21 The directional preference introduced by wave drag. Conventional turbulent drag acts along the wind direction, while the wave drag is always normal to the surface contours.

wide reaching as to include the study of convectively generated gravity waves in the lower atmosphere of Venus [see, for example, Baker, Schuberrt, and Jones, 2000 and references therein]. We cannot treat here in any detail the subject of convectively generated gravity waves; instead, we present a brief literature review.

Smith and Lin (1982) investigated the relative strengths of gravity waves generated by terrain and orographic rain. They included a diabatic heating rate due to condensation, $\dot{H}$, so that the energy equation takes the form

$$c_v \frac{DT}{Dt} + p\frac{D\alpha}{Dt} = \dot{H}\,, \tag{3.126}$$

where T is the sensible temperature and α is the specific volume $1/\rho$. For constant background wind, the equation for the vertical velocity perturbation becomes (Smith and Lin, 1982)

$$\frac{d^2w_1}{dx^2} + \frac{d^2w_1}{dz^2} + \frac{N^2(z)}{u_0}w_1 = \frac{g\dot{H}}{c_pT_0(z)u_0^2}\,. \tag{3.127}$$

Smith and Lin (1982) concluded that for typical wind speeds and rainfall rates the amplitudes of thermally generated gravity waves will equal or exceed the amplitudes of terrain-generated gravity waves. Lin and Chun (1991) examined the effects of diabatic cooling due to evaporation of falling precipitation on a stably stratified shear flow. The cooling was confined to a subcloud layer, and their analysis included both a linear analytical model and a nonlinear numerical model. Their results showed, in part, that nonlinearity acts to reduce the amplitudes of wave disturbances above the cloud layer. The theoretical results of Smith and Lin (1982) were supported by Fritts and Nastrom (1992), who examined representative case

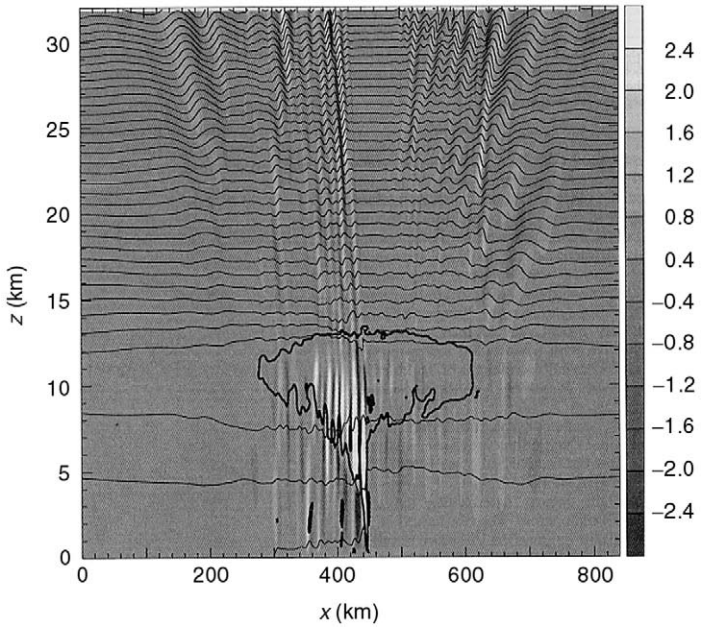

FIGURE 3.22 Isentropes (thin lines) at 4 h of a squall line numerical simulation. The thick line shows the cloud outline and shading represents contours of vertical velocity. The vertical velocities range from 20 to -5 m s^{-1}. (From "The gravity wave response above deep convection in a squall line simulation," M.J. Alexander, J.R. Holton, and D.R. Durran, *J. Atmos. Sci.*, **52**: 2215, 1995.)

studies within the Global Atmospheric Sampling Program (GASP). Their results suggest that convection as a source of gravity waves is at least as important as topographic forcing and possibly the most important source of gravity waves in the Tropics and the Southern Hemisphere.

Fovell, Durran, and Holton (1992) studied gravity waves generated by moving two-dimensional mesoscale storms, *i.e.*, *squall lines* using a nonlinear numerical model. Their results show a preference for excited waves to propagate against the direction of the storm's motion. In the absence of a wind relative to the storm, gravity waves in the stratosphere are excited by mechanical forcing due to oscillatory updrafts, a result first proposed by Pierce and Coroniti (1960) and apparently overlooked. Alexander, Holton, and Durran (1995) used a fully compressible, nonlinear, numerical, two-dimensional model of a midlatitude squall line to study the link between vertically propagating gravity waves and the wave-forcing mechanism. Figure 3.22 shows the results of their simulation. Gravity waves radiating away from the storm's center are most striking, and the induced vertical velocities range from 20 to 5 m s^{-1}. Alexander, Holton, and Durran (1995) related the peak in the frequency and vertical wavelength of the gravity wave spectrum with the updraft oscillation frequency and the vertical scale of the tropospheric heating, respectively. Chun, Song, and Baik (1999) used linear theory and the Advanced

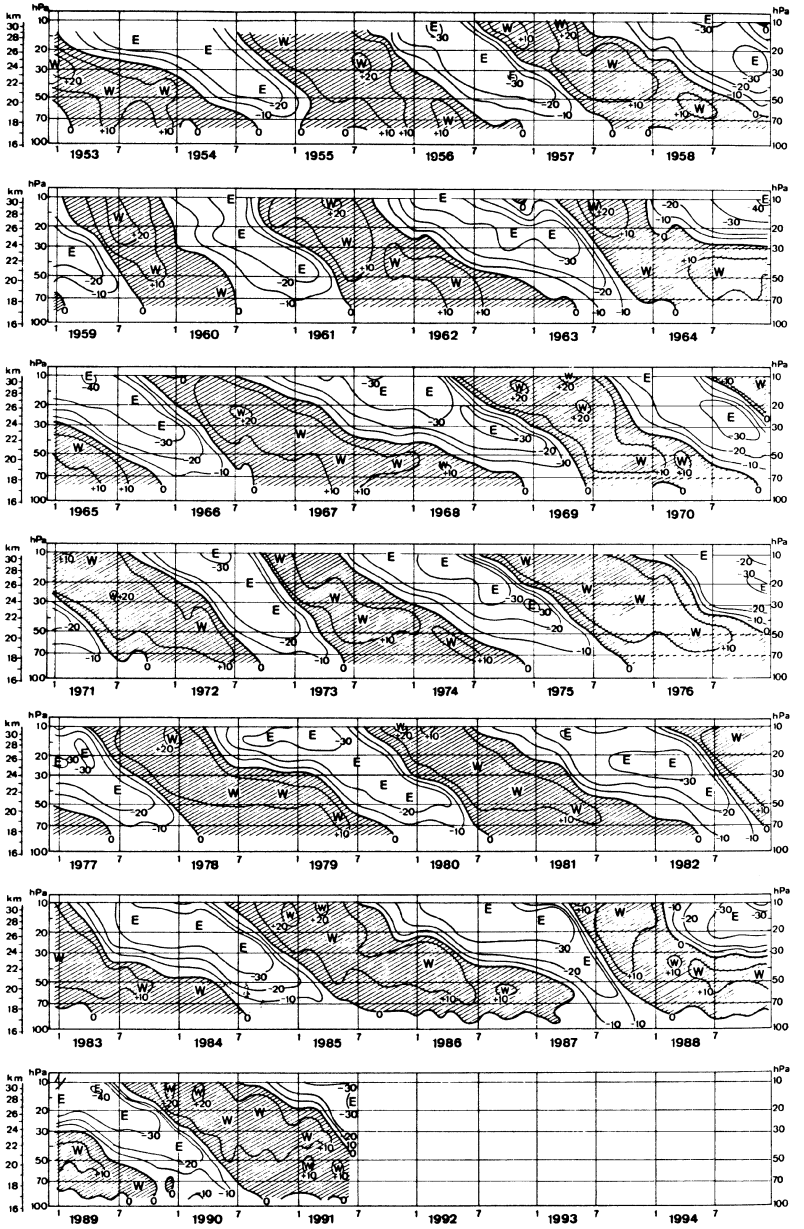

FIGURE 3.23 Time-height cross-section of monthly averaged zonal wind departures from the climatological average for that month at equatorial stations. The alternating downward-propagating regimes of westerly (W) and easterly (E) winds (m s^{-1}) form the quasi-biennial oscillation. (From *An Introduction to Dynamic Meterology*, J.R. Holton, Academic Press, New York, 1992.)

Regional Prediction System (ARPS) (Xue *et al.*, 1995) to study gravity waves generated by a multicell convective system. Their results showed that updrafts, *i.e.*, forced internal gravity waves, at the head of the storm's outflow or density current can generate consecutive convective cells that move downstream and develop as a main convective cell. Thus, it appears that internal gravity waves play a major role in the initiation and maintenance of multicell convective systems.

Piani *et al.* (2000) extended modeling of convective gravity waves to three dimensions and examined the role of these waves in the dynamics of the *quasi-biennial oscillation* (QBO). The QBO (see, for example, Lindzen and Holton, 1968; Holton and Lindzen, 1972; Holton, 1992) consists of zonally[6] symmetric easterly and westerly wind regimes which alternate regularly with a period varying from about 24 to 30 months. These wind regimes first appear above 30 km, but propagate downward at a rate of about 1 km/month. The downward propagation occurs without loss of amplitude between 30 and about 23 km; however, there is rapid attenuation of the wind regime below 23 km. The QBO is symmetric about the equator with a maximum amplitude of about 20 m s^{-1} and a half-width of about 12° latitude. Figure 3.23 illustrates the oscillating wind regimes of the QBO. It is now accepted that the QBO is a result of upward-propagating, convectively generated gravity waves which interact with critical layers (see Chapter 5). At a critical layer, the wave is dissipated (absorbed), resulting in a divergence of wave stress and a deceleration or acceleration of the wind. Research into the links between the QBO and convective gravity waves continues to be an active field of research as typified, for example, by the papers of Alexander, Beres, and Pfister (2000); Vincent and Alexander (2000); and Alexander and Vincent (2000).

[6] In dynamic meteorology, the *zonal wind* is the east–ward component of the wind.

4

Ducted Gravity Waves

Gravity waves are often observed as periodic oscillations of atmospheric pressure and horizontal wind speed and direction (see, for example, the case studies described by Gossard and Hooke, 1975). If such waves are observed over times spans ranging from tens of minutes to a few hours, then it is reasonable to assume that the waves must be propagating horizontally. Horizontal propagation can occur only if the waves are trapped between the ground surface and some upper level. These types of waves have been called *cellular* (Martyn, 1950; Hines, 1965) to denote waves that propagate horizontally and present a standing pattern in the vertical direction. Under ordinary conditions, an upward-propagating gravity wave may encounter a level where the background flow characteristics such as N or u_0 change quickly with height. When this happens, *wave reflection* can occur (see, for example, Pitteway and Hines, 1965). The reflection may be partial or complete. If partial, then some of the wave is transmitted through the level, but with reduced amplitude. The transmitted wave can be either propagating (vertical wavenumber real) or evanescent (vertical wavenumber imaginary). The reflected wave propagates to the ground surface where it is reflected upward. Depending on the height of the reflecting level and the vertical wavelength of the wave, the upward and downward waves will either constructively or destructively interfere. If the waves constructively interfere, then the wave becomes trapped between the ground surface and the reflecting level, as illustrated in Fig. 4.1. The trapped wave is said to be *ducted* and is capable of horizontally transporting energy over long distances with little attenuation. In effect, the wave duct is a *wave guide*. In Chapter 3, we mentioned that lee waves can be generated when a mountain wave becomes trapped between the ground surface and an elevated reflecting level, *i.e.*, lee waves are ducted

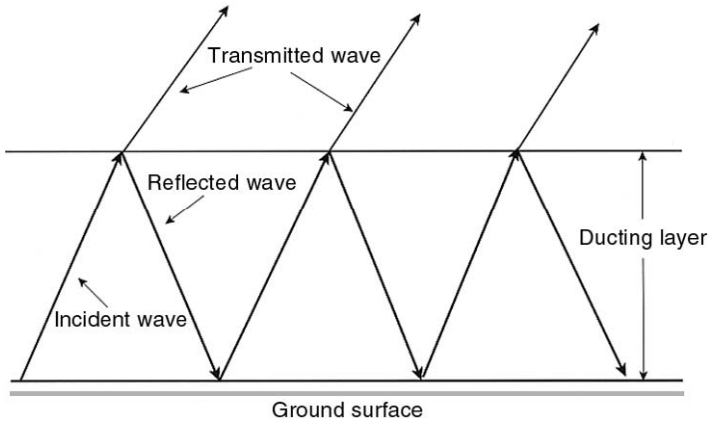

FIGURE 4.1 Illustration of wave reflection and transmission between the ground surface and some upper level. If the incident and reflected waves are in phase, then wave ducting can occur.

waves. Because wave energy is being continuously generated by the mountain, a *resonance* can develop when the upward and downward waves are in phase, and this can lead to extreme downslope winds such as those observed near Boulder, CO (see, for example, Lilly, 1978; Peltier and Calrk, 1979; Durran, 1986). Studies, for example, Bosart and Cussen (1973); Uccellini (1975); Balachandran (1980); and Stobie, Einaudi, and Uccellini (1983) show that thunderstorms often initiate ducted gravity waves which can propagate long distances ($\sim$1000 km) and can initiate new thunderstorms along their paths. Chimonas and Nappo (1987) used gravity wave theory to argue that a long-lived wind gust observed by Doviak and Ge (1984) could be modeled as a ducted thunderstorm *bow wave*. Monserrat and Thorpe (1996) used ducting theory to explain a long-lived gravity wave event observed on Mallorca (Baleric islands), and Rees *et al.* (2000) suggested that most of the high-frequency waves observed in the atmospheric boundary layer over the Brunt Ice Shelf, Antarctica correspond to trapped gravity waves. These few examples illustrate that gravity wave ducting is and continues to be a lively research topic.

4.1 WAVE REFLECTION AT AN ELEVATED LAYER

From optics we know that a change in the index of refraction results in a partial reflection and transmission of a light beam. In the atmosphere, a similar thing happens where there is a change in the vertical wavenumber which can be considered as an index of refraction for gravity waves. In the general case, where the Brunt–Väisälä frequency and background wind speed are changing continuously with height, the wave field can be very complicated and not easily analyzed. We consider here the much simpler case of a two-layer flow with constant but different stratification in each layer, as illustrated in Fig. 4.2. The bottom layer, layer 1,

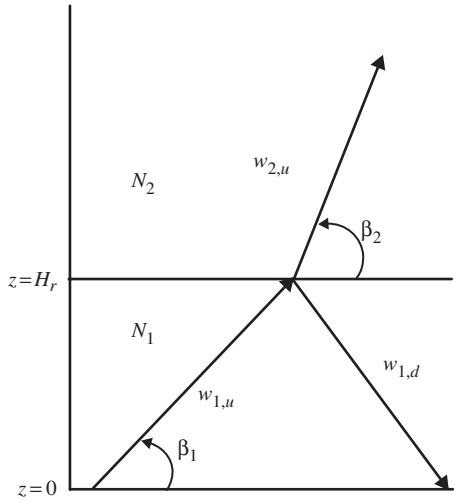

FIGURE 4.2 Wave reflection at height H_r where a discontinuity exists in stratification. $w_{1,u}$ upward-propagating incident wave: $w_{1,d}$ downward-propagating reflected wave: $w_{2,u}$ upward-propagating transmitted wave.

extends from the ground surface (assumed flat and uniform) up to the height of the reflection level, H_r. The upper layer, layer 2, is unbounded. Background conditions in each layer are constant. At the interface, the Brunt–Väisälä frequency changes discontinuously from N_1 below to N_2 above. In the bottom layer there is an upward-propagating wave, $w_{1,u}$, and a downward-propagating reflected wave, $w_{1,d}$. In the upper layer, we have only an upward-directed wave, $w_{2,u}$. To simplify the problem, we select the winds to be calm in each layer. Note that the group velocity of the upward-moving wave is downward and that of the downward-moving wave is upward. From a physical point of view, it might be more meaningful to do our analysis in terms of energy propagation rather than wavenumbers, but this can lead to needless complications. However, in the next section, where we consider wave reflection at the ground surface, we will use group velocity.

The linear analysis requires two conditions at the interface separating layers 1 and 2. The first condition, called the *dynamic boundary condition*, is that the atmospheric pressure be continuous across the interface, *i.e.*,

$$p_{0,1}(H_r) + p_{1,1}(H_r) = p_{0,2}(H_r) + p_{1,2}(H_r), \tag{4.1}$$

where $p_{0,1}$ and $p_{1,1}$ are the background and perturbation pressures in layer 1, *etc.* If (4.1) is not met, then infinite vertical accelerations at the interface are possible. The second condition, called the *kinematic boundary condition*, requires that the two layers remain in contact with each other. If this condition is not satisfied, then voids or cavitation regions at the interface are possible, as illustrated in Fig. 4.3. The kinematic boundary condition is satisfied if the vertical mass fluxes in each

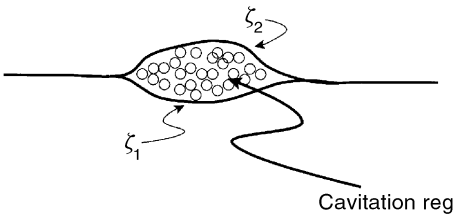

FIGURE 4.3 Cavitation or void between two material surfaces. If the fluid is water, then the circles represent bubbles. If the fluid is moist air, then the circles represent condensation droplets.

layer are equal at the interface, *i.e.*,

$$\rho_{0,1}(H_r)w_1(H_r) = \rho_{0,2}(H_r)w_2(H_r), \tag{4.2}$$

where $\rho_{0,1}$ is the background density in layer 1 and w_1 is the perturbation vertical velocity in layer 1, *etc*. To apply these boundary conditions, we need to know the amplitudes of the waves in each layer; however, generally these are not known. Gill (1982) defines the ratio

$$Z = \frac{p}{\rho_0 w} \tag{4.3}$$

as the *impedance*, which is defined in acoustics as the ratio of the force per unit area to the volume displacement of a given surface across which sound is being transmitted. Impedance can be thought of as the alternating-current analog of resistance in direct current. Note that the impedance is independent of wave amplitude. The dynamic and kinematic conditions require that $Z_1(H_r) = Z_2(H_r)$.

We first examine the case when the transmitted wave is propagating, *i.e.*, m real, and we assume, *a priori*, that ω does not change in the reflection-transmission process. From (2.49), we see then that

$$N_1 \cos\beta_1 = N_2 \cos\beta_2, \tag{4.4}$$

which is similar to Snell's law in optics. Note that β is the angle the wave vector makes with the horizontal and not with the reflecting boundary. Thus, (4.4) would hold even if the interface were sloping. We also see from (2.49) that the wave vector of the reflected wave in layer 1 must also make an angle β with the horizontal.

In layer 2, we have only upward-propagating energy, and so the wave phase fronts must be moving downward. Thus,

$$w_2 = a_2\, e^{-im_2(z-H_r)}\, e^{-i(kx-\omega t)}. \tag{4.5}$$

Using (2.14), (2.16), and (4.5), the pressure perturbation is

$$p_2 = \frac{1}{k^2}\,\rho_0\omega a_2 m_2\, e^{-im_2(z-H_r)}\, e^{-i(kx-\omega t)}. \tag{4.6}$$

The impedance in the upper layer is then

$$Z_2 = \frac{\omega m_2}{k^2}. \tag{4.7}$$

In the bottom layer, we have both upward and downward (reflected) energy propagation, so that

$$w_1 = \left[a_{1,u}\, e^{im_1(H_r-z)} + a_{1,d}\, e^{-im_1(H_r-z)}\right] e^{-i(kx-\omega t)}, \tag{4.8}$$

where subscripts u and d refer to the upward- and downward-moving waves, respectively. We now define a *reflection coefficient*, r, as the ratio of the amplitude of the reflected, downward-moving wave to the incident, upward-moving wave, *i.e.*,

$$r = \frac{a_{1,d}}{a_{1,u}}, \tag{4.9}$$

so that

$$w_1 = a_{1,u}\left[e^{im_1(H_r-z)} + re^{-im_1(H_r-z)}\right] e^{-i(kx-\omega t)}. \tag{4.10}$$

The perturbation pressure in layer 1 is

$$p_1 = \frac{\rho_0\omega a_{1,u} m_1}{k^2}\left[e^{im_1(H_r-z)} - re^{-im_1(H_r-z)}\right] e^{-i(kx-\omega t)}. \tag{4.11}$$

Using (4.10) and (4.11), the impedance in the bottom layer is

$$Z_1 = \frac{\omega m_1}{k^2}\left[\frac{e^{im_1(H_r-z)} - re^{-im_1(H_r-z)}}{e^{im_1(H_r-z)} + re^{-im_1(H_r-z)}}\right]. \tag{4.12}$$

Setting $Z_1(H_r) = Z_2(H_r)$ gives

$$\frac{m_2}{m_1} = \frac{1-r}{1+r}. \tag{4.13}$$

Solving (4.13) for r gives

$$r = \frac{m_1 - m_2}{m_1 + m_2}. \tag{4.14}$$

Note that from (2.41) the vertical wavenumbers of the upward- and downward-moving waves in layer 1 must be equal. Because k does not change in the reflection process, the angle of the wave vector relative to the horizontal plane is the same for both waves. However, because of (4.14) the amplitudes of the waves need not be equal.

If $r = 0$, then there is no reflection, and the wave is upward propagating only. If $|r| = 1$, then there is complete reflection, and the wave is trapped in the bottom layer. If $r = 1$, m_2 must be zero, and the transmitted wave does not propagate in the upper layer. Then, in the lower layer, $w_1 \propto \cos[m_1(H_r - z)]$, and the upward- and downward-moving waves are in phase and have equal amplitudes. The waves constructively interfere to form a *standing wave* much like sound waves in a open pipe. If $r = -1$, then $w_1 \propto i \sin[m_1(H_r - z)]$, *i.e.*, w_1 is purely imaginary, and consequently, $\Re w_1$ must be zero everywhere in the lower layer. This happens because now the upward- and downward-moving waves are exactly out of phase, but they have equal amplitudes. These waves destructively interfere. The effect is the same as if $m_1 = 0$, which is required from (4.14) when $r = -1$.

We consider now the case where $N_2 < \omega < N_1$. The transmitted wave is evanescent, and (4.5) and (4.6) become

$$w_2 = a_2\, e^{q(z-H_r)}\, e^{i(kx-\omega t)} \tag{4.15}$$

and

$$p_2 = \frac{i}{k^2}\, \rho_0 \omega a_2 q\, e^{-q(z-H_r)}\, e^{i(kx-\omega t)}, \tag{4.16}$$

respectively, where

$$q = k\left[1 - \frac{N_2^2}{\omega^2}\right]^{1/2}. \tag{4.17}$$

The impedance in layer 2 is now

$$Z_2 = \frac{i\omega q}{k^2} \tag{4.18}$$

and

$$r = \frac{m_1 - iq}{m_1 + iq}. \tag{4.19}$$

The magnitude of r is unity, so the total reflection occurs at H_r, and the wave is trapped in the bottom layer.

When $N_1 < \omega < N_2$, the waves in the lower layer are evanescent and are not reflected at H_r. However, the transmitted wave is propagating. The vertical velocity in the lower layer is

$$w_1 = a_1 e^{-qz} + b_1 e^{qz}, \tag{4.20}$$

where we have dropped the $e^{-i(kx-\omega t)}$ for convenience. Note that the second term in (4.20) is not the result of wave reflection, but is required for the solution of the Taylor–Goldstein equation. At $z = H_r$, the dynamic and kinematic boundary conditions require that

$$w_1(H_r) = w_2(H_r) \tag{4.21}$$

$$\frac{dw_1}{dz}(H_r) = \frac{dw_2}{dz}(H_r). \tag{4.22}$$

Using (4.20) and (4.5) in (4.21) and (4.22), we can solve for the constants a_1 and b_1 in terms of a_2. The vertical velocity in layer 1 is then

$$w_1 = \frac{a_2}{2}\left[\left(1 + i\frac{m_2}{q}\right)e^{q(H_r - z)} + \left(1 - i\frac{m_2}{q}\right)e^{q(H_r + z)}\right]. \tag{4.23}$$

From the continuity equation (2.8), the horizontal velocity in layer 1 is

$$u_1 = -i\frac{qa_2}{2k}\left[\left(1 + i\frac{m_2}{q}\right)e^{q(H_r - z)} + \left(1 - i\frac{m_2}{q}\right)e^{q(H_r + z)}\right]. \tag{4.24}$$

Using (4.26) and (4.27) in (2.38), the wave stress in layer 1 is

$$\tau = \frac{1}{2}\rho_0\frac{m_2}{k}a_2^2. \tag{4.25}$$

It is often mistakenly assumed that evanescent waves do not vertically transport energy or momentum; however, the above analysis clearly demonstrates that this is not the case. Wave stress is transported vertically at a constant rate and is a function of conditions in the upper propagating layer. Consider, for example, a uniform flow over a surface corrugation as given by (3.35). Figure 4.4 shows the streamline displacements calculated by a numerical model for this case when $u_0 = 2\,\mathrm{m\,s^{-1}}$, $N_1 \approx 0\,\mathrm{s^{-1}}$, $N_2 = 0.02\,\mathrm{s^{-1}}$, $\lambda_s = 1000\,\mathrm{m}$, and $H_r = 200\,\mathrm{m}$. Below H_r the streamlines are almost vertically orientated above the terrain disturbance. The slight upstream tilt of the streamlines represents the small yet finite wave stress transport. Above H_r the wave fronts tilt as expected.

4.2 WAVE TRAPPING, ENERGY FLUX, AND WAVE RESONANCE

In the proceeding section, we examined wave reflection due to a discontinuity in either Brunt–Väisälä frequency or background wind speed at some height, H_r, above the ground surface. In this section, we will look more closely at how waves

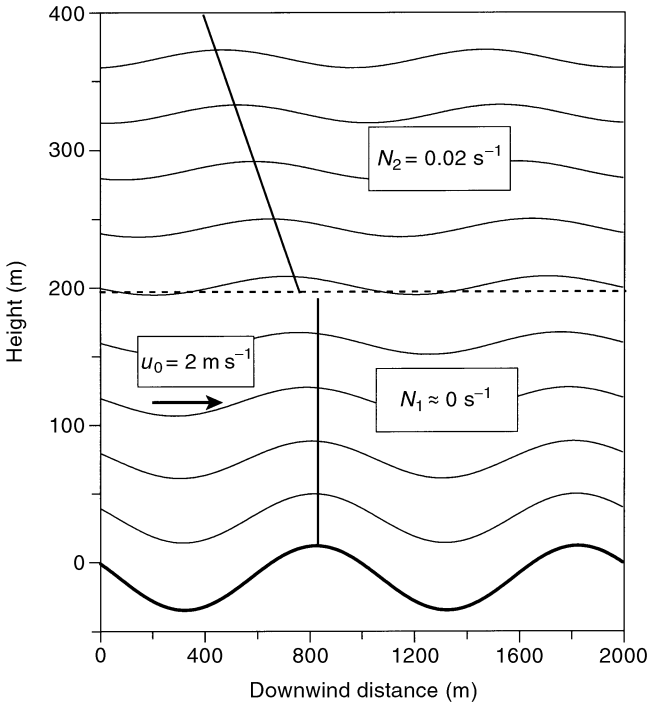

FIGURE 4.4 Leakage of wave energy through an evanescent region. An example of tunneling.

in the lower layer are affected when *wave trapping* occurs. It is useful to consider a continuous source of wave energy caused by a steady flow over a terrain disturbance $h(x)$. Applying boundary condition (3.14), (4.10) becomes

$$w = u_0 \frac{\partial h}{\partial x} \left[\frac{\left[e^{im_1(H_r - z)} + re^{-im_1(H_r - z)} \right]}{e^{im_1 H_r} + re^{-im_1 H_r}} e^{-i(kx)} \right], \tag{4.26}$$

where

$$m_1 = k \left[\frac{N_1^2}{\Omega^2} - 1 \right]^{1/2}. \tag{4.27}$$

Note that if $r = 0$ in (4.26), then w becomes similar to the wave perturbation velocity field above a terrain disturbance studied in Chapter 3. We see from (4.26) that if $r = -e^{i2m_1 H_r}$, then $w \to \infty$. If $m_1 H_r$ is an even multiple of $\pi/2$, then $r = -1$, and as we have seen in the previous section w is purely imaginary. H_r is a *node*, *i.e.*, a place where $w = 0$, and the upward- and downward-moving waves form a *standing wave* much as a vibrating string with both ends fixed, as illustrated in Fig. 4.5. Because the source of energy is continuous and because there is no

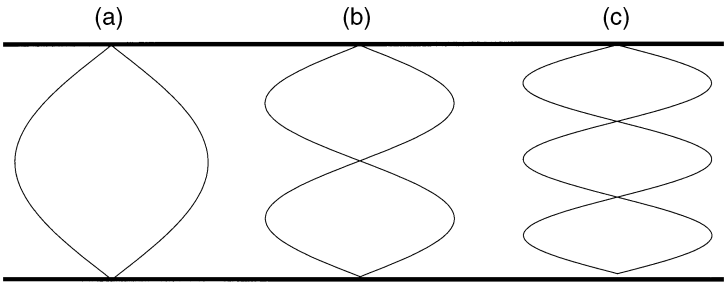

FIGURE 4.5 Standing waves or modes occur when a string is fixed at both ends: (a) fundamental or gravest mode, (b) first harmonic, and (c) second harmonic.

loss of energy through the top of the layer, the wave amplitude in the bottom layer can grow without bound, resulting in *wave resonance*. Using (4.19), we see that

$$r = -e^{i2m_1H_r} = \frac{m_1 - iq}{m_1 + iq}. \tag{4.28}$$

If we rationalize the denominator in (4.28) and then take the square root, we get

$$ie^{im_1H_r} = \frac{m_1 - iq}{\left(m_1^2 + q^2\right)^{1/2}}. \tag{4.29}$$

Separating (4.29) into real and imaginary parts leads to

$$\sin(m_1H_r) = \frac{-m_1}{\left(m_1^2 + q^2\right)^{1/2}}$$

$$\cos(m_1H_r) = \frac{-q}{\left(m_1^2 + q^2\right)^{1/2}},$$

and hence

$$\tan(m_1H_r) = \frac{m_1}{q}. \tag{4.30}$$

Solutions to this transcendental equation will be discussed in Section 4.3.1. For now, we note that (4.30) is an eigenvalue problem. For a given combination of background variables u_0, N, and H_r, there are unique pairs of values (c, k) which are solutions to (4.30).

We can scale the problem by assuming constant flow over a sinusoidal surface with amplitude H and horizontal wavenumber k_s, *i.e.*, (3.4). Comparing (3.24) with (4.26) gives

$$w_1 = -iu_0Hk_s\left[\frac{e^{im_1(H_r-z)} + re^{-im_1(H_r-z)}}{e^{im_1H_r} + re^{-im_1H_r}}\right]e^{-ik_sx}. \tag{4.31}$$

The perturbation pressure (3.26) becomes

$$p_1 = -iu_0^2 H m_1 \left[\frac{e^{im_1(H_r - z)} - re^{-im_1(H_r - z)}}{e^{im_1 H_r} + re^{-im_1 H_r}} \right] e^{-ik_s x}. \tag{4.32}$$

Following Gill (1982), we evaluate the vertical component of the energy flux, (2.98), using (4.31), (4.32), and (4.13) to get

$$F_z = \frac{0.5\rho_0 u_0^3 H^2 k_s m_2}{1 + [(m_2/m_1)^2 - 1]\sin^2(m_1 H_r)}. \tag{4.33}$$

We see that the energy flux is a function not only of the conditions in the bottom layer where the waves are generated, but also in the upper layer. The reflection coefficient determines how much of the wave energy passes through the interface and how much is reflected. The angle $m_1 H_r$ determines the phase difference between the upward- and downward-moving waves in the bottom layer. For example, when $m_1 H_r = n\pi/2$ and n is an even integer, $\sin(m_1 H_r) = 0$, and (4.33) is

$$F_z = 0.5\rho_0 u_0^3 H^2 k_s m_2. \tag{4.34}$$

As we have seen, in this case the upward- and downward-moving waves in the bottom layer form a standing wave with no vertical energy transport. The energy flux is determined only by the transmitted wave in the upper layer. When $m_1 H_r$ is an odd multiple of $\pi/2$, then $\sin(m_1 H_r) = 1$, and

$$F_z = 0.5\rho u_0^3 H^2 k_s m_1^2/m_2. \tag{4.35}$$

Now, the energy flux is a function of the conditions in both layers. As m_2 decreases, the energy increases as the resonance condition is approached. However, if m_2 increases, for example, due to increasing stratification, N_2, then the energy flux decreases. If N_2 becomes so large such that $m_2 \gg m_1$, then $r \approx -1$, and the wave energy would be trapped in the lower layer with no leakage into the upper layer.

4.2.1 REFLECTION AT THE GROUND SURFACE

Wave reflection at an upper level was considered in the previous section. However, wave ducting also requires reflection at the ground surface, which is discussed in this section. This problem is simpler than reflection at an elevated level because we do not consider a transmitted wave. The reflection will be complete in the sense that the total energy of the incident and reflected wave is conserved. In the linear theory it is often assumed that the ground surface is horizontal, but in the real world horizontal surfaces of significant extent are seldom seen.

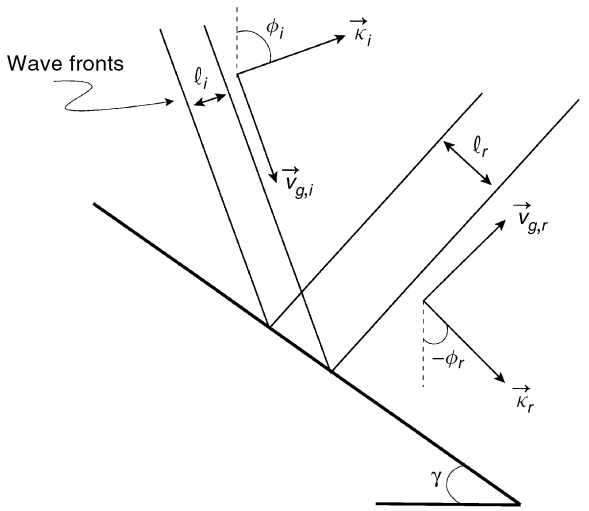

FIGURE 4.6 Wave reflection at a sloping ground surface.

Gravity wave reflections from sloping surfaces are also important in oceanography (see, for example, Wunsch, 1968; Phillips, 1977; Thorpe, 1987).

To examine the effects of surface slope on wave reflection, we let the two-dimensional ground surface be inclined an angle γ to the horizontal, as illustrated in Fig. 4.6. Because the reflected energy flux has the same value as the incident energy flux, it is conceptually easier to do the analysis in terms of group velocity rather than wavenumbers. Then, as shown in Fig. 4.6, the incident wave has downward-directed group velocity $\vec{v}_{g,i}$ with upward-directed wave vector $\vec{\kappa}_i$, and the reflected wave has upward-directed group velocity $\vec{v}_{g,r}$ and downward-directed wave vector $\vec{\kappa}_r$. Let w_i represent the vertical velocity perturbation with amplitude a_i associated with the incident wave, and let w_r represent the vertical velocity perturbation with amplitude a_r associated with the reflected wave. We also assume the background stratification and wind is constant, and accordingly, the frequencies of the incident and reflected waves are equal. Then,

$$w_i(x, z, t) = a_i \, e^{i(k_i x + m_i z - \omega t)} \tag{4.36}$$

and

$$w_r(x, z, t) = a_r \, e^{i(k_r x + m_r z - \omega t)}, \tag{4.37}$$

where subscripts i and r refer to the incident and reflected waves, respectively. The vertical wavenumber can be written as

$$m^2 = k^2 \Delta^2, \tag{4.38}$$

where

$$\Delta^2 = \frac{N^2}{\Omega^2} - 1. \tag{4.39}$$

Then the vertical wavenumbers for the incident and reflected waves are

$$m_i^2 = k_i^2 \Delta^2 \tag{4.40}$$

and

$$m_r^2 = k_r^2 \Delta^2, \tag{4.41}$$

respectively. Since Δ is a constant, $|m_i/k_i| = |m_r/k_r|$, and we see that the magnitudes of the angles the wave vectors make with the horizontal or vertical directions are equal regardless of the inclination of the reflecting surface. This is a surprising result since intuition would suggest that the inclination of the surface would have a strong effect as, for example, reflection of a beam of light from a mirror. However, the propagation of gravity waves is determined by the environment; this is a constraint. This is no less paradoxical than the fact that the speed of sound is independent of the speed of the sound source. However, we note that the vertical and horizontal wavenumbers of the incident and reflected waves are not equal, but rather their ratios are equal. Thus, wave reflection from the sloping surface results in change in wavelength and a corresponding transfer of wave energy from one wavenumber to another.

As shown in Fig. 4.6, the angle the incident wave vector makes with the vertical direction is

$$\tan \phi_i = \frac{k_i}{m_i} = \frac{1}{\Delta}. \tag{4.42}$$

The process of reflection implicitly assumes a reversal of direction of some kind. Either the horizontal or vertical wavenumber must change sign on reflection, but unless we know the inclination angle of the reflecting surface, we cannot say which wavenumber changes sign. Accordingly, we can write

$$\tan \phi_r = \frac{k_r}{m_r} = -\frac{1}{\Delta}. \tag{4.43}$$

From the linearized continuity equation (2.8), we have

$$ku + mw = 0, \tag{4.44}$$

so that

$$u_i = -\frac{m_i}{k_i} w_i = -\Delta w_i \tag{4.45}$$

and

$$u_r = -\frac{m_r}{k_r} w_r = \Delta w_r. \tag{4.46}$$

Using (4.36) and (4.37) along with (4.45) and (4.46), the perturbation velocities are

$$\vec{V}_i = a_i(-\Delta\hat{x} + \hat{z})\, e^{i(k_i x + m_i z - \omega t)} \tag{4.47}$$

$$\vec{V}_r = a_r(\Delta\hat{x} + \hat{z})\, e^{i(k_r x + m_r z - \omega t)}. \tag{4.48}$$

The velocity perturbation is the sum of the incident and reflected velocity perturbations, so that

$$\vec{V} = \vec{V}_i + \vec{V}_r \tag{4.49}$$

$$= a_1(-\Delta\hat{x} + \hat{z})\, e^{i(k_i x + m_i z - \omega t)} + a_r(\Delta\hat{x} + \hat{z})\, e^{i(k_r x + m_r z - \omega t)}. \tag{4.50}$$

Now let the elevation of the ground surface be given by $z_g = -\alpha x$, where $\alpha = \tan\gamma$. At $z = z_g$ we require

$$\vec{V} \cdot \vec{n} = 0, \tag{4.51}$$

where $\vec{n}$ is the outward drawn normal vector to the ground surface. For the configuration shown in Fig. 4.6, $z_g = -\alpha x$, with x negative to the left of an arbitrary origin. The equation for the surface elevation is then

$$\phi_s = z + \alpha x, \tag{4.52}$$

and

$$\vec{n} = \frac{\nabla\phi_s}{|\nabla\phi_s|} = \frac{\alpha\hat{x} + \hat{z}}{(\alpha^2 + 1)^{1/2}}. \tag{4.53}$$

Then at $z = z_g$ we have from (4.51)

$$\left[a_1(-\Delta\hat{x} + \hat{z})\, e^{i(k_i x - m_i \alpha x - \omega t)} + a_r(\Delta\hat{x} + \hat{z})\, e^{i(k_r x - m_r \alpha x - \omega t)}\right] \cdot (\alpha\hat{x} + \hat{z}) = 0. \tag{4.54}$$

Now if (4.54) is to hold for all times, we require

$$k_i x - m_i \alpha x = k_r x - m_r \alpha x. \tag{4.55}$$

Solving for k_r and using (4.42) and (4.43) we get

$$k_r = k_i \frac{(1 - \alpha\Delta)}{(1 + \alpha\Delta)}, \tag{4.56}$$

and we see that when the ground surface is sloped, the horizontal wavenumbers of the incident and reflected wave are not equal. Using (4.55) in (4.54) leads to

$$a_r = -a_i \frac{(1 - \alpha\Delta)}{(1 + \alpha\Delta)}. \tag{4.57}$$

If $\alpha\Delta < 1$, the reflection is forward, the vertical velocities w_i and w_r have opposite phase, and the reflected wavelength ℓ_r is greater than the incident wavelength ℓ_i, as shown in Fig. 4.6. If $\alpha\Delta > 1$, the reverse is true. If slope angle γ equals 0 or $\pi/2$, corresponding to a horizontal or vertical surface, respectively, there is no change in the wave on reflection. A critical slope angle exists where $\gamma = -\phi_i$, *i.e.*, where $\alpha\Delta = 1$. In this case, the incident wave is reflected back on itself, and the waves constructively interfere, resulting in a wave resonance.

4.3 WAVE DUCTS

We have seen that an internal gravity wave can be reflected at some level where either the Brunt–Väisälä frequency or the background wind speed changes abruptly. If the distance between the ground surface and the reflecting level is a multiple of the vertical wavelength, then reflected and incident waves can constructively interfere, resulting in wave resonance. When this happens the wave is trapped or ducted, and the ducting layer becomes a tuned wave guide.

4.3.1 THE TEMPERATURE DUCT

The simplest wave duct is the *temperature duct* caused by a discontinuity in the temperature lapse rate. Figure 4.7 illustrates the problem. Below height H_d, N is constant and positive; above H_d, we set N equal to zero. We assume calm background winds; however, the analysis is unchanged if we have a constant background wind. We shall look for those waves that can exit in this duct. At the

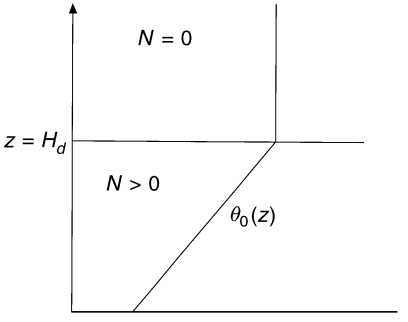

FIGURE 4.7 Schematic of a temperature duct of depth H_d, and potential temperature profile $\theta_0(z)$.

ground surface, $\hat{w}(k, 0) = 0$, and above H_d we require the wave amplitude to be bounded. The wave solutions to (2.39) are then

$$\hat{w}(k, z) = A \sin\left[k\left(\frac{N^2}{\omega^2} - 1\right)^{1/2} z\right] \qquad 0 \le z \le H_d \tag{4.58}$$

$$\hat{w}(k, z) = Be^{k(z-H_d)} + Ce^{-k(z-H_d)} \qquad z > H_d. \tag{4.59}$$

From (4.59), we see that for decreasing wave amplitudes above H_d we must find those *eigenvalues* ω and k in (4.58) and (4.59) which result in $B = 0$. At the interface $z = H_d$, the dynamic and kinematic boundary conditions require that p and w be continuous. From the polarization equations (2.22) and (2.24), we see that $\hat{p} \propto \partial\hat{w}/\partial z$, so that we require both $\hat{w}$ and its derivative be continuous at $z = H_d$. Thus,

$$A \sin\left[H_d k\left(\frac{N^2}{\omega^2} - 1\right)^{1/2}\right] = B + C \tag{4.60}$$

$$Ak\left(\frac{N^2}{\omega^2} - 1\right)^{1/2} \cos\left[H_d k\left(\frac{N^2}{\omega^2} - 1\right)^{1/2}\right] = kB - kC. \tag{4.61}$$

Now multiply (4.60) by k and add to (4.61) to get

$$\left(\frac{N^2}{\omega^2} - 1\right)^{1/2} \cos\left[H_d k\left(\frac{N^2}{\omega^2} - 1\right)^{1/2}\right] + \sin\left[H_d k\left(\frac{N^2}{\omega^2} - 1\right)^{1/2}\right] = \frac{2B}{A}. \tag{4.62}$$

Then $B = 0$ only when

$$\left(\frac{N^2}{\omega^2} - 1\right)^{1/2} \cos\left[H_d k\left(\frac{N^2}{\omega^2} - 1\right)^{1/2}\right] + \sin\left[H_d k\left(\frac{N^2}{\omega^2} - 1\right)^{1/2}\right] = 0. \tag{4.63}$$

Now let $k_* = H_d k$ be a nondimensional wavenumber, and let $\omega_* = (N^2/\omega^2 - 1)^{1/2}$ be a nondimensional frequency. Then (4.63) becomes

$$\tan(k_*\omega_*) = -\omega_*. \tag{4.64}$$

However, (4.64) is identical in form to (4.30). Indeed, if $N_2 = 0$ in (4.18), then (4.64) and (4.30) are identical.

The zeros of (4.64) are easily obtained numerically by iteration, and these eigenvalues (k_*, ω_*) are plotted in Fig. 4.8, which shows the dimensionless dispersion relation for the temperature duct. The slope of the curve in Fig. 4.8 is the

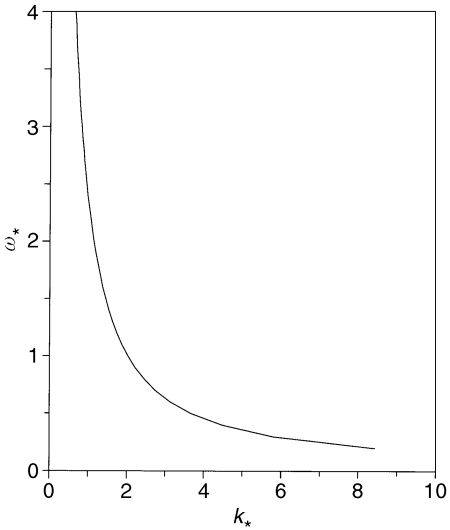

FIGURE 4.8 Dimensionless eigenvalues for the pure temperature duct with constant stratification.

dimensionless horizontal group velocity, *i.e.*,

$$u_{g*} = \frac{\partial \omega_*}{\partial k_*} = \frac{N^2 \left(N^2/\omega^2 - 1\right)^{-1/2}}{\omega^3 H_d} \frac{\partial \omega}{\partial k}, \tag{4.65}$$

where we have used the definitions of ω_* and k_*. If we let $\theta = k_* \omega_*$, we can define the functions $Y_1 = -\theta/k_*$ and $Y_2 = \tan(\theta)$, and the solutions to (4.64) occur where $Y_1 = Y_2$. Figure 4.9 shows plots of Y_1 and Y_2 as functions of θ for the case $k_* = 0.5$. The values of θ at the intersection of these curves are the solutions to (4.64), and we see that there is a family of solutions because Y_2 is periodic with period π. Each solution corresponds to a vertical mode, *i.e.*, $Y_{2,0}$ is the *fundamental mode* and $Y_{2,1}$ is the *first harmonic*, *etc*. If we choose $H_d = 300$ m and $N^2 = 0.003$ s^{-2}, then $k = 0.00167$ m^{-1}, $\omega_0 = 0.0144$ s^{-1}, and $\omega_1 = 0.00566$ s^{-1}. The vertical velocities of the fundamental mode and first harmonic for this case with $A = 1$ are plotted in Fig. 4.10. The fundamental mode does not change sign between the ground surface and H_d, and the first harmonic changes sign once in this layer. Higher modes change sign accordingly, *i.e.*, two sign changes for the second harmonic, *etc*. Note also in Fig. 4.10 that the one-fourth of the vertical wavelength of the fundamental mode is less than the depth of the temperature duct. Above the ducting region the amplitudes of the modes decay exponentially, and there is no vertical transport of energy or stress. Figure 4.11 plots the phase and group velocities and the frequency as functions of wavenumber for the fundamental mode for this problem. These curves were obtained by numerical solutions of the Taylor–Goldstein equation using

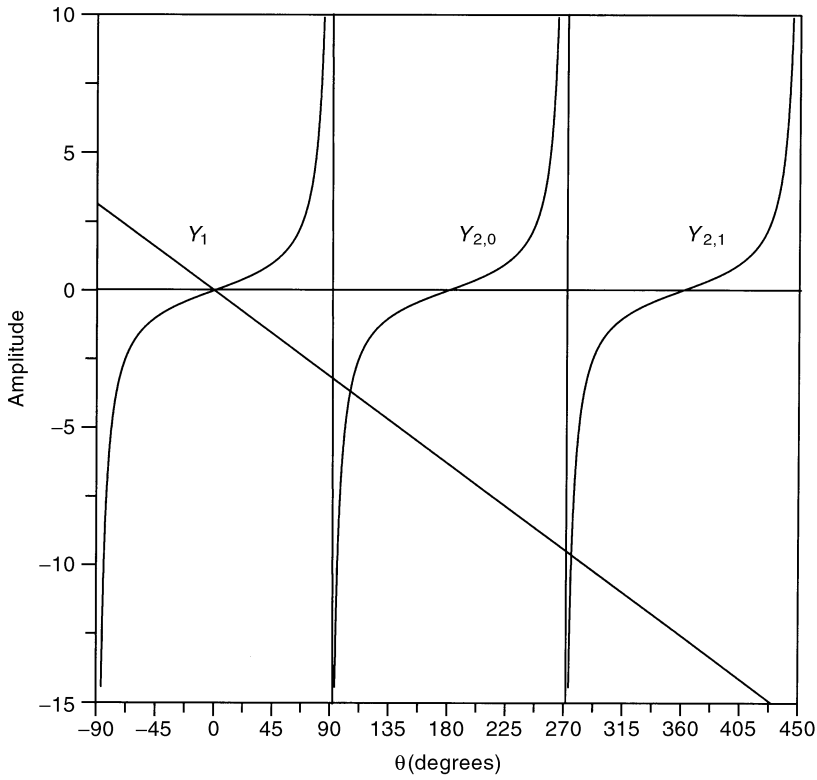

FIGURE 4.9 Graphical solutions to the pure temperature duct. $H_d = 300$ m; $N = 0.055$ s^{-1}.

techniques described in Chapter 9. Because $N = 0$ above the ducting region, the limits on phase speed are $0 < c < N/k$. If c is greater than N/k, the wave becomes evanescent. For the above values of N and k, c must be less than about 32.8 m s^{-1}. For $k = 0.00167$ m^{-1}, the phase velocities of the fundamental mode and first harmonic are calculated to be $c_0 = 8.6$ m s^{-1} and $c_1 = 3.4$ m s^{-1}, respectively. The group velocities are calculated to be $u_{g,0} = 7.0$ m s^{-1} and $u_{g,1} = 3.3$ m s^{-1}. The modes do not propagate along the duct with the same speed, even though the modes have the same horizontal wavenumber. Thus, in any real situation one seldom sees more than one mode, and that mode is usually the fundamental or fastest traveling mode.

4.3.2 THE WIND DUCT

We now examine the *wind duct* which is created by a jet in the background wind in the direction of wave propagation. This type of duct was first described by Chimonas and Hines (1986). It is a very common type of wave duct throughout

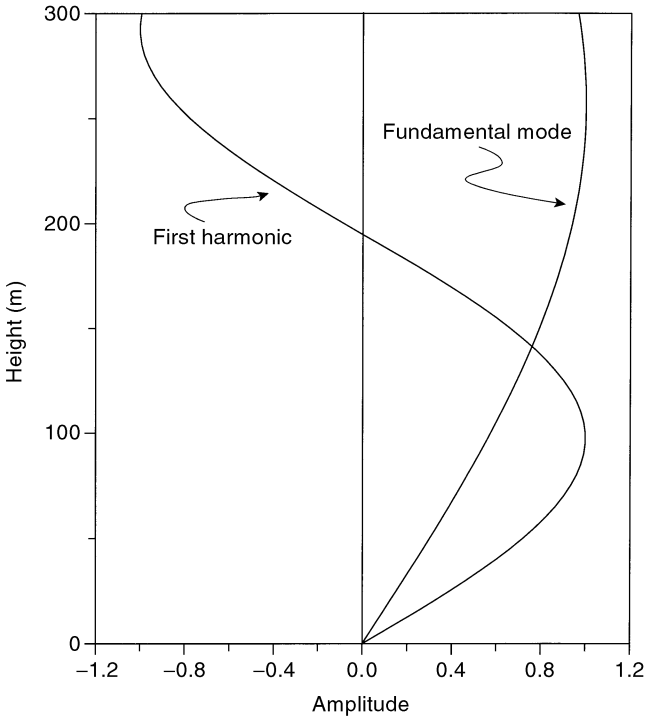

FIGURE 4.10 Fundamental mode and first harmonic for the solutions to the temperature duct shown in Fig. 4.9.

the atmosphere. Consider the Taylor–Goldstein equation

$$\frac{\partial^2 \hat{w}}{\partial z^2} + Q^2 \hat{w} = 0, \tag{4.66}$$

where

$$Q^2 = \frac{N^2}{(c - u_0)^2} + \frac{u_0''}{(c - u_0)} - k^2. \tag{4.67}$$

Figure 4.12 illustrates the wind duct. A jet with maximum speed, $u_{0,max}$, defines a ducting region where $Q^2 > 0$. On either side of this region, $Q^2 < 0$ and the gravity waves are evanescent. Far from the jet, in the evanescent regions,

$$\frac{N^2}{(c - u_{0,min})^2} < k^2. \tag{4.68}$$

Critical levels exist where $c = u_0$, and these will be discussed in Chapter 5. We shall see that at a critical level a gravity wave is absorbed if the Richardson number

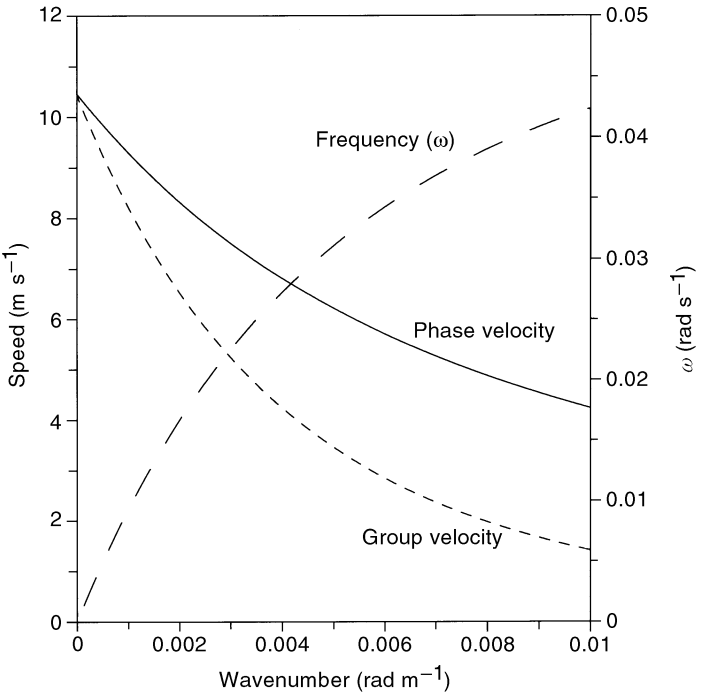

FIGURE 4.11 Phase speed, horizontal group velocity, and frequency as a function of wavenumber obtained from numerical solutions for the pure temperature duct. $H_d = 300$ m; $N = 0.055\ \text{s}^{-1}$.

is greater than 0.25, but becomes unstable if the Richardson number is less than 0.25. In either case, a ducted wave will not exist. To avoid critical levels in our analysis, we consider only waves with phase speeds either less than $u_{0,min}$ or greater than $u_{0,max}$. Because the wind speed is not constant we must use numerical techniques. Let us assume that above the top level of the numerical model, $ztop$, N is constant and $u_0 = u_{0,min}$. In the evanescent region above $ztop$ the wave solutions are

$$\hat{w} = Ae^{q(z-ztop)} + Be^{-q(z-ztop)}, \tag{4.69}$$

where

$$q = k^2 - \frac{N^2}{(u_{0,min})^2}. \tag{4.70}$$

The kinematic and dynamic boundary conditions must be satisfied at $z = ztop$, and hence

$$\hat{w}(k, c, ztop) = A + B \tag{4.71}$$

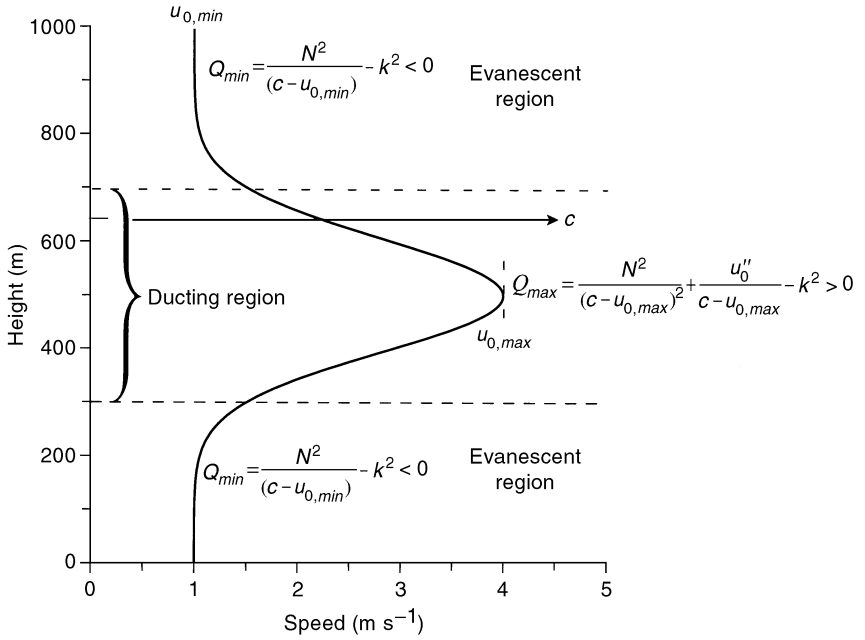

FIGURE 4.12 Schematic diagram of the wind duct.

and

$$\frac{\partial \hat{w}(k, c, ztop)}{\partial z} = qA + qB. \tag{4.72}$$

Solving for (4.71) and (4.72) for A gives

$$2A = \hat{w}(k, c, ztop) + \frac{1}{q}\frac{\partial \hat{w}(k, c, ztop)}{\partial z}. \tag{4.73}$$

The numerical technique uses the so-called *shooting method*. We start at the bottom boundary where we assume $\hat{w}(k, c, 0) = 0$ with a given value of k and an initial guess for the phase speed. We integrate (4.66) upward to $ztop$ where we evaluate A using (4.73) and check for for convergence, *i.e.*, $A < \epsilon$, where ϵ is a small number. If convergence is not reached, then we repeat the calculations again starting at the bottom boundary, but with an updated value of phase speed. The process continues until $A \to \epsilon$. To determine all the characteristics of the duct, *i.e.*, phase and group velocities, the numerical procedure is again repeated, but now with a new value of k.

As an example of the wind duct, consider the *low-level jet* shown in Fig. 4.13 along with the accompanying temperature profile. The analytical expressions for

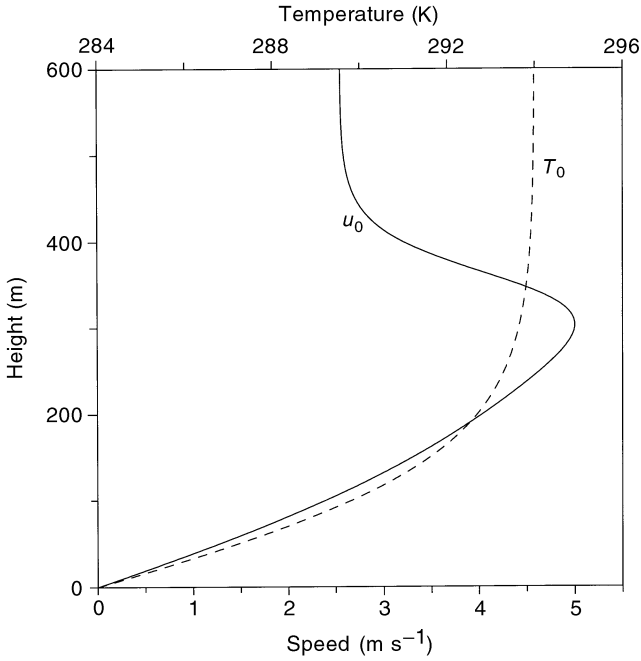

FIGURE 4.13 Wind speed and temperature profiles for a low-level jet. Based on profiles from Mastrantonio *et al.* (1979).

these curves are given by Mastrantonio, Einaudi and Fua (1976), *i.e.*,

$$u_0(z) = \frac{u_s}{1 + \tanh(2)} \left[\frac{sz/H_j}{(s+1) + (z/H_j)^s} + \tanh\left(\frac{2z}{H_j}\right) \right] \tag{4.74}$$

and

$$T(z) = n \tanh(z/H_j) + T_0, \tag{4.75}$$

where u_s is the maximum wind speed at the jet, H_j is the height of the jet above the ground surface, s and n are shape parameters, and T_0 is the temperature at the ground surface. The maximum background wind speed is 5 m s^{-1} at 300 m above the ground surface. To avoid critical levels, we look for waves with phase speeds $c > u_s$. Note that at the speed jet we require

$$\frac{N^2(H_s)}{(c - u_s)^2} > k^2. \tag{4.76}$$

Then the range of phase speeds for ducted waves is

$$\frac{N(ztop)}{k} + u_0(ztop) \leq c \leq \frac{N(H_j)}{k} + u_s. \tag{4.77}$$

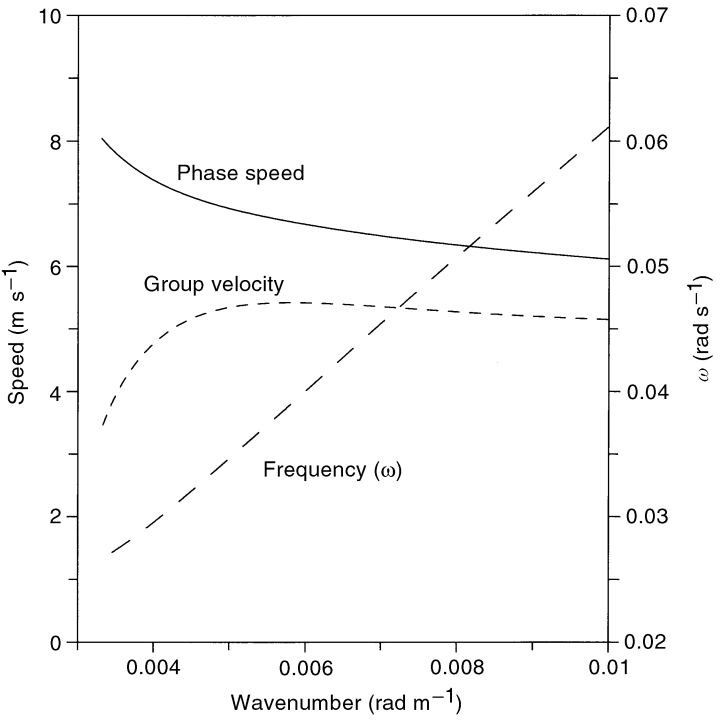

FIGURE 4.14 Phase speed, horizontal group velocity, and frequency as a function of wavenumber obtained from numerical solutions for a duct in a low-level jet defined by the profiles in Fig. 4.13.

We use the FORTRAN codes described in Chapter 9 to calculate the phase speeds, horizontal group velocities, and frequencies as functions of wavenumber. These results for the fundamental mode are plotted in Fig. 4.14. These curves have a markedly different appearance than those shown in Fig. 4.11. With decreasing wavenumber, the horizontal group velocity, $\partial\omega/\partial k$, initially increases slowly, but then rapidly decreases. The values plotted in Fig. 4.14 represent intrinsic values. The actual wave characteristics, *i.e.*, frequency, wavenumber, *etc.*, that would be observed by a stationary observer must be Doppler shifted. Figure 4.15 shows the vertical variation of the perturbation velocities associated with the fundamental mode of the wind duct. Because the wave velocities are known only to within a undetermined constant, the values in Fig. 4.15 have been scaled so that the maximum magnitude of the horizontal velocity is 2 m s^{-1}, which is a reasonable value in the boundary layer. The maximum value of u_1 occurs at the nose of the jet, and the secondary maximum at about 350 m occurs at the inflection point. The background wind is almost constant above 600 m (see Fig. 4.13); from Fig. 4.15 we see that u_1 and w_1 begin to decay exponentially at about 450 m. This marks the top of the ducting layer which extends to the ground surface.

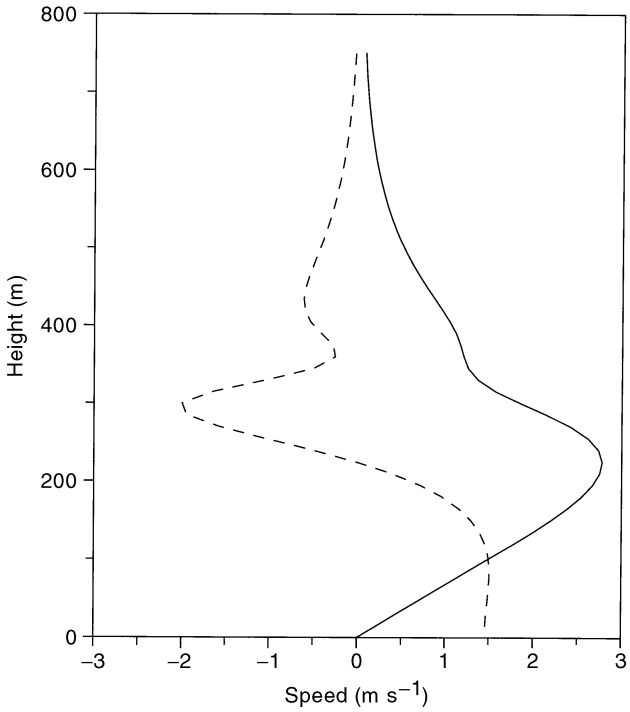

FIGURE 4.15 Profiles of wave perturbation velocities u_1 (dashed line) and w_1 (solid line) for the fundamental mode of the low-level jet shown in Fig. 4.13. The values were obtained from a numerical solution and were maximized so that the absolute magnitude of u_1 is 2 m s^{-1}.

4.3.3 WIND SPIRALS AND DUCTS

In the previous section, we said that the wind duct is very common. If there is a jet in the background wind speed, then there exists a possibility for a wave duct. Thus, the occurrence of wave ducts depends on the occurrence of speed jets, and whenever there is a turning of the background wind direction with height there is a possibility of a speed jet. The background wind speed seen by the wave is the projection of the horizontal wind vector onto the horizontal wave vector, *i.e.*,

$$u_0(z) = \vec{V}(z) \cdot \frac{\vec{k}}{|k|}. \tag{4.78}$$

In the lower troposphere and especially in the nighttime planetary boundary layer, there can be significant turning of the wind with height. To illustrate, we consider the *Ekman wind spiral* which is derived in Appendix A. Briefly, above the planetary boundary layer and away from the frictional force of the ground

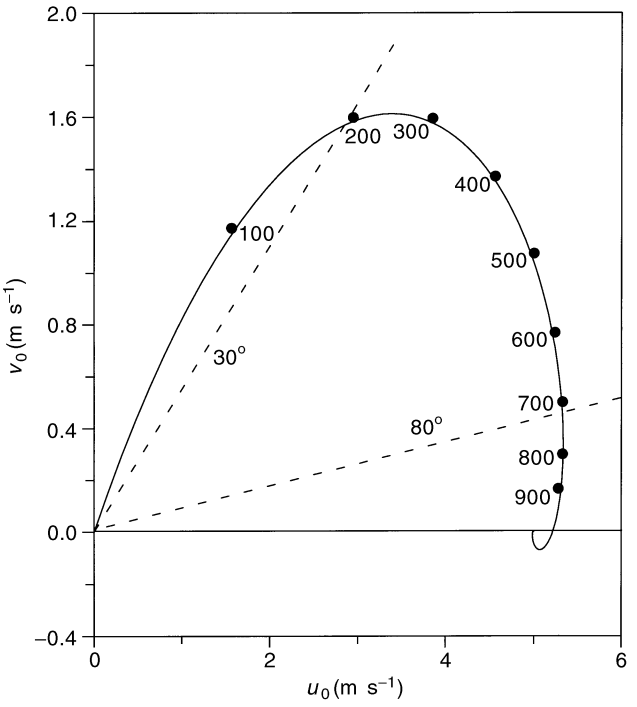

FIGURE 4.16 The Eckman spiral for the case $U_g = 5$ m s^{-1}, $f = 10^{-4}$ s^{-1}, and EKF = 5 m s^{-2}.

surface the wind tends to parallel the *isobars* or lines of constant atmospheric pressure. This type of flow, called *geostrophic wind*, is the result of a balance between the pressure gradient force which accelerates the fluid from high to low pressure and the rotational or *Coriolis* force which, in the Northern Hemisphere, accelerates the fluid to the right of its direction of motion with a force that is proportional to flow speed. Thus, in the Northern Hemisphere the atmospheric flow is clockwise around a high pressure area and counterclockwise around a low pressure area. At lower elevations, ground friction acts to slow the flow speed, and this decreases the magnitude of the Coriolis force. However, the pressure gradient force is unchanged. As a result an imbalance of the forces occurs, and the winds are directed across the isobars. The friction force grows as the ground surface is approached, and as a result the turning of the wind toward lower pressure increases. The result of this interplay of forces is a flow which increases in speed and rotates to the right of its motion (in the Northern Hemisphere) with height forming a wind spiral. Ekman (1904) observed that the current on the ocean's surface was always to the right of the current at greater depth, and his analysis was later applied to the atmosphere. If our coordinate system is rotated so that the x-axis is in the direction to the geostrophic wind, U_g, then the orthogonal components of the background

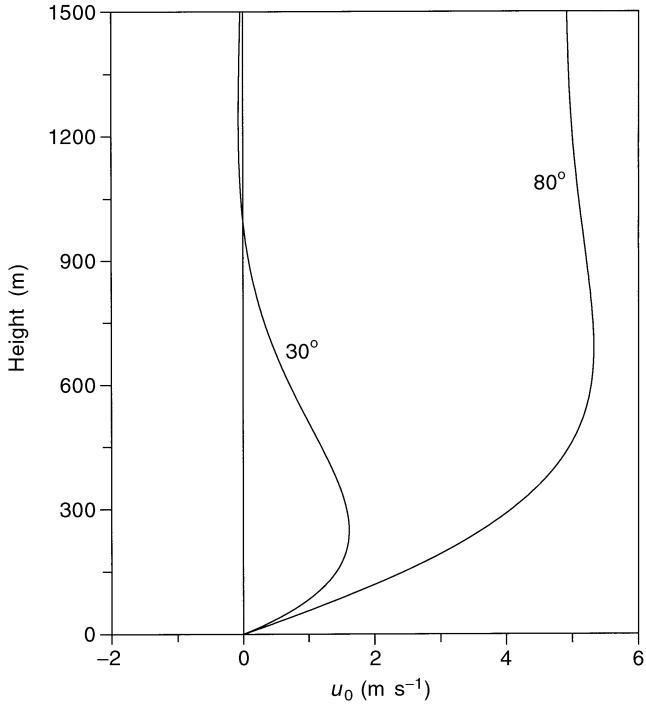

FIGURE 4.17 Vertical profiles of wind speed along vertical planes passing through the Eckman spiral shown in Fig. 4.16 at angles of 30° and 80° from north.

wind in the *Ekman layer* are

$$u_0(z) = U_g\left[1 - e^{-z/z_E}\cos(z/z_E)\right] \tag{4.79}$$

$$v_0(z) = U_g e^{-z/z_E}\sin(z/z_E), \tag{4.80}$$

where z_E is the depth of the Ekman layer, *i.e.*,

$$z_E = \sqrt{\frac{K}{f/2}}, \tag{4.81}$$

where K is the *eddy coefficient of friction* (m^2 s^{-1}) and f is the *Coriolis parameter* (s^{-1}). For midlatitudes, $f \approx 10^{-4}$ s^{-1}. Figure 4.16 shows the Ekman spiral for the case $U_g = 5$ m s^{-1}, $f = 10^{-4}$ s^{-1}, and EKF = 5 m s^{-2}; the dots along the curve mark the altitude. The vertical profiles along the vertical planes with orientations of 30° and 80° from north (shown in Fig. 4.16) are plotted in Fig. 4.17. Along the 30° plane a significant jet exists close to the ground; however, for the 80° plain only a weak jet is seen. Thus, we see that whenever there is a turning of the wind with height, there is the possibility of a jet and ducted waves.

This Page Intentionally Left Blank

5

Gravity Wave Energetics

In Chapter 2, we introduced the subject of wave energy and developed the equation for the total wave energy (2.86). In this chapter we examine the wave energy in more detail. We will also examine the transports of wave energy and stress and look at wave behavior near a critical level.

5.1 Variations of Wave Energy and Stress with Height

We consider the case when the wave is independent of time. As we have seen in Chapter 3, these types of waves are mountain waves. Following Eliassen and Palm (1960), we write the energy equation (2.86) as

$$\frac{\partial}{\partial x}(u_0 E + u_1 p_1) + \frac{\partial}{\partial z}(w_1 p_1) = -\rho_0 u_1 w_1 \frac{du_0}{dz}. \tag{5.1}$$

The left-hand side of (5.1) represents the divergence of the wave-energy flux. The term $(u_0 E + u_1 p_1)$ represents the horizontal flux of wave energy through a unit vertical area, and the term $w_1 p_1$ represents the vertical flux of wave energy through a unit horizontal area. As we have seen in Chapter 2, the right-hand side of (5.1) represents the transfer of kinetic energy between the wave and the mean flow. We have also seen in Chapter 3 that the waves and wave energy generated by an isolated terrain feature tend to remain above the feature, especially if the

waves are hydrostatic. Then, the waves and wave energy vanish as $x \to \pm\infty$, and integration of (5.1) in the x-direction gives

$$\frac{d}{dz}\int_{-\infty}^{+\infty} w_1 p_1 \, dx = -\frac{du_0}{dz}\int_{-\infty}^{+\infty} \rho_0 u_1 w_1 \, dx. \tag{5.2}$$

If we now multiply the linearized horizontal momentum equation (3.88) by $(\rho_0 u_0 u_1 + p_1)$, and integrate the result with respect to x from $-\infty$ to $+\infty$, we get

$$\int_{-\infty}^{+\infty} w_1 p_1 \, dx = -u_0 \int_{-\infty}^{+\infty} \rho_0 u_1 w_1 \, dx. \tag{5.3}$$

If we define

$$\int_{-\infty}^{+\infty} w_1 p_1 \, dx \equiv \overline{w_1 p_1} \tag{5.4}$$

$$\int_{-\infty}^{+\infty} u_1 w_1 \, dx \equiv \overline{u_1 w_1}, \tag{5.5}$$

then (5.2) and (5.3) become

$$\frac{d}{dz}(\overline{w_1 p_1}) = -\rho_0 \overline{u_1 w_1}\,\frac{du_0}{dz} \tag{5.6}$$

$$\overline{w_1 p_1} = -\rho_0 u_0\, \overline{u_1 w_1}, \tag{5.7}$$

respectively. Comparison of (5.6) with (5.7) shows that

$$-\rho_0 \overline{u_1 w_1} = \text{constant when } u_0 \neq 0, \tag{5.8}$$

i.e., the wave stress is constant with height except where $u_0 = 0$. This is a formal proof of the conjecture made in Chapter 3, where it was shown that the stress associated with an internal gravity wave is constant as shown by (3.104). We also see from (5.7) that in a layer where $u_0 \neq 0$ the total vertical flux of wave energy varies with height in proportion to u_0.

5.2 WAVE ACTION

In the previous section, we saw that the total wave energy is conserved only in the absence of a background wind. We now review the argument proposed by Bretherton (1966) which demonstrates that a form of the wave energy is conserved in the presence of a background wind.

We begin by multiplying the linearized equation for horizontal momentum (2.6) by the vertical velocity perturbation, w'. We assume wave-like perturbations of the form $w' = w_1 \exp[i(kx - \omega t)]$ and take the real parts of the terms to get

$$(\omega - u_0 k)\, u_1 w_1 = \frac{k}{\rho_0} w_1 p_1. \tag{5.9}$$

Integrating over (5.9) over a wave period, and making use of the definition of the intrinsic frequency (2.18), we have

$$\rho_0 \overline{u_1 w_1} = \frac{k}{\Omega}\, \overline{w_1 p_1}. \tag{5.10}$$

From (2.98) and (2.101) we see that

$$\overline{w_1 p_1} = w_g \overline{E} \tag{5.11}$$

and

$$\overline{u_1 p_1} = u_g \overline{E}, \tag{5.12}$$

where w_g and u_g are the vertical and horizontal components, respectively, of the group velocity. Then, using (5.11) in (5.10) gives

$$\rho_0 \overline{u_1 w_1} = \frac{k}{\Omega} w_g \overline{E}. \tag{5.13}$$

Using (5.13), the average of the energy transfer term in (5.1) can be written as

$$\rho_0 \overline{u_1 w_1}\, \frac{du_0}{dz} = \frac{k}{\Omega}\, \frac{du_0}{dz} w_g \overline{E} = -\frac{\overline{E}}{\Omega}\, \frac{D_g \Omega}{Dt}, \tag{5.14}$$

where D_g/Dt is defined by (2.103). The equation for the mean wave energy density (2.86) can now be written as

$$\frac{\partial \overline{E}}{\partial t} + \nabla \cdot \vec{v}_g \overline{E} - \frac{\overline{E}}{\Omega} \frac{D_g \Omega}{Dt} = 0, \tag{5.15}$$

or more simply as

$$\frac{\partial}{\partial t}\left(\frac{\overline{E}}{\Omega}\right) + \nabla \cdot \left(\vec{v}_g \frac{\overline{E}}{\Omega}\right) = 0. \tag{5.16}$$

Bretherton (1966) refers to $\overline{E}/\Omega$ as the *wave action*. Unlike wave energy, wave action is a conserved quantity. To illustrate this, use (5.11) in (5.6) to get

$$\frac{d}{dz}\left(w_g\overline{E}\right) = -\rho_0\overline{u_1 w_1}\,\frac{du_0}{dz}. \tag{5.17}$$

If we assume that the wave stress and vertical group velocity are constants, and if $du_0/dz > 0$, then the change in wave energy $\Delta\overline{E}$ of an upward-propagating wave over a vertical distance Δz is proportional to $-(du_0/dz)\Delta z$. From the definition of the intrinsic frequency (2.18),

$$\frac{\partial\Omega}{\partial z} = -k\frac{du_0}{dz}. \tag{5.18}$$

If $du_0/dz > 0$, then the change in Ω over the vertical distance Δz is also proportional to $-(du_0/dz)\Delta z$. However, the ratio $\overline{E}/\Omega$, which is the wave action, does not change.

5.3 THE CRITICAL LEVEL

In this section, we examine gravity wave behavior at a critical level, *i.e.*, where the wave phase speed equals the background wind speed. The analysis follows that given by Booker and Bretherton (1967). If we ignore the terms involving the isothermal scale height, H_s, the Taylor–Goldstein equation (2.34) is

$$\frac{d^2 w_1}{dz^2} + \left[\frac{N^2}{(c-u_0)^2} + \frac{u_0''}{(c-u_0)} - k^2\right] w_1 = 0. \tag{5.19}$$

Clearly, there is a singularity (a second-order pole) in (5.19) where $c - u_0 = 0$, and we must in some way account for this if we are to solve the equation over a reasonable depth of the atmosphere. As we shall see, critical levels are quite common in the atmosphere.

Let us assume that the wave is approaching the critical level, z_c, from above, as illustrated in Fig. 5.1. At a distance ζ above z_c we expand the background wind speed to second order to get

$$u_0(\zeta + z_c) = c + \left.\frac{du_0}{dz}\right|_{z_c}\zeta + \frac{1}{2}\left.\frac{d^2u_0}{dz^2}\right|_{z_c}\zeta^2 + \cdots \tag{5.20}$$

It is easily shown that

$$\frac{1}{c - u_0(\zeta + z_c)} \approx -\frac{1 - (1/2)(a_2/a_1)\zeta}{a_1\zeta} \tag{5.21}$$

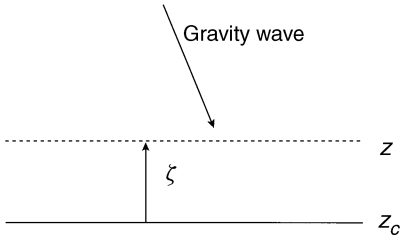

FIGURE 5.1 A gravity wave approaches a critical level from above.

where

$$a_1 = \left.\frac{du_0}{dz}\right|_{z_c} \tag{5.22}$$

and

$$a_2 = \left.\frac{d^2u_0}{dz^2}\right|_{z_c}. \tag{5.23}$$

Using (5.21)–(5.23) in (5.19) leads to

$$\frac{d^2w_1}{d\zeta^2} + \left[\frac{R_c}{\zeta^2} - \frac{\alpha}{\zeta} + \gamma\right] w_1 = 0, \tag{5.24}$$

where

$$R_c = \frac{N^2}{a_1^2} \tag{5.25}$$

is the Richardson number at $z = z_c$,

$$\alpha = \frac{a_2}{a_1}(R_c + 1), \tag{5.26}$$

and

$$\gamma = \frac{1}{2}\frac{a_2^2}{a_1^2}\left(\frac{R_c}{2} + 1\right) - k^2. \tag{5.27}$$

We now introduce the Frobenius expansion (see, for example, Bender and Orzag, 1999), *i.e.*,

$$w_1(k, \zeta + z_c) = \sum_n C_n \zeta^{n+\lambda}. \tag{5.28}$$

Using (5.28) in (5.24), and ordering terms according to powers of ζ, gives

$$\begin{aligned}&[\lambda(\lambda-1)+R_c]C_0\,\zeta^{\lambda-2}+\\&\{[\lambda(\lambda+1)+R_c]C_1-\alpha C_0\}\,\zeta^{\lambda-1}+\\&\{[(\lambda+1)(\lambda+2)+R_c]C_2-\alpha C_1+\gamma C_0\}\,\zeta^{\lambda}+\cdots=0.\end{aligned}\tag{5.29}$$

For a nontrivial solution to (5.29), each coefficient of ζ must be zero. This leads to the recursion relations

$$C_1=\frac{\alpha}{\lambda(\lambda+1)+R_c}C_0\tag{5.30}$$

and

$$C_2=\frac{\alpha^2[\lambda(\lambda+1)]^{-1}-\gamma}{(\lambda+1)(\lambda+2)+R_c}C_0.\tag{5.31}$$

The *indicial* equation is obtained from the first term in (5.29)

$$\lambda(\lambda-1)+R_c=0\tag{5.32}$$

with solution

$$\lambda=\frac{1}{2}\pm i\mu\tag{5.33}$$

where

$$\mu=[R_c-0.25]^{1/2}.\tag{5.34}$$

From (5.33) we see that the powers in the Frobenius expansion are complex numbers. We now expand (5.28) to second order to get

$$w_1(k,z_c+\zeta)=C_0^+\zeta^{\lambda}A(\zeta)+C_0^-\zeta^{\lambda^*}A^*(\zeta)\tag{5.35}$$

where

$$A(\zeta)=1+\frac{C_1}{C_0}\zeta+\frac{C_2}{C_0}\zeta^2.\tag{5.36}$$

In the above equations, C_0^+ refers to values using $\lambda=1/2+i\mu$ and C_0^- refers to values using $\lambda=1/2-i\mu$. At this point, we know the values of all the variables except C_0^+ and C_0^-. We can get another equation by taking the vertical derivative of (5.35) to get

$$\frac{dw_1}{dz}=C_0^+\zeta^{\lambda}B(\zeta)+C_0^-\zeta^{\lambda^*}B^*(\zeta),\tag{5.37}$$

where

$$B(\zeta) = \lambda\zeta^{-1} + \frac{C_1}{C_0}(\lambda+1) + \frac{C_2}{C_0}(\lambda+2)\zeta. \tag{5.38}$$

Using (5.35) and (5.37) to solve for C_0^+ and C_0^- we get

$$C_0^+ = \frac{A^*(dw_1/dz) - B^*w_1}{D} \tag{5.39}$$

$$C_0^- = \frac{A(dw_1/dz) - Bw_1}{D^*} \tag{5.40}$$

where

$$D = A^*B - AB^*. \tag{5.41}$$

Now let us examine the wave below the critical level. At a distance ζ below z_c we have

$$w_1(k, z_c - \zeta) = C_0^+(-\zeta)^\lambda A(-\zeta) + C_0^-(-\zeta)^{\lambda^*}A^*(-\zeta) \tag{5.42}$$

$$\frac{dw_1}{dz}(k, z_c - \zeta) = -C_0^+(-\zeta)^\lambda B(-\zeta) - C_0^-(-\zeta)^{\lambda^*}B^*(-\zeta). \tag{5.43}$$

We now have almost all we need to carry the wave solutions across the critical level. What remains is how to describe $(-\zeta)^\lambda$ and $(-\zeta)^{\lambda^*}$ in (5.42) and (5.43). To evaluate these functions, we introduce a small imaginary phase speed, *i.e.*,

$$c = c_r + ic_i. \tag{5.44}$$

Then (5.19) becomes

$$\frac{d^2w_1}{dz^2} + \left[\frac{N^2}{(c_r + ic_i - u_0)^2} + \frac{u_0''}{c_r + ic_i - u_0} - k^2\right]w_1 = 0. \tag{5.45}$$

As the wave approaches the critical level from above, we expand the background wind speed as

$$c_r - u_0 = -\left.\frac{du_0}{dz}\right|_{z_c}(z - z_c) = a_1(z - z_c), \tag{5.46}$$

where we have used (5.22). As $z \to z_c$, the buoyancy term in (5.45) dominates so that

$$\frac{d^2w_1}{dz^2} + \frac{R_c}{(z - z_c - ic_i/a_1)^2}w_1 = 0. \tag{5.47}$$

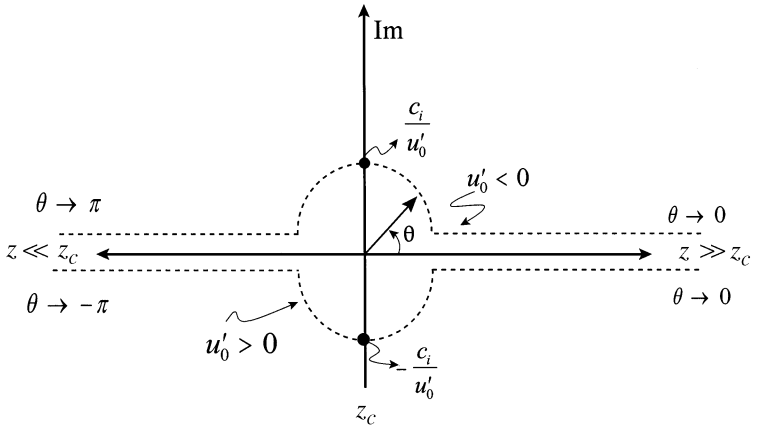

FIGURE 5.2 The path over the singularity at $z = z_c$ in the complex plane determines whether -1 equals $\exp(i\pi)$ or $\exp(-i\pi)$ when $z \ll z_c$.

Now using (5.28) with $\zeta = z - z_c - ic_i/a_1$, the solution to (5.47) takes the form

$$w_1(k, z - z_c) = A\left(z - z_c - i\frac{c_i}{a_1}\right)^{1/2+i\mu} + B\left(z - z_c - i\frac{c_i}{a_1}\right)^{1/2-i\mu}. \quad (5.48)$$

In polar form,

$$z - z_c - i\frac{c_i}{a_1} = re^{i\theta} \quad (5.49)$$

where

$$r = \left[(z - z_c)^2 + \left(\frac{c_i}{a_1}\right)^2\right]^{1/2} \quad (5.50)$$

and

$$\theta = \tan^{-1}\left[-\frac{c_i}{a_1(z - z_c)}\right]. \quad (5.51)$$

We now go to the complex plane illustrated in Fig. 5.2. For $z \gg z_c$, $\theta \to 0$, but for $z \ll z_c$, θ goes to either π or $-\pi$ depending on whether we go over or under the singularity at $z = z_c$. If $a_1 > 0$, then $\theta \to -\pi/2$ at $z = z_c$, and we must go under the singularity. Then for $z \ll z_c$ and letting $c_i \to 0$, we have

$$-(z - z_c) = (z - z_c)\, e^{-i\pi} = \zeta\, e^{-i\pi}. \quad (5.52)$$

From (5.52) we see that

$$(-\zeta)^\lambda = \zeta^\lambda e^{-i\pi\lambda}. \quad (5.53)$$

Using the positive branch of (5.33) for λ in (5.53) gives

$$\begin{aligned}(-\zeta)^{\lambda} &= \zeta^{\lambda}\, e^{-i\pi(1/2+i\mu)} \\ &= \zeta^{\lambda}\, e^{-i\pi/2} e^{\pi\mu} \\ &= -i\zeta^{\lambda}\, e^{\pi\mu}. \end{aligned} \tag{5.54}$$

If $a_1 < 0$, then in a similar way we can show that

$$(-\zeta)^{\lambda} = i\ \zeta^{\lambda}\, e^{-\pi\mu}. \tag{5.55}$$

It will be necessary to know what terms in (5.48) correspond to upward- and downward-moving waves. This can be unambiguously determined by calculating the wave stress. Considering ζ real and $\mu > 0$, then (5.48) takes the form

$$w_1 = A\zeta^{1/2}\zeta^{i\mu} + A\zeta^{1/2}\zeta^{-i\mu}. \tag{5.56}$$

The factor $\zeta^{i\mu}$ can be expressed as $e^{i\mu \ln(z-z_c)}$. Using this and the continuity equation (2.16) gives

$$w_1 = \zeta^{1/2}\left[Ae^{i\mu\zeta} + Be^{-i\mu\zeta}\right] \tag{5.57}$$

$$u_1 = \zeta^{-1/2}\left[\left(i\frac{1}{2} - \mu\right)\frac{A}{k}e^{i\mu\ln\zeta} + \left(i\frac{1}{2} + \mu\right)\frac{B}{k}e^{-i\mu\ln\zeta}\right]. \tag{5.58}$$

Using (5.57) and (5.58) in (3.102), the wave stress is

$$\tau = \frac{0.5\mu}{k^2}(A^2 - B^2). \tag{5.59}$$

We see that the A term represents an upward-moving wave (positive wave stress), and the B term represents a downward-moving wave.

Consider now the case when the wind shear at the critical level is positive, *i.e.*, $a_1 > 0$, then above the critical level we can write (5.48) as

$$w_1^{+} = A(z - z_c)^{(1/2)+i\mu} + B(z - z_c)^{(1/2)-i\mu} \tag{5.60}$$

$$= |z - z_c|^{1/2}\left(Ae^{i\mu\ln|z-z_c|} + Be^{-i\mu\ln|z-z_c|}\right), \tag{5.61}$$

and below the critical level it can be

$$w_1^{-} = -ie^{\pi\mu}\, A(z - z_c)^{(1/2)+i\mu} - ie^{-\pi\mu}B(z - z_c)^{(1/2)-i\mu} \tag{5.62}$$

$$= -i|z - z_c|^{1/2}\left(Ae^{\pi\mu}\, e^{i\mu\ln|z-z_c|} + Be^{-\pi\mu}\, e^{-i\mu\ln|z-z_c|}\right). \tag{5.63}$$

For the upward-moving wave, the wave amplitude below z_c is $Ae^{\pi\mu}$, and above z_c it is A. We see that there is an exponential decrease in wave amplitude across the critical level. However, as Booker and Bretherton (1967) point out, the wave stress is a truer measure of wave amplitude. Then, above the critical level and using the continuity equation (2.8), we see that

$$u_1 \propto \frac{dw_1}{dz} \propto \zeta^{\lambda-1}, \tag{5.64}$$

so that the wave stress $\tau^+ \propto \zeta^{2\lambda-1}$. Similarly, below the critical level the wave stress is $\tau^- \propto e^{2\pi\mu}\ \zeta^{2\lambda-1}$. Thus, in passing through the critical wave level, the wave stress is reduced an amount $e^{-2\pi\sqrt{R_c-0.25}}$. This is a large reduction. For example, if $R_c = 0.5$, the reduction is 0.04; if $R_c = 1$, the reduction is 0.004; and if $R_c = 10$, the reduction is 3×10^{-9}. Thus, for almost all cases the wave is essentially dissipated on passing through a critical level. This is an extremely important result. We have seen in Chapter 3 that terrain features can generate gravity waves, which in turn vertically transport horizontal momentum. However, unless the wave is dissipated, the momentum transport is constant. Critical levels provide this dissipation. For terrain-generated gravity waves, critical levels exist where $u_0 = 0$.

Let us now take a more physical rather than mathematical look at what happens when a wave approaches a critical level; however, we still remain within the linear theory. Imagine now an upward-propagating wave approaching z_c from below. Then, using (2.8), (5.62), and (5.63) and taking real parts, we have

$$w_1 \propto |z - z_c|^{1/2} \sin(\mu \ln |z - z_c|) \tag{5.65}$$

$$u_1 \propto |z - z_c|^{-1/2} \sin(\mu \ln |z - z_c|). \tag{5.66}$$

The term $\sin(\mu \ln |z - z_c|)$ behaves as if the local wavenumber is

$$m = \frac{\mu}{z - z_c}. \tag{5.67}$$

Then, as illustrated in Fig. 5.3, we see that as the wave approaches the critical level $w_1 \to 0$, $u_1 \to \infty$, and the vertical wavelength $\lambda_z \to 0$, resulting in increasingly rapid oscillations. However, in reality the vertical shear in the horizontal wind speed perturbation, which varies as $|z - z_c|^{-3/2}$, will become large and exceed the shear of the background wind. When this happens, the Richardson number near the critical level will become small, indicating the production of turbulence. Thus, the wave field breaks down into turbulence before the wave reaches z_c. This important result will be discussed further in Chapter 7. Using (5.67) in (2.69),

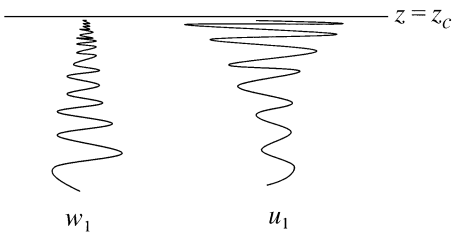

FIGURE 5.3 As a gravity wave approaches a critical level, $w_1 \to 0$, $u_1 \to \infty$, and $\lambda_z \to 0$.

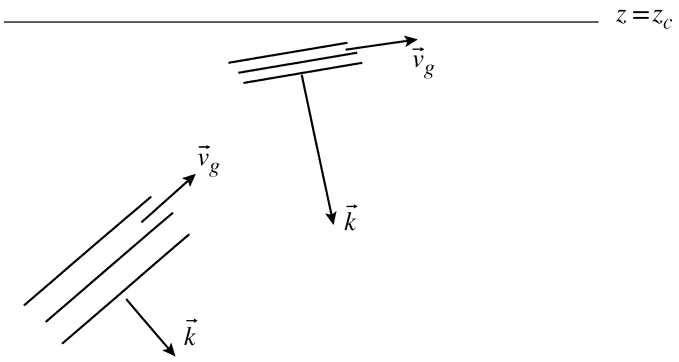

FIGURE 5.4 Schematic illustration of a wave packet approaching a critical level from below. Because the vertical group velocity approaches zero near the critical level, the packet never reaches the critical level.

we see that the vertical group velocity below the critical level ($z < z_c$) is

$$w_g = \frac{k\mu}{N^2} \frac{(c - u_0)^3}{|z - z_c|}. \tag{5.68}$$

As the wave approaches the critical level, $(u_0 - c)^3 \to 0$ much more rapidly than $(z_c - z) \to 0$ so that $w_g \to 0$. In effect, the wave packet never reaches the critical level. Figure 5.4 illustrates the changes in a wave packet as it approaches a critical level from below. Because the vertical wavelength $(z - z_c)$ decreases, the vertical wavenumber increases as the wave packet approaches z_c. We see also that as the wave fronts become increasingly horizontally oriented, the vertical group velocity becomes less.

However, as pointed out by Booker and Bretherton (1967), these infinities at the critical level disappear if $c_i \neq 0$. These singularities are characteristic of standing waves, *i.e.*, mountain waves, that have persisted for a long time. The spectrum of waves generated by a mountain have the same intrinsic frequency, and they combine to form a standing disturbance of finite magnitude. Transient waves, each with first-order (infinitesimal) amplitudes and dispersive wavenumbers, do not

"build up," and singularities in the total integrated disturbance may never appear. These waves might pass through a critical level only lightly modified.

We can determine the changes in the characteristics of a transient wave when it passes through a critical level by noting the changes in the wavenumbers. Consider first the case where $a_1 > 0$. Then (5.60) applies. Using (5.67) in (2.63), the phase equations are

$$kx + \frac{\mu}{(z - z_c)} z = c_I t \quad \text{for the } A \text{ solution} \tag{5.69}$$

and

$$kx - \frac{\mu}{(z - z_c)} z = c_I t \quad \text{for the } B \text{ solution,} \tag{5.70}$$

where $c_I = c - u_0$ is the intrinsic phase speed, and we have taken phase angle ϕ equal to zero. Below z_c, *i.e.*, $z < z_z$, c_I is positive since $c > u_0$, and $\mu/|z - z_c|$ is negative for both the A and the B solutions. Then, k is positive for both solutions, but from (5.69) and (5.70) we see that the vertical phase velocity is negative for the A solution, *i.e.*, $m < 0$, and positive for the B solution, *i.e.*, $m > 0$. Above z_c, c_I and k are both negative for both solutions; however, m is still negative for the A solution and positive for the B solution. Thus, we see that the A solution corresponds to a downward-moving wave and the B solution corresponds to an upward-moving wave.

If $a_1 < 0$, (5.60) takes the form

$$w_1 = A(z - z_c)^{(1/2) - i\mu} + B(z - z_c)^{(1/2) + i\mu}. \tag{5.71}$$

Applying the same arguments as above on (5.69) and (5.70), we see that now the A solution corresponds to an upward-moving wave and the B solution corresponds to a downward-moving wave. These results are summarized in Fig. 5.5, which illustrates the orientation of the wave vector on either side of the critical level for positive and negative wind shears.

The above results were developed for a frictionless adiabatic atmospheric flow. If we included viscosity and heat conduction, then as shown by Hazel (1967)

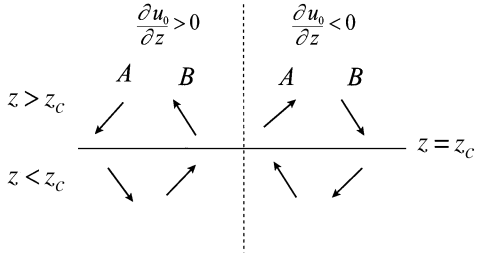

FIGURE 5.5 Orientation of the wave vector as a transient wave passes through a critical level for both positive and negative background wind shears.

and Fritts and Geller (1976) the equation for the vertical velocity perturbation would be

$$\left[ik(c-u_0)+K\left(\frac{\partial^2}{\partial z^2}-k^2\right)\right]\left\{\left[-ik(c-u_0)\nu\left(\frac{\partial^2}{\partial z^2}-2k^2\right)\right]\frac{\partial^2}{\partial z^2}\right.$$
$$\left.-ik[u_0''-k^2(c-u_0)]-\nu k^4\right\}w-k^2N^2w=0, \tag{5.72}$$

where ν is the kinematic viscosity and K is the thermal conductivity. Equation (5.72) is a sixth-order differential equation, which must be solved numerically. We see that the singularity at the critical level has been removed. Now, instead of $w_1 \to 0$ and $u_1 \to \infty$ as the critical level is approached, the flow variables vary continuously at the critical level is approached. However, the reductions in wave amplitude and wave stress predicted by the linear model still occur.

This Page Intentionally Left Blank

6

Waves and Turbulence

Gravity wave and turbulence are often observed to exit simultaneously in almost all stably stratified flows (see, for example, Turner, 1973; Caughey and Readings, 1975; Hunt, Kaimal, and Gaynor, 1985; Finnigan, 1988; Nappo and Johansson, 1999). Indeed, gravity wave instability is the ultimate source of turbulence in the stable atmosphere and oceans. For example, we have seen in the previous chapter that turbulence may be observed near a critical level where wave breaking occurs. There are other ways in which gravity waves can produce turbulence, and these will be examined in this chapter.

6.1 Parcel Exchange Analysis of Flow Stability

We begin our study with a somewhat mechanistic examination of turbulence production. The method is based on the stability analyses performed by Chandrasekhar (1961) and Ludlum (1967) and generalized by Hines (1971) to include the effects of stratification along slanting surfaces. The method looks at the total energy of two fluid parcels before and after a virtual vertical exchange of their positions. If the total energy of the system increases, then work has been done on the system, and the system is stable. However, if the total energy decreases, then work has been done by the system, and the system is unstable.

Figure 6.1 illustrates the flow under study. Fluid A has constant density ρ_A and uniform speed u_A. Fluid B has constant density ρ_B and uniform speed u_B. Fluid parcel A is at height z_A above some arbitrary reference height, and fluid parcel B

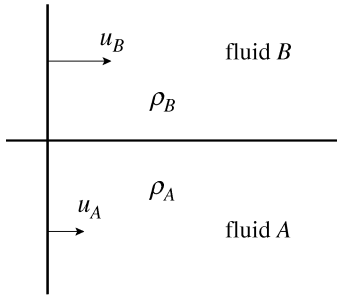

FIGURE 6.1 Fluid parcels in their initial configuration. After parcels A and B exchange positions, the new kinetic and potential energies will be evaluated. The stability of the system is determined in change in the total energy of the system after parcel exchange.

is at height z_B. The interface between the two fluids lies between z_A and z_B. The initial potential energy, P_I, and kinetic energy, K_I, of the system are

$$P_I = g(\rho_A z_A + \rho_B z_B) \tag{6.1}$$

and

$$K_I = \frac{1}{2}\left(\rho_A u_A^2 + \rho_B u_B^2\right). \tag{6.2}$$

We now exchange the parcel positions. The exchange process is adiabatic, and we require conservation of mass and momentum. Conservation of mass requires

$$\rho_A + \rho_B = \rho'_A + \rho'_B, \tag{6.3}$$

where the primes indicate values after parcel exchange. Conservation of momentum gives

$$\rho_A u_A + \rho_B u_B = \left(\rho'_A + \rho'_B\right) u_f = (\rho_A + \rho_B) u_f, \tag{6.4}$$

where u_f is an effective final speed. Solving (6.4) for u_f gives

$$u_f = \frac{\rho_A u_A + \rho_B u_B}{\rho_A + \rho_B}. \tag{6.5}$$

The final potential and kinetic energies are

$$P_F = g\left(\rho'_A z_B + \rho'_B z_A\right) \tag{6.6}$$

and

$$K_F = \frac{1}{2}(\rho_A + \rho_B)u_f^2$$
$$= \frac{1}{2}\frac{(\rho_A u_A + \rho_B u_B)^2}{\rho_A + \rho_B}, \tag{6.7}$$

respectively, and where we have used (6.5) in (6.7). The change in kinetic energy as a result of the exchange is

$$K_F - K_I = -\frac{\rho_A \rho_B}{2(\rho_A + \rho_B)}\,(u_A - u_B)^2\,. \tag{6.8}$$

If we assume that the density of the parcels is constant during the exchange, then the change in potential energy is

$$P_F - P_I = g(\rho_A - \rho_B)(z_B - z_A). \tag{6.9}$$

The work done on the system, W, is

$$W = (K_F + P_F) - (K_I + P_I)$$
$$= (P_F - P_I) + (K_F - K_I). \tag{6.10}$$

Using (6.8) and (6.9) in (6.10) gives

$$W = g(\rho_A - \rho_B)(z_B - z_A) - \frac{1}{2}\,\frac{\rho_A \rho_B}{(\rho_A + \rho_B)}\,(u_A - u_B)^2. \tag{6.11}$$

If $W > 0$, then work has been done on the system, and the total energy of the system has increased. If $W < 0$, then work has been done by the system, and the total energy has decreased. Expressed more simply,

$$W > 0 \Rightarrow \text{stable flow}$$
$$W < 0 \Rightarrow \text{unstable flow.}$$

The change in kinetic energy (6.8) is always negative and will always act to decrease the total energy of the system. Thus, changes in kinetic energy act to create turbulence; it is a *production term*. However, the change in potential energy (6.9) can be either positive or negative. Consider the case when $\rho_A = \rho_B = \rho$ and $u_A \neq u_B$. Then,

$$W = -\tfrac{1}{4}\rho(u_A - u_B)^2, \tag{6.12}$$

and we see that the system is always unstable. We refer to such a system as being *dynamically* unstable. If $\rho_A > \rho_B$ and $u_A = u_B$, then from (6.11) we see that if $z_B > z_A$, the system is *convectively* stable, but if $z_B < z_A$, the system is *convectively* unstable. In the latter case, fluid of greater density is forced to lie over fluid of lesser density.

We consider next the case of height-varying density and speed. Instead of exchanging two fluid parcels, we vertically move a fluid parcel from its initial location at point A to a nearby location B. Expanding ρ_B and u_B to first order about the point A, we have

$$\rho_B = \rho_A + \left.\frac{\partial \rho}{\partial z}\right|_{z_A} (z_B - z_A) \tag{6.13}$$

$$u_B = u_A + \left.\frac{\partial u}{\partial z}\right|_{z_A} (z_B - z_A). \tag{6.14}$$

Substitution of (6.13) and (6.14) into (6.11) leads to

$$W = -g\frac{\partial \rho}{\partial z}(z_B - z_A)^2 - \frac{1}{2}\,\frac{\rho_A^2 + \rho_A(\partial\rho/\partial z)(z_b - z_A)}{2\rho_A + (\partial\rho/\partial z)(z_B - z_A)}\left[\frac{\partial u}{\partial z}(z_b - z_A)\right]^2. \tag{6.15}$$

Note that

$$\frac{\rho_A^2 + \rho_A(\partial\rho/\partial z)(z_b - z_A)}{2\rho_A + (\partial\rho/\partial z)(z_B - z_A)} \approx \frac{\rho_A}{2}, \tag{6.16}$$

so that (6.15) becomes

$$W = \rho_0 N^2 (z_B - z_A)^2 - \frac{\rho_0}{4}\left(\frac{\partial u}{\partial z}\right)^2 (z_B - z_A)^2, \tag{6.17}$$

where we have set $\rho_A = \rho_0$ and used (1.68). Equation (6.17) can be further simplified, *i.e.*,

$$W = \rho_0 (z_B - z_A)^2 \left(\frac{\partial u}{\partial z}\right)^2 (R_i - 0.25), \tag{6.18}$$

where

$$R_i = \frac{N^2}{(\partial u/\partial z)^2}\,. \tag{6.19}$$

R_i is called the *Richardson number* and is a fundamental parameter in turbulence theory. The Richardson number will be discussed in Chapter 7. We see that the criterion for stability is the value of R_i relative to one-fourth. If $R_i > 1/4$, the flow

is stable, *i.e.*, if the fluid is disturbed by a small vertical displacement, it will return to its initial configuration or harmonically oscillate about that state. The Richardson number is a fundamental turbulence parameter and represents the ratio of the production of turbulence by buoyancy to the production of turbulence by velocity shear. The condition for convective instability is $R_i < 0$. Dynamic instability occurs over the range $0 \leq R_i \leq 0.25$. A flow is said to be dynamically stable if $R_i > 0.25$.

6.2 SHEAR INSTABILITY AND UNSTABLE MODES

In this section, we examine the stability of stratified shear flows. The analysis is straightforward. A small, linear, wave-like disturbance, usually a vertical displacement of a streamline, is introduced into the flow, and we examine the temporal evolution of the disturbance. If the amplitude of the disturbance remains bounded, then we say that the flow is dynamically stable. However, if the amplitude grows without limit, then we assume an instability results. Note that this *linear stability analysis* can trace the evolution of a flow only to the onset of an instability. Subsequent flow development is not accessible to the linear theory. Also note that a stability analysis usually gives the conditions for the flow to be stable to small disturbances. The fact that a certain flow condition may be unstable to small disturbances is not a sufficient condition for instability. For example, in the linear analysis we usually assume a frictionless flow; however, all real fluids have some viscosity, and this can act to stabilize a flow (see, for example, Fritts and Geller, 1976; Thorpe, 1981). Baines (1995) points out that if a gravity wave approaches a critical level slowly, the viscous dissipation in the critical layer may be large enough to prevent explosive growth and overturning. In this case, the wave never reaches the critical level. The linear theory also neglects surface tension effects, and these may be strong enough to stabilize a shear flow between immiscible fluids. It is also possible that the disturbance wavenumber or phase velocity required for instability is not present. Thus, we see that there are many reasons why a flow may be stable even though a linear stability analysis indicates it is unstable.

In the previous section we examined the stability of a stratified flow by evaluating the total energy of a two-particle system before and after an adiabatic exchange of fluid parcel positions. The analysis was kinematic. We did not look at how the instability developed. Indeed, the question of time dependence did not enter the analysis. It would therefore seem that the results are perhaps not very helpful; however, it did show that the source of flow instability is the velocity shear. We saw that the Richardson number provides a means for estimating flow stability and that there is a range of values of R_i between 0 and 0.25 where the flow can be dynamically unstable. In this section we will examine the dynamic stability of stratified flows and examine the effects of this shear instability on the generation of gravity waves. We begin with the most simple flow situation and proceed to more complicated flows.

6.2.1 KELVIN–HELMHOLTZ INSTABILITY

The simplest model of a shear layer is the so-called Helmholtz profile illustrated in Fig. 6.2. The flow is constant but different in each of two semi-infinite planes, and the change in background speed occurs sharply across a thin interface. Thus, the vertical shear can be considered large or infinite. We wish to examine the stability of the interface to small wave perturbations. We assume that the flow in each half-plane is inviscid, incompressible, and irrotational and that the Brunt–Väisälä frequencyis zero. Further, we assume that the background pressures are in hydrostatic balance. Because the Brunt–Väisälä frequencyis zero in each layer, we can anticipate that waves in each layer will be evanescent. The linearized Eulier equations are

$$\frac{\partial u_1}{\partial t} + u_0 \frac{\partial u_1}{\partial x} = -\frac{1}{\rho_0} \frac{\partial p_1}{\partial x} \tag{6.20}$$

$$\frac{\partial w_1}{\partial t} + u_0 \frac{\partial w_1}{\partial x} = -\frac{1}{\rho_0} \frac{\partial p_1}{\partial z} \tag{6.21}$$

$$\frac{\partial u_1}{\partial x} + \frac{\partial w_1}{\partial z} = 0. \tag{6.22}$$

We assume that as $z \to \pm \infty$, the perturbations go to zero. At the interface $z = 0$, we apply the dynamic and kinematic boundary conditions. We assume wave solutions of the form

$$u_1 = \tilde{u}(z)\, e^{i(kx - \omega t)} \tag{6.23}$$

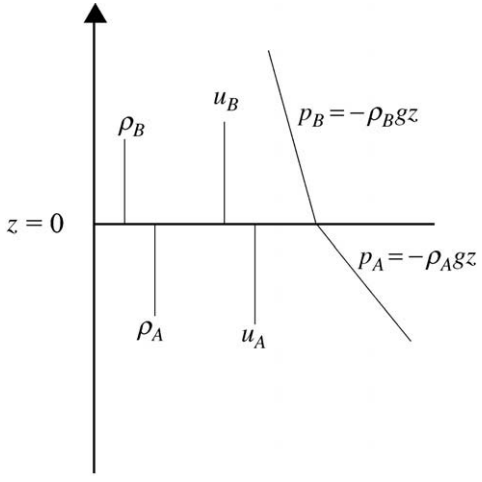

FIGURE 6.2 The Helmholtz profile. Similar to Fig. 6.1, but now the interface between the two fluids is important.

$$w_1 = \tilde{w}(z)\, e^{i(kx-\omega t)} \tag{6.24}$$

$$p_1 = \tilde{p}(z)\, e^{i(kx-\omega t)}, \tag{6.25}$$

so that the polarization equations in the upper fluid are

$$\Omega_B \tilde{u}_B = \frac{k\tilde{p}_B}{\rho_B} \tag{6.26}$$

$$\Omega_B \tilde{w}_B = \frac{i}{\rho_B}\frac{\partial \tilde{p}_B}{\partial z} \tag{6.27}$$

$$\tilde{u}_B = \frac{i}{k}\frac{\partial \tilde{w}_B}{\partial z}, \tag{6.28}$$

where Ω is the intrinsic frequency and ρ_B is the density of fluid B. A similar set of equations is written for the lower fluid. The dynamic boundary condition requires that the pressure be continuous across the interface between two fluids. Thus, we need to solve (6.26)–(6.28) in terms of $\tilde{p}_B$. This leads to

$$\frac{\partial^2 \tilde{p}_B}{\partial z^2} - k^2 \tilde{p}_B = 0. \tag{6.29}$$

Then, using (6.29), the equations for the vertical variations in the upper fluid become

$$\tilde{p}_B = \tilde{p}_B(0)\, e^{-kz} \tag{6.30}$$

$$\tilde{u}_B = \frac{k\tilde{p}_B(0)}{\Omega_B \rho_B}\, e^{-kz} \tag{6.31}$$

$$\tilde{w}_B = \frac{ik\tilde{p}_B(0)}{\Omega_B \rho_B}\, e^{-kz}. \tag{6.32}$$

In the lower fluid we have

$$\tilde{p}_A = \tilde{p}_A(0)\, e^{kz} \tag{6.33}$$

$$\tilde{u}_A = \frac{k\tilde{p}_A(0)}{\Omega_A \rho_A}\, e^{kz} \tag{6.34}$$

$$\tilde{w}_A = \frac{ik\tilde{p}_A(0)}{\Omega_A \rho_A}\, e^{kz}. \tag{6.35}$$

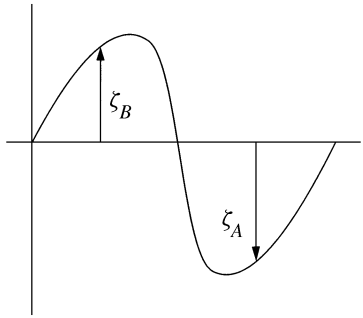

FIGURE 6.3 The disturbed interface between two different fluids.

The disturbed interface is illustrated in Fig. 6.3. The vertical displacements in the upper and lower fluids are

$$\zeta_B = \tilde{\zeta}_B \, e^{-kz+i(kx-\omega t)} \tag{6.36}$$

$$\zeta_A = \tilde{\zeta}_A \, e^{kz+i(kx-\omega t)}. \tag{6.37}$$

The interface displacements are related to the vertical velocity perturbations, *i.e.*,

$$\frac{D\zeta_B}{Dt} = \frac{\partial \zeta_B}{\partial t} + u_B \frac{\partial \zeta_B}{\partial x} = w_{1,B} \tag{6.38}$$

$$\frac{D\zeta_A}{Dt} = \frac{\partial \zeta_A}{\partial t} + u_A \frac{\partial \zeta_A}{\partial x} = w_{1,A}. \tag{6.39}$$

Using (6.24), (6.32), and (6.36) in (6.38) and solving for $\tilde{p}_B$ gives

$$\tilde{p}_B = -\frac{\Omega_B^2 \rho_B}{k} \, \tilde{\zeta}_B. \tag{6.40}$$

Likewise, in the lower layer we have

$$\tilde{p}_A = \frac{\Omega_A^2 \rho_A}{k} \, \tilde{\zeta}_A. \tag{6.41}$$

The dynamic boundary condition requires that the total pressure be continuous across the interface, *i.e.*,

$$p_{0,B} + p_{1,B} = p_{0,A} + p_{1,A}, \tag{6.42}$$

where $p_{0,A}$ and $p_{0,B}$ are the background pressures in lower and upper fluids, respectively. The background pressures are given by the hydrostatic

equation (1.37). Assuming that the mean interface height is zero and using (6.36) and (6.37), we get

$$p_{0,B} = -\rho_B g \zeta_B = -\rho_B g \tilde{\zeta}_B \, e^{i(kx-\omega t)} \tag{6.43}$$

$$p_{0,A} = -\rho_A g \zeta_A = -\rho_A g \tilde{\zeta}_A \, e^{i(kx-\omega t)}. \tag{6.44}$$

Note that the background pressures are neither steady nor horizontally uniform, but vary with the height of the interface. This is a consequence of the hydrostatic condition. Using (6.40) and (6.41), the perturbation pressures are

$$p_{1,B} = -\frac{\Omega_B^2 \rho_B}{k} \, \tilde{\zeta}_B e^{i(kx-\omega t)} \tag{6.45}$$

$$p_{1,A} = \frac{\Omega_A^2 \rho_A}{k} \, \tilde{\zeta}_A e^{i(kx-\omega t)}. \tag{6.46}$$

Using (6.43)–(6.46) in (6.42) gives

$$-\rho_B g \tilde{\zeta}_B - \frac{\Omega_B^2 \rho_B \tilde{\zeta}_B}{k} = -\rho_A g \tilde{\zeta}_A + \frac{\Omega_A^2 \rho_A \tilde{\zeta}_A}{k}. \tag{6.47}$$

The kinematic boundary condition requires that the two fluids remain in contact at the interface; therefore, $\tilde{\zeta}_B = \tilde{\zeta}_A$, and (6.47) becomes

$$(\rho_A - \rho_B) g k = \Omega_A^2 \rho_A + \Omega_B^2 \rho_B. \tag{6.48}$$

Using the definition of intrinsic frequency, Ω, (6.48) becomes

$$\frac{\omega}{k} = \frac{\rho_A u_A + \rho_B u_B}{\rho_A + \rho_B} \pm \left[\frac{g}{k} \frac{(\rho_A - \rho_B)}{(\rho_A + \rho_B)} - \frac{\rho_A \rho_B (u_B - u_A)^2}{(\rho_A + \rho_B)^2} \right]^{1/2}, \tag{6.49}$$

where u_B and u_A are the mean speeds in the upper and lower fluids, respectively. Equation (6.49) is our final result; it represents the complex horizontal phase velocity of interface disturbances. The first term on the right-hand side represents the mean horizontal speed across the interface. The first term in braces is called the *buoyancy term*. It represents the buoyant forces acting on the interface. If $\rho_A > \rho_B$, then the stratification is stable, and the buoyant force acts to suppress the growth of the disturbances. If $\rho_A < \rho_B$, then a convective instability results. The second term in braces is called the *production term*. It is always positive. In their effects, the the buoyancy and production terms are similar to the potential

and kinetic energy terms appearing in (6.11). If the buoyancy term is greater than the production term, ω is real and the interface displacements are given by

$$\zeta = \zeta(0)\, e^{-kz} \cos(kx - \omega t) \qquad z > 0 \tag{6.50}$$

$$\zeta = \zeta(0)\, e^{kz} \cos(kx - \omega t) \qquad z < 0. \tag{6.51}$$

Note that the size of the disturbances decrease exponentially away from the interface. These are evanescent waves, as illustrated in Fig. 2.4.

Now consider the case when $u_A = u_B = u_0$. Then, (6.49) becomes

$$\frac{\omega}{k} = u_0 \pm \left[\frac{g(\rho_A - \rho_B)}{k(\rho_A + \rho_B)}\right]^{1/2}. \tag{6.52}$$

We have already seen that if $\rho_A > \rho_B$, the interface is convectively stable, and if $\rho_A < \rho_B$ the interface is convectively unstable. If $\rho_B \ll \rho_A$ and if $u_0 = 0$, then (6.57) reduces to

$$\omega = \sqrt{kg}, \tag{6.53}$$

which is the dispersion relation for waves on deep water. When $\rho_A = \rho_B$ and if $u_A \neq u_B$, then

$$\frac{\omega}{k} = \frac{1}{2}(u_A + u_B) \; \pm i\frac{1}{2}|u_A - u_B|. \tag{6.54}$$

In this case the interface is always unstable because it will grow as $e^{0.5|u_A - u_B|t}$.

We have said that the Helmholtz profile is dynamically unstable, and this is confirmed in (6.49) where we see that for wavenumbers greater than k_{crit}, where

$$k_{crit} = \frac{g}{\rho_A \rho_B} \frac{\rho_A^2 - \rho_B^2}{(u_A - u_B)^2}, \tag{6.55}$$

the production term will be greater than the buoyancy term, and ω will be complex, *i.e.*, $\omega = \omega_r + i\omega_i$. In the upper layer,

$$\zeta = \zeta(0)\, e^{-kz}\, e^{\omega_i t} \cos(kx - \omega_r t), \tag{6.56}$$

with a similar result for the lower layer. Recall that in Section 6.1 we conjectured that instability would somehow lead to turbulence. However, we see now that instabilities of the Helmholtz profile take the form of exponential growth of the interface displacements, as illustrated in Fig. 6.4. The flow in each layer pushes the crests of the interface wave in the respective forward directions causing the wave to "roll up" and limit vertical growth. In nature, Kelvin–Helmholtz instabilities manifest themselves as Kelvin–Helmholtz waves that can also be observed with radars and sonars as billow clouds, as shown in Figs. 6.5–6.7. These waves do not persist

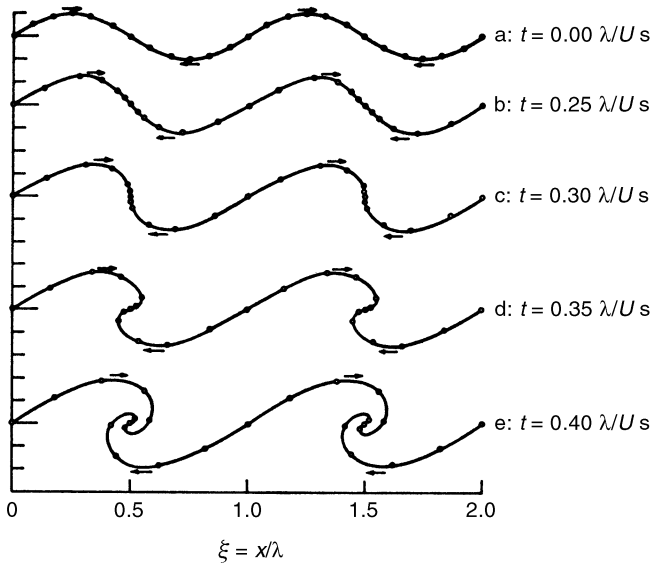

FIGURE 6.4 Rolling up of a vortex sheet as a function of dimensionless time and distance. (From "The formation of vortices from a surface discontinuity," L. Rosenhead, *Proc. R. Soc. London A*, **143**: 187, 1931.)

FIGURE 6.5 Billow clouds in Frösön, Sweden. Photo by Roger Gyllenhammar.

even if the flow is steady. This is because the growth of wave amplitude and the effects of velocity shear cause the heavier (more dense) fluid in the lower layer to be displaced above the lighter (less dense) fluid of the upper layer—a process not unlike the parcel exchange discussed in Section 6.1. When this happens, a convective instability develops, and the waves break down, resulting in turbulence. We see that the wave-turbulence process begins with a dynamic instability which

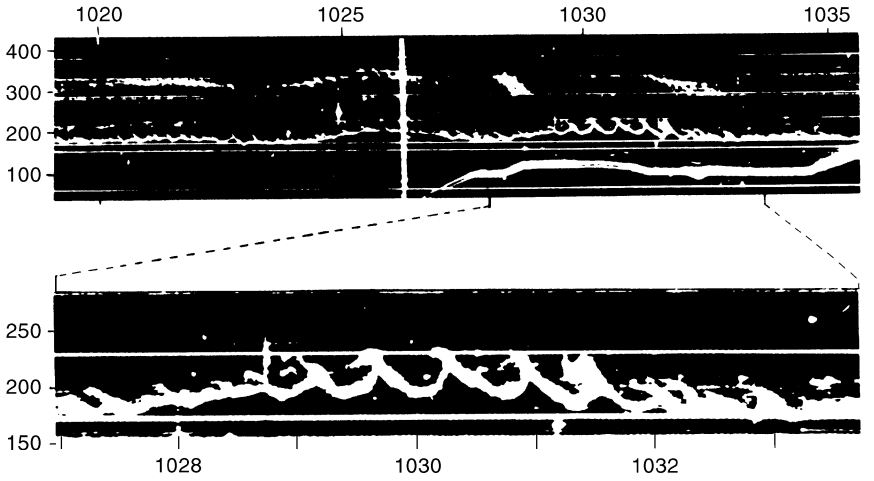

FIGURE 6.6 Kelvin–Helmholtz waves observed with frequency-modulated, continuous-wave (FM/CW) radar on June 25, 1970, at the Navy Research Facility, San Diego, CA, by E.E. Gossard, J.R. Richter, and D.R. Jensen. The horizontal axis is time (PST) and the vertical axis is height in meters. (From "Steps, waves and turbulence in the stably stratified planetary boundary layer," G. Chimonas, *Boundary-Layer Meterol.*, **90**: 397, 1999.)

leads to a convective instability and then to turbulence. It is often assumed that turbulence occurs when $R_i < 0.25$; however, this is not accurate. Indeed, as we shall see in the next sections, a linear analysis of shear flows shows that a sufficient condition for stability against infinitesimal disturbances is $R_i > 0.25$.

6.2.2 THE STABILITY OF SHEAR FLOWS

We have seen in the previous section that flow stability is controlled by the imaginary component of the wave frequency or, equivalently, the imaginary component of the phase velocity, c_i. Linear stability analysis determines under what flow conditions the phase velocity of small disturbances remains real. In the previous section we saw that for an infinite shear layer (Fig. 6.2) the phase velocity of small disturbances remains real if the wavenumber of the disturbance is less than some critical wavenumber. For wavenumbers greater than the critical value, the flow can become unstable and break down into turbulence. In real flows, this turbulence will vertically mix the two fluids, producing a third layer in which the velocity shear is now finite. In this section we examine the stability of such a finite shear layer.

6.2.2.1 Inflection Point Instability

The simplest problem involving instability of a shear flow is the case of a bounded homogeneous flow. This type of flow was first analyzed by Rayleigh (1945) and is sometimes called the *Rayleigh instability* problem. We consider a

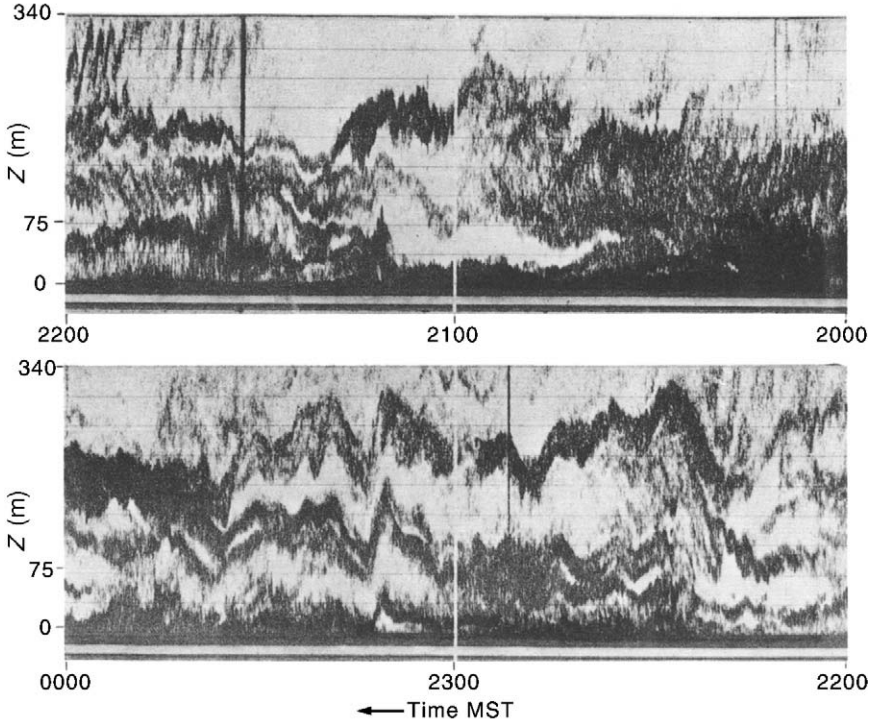

FIGURE 6.7 Kelvin–Helmholtz waves observed near Boulder, CO, with an acoustic sounder. (From *Studies of Nocturnal Stable Layers at BAO*, R.L. Zamora, National Atmospheric and Oceanic Administration, NOAA/ERL, Boulder, CO, 1983, p. 109.)

two-dimensional homogeneous flow with vertical boundaries at heights z_1 and z_2 such that $w' = 0$ at these heights. One can imagine a flow in an enclosed tank or channel. However, z_1 and z_2 can be infinitely large if the flow perturbations, *i.e.*, the streamline displacements, vanish there. The Taylor–Goldstein equation (2.34) takes the form

$$\frac{\partial^2 \hat{w}}{\partial z^2} + \left[\frac{u_0''}{(c - u_0)} - k^2 \right] \hat{w} = 0, \tag{6.57}$$

where primes denote differentiation with respect to z. We assume c is a complex number, *i.e.*, $c = c_r + ic_i$. We now multiply (6.57) by $\hat{w}^*$, the complex conjugate of $\hat{w}$, and integrate from z_1 to z_2 to get

$$-\int_{z_1}^{z_2} \left| \frac{\partial \hat{w}}{\partial z} \right|^2 dz - \int_{z_1}^{z_2} k^2 |\hat{w}|^2 \, dz = \int_{z_1}^{z_2} \frac{u_0''}{c_r + ic_i - u_0} |\hat{w}|^2 \, dz, \tag{6.58}$$

where we have integrated the first term by parts, *i.e.*,

$$\int_{z_1}^{z_2} \hat{w}^* \frac{\partial^2 \hat{w}}{\partial z^2}\, dz = -\int_{z_1}^{z_2} \left|\frac{\partial \hat{w}}{\partial z}\right|^2 dz. \tag{6.59}$$

The imaginary part of (6.58) is

$$c_i \int_{z_1}^{z_2} \frac{u_0''}{|c-u_0|^2} |\hat{w}|^2\, dz = 0. \tag{6.60}$$

For instability, $c_i \neq 0$, and if (6.60) is to hold and if $|\hat{w}| \neq 0$, then $u_0'' = 0$ somewhere between z_1 and z_2. If u_0' is continuous, then for instability there must be at least one inflection point between the two vertical boundaries. Inflection points are often associated with velocity jets. At an inflection point, the velocity shear has a maximum, and we can expect a high probability for shear instability. However, the presence of a stable stratification, which is absent in the above analysis, can suppress the destabilizing effect of the wind shear. This is why instabilities are not always found near inflection points in stratified flows.

6.2.2.2 The Stability of Stratified Shear Flows

The introduction of a stable stratification into the shear flow problem results in an immediate complication; however, the complication is more algebraic than physical. The problem was solved in detail by Miles (1961) who developed 10 theorems relating to stratified shear flow. Theorem 10 states that sufficient conditions for stability of a heterogeneous shear flow are the mean wind speed is nonzero and the Richardson number is greater than 0.25. Howard (1961) analyzed this problem from a more simple perspective. Here, we shall follow Howard's analysis, but the interested reader should look at Miles' paper for details and insights not contained in Howard. We assume a two-dimensional, frictionless, irrotational flow and make the Boussinesq approximation. The first-order vertical displacement, ζ_1, of a fluid particle from its equilibrium position is described by

$$\zeta_1(x, z, t) = F(z)\, e^{ik(x-ct)}, \tag{6.61}$$

where k is real and phase speed c can be a complex number. The boundary conditions are that $F(z) = 0$ at $z = z_1$ and $z = z_2$ which can recede to $\pm\infty$. Then noting that

$$\frac{D\zeta_1}{Dt} = \frac{\partial \zeta_1}{\partial t} + u_0 \frac{\partial \zeta_1}{\partial x} = w_1, \tag{6.62}$$

and using (6.62) in (2.6)–(2.8), we obtain

$$u_1 = [(c-u_0)\zeta_1]' \tag{6.63}$$

$$w_1 = -ik(c - u_0)\zeta_1 \tag{6.64}$$

$$p_1 = \rho_0(c - u_0)^2\zeta_1' + p_0. \tag{6.65}$$

Equations (6.63)–(6.65) can be combined along with the hydrostatic equation and solved for ζ to give

$$[\rho_0(c - u_0)^2 F']' + \rho_0[N^2 - k^2(c - u_0)^2]F = 0. \tag{6.66}$$

If we define a new variable as $G = W^{1/2} F$, where $W = u_0 - c$, then (6.66) can be written as

$$(\rho_0 W G')' - \left[\frac{1}{2}(\rho_0 u_0')' + k^2\rho_0 W + \rho_0 w^{-1}\left(\frac{1}{4}u_0'^2 - N^2\right)\right] G = 0. \tag{6.67}$$

If we now multiply (6.67) by G^* and integrate from z_1 to z_2 just as we did in the previous section, we get

$$\int \rho_0 W[|G'|^2 + k^2|G|^2] + \int \frac{1}{2}(\rho_0 u_0')'|G|^2 + \int \rho_0\left[\frac{1}{4}u_0'^2 - N^2\right] W^*\left|\frac{G}{W}\right|^2 = 0, \tag{6.68}$$

where it is understood that the limits on the integrals are still z_1 and z_2, and we have dropped dz in the integrals. From (6.61) it is clear that for an instability to occur the imaginary part of c must be positive, *i.e.*, $c_i > 0$. The imaginary part of (6.68) is

$$\int \rho_0\left[|G'|^2 + k^2|G|^2\right] + \int \rho_0\left[N^2 - \frac{1}{4}u_0'^2\right]\left|\frac{G}{W}\right|^2 = 0, \tag{6.69}$$

where we have divided (6.69) by W. The only way (6.69) can be true is if the term $N^2 - \frac{1}{4}u_0'^2$ changes sign somewhere between z_1 and z_2. Thus, a necessary condition for instability is that

$$\frac{N^2}{u_0'^2} = R_i < \frac{1}{4}. \tag{6.70}$$

We have formally proved the conjecture in Section 6.1, *i.e.*, for flow instability a necessary condition is $R_i < \frac{1}{4}$.

When an instability develops in a stratified flow, a gravity wave is excited. However, what is the phase speed of this wave? Howard (1961) elegantly answered this question. The method is straightforward. We multiply (6.66) by F^* and integrate over height to get

$$\int \rho_0(u_0 - c)^2\left[|F'|^2 + k^2|F|^2\right] - \int \rho_0 N^2|F|^2 = 0. \tag{6.71}$$

Now separate (6.71) into real and imaginary parts to get

$$\int \left[(u_0 - c_r)^2 - c_i^2\right]\left[|F'|^2 + k^2|F|^2\right] - \int N^2|F|^2 = 0 \tag{6.72}$$

and

$$2ic_i \int (u_0 - c_r)\left[|F'|^2 + k^2|F|^2\right] = 0. \tag{6.73}$$

If (6.73) is to hold, then $[u_0(z) - c_r]$ must change sign at least once between the limits z_1 and z_2. This means that c_r must lie between the minimum and maximum values of u_0. Thus, the wave speed cannot be arbitrary. Now, let $Q = |F'|^2 + k^2|F|^2$, and assuming $c_i > 0$, (6.72) and (6.73) become

$$\int \left(u_0^2 - 2u_0c_r + c_R^2 - c_i^2\right)Q = \int N^2|F|^2 \tag{6.74}$$

and

$$\int u_0 Q = c_r \int Q. \tag{6.75}$$

Now if we multiply (6.75) by $2c_r$, and use this result in (6.74), the resulting equations become

$$\int u_0^2 Q = \left(c_r^2 + c_i^2\right)\int Q + \int N^2|F|^2 \tag{6.76}$$

and

$$\int u_0 Q = c_r \int Q, \tag{6.77}$$

respectively. Now suppose that between z_1 and z_2, u_0 lies between u_{min} and u_{max}. Then using (6.76) and (6.77) and some algebra, we have

$$\begin{aligned}
0 \le & \int (u_0 - u_{min})(u_0 - u_{max}) \\
&= \int u_0^2 Q - (u_{min} + u_{max}) \int u_0 Q + u_{min}u_{max} \int Q \\
&= \left[c_r^2 + c_i^2 - (u_{min} + u_{max})c_r + u_{min}u_{max}\right] \int Q + \int N^2|F|^2 \\
&= \left\{\left[c_r - \tfrac{1}{2}(u_{min} + u_{max})\right]^2 + c_i^2 - \left[\tfrac{1}{2}(u_{min} - u_{max})\right]^2\right\} \int Q + \int N^2|F|^2.
\end{aligned} \tag{6.78}$$

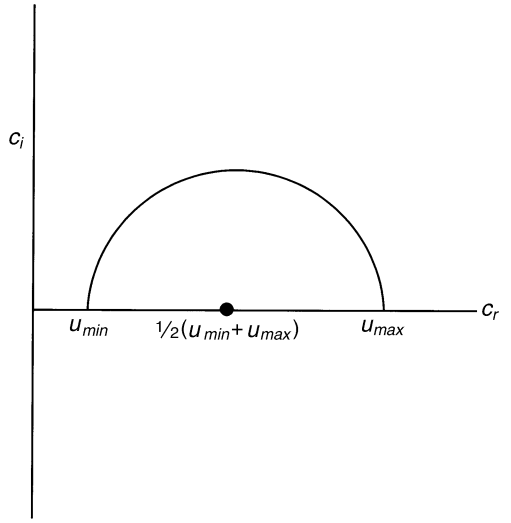

FIGURE 6.8 Schematic illustration of Howard's semi-circle theorem. If a gravity wave is generated by wind shear, then the phase speed of the wave must lie between some minimum and maximum wind speed.

Because $Q > 0$, the only way (6.78) can be true is if

$$[c_r - \tfrac{1}{2}(u_{min} + u_{max})]^2 + c_i^2 \leq [\tfrac{1}{2}(u_{min} - u_{max})]^2. \tag{6.79}$$

Equation (6.79) says that the complex phase velocity of any unstable mode must lie inside a semi-circle of radius $\frac{1}{2}(u_{max} - u_{min})$ centered at the point $c_i = 0$, $c_r = \frac{1}{2}(u_{min} + u_{max})$. This famous result is known as *Howard's semi-circle theorem*. Figure 6.8 illustrates the result. The semi-circle theorem tells us that if a gravity wave is excited by wind shear, then there must be a critical level for that wave since $u_{min} < c < u_{max}$. If, for example, one observes a wave with a speed of, say, 100 m s^{-1}, but the maximum wind speed is 30 m s^{-1}, then we can conclude that the wave was not generated by wind shear. However, if c lies within the semi-circle as illustrated in Fig. 6.8, then the wave most likely was generated at a critical level where $R_i < \frac{1}{4}$.

6.3 WAVE-MODULATED RICHARDSON NUMBER

In the above analyses of shear instability, the Richardson number was defined in terms of constant background quantities. From (2.37) we see that the amplitudes of upward-propagating gravity waves grow exponentially with height due to the decrease in atmospheric density. Hines (1960, 1963) proposed that gravity waves propagating into the upper atmosphere can generate turbulence there.

Hodges (1967) used this fact to demonstrate how gravity waves can modulate local Richardson numbers with the possibility of generating turbulence. Consider now the local Richardson number defined by the total temperature and velocity, *i.e.*,

$$R_i = \frac{g}{\theta}\frac{(\partial\theta/\partial z)}{(\partial u/\partial z)^2} = \frac{g}{\theta_0}\frac{(\partial/\partial z)[\theta_0+\theta_1]}{[(\partial/\partial z)(u_0+u_1)]^2}. \tag{6.80}$$

If we assume a wave perturbation vertical velocity of the form $w_1 = A\cos\phi$, where $\phi = kx + mz - \omega t$, then using (2.24) and (2.25) along with (1.67), we have

$$u_1 = -\frac{Am}{k}\cos\phi \tag{6.81}$$

and

$$\theta_1 = \frac{A}{\omega - u_0 k}\frac{\partial\theta_0}{\partial z}\sin\phi. \tag{6.82}$$

Using (6.81) and (6.82) in (6.80) gives

$$R_i = \frac{g}{\theta_0}\frac{(\partial/\partial z)(\theta_0 + (A/(\omega - u_0 k))(\partial\theta_0/\partial z)\sin\phi)}{[(\partial/\partial z)(u_0 - (Am/k)\cos\phi)]^2}. \tag{6.83}$$

Clearly, for certain values of the constants in (6.83) we can expect $R_i < 0.25$ over some range of ϕ. To illustrate this consider a constant flow over a corrugated surface. Then using (3.31) and (3.32) in (6.80) and assuming that $\partial^2\theta_0/\partial z^2 \ll 1$ gives

$$R_i = \frac{1 - m_s H\sin\phi}{[(u_0 m_s/N)(m_s H\cos\phi)]^2}, \tag{6.84}$$

where $\phi = k_s x + m_s z$; k_s is the wavenumber for the surface corrugation and H is the corrugation amplitude. If the stratification is strong and the wavelength of the corrugation is large, then

$$m_s^2 = \frac{N^2}{u_0^2} - k_s^2 \approx \frac{N^2}{u_0^2}, \tag{6.85}$$

so that (6.84) takes the simple form

$$R_i = \frac{1 - m_s H\sin\phi}{(m_s H\cos\phi)^2}. \tag{6.86}$$

If $m_s H \geq 1$, the flow will be convectively unstable over some range of ϕ. The quantity $m_s H = NH/u_0 = F^{-1}$, where F is similar to the *internal Froude number* (Turner, 1973).

The ordinary Froude number is defined as the ratio of a characteristic speed to the speed of long waves on a free surface (6.58), *i.e.*, $V/\sqrt{g\lambda}$, where V is a velocity scale and λ is a wavelength. The Froude number can also be defined as the square root of the inertia force to the gravity force. The internal Froude number, F_i, is defined as

$$F_i = \frac{V}{\sqrt{((\rho_2 - \rho_1)/(\rho_2 + \rho_1))\,\lambda}}, \tag{6.87}$$

where ρ_1 and ρ_2 are the densities in adjoining fluid layers. In the case of a continuous stratification, it is common to define V/NH as the Froude number. Thus, we can write (6.86) as

$$R_i = \frac{F^2 - F\sin\phi}{\cos^2\phi}. \tag{6.88}$$

We see that convective instability over the surface corrugation occurs when $F < 1$. Rottman and Smith (1989) showed experimentally that wave breaking occurs over a two-dimensional ridge in a linearly stratified flow for $F = 0.8$, 0.9, and 1.0 for steep ($H/L = 0.56$), intermediate ($H/L = 0.34$), and gentle ($H/L = 0.16$) ridges, respectively. Here L is the half-width of the ridge and H/L is the aspect ratio of the ridge. Figure 6.9 shows plots of (6.88) as functions of ϕ for $F = 0.9$ and 1.1. R_i is always greater than 0.25 for $F = 0.9$, but for $F = 1.1$ the ranges of ϕ for dynamic and convective instability are evident. Figure 6.10 shows the regions of convective instability ($R_i \leq 0$) over a corrugated surface calculated using the linear wave model described in Chapter 9. The calculation used $u_0 = 1$ m s^{-1}, $H = 60$ m, $\lambda_s = 500$ m, and $N = 0.022$ s^{-1}, and for this case, $F = 0.8$. The unstable regions tilt upwind with an angle $\tan^{-1}(m_s/k_s)$. For this case, the half-width of corrugation is 250 m, so the aspect ratio is 0.24. This is gentle topography, yet gravity waves can generate regions of *clear air turbulence*. Figure 6.11 plots the convectively unstable regions over a two-dimensional Gaussian ridge with $H = 50$ m, $b = 1000$ m, $u_0 = 1$ m s^{-1}, and $N = 0.022$ s^{-1}. The unstable patches remain directly above the ridge. The Froude number for this case is 0.9. The half-width of the ridge is $0.83b$, so the aspect ratio for this case is 0.06. This is a very gentle topography, but even so turbulence can be generated by the ridge.

Chimonas (1972) used the concept of a wave-modulated Richardson number in a quasi-linear theory of wave-generated breakdowns of a stratified flow. He included terms in the linearized equations (2.6)–(2.9) to account for the fluxes of heat and momentum due to wave-generated turbulence. These flux terms are switched on whenever the Richardson number drops below 0.25. When this happens, the turbulence feeds momentum and energy from the background flow into the wave, causing the wave amplitude to increase. This, in turn, increases the intensity and spatial extent of the regions of turbulence. The result is a rapid rise of turbulence and wave amplitude; however, the linear theory cannot follow this process to a conclusion because the wave amplitudes become too large.

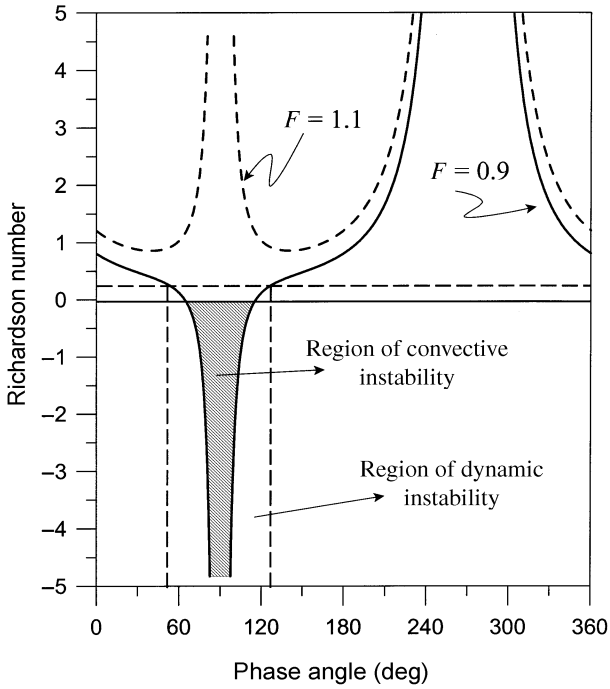

FIGURE 6.9 Richard number (6.88) as a function of phase angle for Froude numbers of 0.9 and 1.1. Region of dynamic instability extends below $R_i = 0.25$ and between the dashed lines. Region of convective instability is shaded.

6.4 WAVE-TURBULENCE COUPLING

In a series of articles including Einaudi and Finnigan (1981, 1993), Finnigan and Einaudi (1981), Fua *et al.* (1982), Finnigan, Einaudi, and Fua (1984), and Finnigan (1988), Finnigan and Einaudi examined the interactions of waves and turbulence. The mechanism by which waves and turbulence interact and modify the mean flow is commonly referred to as *wave-turbulence coupling*. Fua *et al.* (1982) lists the four basic ideas underlying the process:

1. The occurrence of turbulence can be related to the local (wave-modified) Richardson number.
2. Turbulence occurs with a mean and periodic component.
3. Turbulence extracts energy from the wave, limiting its growth, or feeds energy into the wave.
4. Turbulence modifies the mean fields.

The analysis of wave-turbulence coupling is based on a triple decomposition of the flow variables based on the work of Reynolds and Hussain (1972). The decomposition separates the atmospheric variables into mean, $\overline{a}$, turbulence, a',

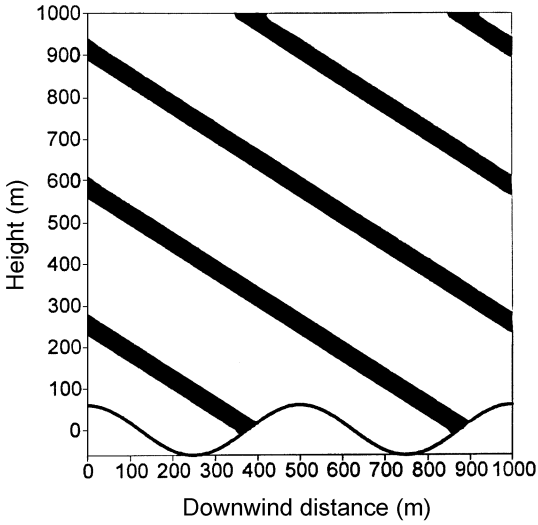

FIGURE 6.10 Regions of convective instability (dark bands) above a corrugated surface. $u_0 = 1\ \mathrm{m\ s^{-1}}$, $H = 60$ m, $N = 0.022\ \mathrm{s^{-1}}$, and $\lambda_s = 500$ m; Froude number, $F = 0.8$.

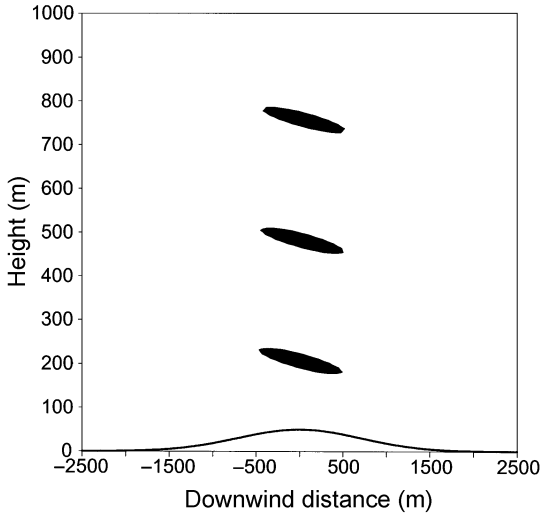

FIGURE 6.11 Regions of convective instability above a Gaussian-shaped ridge. $u_0 = 1\ \mathrm{m\ s^{-1}}$, $H = 50$ m, $b = 1000$ m, and $N = 0.022\ \mathrm{s^{-1}}$; Froude number, $F = 0.9$.

and wave, $\tilde{a}$, components, *i.e.*,

$$a(x_i, t) = \overline{a}(x_i) + a'(x_i, t) + \tilde{a}(x_i, t), \tag{6.89}$$

where x_i represents the spatial coordinates. The triple decomposition puts requirements on the wave field. It must be linear, monochromatic, and have constant

frequency and amplitude. The problem involves writing equations for turbulence and wave variables and examining the terms that connect these equations. The time average or background is defined in the usual way, *i.e.*,

$$\overline{a}(x_i) = \lim_{t\to\infty}\left\{\frac{1}{2t}\int_{-t}^{+t} a(x_i, t')\,dt'\right\}. \tag{6.90}$$

If the wave has period τ, then the *phase average* is defined as

$$\langle a(x_i, t)\rangle = \lim_{N\to\infty}\left\{\frac{1}{N}\sum_{n=1}^{N} a(x_i, t + n\tau)\right\}, \tag{6.91}$$

where N now is the number of wave cycles, not the Brunt–Väisälä frequency. Figure 6.12 illustrates the phase averaging process. A turbulence signal illustrated in Fig. 6.12 has zero mean and standard deviation 0.6 m s^{-1} and is added to a sine wave with period 157 s and amplitude 0.25 m s^{-1}. The value of $\langle a\rangle$ at time t is the average of N data points, with each point separated by time period τ. Because the turbulence is random, it is removed by the ensemble averaging. The illustration in Fig. 6.12 is conceptual; in order to reveal the actual wave signal from the raw data, averaging over many cycles would be required. After phase averaging, the *wave average* component and the turbulent component of the raw signal are calculated

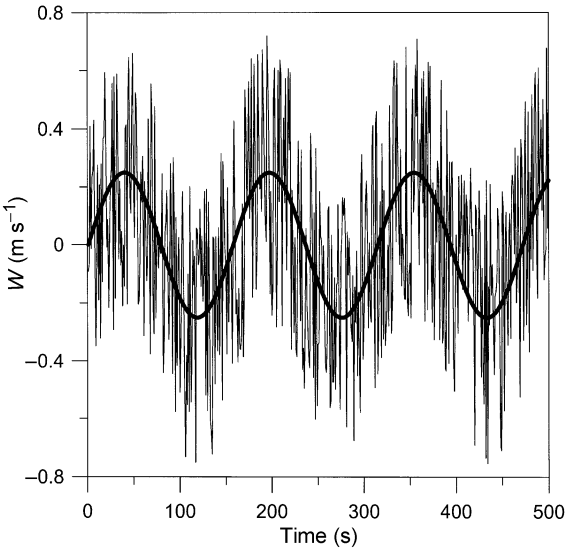

FIGURE 6.12 An illustration of phase averaging. The heavy line represents an underlying wave signal which would be revealed by phase averaging.

using

$$\tilde{a}(x_i, t) = \langle a(x_i, t)\rangle - \overline{a}(x_i) \tag{6.92}$$

$$a'(x_i, t) = a(x_i, t) - \langle a(x_i, t)\rangle\,. \tag{6.93}$$

Using the triple decomposition defined by (6.89) in (2.1)–(2.4) along with (1.67) gives equations for the wave field. However, several averaging identities are required, specifically for variables a and b:

$$\begin{array}{lll}
\text{(i) } \langle a'\rangle = 0 & \text{(ii) } \overline{\tilde{a}} = 0 & \text{(iii) } \overline{a'} = 0 \\
\text{(iv) } \overline{\overline{a}b} = \overline{a}\,\overline{b} & \text{(v) } \langle\tilde{a}b\rangle = \tilde{a}\langle b\rangle & \text{(vi) } \langle\overline{a}b\rangle = \overline{a}\langle b\rangle \\
\text{(vii) } \langle\overline{a}\rangle = \overline{a} & \text{(viii) } \overline{\langle a\rangle} = \overline{a} & \text{(ix) } \overline{\tilde{a}b'} = \overline{\langle\tilde{a}b'\rangle} = 0.
\end{array}$$

Using these identities, and assuming that the density is constant over the small vertical scales considered and that the flow is inviscid, the dynamical equations for the wave and turbulence fields are (Reynolds and Hussain, 1972)

$$\begin{aligned}
&\frac{\partial\tilde{u}_i}{\partial t} + u_{0,j}\,\frac{\partial\tilde{u}_i}{\partial x_j} + \tilde{u}_j\,\frac{\partial u_{0,i}}{\partial x_j} \\
&\quad = -\frac{\partial\tilde{p}}{\partial x_i} - \frac{\partial\tilde{r}_{ij}}{\partial x_j} - \frac{\partial}{\partial x_j}\big(\tilde{u}_i\tilde{u}_j - \overline{\tilde{u}_i\tilde{u}_j}\,\big) + \frac{g}{T_0}\,\tilde{\theta}\delta_{i3}
\end{aligned} \tag{6.94}$$

and

$$\frac{\partial u_i'}{\partial t} + u_{0,j}\,\frac{\partial u_i'}{\partial x_j} + u_j'\,\frac{\partial u_{0,i}}{\partial x_j} = -\frac{\partial p'}{\partial x_i} + \frac{\partial\tilde{r}_{ij}}{\partial x_j} + \frac{g}{T_0}\,\theta'\delta_{i3}, \tag{6.95}$$

where

$$\tilde{r}_{ij} = \langle u_i'u_j'\rangle - \overline{u_i'u_j'}. \tag{6.96}$$

Similar equations can be written for the temperature wave and turbulence fields. The term $(\tilde{u}_i\tilde{u}_j - \overline{\tilde{u}_i\tilde{u}_j})$ in (6.94) represents the fluctuation part of the wave stress. Note that except for $\tilde{r}_{ij}$ all the terms in the equation for the organized wave (6.94) involve wave terms and all the terms in the turbulence equation (6.95) involve turbulence terms. The term $\tilde{r}_{ij}$ represents the oscillating part of the Reynolds stress due to the presence of the wave, *i.e.*, the wave-modified turbulence. The term appears with negative sign in (6.94) and with positive sign in (6.95). Thus, if it is a sink term in the wave equation (6.94), then it is a source term in the turbulence equation (6.95). We see that the wave-modified Reynolds stress is a mechanism for transferring energy between the turbulence and the wave. The term $(\tilde{u}_i\tilde{u}_j - \overline{\tilde{u}_i\tilde{u}_j})$ in the wave equation does not have a counterpart in the turbulence equation. This term represents wave-like fluctuations in the wave stress; however, similar organized motions do not appear in the turbulence field. Recall it is the

integral of the wave stress, *i.e.*, (5.8), that is constant with height. In (6.94) we see that wave amplitude changes according to the variations of the wave stress from its average value.

The equations for the wave and turbulence kinetic energies are

$$\begin{aligned}\frac{D\overline{\tilde{q}^2}}{Dt} &= \frac{D}{Dt}\left(\frac{\overline{\tilde{u}_i\tilde{u}_i}}{2}\right)\\ &= -\frac{\partial}{\partial x_j}\left\{\overline{\tilde{u}_j\left(\tilde{p}+\frac{\tilde{u}_i\tilde{u}_i}{2}\right)}\right\} - \overline{\tilde{u}_i\tilde{u}_j}\,\frac{\partial u_{0,i}}{\partial x_j}\\ &\quad + \overline{\tilde{r}_{ij}\frac{\partial\tilde{u}_i}{\partial x_j}} - \frac{\partial}{\partial x_j}\left(\overline{\tilde{u}_i\tilde{r}_{ij}}\right) + \frac{g}{\theta_0}\,\overline{\tilde{\theta}\tilde{u}_i}\,\delta_{i3} + \text{viscous terms}\end{aligned} \tag{6.97}$$

and

$$\begin{aligned}\frac{D\overline{q'^2}}{Dt} &= \frac{D}{Dt}\left(\frac{\overline{u_i'u_i'}}{2}\right)\\ &= -\frac{\partial}{\partial x_j}\left\{\overline{u_j'\left(p'+\frac{u_i'u_i'}{2}\right)}\right\} - \overline{u_i'u_j'}\,\frac{\partial u_{0,i}}{\partial x_j}\\ &\quad - \overline{\tilde{r}_{ij}\frac{\partial\tilde{u}_i}{\partial x_j}} - \overline{\tilde{u}_j\frac{\partial}{\partial x_j}\left(\frac{\tilde{r}_{ii}}{2}\right)} + \frac{g}{\theta_0}\,\overline{\theta'u_i'}\,\delta_{i3} + \text{viscous terms.}\end{aligned} \tag{6.98}$$

Equations (6.97) and (6.98) are similar to conventional turbulence budgets; however, the term $\overline{\tilde{r}_{ij}(\partial\tilde{u}_i/\partial x_j)}$ is the direct result of the triple decomposition. This is a production term and represents the rate of work of wave-modified Reynolds stress against the wave rate of strain. It is this term that is responsible for the transfer of energy between the wave and turbulence fields. Because $\tilde{r}_{ij}$ and $\partial\tilde{u}_i/\partial x_j$ represent linear wave fluctuations, their average product is zero if the two terms have a phase difference of $\pi/2$. Then, there is little energy transfer between the wave and turbulence fields. Finnigan (1988) reports the observations of four episodes observed at the Boulder Atmospheric Observatory in Colorado with substantial gravity waves. Phase differences of about $\pi/4$ between $\tilde{r}_{ij}$ and $\partial\tilde{u}_i/\partial x_j$ were observed to occur with significant transfer of energy from the wave to the turbulence.

In the wind tunnel experiments on wave turbulence–turbulence coupling reported on by Hussain and Reynolds (1972), the turbulence component was very weak, and so a large number of wave cycles (typically 10^5) was required in the averaging process. In the atmosphere, the conditions required for phase averaging, *i.e.*, a linear, monochromatic wave with constant frequency and amplitude, will hardly ever be observed in the atmospheric boundary layer (see, for example, Finnigan, 1988). Thus, wave-turbulence coupling is perhaps more useful as a theoretical rather than an observational tool.

6.5 JEFFERYS' ROLL-WAVE INSTABILITY MECHANISM

Chimonas (1993, 1994) calls attention to a wave instability mechanism proposed by Jefferys (1925) to explain *progressive waves* on the surface of water flowing in a channel. As Jefferys (1925) describes ". . .in certain Alpine conduits, with plane bottoms and rectangular sections, (water) does not flow in a steady stream but in a series of waves." Chimonas (1993) draws a parallel between progressive waves in conduits and the wave systems that appear on water-covered slopes on a road during a heavy rainfall. He notes that the waves ". . .seem to be in a continuous state of breaking, like rollers approaching a beach and somehow achieve a lasting state of overturning." These progressive waves are instabilities that develop on the turbulent sheet of water as the water flows downslope. The downslope acceleration of flow is balanced by the aerodynamic drag at the ground surface, as illustrated in Fig. 6.13. The instabilities develop because variations in the surface drag result in a readjustment of the downslope mass flow. An increase in drag causes an upslope build up of water. This flow convergence can lead to wave excitation. Once initiated, the wave produces periodic variations in surface drag, and a resonance develops. Chimonas (1993) applied this mechanism in the atmosphere, where the turbulent water is replaced by a turbulent planetary boundary layer and the downslope acceleration is replaced by the atmospheric mean pressure gradient. Figure 6.14 illustrates this case. The atmospheric waves illustrated in Fig. 6.14 are different than the *roll waves* studied, for example, by Brown (1980),

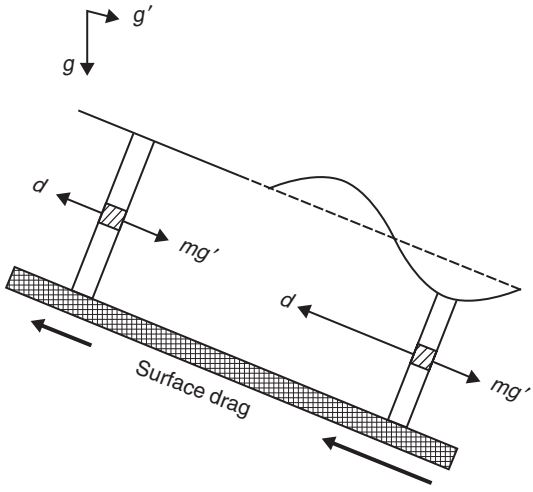

FIGURE 6.13 "Drag waves" on a downslope flow. The instabilities develop because variations in the surface drag result in a readjustment of the downslope mass flow. (From "Surface drag instabilities in the atmospheric boundary layer," G. Chimonas, *J. Atmos. Sci*., **50**: 1915, 1993.)

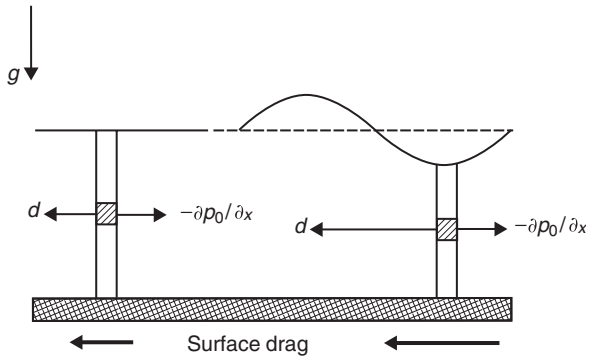

FIGURE 6.14 Drag waves in the ageostrophic boundary-layer flow. This instability mechanism is similar to that illustrated in Fig. 6.13 except now the gravity force is replaced by the pressure gradient force (From "Surface drag instabilities in the atmospheric boundary layer," G. Chimonas, *J. Atmos. Sci.*, **50**: 1916, 1993.)

Mason and Sykes (1982), and Etling and Raasch (1987). Those roll waves are associated with a critical level; however, the Jefferys waves have phase speeds considerably greater than the flow speeds. An assumption of Jefferys mechanism is a fully turbulent flow so that variations in surface drag are felt immediately through the depth of the water layer. A similar assumption is required for the atmospheric case.

We now assume a steady, two-dimensional, hydrostatic, irrotational, atmospheric background flow above a level ground surface. Figure 6.15 illustrates the flow geometry. A three-layer model provides the possibility for a ducting region with little change in the model physics. A turbulent surface layer of depth h and mean depth h_0 is in contact with the ground surface. In the two-layer model, a capping inversion separates the surface layer from the free atmosphere which has constant wind speed and stratification. In the case of three layers, the middle layer has intermediate wind and stratification between the surface layer and the semi-infinite layer. The middle layer allows for the ducting of gravity waves, but the physics is the same as for the two-layer case. The balance of forces in the surface layer is

$$\frac{\partial p_0}{\partial x} + \rho_0 d_0 = 0 \tag{6.99}$$

where d_0 is the force per unit mass due to the Reynolds stress. The turbulence in the surface layer is the result of surface friction so that

$$\int_0^{h_0} \rho_0 d_0 \, dz = 0.5 \rho_0 C_D U^2 \tag{6.100}$$

where C_D is the surface drag coefficient and U is a velocity scale for the surface layer. In the free atmosphere, the Taylor–Goldstein equation (2.34) applies, and at any layer of discontinuity in wind speed or stratification, *i.e.*, at $z = h$, we impose

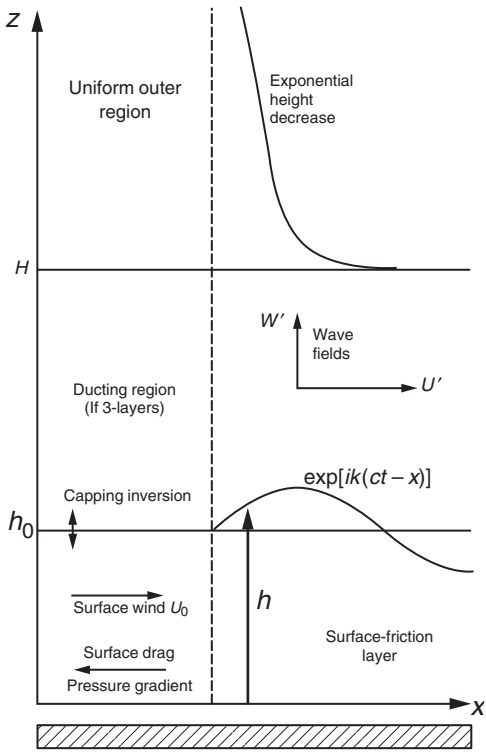

FIGURE 6.15 Schematic of the flow geometry. A fully turbulent surface has a mean depth h_0. In the two-layer case, the surface layer is capped by a semi-infinite layer with constant wind and stable stratification. The optional middle layer allows for the ducting of gravity waves. (From "Surface drag instabilities in the atmospheric boundary layer," G. Chimonas, *J. Atmos. Sci.*, **50**: 1918, 1993.)

the kinematic and dynamic boundary conditions. The equation of continuity for the surface layer is (Jefferys, 1925)

$$\frac{\partial h}{\partial t} = -\frac{\partial uh}{\partial x}. \tag{6.101}$$

We assume that in the surface layer the horizontal velocity is vertically uniform and the vertical acceleration is balanced by the hydrostatic force so that

$$p(z) = p(h_0) + \rho_0 g(h_0 - z). \tag{6.102}$$

We integrate the horizontal momentum equation with height and linearize in terms of a mean background and wave perturbation, for example, u_0 and u_1, to get

$$ikh_0(c - u_0)u_1 = -h_1\frac{\partial p_0}{\partial x} + ikh_0 p_1 - \rho_0 C_D u_0 u_1, \tag{6.103}$$

where scale velocity U in (6.100) has been replaced by u_0 and pressures p_0 and p_1 are evaluated at $z = h_0$. Combining (6.101)–(6.103) gives the relation between $p_1(h_0)$ and h_1, *i.e.*,

$$\left[kh_0(c-u_0)^2 + i0.5u_0^2 C_D - iu_0(c-u_0)C_D\right]\frac{h_1}{h_0} = \frac{1}{\rho_0}\,kh_0 p_0. \tag{6.104}$$

The most simple model has two layers. In the upper layer, $N = 0$ and $u_0 = u_\infty =$ constant. Such a model approximates a shallow nocturnal boundary layer beneath a residual convective layer (Stull, 1988) or a density current undercutting well-mixed air. The solutions in the upper layer are

$$w_1(z) = Ae^{-kz}\,e^{-ik(x-ct)} \tag{6.105}$$

and

$$p_1 = i(c-u_\infty)\rho_0 w_1, \tag{6.106}$$

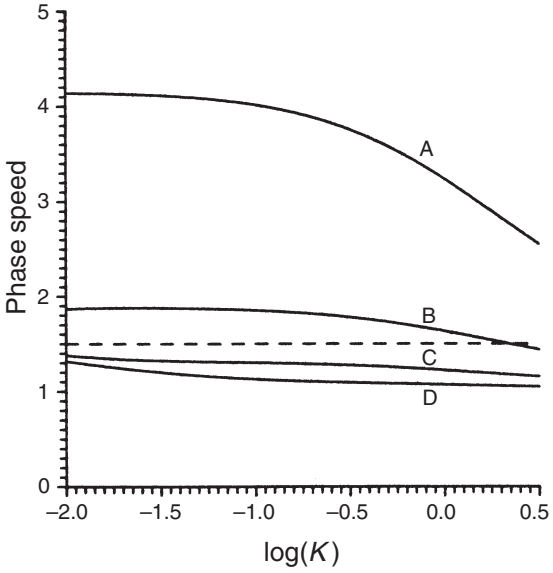

FIGURE 6.16 Dimensionless phase speeds versus dimensionless wavenumber for the two-layer drag wave model with $C_D = 0.005$. The dashed line indicates the threshold wave speed of $1.5\,u_0$ for wave growth. (A) $g' = 10$, the waves are similar to shallow-waver surface waves. (B) $g' = 0.8$, the phase speed crosses the threshold value of 1.5. (C) $g' = 0.1$, surface drag begins to have an effect. (D) $g' = 0.01$, the wave is dominated by the surface drag. (From "Surface drag instabilities in the atmospheric boundary layer," G. Chimonas, *J. Atmos. Sci.*, **50**: 1918, 1993.)

where $u_\infty \hat{x}$ is the constant undisturbed velocity in the upper layer. The vertical displacement of the interface is

$$\zeta_1 = -i \frac{w_i}{k(c - u_\infty)}. \tag{6.107}$$

At the interface between the two layers we apply the dynamic and kinematic boundary conditions, and with (6.104)–(6.107) we get the dispersion relation

$$(c - u_0)^2 + i \frac{C_D u_0}{k h_0} \left(\frac{3}{2} u_0 - c \right) + (c - u_0)^2 k h_0 (1 - f) - g' h_0 = 0, \tag{6.108}$$

where f is now the fractional decrease in density between the two layers and $g' = fg$ is the reduced gravity.

The stability analysis of the interface displacements proceeds as before. We divide the dispersion relation into real and imaginary parts and look for conditions where $c_i > 0$. The imaginary part of (6.108) with the assumption that $kh_0 < 1$ (*i.e.*, the horizontal wavelength is large compared to the fluid depth) is

$$c_i = -C_D u_0 \frac{((3/2)u_0 - c_r)}{2kh_0(c_r - u_0)}. \tag{6.109}$$

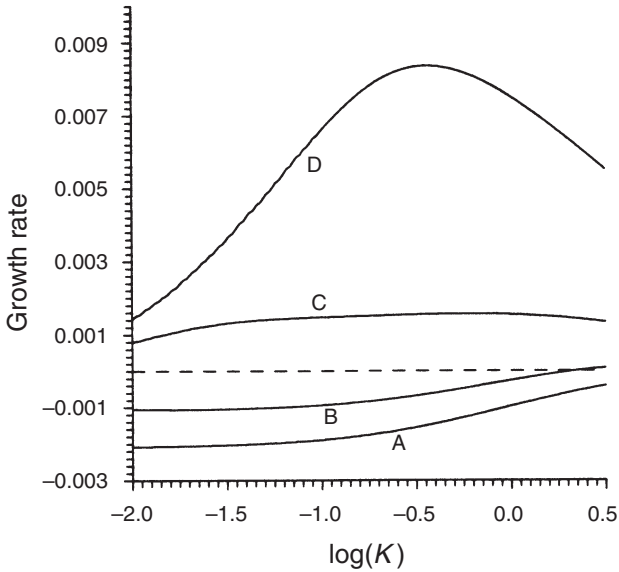

FIGURE 6.17 Growth rates versus dimensionless wavenumber. Surface friction causes instabilities in waves traveling slower than 1.5 u_0, but dampens wave traveling faster. (From "Surface drag instabilities in the atmospheric boundary layer," G. Chimonas, *J. Atmos. Sci.*, **50**: 1918, 1993.)

The phase speeds for the instabilities are bounded by the *neutral modes* where $c_i = 0$. Thus, instabilities occur within the region $u_0 \leq c \leq 1.5\, u_0$. Figures 6.16 and 6.17 plot the normalized phase speed c/u_0 and growth rates, respectively, as functions of normalized wavenumber $K = kh_0$ for various values of the dimensionless group $g'h_0/u_0^2$. For these results, the wind speed in the upper layer is set equal to the mean speed of the surface layer. The dashed line in Fig. 6.16 marks the value $c = 1.5\, u_0$, and it is seen from Fig. 6.17 that this is indeed a boundary between stable and unstable modes. It is seen that the Jefferys instabilities favor high surface-layer speeds and weak capping inversions, *i.e.*, small f. Chimonas (1994) expands on the Jefferys mechanism and presents some examples of observed wave events that resemble to a high degree this mechanism.

7

The Parameterization of Wave Stress

One of the most important effects of gravity waves on the atmosphere is the ability to transport momentum and energy from one region of the atmosphere to another. The momentum and energy transported by gravity waves reflects the conditions where the waves were generated. Over terrain features, the stress is produced as a response to the torque exerted on the terrain by the mean flow. Accordingly, the gravity waves carry upward a stress which will act against the mean flow. The upward transport of stress by waves generated by flow over mountains and hills has, perhaps, more impact on atmospheric dynamics than any other type of wave. Sawyer (1959) was one of the first to recognize the necessity of accounting for the effects of mountain-generated gravity waves in numerical forecast models. Bretherton (1969) computed the wave stress over the hilly terrain in north Wales and showed that for a 19 m s^{-1} wind speed the wave stress can reach 0.4 Pa,[1] of which 0.3 Pa probably acted on the atmosphere above 20 km. To scale the effect of this stress on the atmosphere, let us assume that the stress is dissipated over a 5-km height range. Then, the atmospheric flow would be slowed at a rate of 5 m s^{-1} day^{-1}. Lilly (1972) measured the lee-wave drag over the Front Range of the Colorado Rockies and reported values of between 0.5 and 1 Pa in the troposphere averaged over a horizontal distance of 100–200 km. Blumen and McGregor (1976) calculated a wave-drag coefficient of 0.21×10^{-2} over a two-dimensional ridge and 0.11×10^{-2} over a three-dimensional hill. They calculated a wave stress on the order of 1 Pa over a series of ridges situated 25 km apart.

[1] A Pascal, Pa, is a stress or pressure of 1 N m^{-2}.

Terrain-generated waves carry upward a stress that acts against the mean flow; however, gravity waves generated aloft can transport stress upward and downward which can decelerate and accelerate the mean flow, respectively. For example, Chun and Baik (1998) calculated the momentum transport by gravity waves generated by thermal forcing due to cumulus convection. Their simulations show that in the region of diabatic heating (due to the release of latent heat within the cloud), a maximum positive tendency (acceleration) of the zonal wind by the gravity wave momentum flux is about 10 m s^{-1} day^{-1} at 3.4 km height, and a negative tendency (deceleration) is about -24 m s^{-1} day^{-1} at 10 km height. The deceleration in the upper troposphere is quite large compared with the mountain-induced gravity wave drag.

When the effects of gravity waves on the atmospheric flow were first being realized, forecast models of the period were based on the *quasi-geostrophic* approximation which filters gravity waves (see, for example, Holton, 1992). Thus, these gravity wave effects were eliminated from forecasts *a priori*. Over the last half century, our ability to numerically model the atmosphere has advanced to the point where it is limited mostly by computer capabilities. Models of the general circulation, mesoscale air quality models, and atmospheric chemistry models are *computationally bound*, *i.e.*, they spend most of their time solving many equations in addition to the dynamical equations. In order to make model execution time reasonable, the number of points where these equations are solved must not be large. Accordingly, the spatial resolution of the model must be limited. The smallest horizontal feature that can be resolved by a numerical model has size $4\Delta x$, where Δx is the horizontal length of a grid cell (see, for example, Pielke, 1984; Grasso, 2000). Global-scale models have horizontal resolutions on the order 10×10 degrees of latitude and longitude, and accordingly, only the largest terrain features, for example, continents, will be resolved. Mesoscale models with horizontal grid resolutions of 5×5 km are considered fine scale; however, topographic features less than 20 km will not be resolved. Cumulus convective cells with horizontal scales of a few tens of kilometers will not be seen by these model grid sizes; however, their dynamical effects may be significant (see, for example, Chun, Song, and Baik, 1999). While research-grade models can achieve high horizontal resolutions, operational models are still limited and will continue to be until the next generation of supercomputers. Thus, for most numerical applications in regions of mountainous terrain or active cumulus convection, there will be unresolved wave effects, and these *subgrid-scale* effects must be parameterized. In this chapter we shall examine the basics of these wave stress parameterizations.

7.1 WAVE SATURATION AND WAVE BREAKING

We have seen in Chapter 3 that the terrain irregularities, *i.e.*, mountains, hills, ridges, valleys, *etc.*, as well as areas of active convection can launch gravity waves and vertically transport energy and mean-flow horizontal momentum. In Chapter 5

we have seen that this vertical flux of horizontal momentum, $\rho_0\overline{u_1 w_1}$, is constant unless the wave breaks. We have also seen in Chapter 5 that in linear theory wave breaking occurs at or near a critical level, and then the wave stress is reduced by a factor of $\exp(-2\pi\sqrt{R_i - 0.25})$, where R_i is the Richardson number at the critical level. The deposition of this momentum onto the mean flow results in either an acceleration or deceleration depending on where the wave stress was generated. In either case,

$$\frac{\partial u_0}{\partial t} = -\frac{1}{\rho_0}\frac{\partial}{\partial z}(\rho_0\overline{u_1 w_1}). \tag{7.1}$$

Consider now that the wave stress is generated over a mountain, and note that $\rho_0\overline{u_1 w_1}$ is negative for linear gravity waves. However, because the wave stress decreases with height during wave dissipation, the vertical derivative of the stress will always be negative. From the third law we see that the stress exerted on a mountain by the flow is balanced by an equal but opposite stress on the flow where wave breaking occurs. However, there is something not quite right about this picture. The linear theory tells us that the reduction of wave stress occurs almost discontinuously across a very small distance. In this case, (7.1) would predict extremely large decelerations, but these are not observed. Hazel (1967) considered the effects of fluid viscosity and heat conduction near a critical level and showed that near a critical level inertial effects are balanced by viscosity within a *viscous length scale*, z_ν,

$$z_\nu = \left(\frac{\nu}{k(\partial u_0/\partial z)}\right)^{1/3}, \tag{7.2}$$

where ν is the atmospheric *kinematic viscosity* with units of $\mathrm{m}^2\ \mathrm{s}^{-1}$ and k is the horizontal wavenumber. The decrease in wave stress occurs across a distance of several z_ν. Fritts and Geller (1976) also considered the effects of fluid velocity and heat conduction near a critical level and showed that the maximum wave instability, $R_i < 1/4$, occurs approximately 2.5 z_ν below a critical level for upward-propagating waves.

An encounter with a critical level is not the only way a wave can become unstable. From (3.97), repeated here,

$$w(x, z, t) = \tilde{w}e^{z/2H_s}e^{i(kx+mz-\omega t)}, \tag{7.3}$$

we see that for an upward-propagating wave when $z > H_s$, wave amplitudes can become large. If either ω or m in (7.3) become complex, then wave amplitude can grow as either $e^{\omega_i t}$ or $e^{m_i z}$, where ω_i and m_i are the imaginary parts of the complex frequency and vertical wavenumber, respectively.

We see that wave amplitudes can grow, but can they grow indefinitely? Within the context of linear theory, the answer is yes. There are no factors such as viscosity

or wave–wave interactions which could limit wave growth. There are no mechanisms to tell the wave it is unstable and that it should break. However, the solutions under these extreme conditions may not be physical, for example, negative pressures or temperatures, *etc*. In the real world, we know that wave amplitudes must be bounded. Waves or other disturbances with great amplitudes ($\sim\infty$) have never been observed. The reason is simple. The waves eventually break. However, we observe that the wave does not collapse. Instead, only the top parts of the wave collapse. This dissipation process is known as *wave saturation* (see, for example, Fritts, 1984; Baines, 1995). The term originally described the damping of exponential growth of an instability as environmental conditions forced a return to finite amplitude. Wave saturation limits wave growth. In the atmosphere, even in the absence of an instability, unbounded wave growth is balanced by saturation. Previously, we conjectured that unbounded wave growth would eventually lead to dynamic instability and even convective instability. But this does not mean complete wave breakdown. Indeed, we shall see that wave saturation is a process where wave dissipation exactly balances wave growth. An analogous process is the breaking of waves as they approach a beach. As these waves grow, they eventually break, but only at the top, as shown in Fig. 7.1. Wave saturation theory assumes that wave breaking results in turbulence. However, linear theory does not contain a wave saturation counterpart. Figure 7.2 shows isotherms above a surface corrugation in the presence of a constant stratification, but a varying background wind. The wind profile used is a hyperbolic tangent, which is plotted in Fig. 7.3. In Fig. 7.2, we see regions that should be convectively unstable, but are not. It is clear that in these circumstances linear theory gives quite nonphysical results; yet the simplicity and computational ease of the linear theory makes

FIGURE 7.1 Breaking waves at the shore. Only the top portion of the wave breaks and continues to break as the wave continues to grow.

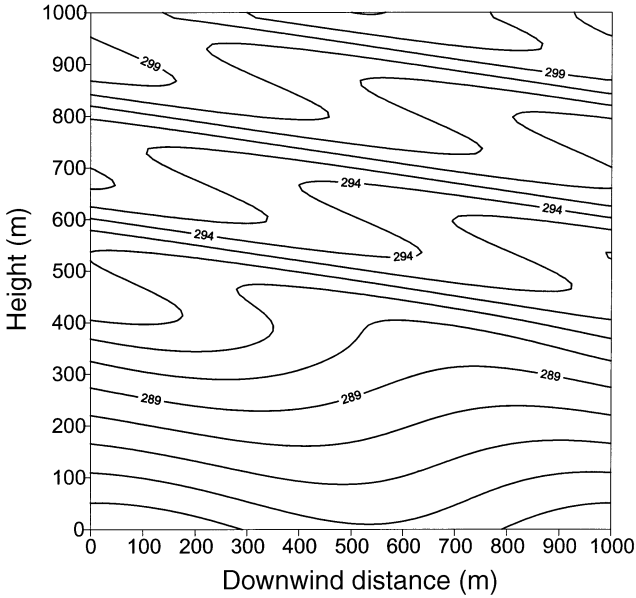

FIGURE 7.2 Isotherms over one cycle of a corrugated surface of wavelength 1000 m and amplitude 60 m. $N = 0.022\ \mathrm{s}^{-1}$. The background wind speed profile is shown in Fig. 7.3. Regions of convective instability are seen above a height of 400 m. In reality, these regions would be unstable and collapse.

it very desirable. If we want to use linear theory, then we must find a way to adjust it so that its results approach reality. This is the objective of wave saturation parameterization.

One of the first things we must do is determine the conditions for wave breaking. Consider a section of an isotherm such as that shown in Fig. 7.4 which could have come from a wave field similar to that shown in Fig. 7.2. Along the isotherm, which is also a streamline,

$$\theta_0(z) + \theta_1(x, z_Q) = Q(x, z_Q) = \text{constant}, \tag{7.4}$$

where $\theta_0(z)$ is the background potential temperature, $\theta_1(x, z)$ is a perturbation potential temperature, and z_Q is the height of the streamline. The total differential of Q is

$$\frac{\partial Q}{\partial x} + \frac{\partial Q}{\partial z_Q}\,\frac{\partial z_Q}{\partial x} = 0. \tag{7.5}$$

Using (7.4) in (7.5) gives

$$\frac{\partial \theta_1}{\partial x} + \frac{\partial z_Q}{\partial x}\,\frac{\partial}{\partial z_Q}(\theta_0 + \theta_1) = 0. \tag{7.6}$$

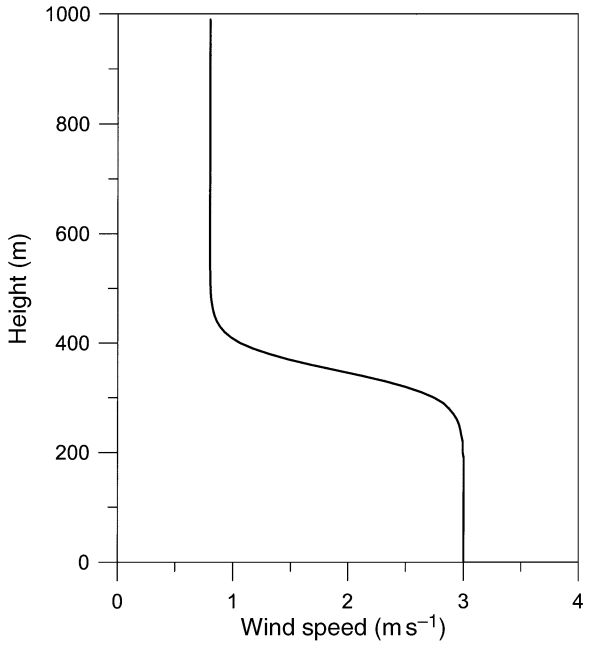

FIGURE 7.3 Hyperbolic-tangent wind profile is used in the calculation of the wave field shown in Fig. 7.2.

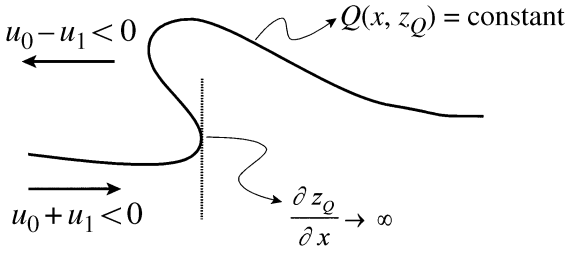

FIGURE 7.4 Section of an isotherm which is a streamline in the linear theory. When the slope of the streamline becomes vertical, the flow becomes convectively unstable. This is also the condition for flow blocking where $u_0 + u_1 = 0$.

The condition for convective stability is

$$\frac{\partial}{\partial z}(\theta_0 + \theta_1) \geq 0. \tag{7.7}$$

Then because $\partial\theta_1/\partial x$ in (7.6) need not be zero,

$$\lim_{(\partial/\partial z)(\theta_0+\theta_1)\to 0} \frac{\partial z_Q}{\partial x} \to \infty. \tag{7.8}$$

Thus, the flow streamlines are vertical at the onset of convective instability, as shown in Fig. 7.4. Using the continuity equation (2.8), we can define a stream function $\psi(x, z_\psi)$ where z_ψ is the height of the line along which ψ is constant. Then,

$$w_1 = \frac{\partial \psi}{\partial x} \tag{7.9}$$

$$u_0 + u_1 = -\frac{\partial \psi}{\partial z_Q}, \tag{7.10}$$

where we have taken u_0 to be horizontally uniform. Proceeding as above, if we take the total differential of ψ and use (7.9) and (7.10), then we get

$$w_1 - \frac{\partial z_Q}{\partial x}(u_0 + u_1) = 0. \tag{7.11}$$

Flow blocking occurs when $u_0 + u_1 = 0$, and if we assume that $w_1 \neq 0$, then

$$\lim_{(\partial/\partial z)(u_0+u_1)\to 0} \frac{\partial z_Q}{\partial x} \to \infty, \tag{7.12}$$

and we see that convective instability and flow blocking occur simultaneously, as illustrated in Fig. 7.4.

The convective stability limit (7.7) can be put into a more useful form by noting that the vertical displacement, ζ, of a flow streamline is related to the vertical velocity by

$$\frac{D\zeta}{Dt} = w. \tag{7.13}$$

Linearizing (7.13) to first order gives

$$\frac{\partial \zeta_1}{\partial t} + u_0 \frac{\partial \zeta_1}{\partial x} = w_1. \tag{7.14}$$

If we now assume wave solutions of the form (2.13) for ζ_1 and w_1, (7.14) becomes

$$-i\Omega\tilde{\zeta_1} = \tilde{w_1}. \tag{7.15}$$

Using (1.67) in the polarization equation for ρ_1, *i.e.*, (2.25), gives

$$\tilde{\theta}_1 = i\frac{\tilde{w}_1}{\Omega}\frac{\partial \theta_0}{\partial z}, \tag{7.16}$$

and combining (7.15) with (7.16) gives

$$\theta_1 = -\zeta_1 \frac{\partial \theta_0}{\partial z}, \tag{7.17}$$

where we have dropped the tildes. If we now use (7.17) in (7.7) and assume that the background potential temperature gradient is slowly varying, the condition for convective stability is

$$\frac{\partial \theta_0}{\partial z}\left(1 - \frac{\partial \zeta_1}{\partial z}\right) \geq 0. \tag{7.18}$$

The condition for convective stability is now

$$\frac{\partial \zeta_1}{\partial z} \leq 1. \tag{7.19}$$

7.2 SATURATION PARAMETERIZATION SCHEMES

Parameterizations of wave saturation are of two types which can be referred to as either *analytical* or *analog*. Analytical parameterization schemes use mathematical expressions for wave stress and eddy diffusion directly in the model equations (see, for example, Holton, 1982). Analog schemes adjust the flow fields according to saturation theory. In this section we will discuss both types of schemes. Most of these schemes are based on the WKB approximation, and the reader may wish to refer to Section 2.3.

7.2.1 ANALYTICAL PARAMETERIZATION SCHEMES

One of the first analytical parameterizations was proposed by Sawyer (1959). As previously mentioned, early numerical forecast models were based on the quasi-geostrophic approximation, and because of this gravity waves could not be simulated. Sawyer (1959) proposed the use of linear wave theory to evaluate the wave drag over a bell-shaped ridge and assumed that this drag decreased with height in a manner similar to the decrease in the amplitudes of streamline displacements. Thus, he assumed that about half of the drag is exerted on the lowest 3 km of the atmosphere, and the remainder is distributed over the upper troposphere and stratosphere. He proposed the introduction of a force into the equation of motion directed against the low-level wind and decreasing linearly from a maximum near the ground surface to zero at the tropopause. We know now that such a scheme would fail because the wave drag is constant with height, unless wave breaking occurs.

Wave saturation theory assumes that wave breaking results in turbulence. However, turbulence is not passive; it is dispersive. The possibility of turbulence production by breaking gravity waves was posed by Hines (1963), Hodges (1967), and Lindzen (1967). Hodges (1969) suggested that this turbulence could be represented by an *eddy diffusivity*. Thus, vertical diffusion is associated with wave breaking, and we must add this effect to the dynamical equations. Following Holton (1982), we can write

$$\frac{\partial u_0}{\partial t} = -\frac{1}{\rho_0}\frac{\partial}{\partial z}(\rho_0 \overline{u_1 w_1}) + \frac{\partial}{\partial z}\left(D\frac{\partial u_0}{\partial z}\right), \tag{7.20}$$

where D is an eddy diffusivity produced by the wave breaking. The first term on the right-hand side of (7.20) represents the effect of the wave stress, and the second term represents the effect of the Reynolds stress, *i.e.*, the turbulence stress. The eddy diffusion also affects the background temperature, *i.e.*,

$$\frac{\partial \theta_0}{\partial t} = \frac{\partial}{\partial z}\left(D\frac{\partial \theta_0}{\partial z}\right). \tag{7.21}$$

Lindzen (1981) and Holton (1982) investigated this problem and developed expressions for the wave stress convergence and eddy diffusivity, D, in wave-breaking regions. In the discussion here, we rely much on the review paper by Fritts (1984) which presented Lindzen's model in greater detail than the original. Also, note that the notation in those papers has been changed to conform with that used in this book. The zone of application is the middle and upper atmosphere where the WKB approximation is most valid. We make the following assumptions: N^2 is constant, u_0'' is small, H_s is large, and $\Omega = k(c - u_0) \ll kN$. Then, the Taylor–Goldstein equation reduces to the hydrostatic form,

$$\frac{\partial^2 \hat{w}_1}{\partial z^2} + \frac{N^2}{(c-u_0)^2}\hat{w}_1 = 0, \tag{7.22}$$

with the WKB solution

$$\hat{w}_1 = Am^{-1/2}e^{i\int_0^z m\,dz}, \tag{7.23}$$

where A is an unknown amplitude, and

$$m = \frac{N}{c-u_0} \tag{7.24}$$

is slowly varying with height. Note that (7.22) is the equation for freely propagating waves ($c \neq 0$). In applications to the mountain wave problem, we must set $c = 0$, *etc*. The complete solution is

$$w_1(x,z,t) = Am^{-1/2}e^{z/2H_s}e^{i(kx+mz-\omega t)}. \tag{7.25}$$

Using polarization equations (2.24) and (2.25) along with (1.67), we get

$$u_1(x, z, t) = -\frac{m}{k} w_1(x, z, t) \tag{7.26}$$

and

$$\theta_1(x, z, t) = -\frac{i}{k(c - u_0)} \frac{\partial \theta_0}{\partial z} w_1(x, z, t). \tag{7.27}$$

Lindzen (1981) assumed that the vertical variation of θ_1 is dominated by the perturbations e^{imz} in (7.25) so that

$$\frac{\partial \theta_1}{\partial z} = \frac{m}{k(c - u_0)} \frac{\partial \theta_0}{\partial z} w_1. \tag{7.28}$$

If we use (7.24) and (7.25) in (7.28), then the magnitude of $\partial \theta_1 / \partial z$ is primarily

$$\left| \frac{\partial \theta_1}{\partial z} \right| \propto m^{3/2} e^{z/2H_s}. \tag{7.29}$$

The condition for convective stability is given by (7.7), and we see that this condition will be governed by the change of $\partial \theta_1 / \partial z$ with height, since we have assumed that N is constant and by implication $\partial \theta_0 / \partial z$ is either constant or changes very slowly with height. From (7.24) we see that the factor $m^{3/2}$ in (7.29) causes growth if $|c - u_0|$ decreases and causes decay if $|c - u_0|$ increases. If we express $m^{3/2}$ as an exponential, say, e^{az}, then

$$\left| \frac{\partial \theta_1}{\partial z} \right| \propto e^{(a + 1/2H_s)z}. \tag{7.30}$$

In the case $|c - u_0| \to 0$, which does not imply that a critical level is present, $m^{3/2}$ adds to the $1/2H_s$ exponential growth rate an amount of

$$a = \frac{1}{m^{3/2}} \frac{\partial m^{3/2}}{\partial z} = \frac{3}{2} \frac{1}{(c - u_0)} \frac{\partial u_0}{\partial z}, \tag{7.31}$$

so that

$$\left| \frac{\partial \theta_1}{\partial z} \right| \propto e^{((3/2)(1/(c-u_0))(\partial u_0/\partial z) + 1/2H_s)z}. \tag{7.32}$$

Therefore, the eddy diffusion created by wave breaking must be such as to cancel the exponential growth with a rate equal to

$$\frac{1}{2H_s} + \frac{3}{2} \frac{1}{(c - u_0)} \frac{\partial u_0}{\partial z}. \tag{7.33}$$

Using (7.26) in (7.28) gives

$$\frac{\partial \theta_1}{\partial z} = -\frac{u_1}{c - u_0} \frac{\partial \theta_0}{\partial z}, \tag{7.34}$$

and using this in (7.7) gives the condition for convective stability,

$$\frac{\partial}{\partial z}(\theta_0 + \theta_1) = \frac{\partial \theta_0}{\partial z} \left(1 - \frac{u_1}{(c - u_0)}\right) \geq 0. \tag{7.35}$$

Instability occurs when $u_1 > c - u_0$ or

$$u_0 + u_1 > c. \tag{7.36}$$

Thus, wave breaking occurs when the total velocity exceeds the wave phase velocity. For the case of terrain-generated waves, $c = 0$, and we see that wave breaking occurs with flow blocking as discussed in Section 7.1. Lindzen (1981) assumed that convectively unstable regions in the wave field result in the production of turbulence and just that level of eddy diffusion necessary to keep wave amplitudes to values near neutral stability. This is the saturation hypothesis. Wave amplitudes are constrained to values such that the slopes of the flow streamlines are not greater than $\pi/2$ or, equivalently, there are no flow reversals of the type illustrated in Fig. 7.4. It is also assumed that wave saturation does not otherwise affect wave propagation or wave characteristics.

Let wave saturation begin at height z_s. Following Holton (1982), we can use (7.7), (7.25), and (7.28) to show that

$$z_s = 2H_s \ln \left[\frac{k(c - u_0)^2}{AN^{1/2}}\right]. \tag{7.37}$$

As an example, for the case of constant flow over a surface corrugation of amplitude H,

$$z_s = 2H_s \ln \left[\frac{u_0}{NH}\right]. \tag{7.38}$$

For $z > z_s$, the amplitude of the horizontal perturbation velocity is constrained by (7.36) to be

$$|u_s| = |c - u_0|, \tag{7.39}$$

where u_s is the value of u_1 in the saturation zone, say, between z_s and a critical level at height z_c. From (7.26), the amplitude of the vertical velocity is

$$w_s = -\frac{k}{m} u_s = -\frac{k}{N}(c - u_0)^2 \tag{7.40}$$

where we have used (7.24). In the absence of wave saturation, wave amplitudes grow in response to conservation of wave stress in regions of decreasing density, as discussed following (2.38). Following Fritts (1984), we represent the departure of the wave from conservative growth as

$$w_s = w_1 \, e^{-m_i (z - z_s)}, \tag{7.41}$$

where m_i is the imaginary part of a complex vertical wavenumber and w_1 is given by (7.25). Because the difference between w_s and w_1 is not large, we can write

$$\ln\left(\frac{w_s}{w_1}\right) \approx \frac{w_s}{w_1} - 1. \tag{7.42}$$

Using (7.41) in (7.42) gives

$$m_i = \frac{1}{\delta z}\left[1 - \frac{w_s(z_s + \delta z)}{w_1(z_s + \delta z)}\right], \tag{7.43}$$

where $\delta z = z - z_s$. Expanding $w_s(z + \delta z)$ and $w_1(z + \delta z)$ to first order in δz leads to

$$m_i = \frac{1}{w_1(z_s)}\left[\left.\frac{\partial w_1}{\partial z}\right|_{z_s} - \left.\frac{\partial w_s}{\partial z}\right|_{z_s}\right]. \tag{7.44}$$

Using (7.25) and (7.40) in (7.44) gives

$$m_i = \frac{1}{2H_s} + \frac{3}{2}\frac{1}{(c - u_0)}\frac{\partial u_0}{\partial z}, \tag{7.45}$$

and using (7.45), (7.41), and (7.25) gives

$$w_s = A\sqrt{\frac{|c - u_0|}{N}}\, e^{z/2H_s}\, e^{-3/2((z - z_s)/(c - u_0))u_0'}\, e^{i(kx + m_r z - \omega t)}, \tag{7.46}$$

where m_r is the real part of m. Note that the term $u_0'(z - z_s)/(c - u_0)$ is always positive, and so the negative exponential in (7.46) leads to smaller values of w_s as the wave approaches the critical level.

Lindzen (1981) defined an eddy diffusivity for momentum as

$$D\frac{\partial^2 u_0}{\partial z^2} = -m^2 D u_0 \tag{7.47}$$

with a similar equation for θ_0. Then, the linearized form of the horizontal momentum equation is

$$ik(c - u_0)u_1 + w_1\frac{\partial u_0}{\partial z} = -m^2 D u_1. \tag{7.48}$$

Now assume a complex phase velocity, and then the real part of (7.48) is

$$kc_i = -m^2 D. \tag{7.49}$$

From (7.24) we have

$$m_r + im_i = \frac{N}{c - u_0}, \tag{7.50}$$

and the imaginary part of (7.50) is

$$m_i \approx -\frac{Nc_i}{(c - u_0)^2}. \tag{7.51}$$

Using (7.45), (7.49), and (7.51), the eddy diffusivity is

$$D = \frac{k}{N^3}(c - u_0)^4 \left[\frac{1}{2H_s} + \frac{3}{2}\frac{1}{(c - u_0)}\frac{\partial u_0}{\partial z}\right]. \tag{7.52}$$

Note that because eddy dissipation must be positive, there exists the possibility that (7.52) is nonphysical if $(c - u_0)$ and $\partial u_0/\partial z$ are of opposite signs. However, if a critical level is present, then from (7.56) we see that $(c - u_0)$ and $\partial u_0/\partial z$ are always of the same sign, and $D \to 0$ as $z \to z_c$.

We now calculate the wave stress. Using (7.39) and (7.40), the wave stress in the saturation zone is

$$-\rho_0 \overline{u_s w_s} = \frac{1}{2}\rho_0 \Re u_s w_s^* = -\frac{1}{2}\rho_0 \frac{k}{N}(c - u_0)^3. \tag{7.53}$$

Using (7.53) in (7.1) and assuming that N is constant or slowly varying gives

$$\frac{\partial u_0}{\partial t} = -\frac{k}{N}(c - u_0)^3 \left[\frac{1}{2H_s} + \frac{3}{2}\frac{1}{(c - u_0)}\frac{\partial u_0}{\partial z}\right]. \tag{7.54}$$

The first term in brackets comes about as a response to exponential growth, and the second term balances the $m^{3/2}$ growth term and is a function of whether the mean wind shear is positive or negative. In a flow where $c - u_0$ is constant or varies little, the induced acceleration is constant,

$$\frac{\partial u_0}{\partial t} = -\frac{k}{2NH_s}(c - u_0)^3. \tag{7.55}$$

In a sheared environment, the induced acceleration is not constant and is governed by $(c - u_0)$. If a critical level exists, and if the wave is approaching it from below, then

$$\frac{\partial u_0}{\partial z} \approx \frac{c - u_0}{z_c - z}. \tag{7.56}$$

Using this in (7.54) we see that as the critical level is approached the induced acceleration is proportional to $(c - u_0)^2$ and is always negative. Comparing (7.52) with (7.54) we see that the induced flow acceleration due to wave stress is

$$\frac{\partial u_0}{\partial t} = -\frac{N^2}{c - u_0} D. \tag{7.57}$$

As pointed out by Fritts (1984), (7.57) would suggest that the induced acceleration produced by saturation and the eddy diffusion responsible for wave dissipation are related; however, Lindzen (1981) points out that these two effects addressed by the simple linear model while related are separate manifestations of gravity wave saturation.

To scale the induced acceleration, Fritts (1984) gives the following example. We consider at mesospheric heights a uniform flow, with isothermal scale height $H_s = 6$ km, Brunt–Väisälä frequency $N = 0.02$ s^{-1}, intrinsic phase velocity $c - u_0 = 30$ m s^{-1}, and horizontal wave length $\lambda_x = 200$ km. From (7.52), the eddy diffusivity $D = 265$ m^2 s^{-1}. Using (7.57), the induced flow acceleration is

$$\frac{\partial u_0}{\partial t} = -305 \text{ m s}^{-1} \text{ day}^{-1}. \tag{7.58}$$

This is a substantial reduction in the zonal wind, and such a reduction in velocity has not been observed. However, if the gravity waves were generated by terrain, then this deceleration would be confined to regions directly above the mountain. However, even if limited to a small region, it is reasonable that such a deceleration would have some impact on the global scale. Therefore, it is reasonable to think that this effect must be compensated by an acceleration of similar magnitude. A likely possibility proposed by Lindzen (1981) is the *Coriolis acceleration* produced by the meridional wind, v_0, *i.e.*,

$$\frac{\partial u_0}{\partial t} = 2\Omega_E \sin \Phi v_0 = -305 \text{ m s}^{-1} \text{ day}^{-1}, \tag{7.59}$$

where Ω_E is the angular velocity of the Earth, Φ is the latitude, and v_0 is the meridional wind. Solving for v_0 gives

$$v_0 \approx -\frac{24 \text{ m s}^{-1}}{\sin \Phi}. \tag{7.60}$$

Nastrom, Balsley, and Carter (1982) showed observations of mean meridional wind near the *mesopause* at Poker Flat, AK (65°N) for the summer season. Values of v_0 ranged between approximately -10 and -30 m s^{-1}. From (7.60), v_0 at 65°N is about -26.5 m s^{-1}. This agreement between the theoretical estimates and observations seems to support the validity of the wave saturation mechanism.

7.2.2 ANALOG PARAMETERIZATION SCHEMES

While the analytical parameterizations are both elegant and physically consistent, they do not lend themselves easily to operational forecast models. These types of models are limited by the number of grid cells and execution times. Many models of the general circulation solve the primitive equations of motion in terms of *vorticity* and *divergence* (see, for example, Holton, 1992; Pedlosky, 1979), which do not lend themselves to analytical expressions for eddy dissipation and wave drag. Thus, indirect techniques to account for wave saturation are required. Wave stress must be calculated "off line" as illustrated in Fig. 7.5. At the end of a computational time step and before the next time step, say, at time step $t + 1/2$, the vertical profiles of the newly calculated background wind speed and temperature are put into a wave saturation model where they are used to calculate the wave stress profile $\tau(z)$. The time step is completed by updating the wind speed, *i.e.*,

$$u_0(z, t) = u_0(z, t + 1/2) + \frac{1}{\rho_0}\frac{\partial \tau}{\partial z}\Delta t, \tag{7.61}$$

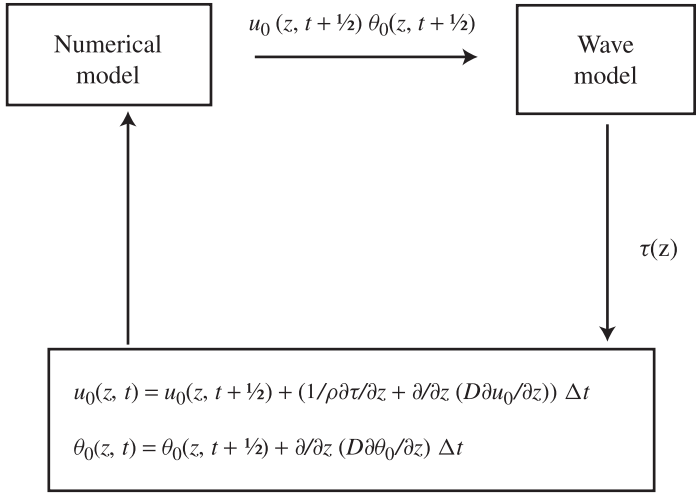

FIGURE 7.5 Schematic diagram of an off-line wave saturation parameterization.

where Δt is the size of the time step. If an eddy diffusivity, D, is calculated, then this contribution can be included in the momentum and the temperature equations, *i.e.*,

$$u_0(z,t) = u_0(z, t+1/2) + \left[\frac{1}{\rho_0}\frac{\partial \tau}{\partial z} + \frac{\partial}{\partial z}\left(D\frac{\partial u_0}{\partial z}\right)\right]\Delta t \tag{7.62}$$

and

$$\theta_0(z,t) = \theta_0(z, t+1/2) + \frac{\partial}{\partial z}\left(D\frac{\partial \theta_0}{\partial z}\right)\Delta t. \tag{7.63}$$

7.2.2.1 The Palmer Method

In order to improve the performance of the Meteorological Office 15-layer operational forecast model and 11-layer general circulation model, Palmer, Shutts, and Swinbank (1986) accounted for subgrid-scale terrain effects by implementing wave saturation theory. Using (3.33) and (7.34), the local Richardson number (6.80) is

$$R_i = \frac{g}{\theta_0}\frac{(\partial\theta_0/\partial z)(1 - \partial\zeta_1/\partial z)}{(\partial u_0/\partial z)^2\,[1 + (\partial u_1/\partial z)/(\partial u_0/\partial z)]^2}, \tag{7.64}$$

where ζ_1 is the vertical displacement of a flow streamline defined by (7.14). Defining $R_{i,0}$ as the background Richardson number, we can write (7.64) as

$$R_i = R_{i,0}\frac{(1 - \partial\zeta_1/\partial z)}{(1 + (R_{i,0}^{1/2}/N)(\partial u_1/\partial z))^2}. \tag{7.65}$$

Using (7.28) and (3.33) it is easily shown that

$$u_1 = -u_0\frac{\partial \zeta_1}{\partial z} = -iu_0 m\zeta_1. \tag{7.66}$$

From (6.83) we see that the local or wave-modulated R_i is a nonlinear function of wave phase, and from Fig. 6.10 we see that instability occurs over only a limited range of the wave field. Palmer, Shutts, and Swinback (1986) argued that ultimately the parameterization seeks to account for the ensemble subgrid-scale effects of terrain features on various space scales. The effects of these "phase-incoherent subgrid-scale gravity waves" are parameterized by ignoring the phase differences in (6.83). Then, using (7.66) in (7.65) gives

$$R_{i,min} = R_{i,0}\frac{1 - N|\zeta_1|/u_0}{\left[1 + R_0^{1/2}(N|\zeta_1|/u_0)\right]^2}, \tag{7.67}$$

where $R_{i,min}$ represents the smallest value of the Richardson number that can be realized under the action of gravity waves. The free parameter in (7.67) is the wave

displacement $|\zeta_1|$. Thus, (7.67) provides the mechanism for parameterizing wave saturation. This is done by controlling the value of $|\zeta_1|$ so the $R_{i,min} \geq 1/4$. For example, if an upward-propagating gravity wave enters a region of decreasing wind speed and/or increasing stratification, then the quantity $N|\zeta_1|/u_0$ will increase and $R_{i,min}$ will decrease. Decreasing $|\zeta_1|$ will balance the increase in N/u_0 so that $R_{i,min} \geq 1/4$, but this adjustment also leads to a decrease in wave stress. Thus, the effects of wave saturation are parameterized. Note that Palmer, Shutts, and Swinbank (1986) used the dynamic stability condition $R_{i,min} \geq 1/4$ for the wave saturation criterion. This limit was chosen to account for large isotropic displacements which could induce Kelvin–Helmholtz instability.

Under the WKB approximation, the wave stress over sinusoidal topography is given by (3.106). Palmer, Shutts, and Swinbank (1986) assumed that the stress in the surface layer of the model, τ_s, is directed against the surface-layer wind and is given by

$$\tau_s = \rho_0 \kappa N u_0 \sigma_H^2, \tag{7.68}$$

where σ_H is the root mean square value of the subgrid-scale topography and κ is a "tunable" parameter which accounts for the fact that subgrid-scale topography is not represented by a single wavenumber. They use $\kappa = 2.5 \times 10^{-5}$ m^{-1}, which corresponds to a wavelength of 250 km if the topography is sinusoidal. In the absence of wave dissipation, $\tau(z) = \tau_s$. In the case of wave dissipation, it is assumed that the direction of the wave stress will still be against the surface-layer wind. The wave stress at any level above the surface layer is given by

$$\tau(z) = \rho_0 \kappa N U_0 |\zeta_1|^2, \tag{7.69}$$

where U_0 is the component of the background wind parallel to the surface-layer wind.

The analog parameterization begins with the calculations of surface-layer stress (7.68) in each model grid cell. At the next layer, $R_{i,0}$ is calculated using the values of N, u_0, and v_0 at adjacent vertical levels. Then assuming that $\tau = \tau_s$, $|\zeta_1|$ is calculated using (7.69). This value is then used in (7.67) to evaluate $R_{i,min}$. If $R_{i,min} \geq 1/4$, then τ is unchanged, and we proceed to the next upper layer. The preceding steps are repeated layer by layer, always initially setting the stress equal to the stress in the adjacent lower layer. If $R_{i,min}$ remains about one-fourth, then the wave stress remains constant and at its surface value. However, if this criterion is not met at a certain layer, then $R_{i,min}$ is set equal to one-fourth, and (7.67) is used to calculate a new displacement, which we call $|\zeta_1|_{sat}$. The wave stress for the layer is then calculated using (7.69), but now with $|\zeta_1|_{sat}$ used in place of $|\zeta_1|$. This new value of stress is called τ_{sat}. We now go to the next upper layer and proceed as before, with the initial estimate of displacement calculated using (7.69) but now using τ_{sat} calculated for the adjacent lower layer. When the top model layer has been reached, we have a vertical profile of wave stress which can then be used to update the velocity fields in each grid cell.

7.2.2.2 The Schoeberl Method

The parameterization schemes discussed thus far assume that wave growth stops when the saturation condition is satisfied. However, Schoeberl (1988), citing the work of Fritts and Dunkerton (1984), argues that wave growth does not immediately stop with the onset of wave breaking. As we discussed with regards to Fig. 6.10, dynamic and convective instability first occur over a limited range of the wave field. Thus, the Reynolds stress produced by breaking waves may be different than that calculated with the assumption of constant wave amplitude. As an alternative procedure, Schoeberl (1988) presented a scheme where the flow streamlines are adjusted locally rather than globally, *i.e.*, over the whole wave. The WKB solution to the Taylor–Goldstein equation along with (3.33) is

$$\hat{\zeta}_1(z,k) = \hat{\zeta}_1(0)\left(\frac{m(0)}{m(z)}\right)^{1/2} e^{i\int m\,dz}, \tag{7.70}$$

where $\hat{\zeta}_1(0)$ is the Fourier-transformed streamline displacement at the ground surface and $m(0) = N(0)/u_0(0)$ is the vertical wavenumber at the ground surface. The saturation parameterization scheme consists of evaluating (7.70) upward layer-by-layer with the constraint that the flow be convectively stable. The WKB solution is constructed at each model level according to

$$\hat{\zeta}_1(z+\Delta z,k) = \hat{\zeta}_1(z,k)\left(\frac{m(z)}{m(z+\Delta z)}\right)^{1/2} e^{i\int_z^{z+\Delta z} m\,dz}. \tag{7.71}$$

This so-called *streamline adjustment* algorithm begins at the ground surface or, equivalently, at the model surface layer where $\hat{\zeta}_1(0)$ is evaluated. Then (7.71) is used to carry the solution to the next upper level, z_1, where $\hat{\zeta}_1(z_1) = \hat{\zeta}_1(0)$. Next, the inverse Fourier transform of $\hat{\zeta}_1(k,z)$ gives the streamline displacement in physical[2] space, $\zeta_1(x,z)$. This value is used in (7.19) to test the stability in the subgrid domain. If the layer is stable, then the solution is carried to the next layer. If the layer is unstable, then $\partial\zeta_1/\partial z$ is set to unity, and the new displacement is given by

$$\zeta_1(x,z+\Delta z) = \zeta_1(x,z) + \Delta z. \tag{7.72}$$

When all of the points in the wave field have been adjusted, the displacement is Fourier transformed into wave space, and (7.71) is used to carry the solution to the next layer. Figure 7.6 illustrates the adjustment process, and we see that convective adjustment is done only to part of the wave field and does not initially limit wave growth, as shown in Fig. 7.7 which displays potential temperature isotherms as function of altitude. In Fig. 7.7 we see that in regions of convective adjustment, the

[2] Note that the streamline displacement in physical space, $\zeta_1(x,z)$, is a function of along-wind distance, x. Obviously, since we are working toward a subgrid-scale parameterization, this distance must also be on the subgrid scale, a point not discussed in Schoeberl (1988).

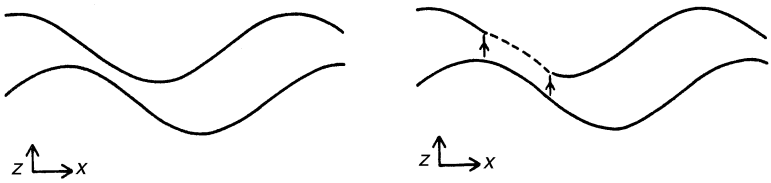

FIGURE 7.6 Schematic illustration of the convective adjustment process. Only a part of the wave is adjusted so that $(\partial \eta_1 / \partial z) \leq 1$. (From "A model of stationary gravity wave breakdown with convective adjustment," M.R. Schoeberl, *J. Atmos. Sci.*, **45**: 987, 1988.)

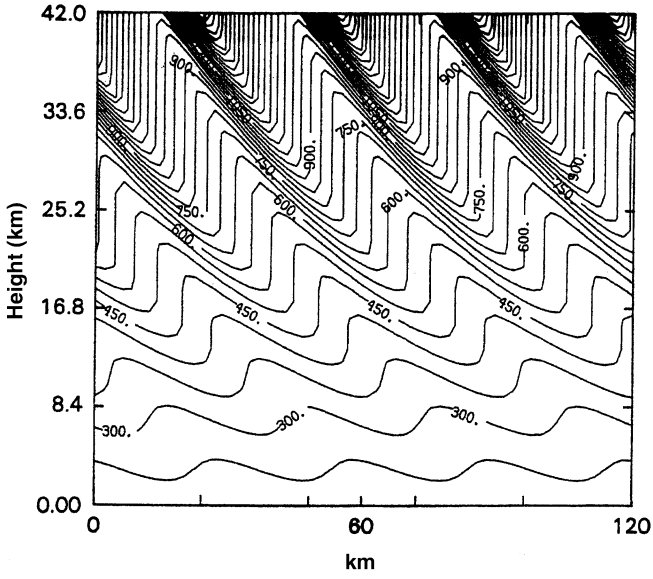

FIGURE 7.7 Potential temperature isotherms with convective adjustment over a surface corrugation. Wave breaking begins at about 14 km. (From "A model of stationary gravity wave breakdown with convective adjustment," M.R. Schoeberl, *J. Atmos. Sci.*, **45**: 985, 1988.)

slopes of the isotherms become vertical as indicated by (7.8). We also see that wave amplitude continues to grow even when convective adjustment is occurring. If the wave encounters a region of the atmosphere where saturation does not occur, then wave amplitude growth ends; however, the vertically oriented slopes of the wave remain unchanged. Figure 7.8 plots the variation of displacement amplitude with height for the case shown in Fig. 7.7. For conventional saturation theory (Hodges, 1967), displacement amplitude is constant after the start of wave breaking; however, convective adjustment results in displacements which continue to grow after wave breaking, but at a decreasing rate. The dashed line in Fig. 7.8 shows the result without wave saturation. The continued growth of wave amplitudes after wave breaking is referred to as *supersaturation* (Lindzen, 1987).

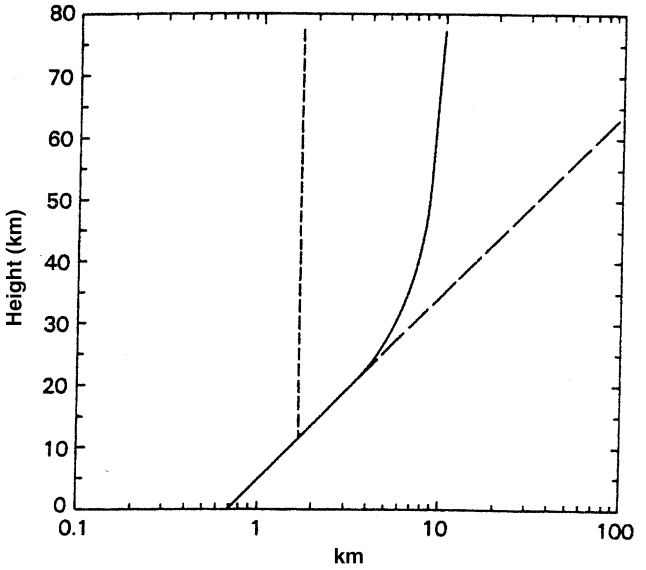

FIGURE 7.8 Displacement amplitude as a function of height for the experiment shown in Fig. 7.7. The dotted line shows results using saturation theory, the solid line shows the results using streamline adjustment saturation parameterization, and the dashed line shows result of no adjustments. (From "A model of stationary gravity wave breakdown with convective adjustment," M.R. Schoeberl, *J. Atmos. Sci.*, **45**: 986, 1988.)

7.2.2.3 The Terrain Height Adjustment Scheme

The preceding wave saturation parameterization schemes made use of the WKB approximation which is applicable to the middle and upper atmosphere. However, in the lower troposphere and especially in the planetary boundary layer, vertical wavelengths are not necessarily small compared to background variations. For example, consider the vertical wavelength of a terrain-generated wave when the background wind and stratification are constant,

$$\lambda_z = \frac{2\pi}{m} = 2\pi \left(\frac{N^2}{u_0^2} - k^2 \right)^{-1/2} . \tag{7.73}$$

While (7.73) applies only for the case where N and u_0 are constants, we can still use it for scaling. Let the terrain feature have a horizontal scale b such that $k = 1/b$. Then, with $u_0 = 5\,\mathrm{m\,s^{-1}}$, $N = 0.03\,\mathrm{s^{-1}}$, and $b = 1000\,\mathrm{m}$, $\lambda_z \approx 1050\,\mathrm{m}$. A scale for the vertical variation boundary-layer flow is the Ekman layer depth, z_E, given by (4.81). Using the typical boundary-layer values of $5\ \mathrm{m\ s^{-2}}$ for the eddy coefficient of friction (EKF) and $f = 10^{-4}\ \mathrm{s^{-1}}$, $z_E \approx 1000$ m, which is on the same order as vertical wavelength of the terrain-generated wave. We also

note that within the stable boundary layer the vertical gradient of potential temperature changes with height, especially near the ground surface. Thus, gravity waves generated in the boundary layer and lower troposphere can be expected to have reflection levels. Because the background winds turn with height in the boundary layer, we can anticipate that there will be critical levels in the boundary layer (Nappo and Chimonas, 1992). Critical levels can also be the result of frontal systems, density currents, thunderstorm gust fronts, *etc*. For example, Fig. 7.9 shows the wind and temperature fields in the nighttime planetary boundary layer constructed from instrumented aircraft flights over moderately complex topography in central Oklahoma. During these flights, a northerly surface flow undercut a less stable southerly flow. In Fig. 7.9 we see regions of high turbulence (regions of vertical velocity variance greater than 0.01 $m^2\ s^{-2}$) centered in regions of wind reversals. For terrain-generated flows, critical levels occur at wind reversals, *i.e.*, where $u_0 = 0$. However, strictly speaking, the WKB is not applicable near a critical level. Thus, streamline adjustment parameterization schemes are not expected to work well, if at all, in the lower troposphere.

In an effort to account for wave saturation effects in the nighttime planetary boundary layer over complex terrain, Nappo and Physick (2000) proposed an alternative to streamline adjustment. For simplicity and reduced computer time, subgrid-scale terrain features are represented by one cycle of a surface corrugation. In physical space, this cycle ranges over a series of subgrid "grid points." The amplitude and horizontal wavelength of the corrugation is chosen to best represent the wave stress over the real terrain feature in the presence of constant wind and stratification. At each model level, wave breaking is determined by the flow blocking criterion (7.12) rather than (7.7). This saves computer time because vertical derivatives of $\zeta_1(x, z)$ need not be calculated at every subgrid point; also, (7.20) is more accurate because finite differencing of the vertical derivative of ζ_1 is not done. At the end of each model time step, the blocking condition is tested level by level at each subgrid point according to

$$\left| \frac{u_1(x, z)}{u_0(z)} \right| \leq 1. \tag{7.74}$$

From (3.31) we see that u_1 is proportional to H, the amplitude of the surface corrugation, and from (3.105) we see that the wave stress is proportional to H^2. If (7.74) is not satisfied, then H is incrementally reduced until it is. The reevaluation of u_1 is trivial since the computer solution of the Taylor–Goldstein equation (see Chapter 9) is based on a nondimensional vertical velocity shape function. Thus, the shape function needs only to be multiplied by H to evaluate u_1. This flow blocking adjustment proceeds upward level by level. With each adjustment, the terrain height is reduced, and this also causes the wave stress, $\tau(z)$, to be reduced. If flow blocking does not occur, then H is not reduced, and the wave stress is unchanged from its value calculated at the adjacent lower level. If there is continued wave breaking with height, then H will eventually be reduced to zero. In this case, the

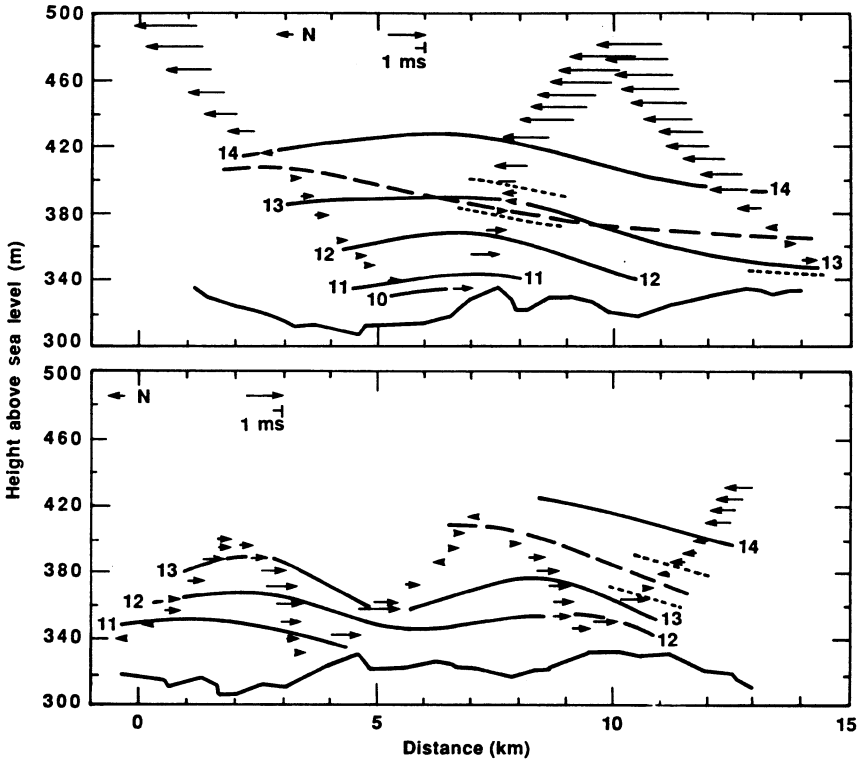

FIGURE 7.9 Two cross-sections of low-level airflow constructed from aircraft data taken with two similar undulating flight tracks. The lower solid line in each figure marks the terrain surface. Solid lines are isotherms of potential temperature (°C), and dotted lines enclose regions of vertical velocity variance greater than 0.01 $m^2\ s^{-2}$. (From "Vertical structure and turbulence in the very stable boundary layer," L. Mahrt, *J. Atmos. Sci.*, **42**: 2337, 1985.)

wave has been completely dissipated, and the wave stress is zero for all the upper levels. When the flow adjustment has been completed, the wave stress profile is used to update the background wind fields according to (7.61). If a critical level exists, then it is assumed that the wave will be completely absorbed in the layer containing the critical level. Then, the wave stress is decreased linearly from its value where wave breaking first occurs to zero at the model level just above the critical level. Figure 7.10 shows the effect of this saturation algorithm for the same experiment shown in Fig. 7.2. The convectively unstable regions seen in Fig. 7.2 do not appear in Fig. 7.10. Figure 7.11 shows the vertical profiles of wave stress and the changes in the amplitude of the surface corrugation made during the saturation adjustment for the experiment shown in Fig. 7.10. The wave-breaking region seen in Fig. 7.11 is between about 350 and 500 m. From Fig. 7.3, we see that this is a region of strong shear and curvature in the wind speed profile. Because the background wind speed is constant above the breaking level, the displacements of

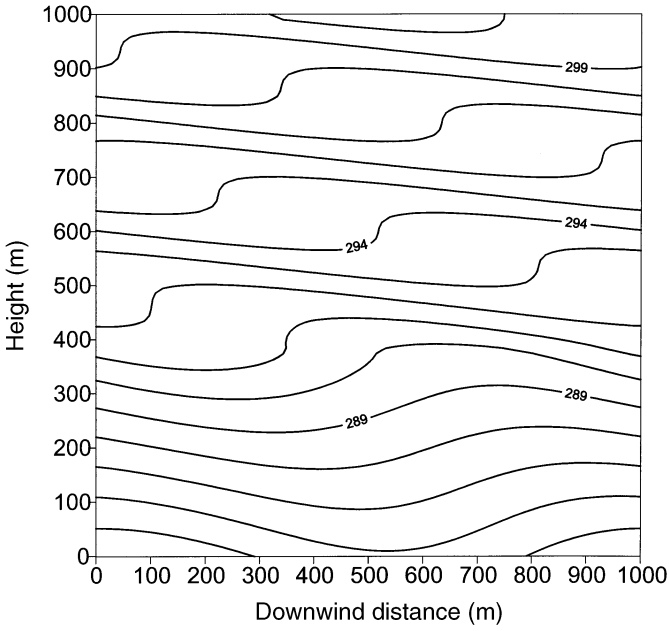

FIGURE 7.10 The same experiment as shown in Fig. 7.2, but now with terrain-height adjustment saturation parameterization.

the streamlines at higher elevations remain at the adjusted values. If the wind speed continued to change, then additional saturation adjustments to the streamlines would be required. The results shown in Fig. 7.10 appear more physically realistic than those shown in Fig. 7.2.

7.3 SATURATION LIMITS AND OTHER PROBLEMS

Linear saturation theory and the parameterization schemes discussed in this chapter have limitations and omissions. Fritts (1984) listed several shortcomings, for example, neglect of wave superposition and interaction, wave transience and horizontal localization, quasi-linear mean-flow accelerations, and the detailed nature of the saturation process, that may not be justified in general. McFarlane (1987) noted several deficiencies in parameterization schemes, including the failure to account for the orientation of the surface-layer winds relative to the terrain and the neglect of nonlinearity. Miller, Palmer, and Swinbank (1989) enhanced the Palmer, Shutts, and Swinbank (1986) scheme by introducing directionally dependent subgrid-scale orographic variance, and this led to significant improvements in forecast skill and reduction in model systematic errors. As shown by Smith (1977), nonlinearity and nonlinearity in the bottom boundary condition can lead to enhanced wave steeping in some vertical regions while suppressing

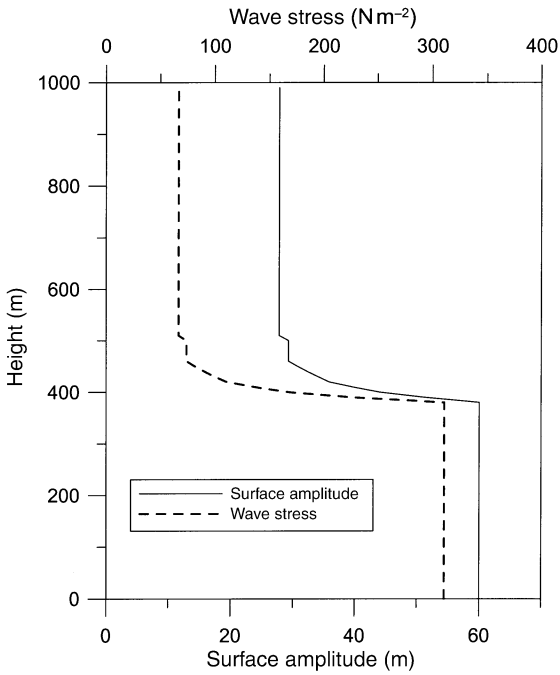

FIGURE 7.11 Vertical profile of wave stress and variation of surface amplitude resulting from the terrain-height adjustment wave saturation parameterization scheme used in the experiment shown in Fig. 7.10.

steepening in others. This can have a pronounced effect on wave saturation which would be missed in linear theory. McFarlane (1987) also pointed out that the failure to account for wave reflection because of the use of the WKB approximation negates the possibility of simulating wave resonance and wave amplification effects observed by Lilly and Zipser (1972) and Lilly (1978) and numerically studied by Peltier and Calrk (1979). Schoeberl (1988) noted that the schemes developed for general circulation models by Palmer, Shutts, and Swinbank (1986) and McFarlane (1987) should not be used to discriminate between various subgrid-scale processes because of the parameterization's crude estimates of breaking heights and induced acceleration. He pointed out that these schemes are not accurate enough representations for even idealized definitive conclusions about the influence of topography on the general circulation.

Saturation parameterization schemes developed for general circulation and forecast models usually represent subgrid orography in terms of a sinusoidal function. However, stratified flows over real ridges and mountains are much more complex (Baines, 1995). Kim and Mahrt (1992) compared calculated with observed wave stress over a coastal mountain range in Croatia. They pointed out that stable flows over two-dimensional ridges are influenced by terrain-induced

disturbances such as the blocking of low-level flow, the development of turbulent boundary layers, and the formation of stagnant cold air pools in topographic depressions. These effects act to limit the vertical displacements of streamlines near the ground surface so that the *effective height* of the obstacle is less than its real height. Stern and Pierrehumbert (1988) proposed that the effective height, H_e, is

$$H_e = \min\left[H, c\frac{u_0(0)}{N(0)}\right], \tag{7.75}$$

where H is the real terrain height, $u_0(0)$ and $N(0)$ are surface-layer values of wind speed and Brunt–Väisälä frequency, and c is a constant estimated to be between 0.4 and 0.8. Lott and Miller (1997) developed an orographic drag parameterization for subgrid-scale, three-dimensional objects based on the ideas presented by Baines and Palmer (1990). Figure 7.12 illustrates the low-level flow behavior over an elliptically shaped mountain. The non-dimensional height of the mountain, H_n, is taken to be

$$H_n = \frac{HN}{|U|}, \tag{7.76}$$

where U is the scale speed of the incident flow. H_n corresponds to an inverse internal Froude number. For small H_n, all the flow goes over the mountain, and the effective height for gravity wave generation is H. However, for large H_n there is insufficient energy of the incident flow to overcome the buoyancy, and part of the low-level flow goes around the mountain. Then, as shown in Fig. 7.12, the effective height of the mountain is $H - z_b$, where z_b is the depth of the blocked layer. For constant U and N,

$$z_b = H \max\left(0, \frac{H_n - H_{nc}}{H_n}\right), \tag{7.77}$$

where H_{nc} is a critical nondimensional height of order unity.

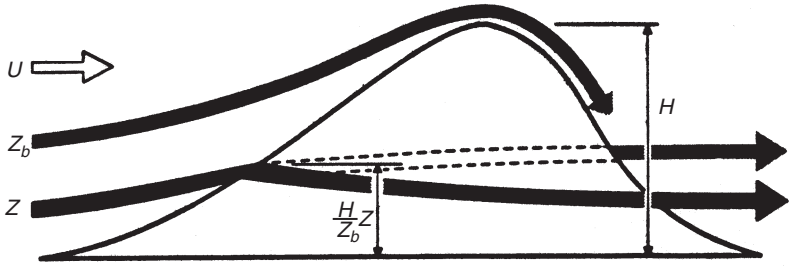

FIGURE 7.12 Schematic representation of the low-level flow behavior over a three-dimensional obstacle. (From "A new subgrid-scale orographic drag parameterization: its formulation and testing," F. Lott and M.J. Miller, *Q. J. R. Meteorol. Soc.*, **123**: 103, 1997.)

A current important problem is the parameterization of stress carried by convectively generated gravity waves in general circulation models (see, for example, Chun *et al.*, 2001 and references therein). The problem is complicated because it requires a cumulus cloud parameterization, and these schemes require the model atmosphere to be conditionally unstable. Thus, a difficulty arises in attempting to account for internal gravity waves in an unstable flow. Chun and Baik (1998) pointed out that above the cloud top height internal gravity waves can propagate and affect the larger scale flow. They proposed that convection-induced gravity wave momentum flux be considered in the region above the cloud top height, but not considered inside the cloud region.

8

Observational Techniques

Thus far, this book has dealt mostly with theoretical issues. However, this information is meaningful only if it can be used in some real sense. The first step in this process is the ability to observe gravity waves. However, from the start we have a problem because we cannot observe gravity waves. We can only observe the effects of these waves. It is only through an analysis of these observed effects that we can begin to perceive waves. These data analyses are based on what we know about wave behavior, and for the most part this is limited to the linear theory. It often happens that the waves detected through these analyses do not agree with linear theory. In these cases, we often assume that the waves are nonlinear. However, it may be that the apparent nonlinearity is, in fact, due to errors in the observations. Thus, the study of real waves in the atmosphere is a daunting task, and this may explain why the majority of published studies of gravity waves are of a theoretical nature.

In Chapter 2, we saw that a linear wave field is specified to within an undetermined wave amplitude when we know the dispersion relation, $\omega(\vec{\kappa})$. Thus, the objectives of all gravity wave observations are the estimations of wave frequency and wavenumber or, equivalently, phase speed and wavelength. While this

specification seems at first glance straightforward, in practice it is not. The problem lies in the fact that we can observe only perturbations of wind speed and direction, temperature, density, pressure, trace gas and aerosol concentrations, and streamline displacements. The observations that can be made are determined by the characteristics of the instrument and its platform. The instrument may measure *in situ* or *remotely*, and the platform may be stationary or moving. The analyses of these data are limited by how the measurements were made. For example, a radiosonde or an upward-looking radar can be used to estimate the vertical structure of a wave field, but the horizontal characteristics of the wave, *i.e.*, wavelength and phase velocity, can be estimated only by indirect means. A horizontal array of sensors can be used to estimate horizontal phase speed and wavenumber directly, but the vertical structure of the wave cannot be determined. Generally, obtaining the entire wave field from a single measuring technique is not possible.

Gravity wave characteristics must be estimated by measuring perturbations to the mean atmospheric flow. Measurements include (1) ground-based meteorological observations of wind speed, wind direction, temperature, and pressure; (2) vertical profiles of wind speed and temperature derived from tall towers, captured balloons, kites, sounding balloons, rocket sondes, and remote sensors; (3) horizontal fields of vertical velocity and temperatures derived from instrumented aircraft, constant volume balloons, and remote sensors; (4) images of clouds captured by high-altitude aircraft flights and satellites; and (5) images of wave perturbations of the nighttime sky glow. All of these types of measurements have been used to some degree in analyses of gravity waves.

8.1 SINGLE-STATION OBSERVATIONS

Observations made at a geographical point or within a vertical column above a fixed point will be considered as *single-station* observations. Examples of single-station observations include *in situ* time-continuous meteorological measurements made near the ground surface and above the ground surface using masts, tall towers, kites, and captured balloons; time-discrete measurements made by radiosondes, rawinsonde, and tethersondes; and time-continuous measurements of vertical and horizontal velocity made by upward-directed remote sensors.

8.1.1 GROUND-BASED METEOROLOGICAL MEASUREMENTS

Operational, ground-based meteorological measurements are generally made in support of weather forecasting, airport operations, fire hazard, *etc.* These observations usually include horizontal wind speed and direction, temperature, relative humidity, surface pressure, precipitation, visibility, *etc*. Except for large-amplitude, solitary-wave disturbances of the type described, for example,

by Rottman and Einaudi (1993), gravity wave perturbations are generally not detected by these types of measurements because the instrument sensitivities and reporting frequency are too low. For example, from the *Federal Meteorological Handbook No. 1*, we see that the wind direction is determined by averaging the direction over a 2-min period, and the direction is reported in tens of degrees with reference to true north. Also from the handbook we note that, "When the wind direction sensor(s) is out of service, at designated stations, the direction may be estimated by observing the wind cone or tee, movement of twigs, leaves, smoke, *etc.*, or by facing into the wind in an unsheltered area." We also see from that handbook that the wind speed shall be determined by averaging the speed over a 2-min period, and at designated stations, a table shall be used to estimate wind speeds when instruments are out of service or the wind speed is below the starting speed of the anemometer in use. This table relates wind speed ranges to events, for example, such as "smoke rises vertically" = calm wind; "wind felt on face, leaves rustle" = 4–6 knots (kn); "wind raises dust and loose paper, small branches moved" = 11–16 kn, *etc*. These observations are generally reported every 3 hours. It is clear that these data would not be helpful in gravity wave analyses.

Gravity wave analyses using ground-based observations require research-grade instrumentation, and the sampling rates of the data should scale with the frequency of the waves under consideration. For high-frequency waves in the atmospheric boundary layer, sampling rates of at least 0.1 Hz should be used. For lower frequency mesoscale gravity waves, the sampling rates can be much lower. These data should include static pressure with a precision of at least 0.1 mb and wind speeds with a precision of 0.1 m s^{-1}. Sonic anemometers should be used when possible. Examples of ground-based meteorological observations of gravity waves can be found, for example, in Gossard and Munk (1954), Bosart and Cussen (1973), Gossard and Sweezy (1974), Gossard and Hooke (1975), Bosart and Sanders (1983), and Koch and Golus (1988). Observations made on tall towers can be used to determine the vertical structure of the wave field (see, for example, Caughey and Readings, 1975; Finnigan and Einaudi, 1981; De Baas and Driedonks, 1985). In Chapter 9 we shall discuss how these observations can be used to estimate wave parameters.

8.1.2 FREE-BALLOON SOUNDINGS

Free-balloon soundings include *radiosondes* and *rawinsondes*. A radiosonde is a balloon-borne instrument for the simultaneous measurement and transmission of pressure, temperature, and humidity. A rawinsonde is a method of upper air observation consisting of an evaluation of the wind speed and direction, temperature, pressure, and relative humidity aloft by means of a balloon-borne radiosonde tracked by a radar or radio direction finder. Today, some rawinsondes use global positioning systems instead of being tracked by radar. Corby (1957) suggested that observed periodic variations of a few meters per second of the vertical velocities of ascending radiosondes could be related to atmospheric gravity waves. Reid (1972)

improved Corby's analysis method by relating departures of the vertical velocity of the airsonde from a mean value to changes in the gradient of the pressure trace which were automatically recorded on a paper chart. Typical changes in the vertical velocities were about 1 m s^{-1}. Lalas and Einaudi (1980) tested the ability of operational rawinsonde data to observe gravity waves in the troposphere. To couple the observed motion of the balloon with the gravity wave (observed by Doppler radar and a microbarograph array), the vertical position of the balloon, $z(t)$, was obtained by interpolation of its reported height, which was once per minute, and the horizontal position was obtained by integrating the kinematic equation of motion,

$$\frac{dx}{dt} = u(z,t) = u_0[z(t)] + u_1[x(t), z(t), t : \phi_0], \tag{8.1}$$

where ϕ_0 is the initial phase of the wave. The motivation for this study was, in part, to devise a method for determining the climatology of tropospheric gravity waves. Shutts, Kitchen, and Hoare (1988) analyzed a large-amplitude gravity wave in the lower stratosphere detected by a radiosonde launched from Shanwell, UK. Figure 8.1 shows the ascent profiles where we can clearly see pronounced

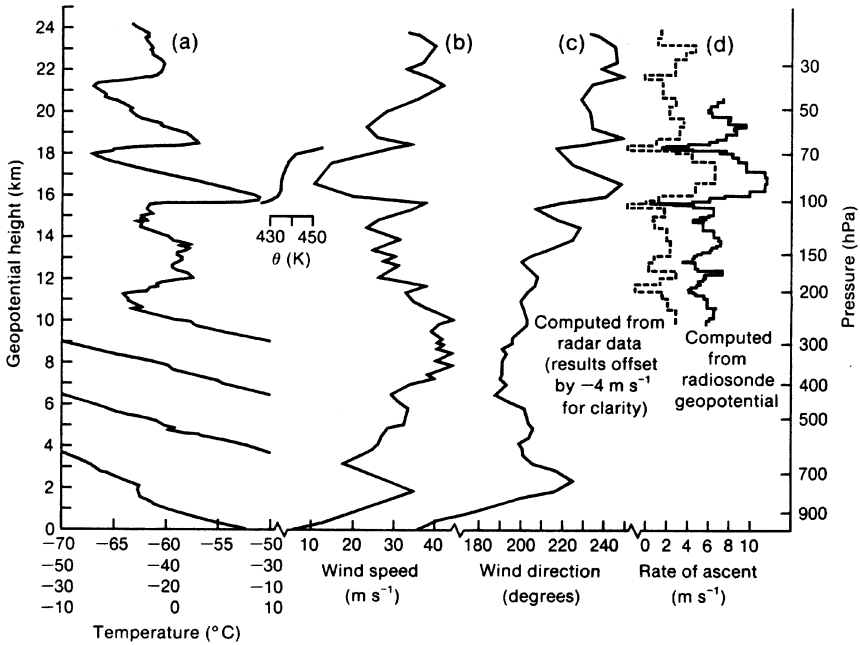

FIGURE 8.1 Radiosonde ascent profiles at Shanwell, 2318 GMT December 12, 1986: (a) temperature and potential temperature; (b) wind speed; (c) wind direction; (d) ascent rate, computed from the geopotential (solid line) and radar data (dashed line) and offset by −4 m s^{-1}. (From "A large amplitude gravity wave in the lower stratosphere detected by radiosonde," G.J. Shutts, M. Kitchen, and P.H. Hoare, *Q. J. R. Meteorol. Soc.*, **114**: 580, 1988.)

wave activity between 15 and 22 km. Shutts, Kitchen, and Hoare (1988) used linear wave saturation theory to argue that the disturbance was a quasi-stationary, terrain-generated gravity wave with a horizontal wavelength of about 16 km and a vertical wavelength of about 6 km. The wave temperature-perturbation amplitude was about 8 K, which is shown as only slightly smaller than the critical amplitude for wave saturation. Shutts, Healey, and Mobbs (1994) described a pilot study to assess the potential of rapidly released radiosondes for studying terrain-generated gravity waves. The idea is that each sonde will be nearly simultaneously responding to a different part of the wave field. As Shutts, Healey, and Mobbs (1994) pointed out, sondes that are too close together in space and time provide no new information on the wave, since they are all experiencing the same part of the wave. Sondes which are separated over space scales greater than the wave scales are impossible to correlate. However, if the spacings of the sondes are between these limits, then this technique offers the possibility of determining not only the horizontal wavelengths, but also the slopes of the constant phase lines. These values can then be used to infer wave drag. Gardner and Gardner (1993) and de la Torre and Alexander (1995) investigated the distortions to density and temperature spectra introduced by the characteristics of balloon motion and wave propagation. These studies sought methods to infer the "real" wavelengths and frequencies from the "apparent" ones measured during soundings. Balloon soundings have been extensively used to study gravity waves in the troposphere and lower stratosphere.

8.1.3 REMOTE SENSORS

Remote sensing can be defined as measuring the characteristics and properties of the atmosphere in a region far removed from the sensing instrument. Examples of remote sensors include radar, lidar, and sodar.

8.1.3.1 Radar

Radar has been extensively used to study gravity waves throughout the atmosphere. For example, using radar Ottersten, Hardy, and Little (1973) described gravity wave observations in the planetary boundary layer; Gauge and Balsley (1978) described probings of the troposphere and stratosphere; Manson (1990) presented a climatology wave structure in the mesosphere; and Fritts and Isler (1994) described wave motions in the mesosphere and lower thermosphere. Perhaps one of the first reported radar observations of a gravity wave was made by Hicks and Angell (1968) who described ". . .a hitherto undetected phenomenon observed on several occasions. . ." which ". . .is an apparent horizontally twisted, braided, or helical-appearing atmospheric structure. . .." They concluded that the object in question is a breaking Kelvin–Helmholtz gravity wave. Since then, numerous studies of gravity waves have been performed using radar. A discussion of the basic concepts of radar can be found in Chadwick and Gossard (1986).

Two types of radar are commonly used in atmospheric research: Doppler radar and frequency-modulated continuous-wave (FM-CW) radar.

8.1.3.2 Doppler Radar

The principles of *Doppler radar* as used in atmospheric studies can be found, for example, in Gauge and Balsley (1978) and Kropfli (1986). Basically, pulses of radiofrequency energy are transmitted via a directional antenna. These pulses are scattered by refractive inhomogeneities caused by temperature and humidity fluctuations on scales of half a wavelength of the pulse. These fluctuations are generally caused by turbulence or large gradients of temperature or humidity along the radar beam. Ultra high frequency (UHF) radars operate over frequency ranges from 300–3000 MHz, with wavelengths ranging from 1–0.1 m. Sensitive Doppler radars operate in the very high frequency (VHF) range from 30–300 MHz, with wavelengths ranging from 10–1 m. The component of the scattered beam parallel to the incident beam is received by the antenna, and the time delay between transmitted and received pulses is a function of the distance to the scattering region. If the scattering region is moving, then the frequency of the returned pulse is Doppler shifted by an amount that is proportional to the velocity component in the direction of the radar beam. If the radar is directed vertically, then only the vertical velocity of the scattering region is observed. If, however, the beam is inclined to the vertical by angle θ, then the instantaneous Doppler velocity, v, at range R is

$$v(\theta, R, t) = w(\theta, R, t)\cos\theta + u_h(\theta, R, t)\sin\theta\,, \tag{8.2}$$

where w and u_h are the instantaneous vertical and horizontal velocities, respectively. If the tilted beam is aimed along orthogonal azimuth angles, and if it is assumed that the horizontal wind speed is much greater than the vertical wind speed, then as demonstrated by Farley *et al.* (1979) the instantaneous horizontal winds speeds u and v can be resolved. By making similar measurements at various range distances, the wind profile can be resolved. Figure 8.2 shows plots of radar-derived wind profiles observed with the Arecibo radar in Puerto Rico compared with rawinsonde wind profiles. The agreement between radar winds and airsonde winds seen in Fig. 8.2 is very good. The radiosonde was launched from San Juan, Puerto Rico, about 70 km east of Arecibo, and Farley *et al.* (1979) attributed the differences between the profiles to the physical separation between the observing points rather than to experimental uncertainties. Vincent and Reid (1983) used these techniques to measure gravity wave momentum fluxes in the mesosphere. At a height range of 80–90 km, they calculated a westerly acceleration due to momentum flux convergence of about 20 m s^{-1} day^{-1} due to waves with a dominant wavelength of about 50 km and a phase speed of about 50 m s^{-1}. While this induced acceleration is almost an order of magnitude smaller than that predicted by Fritts (1984) using saturation theory (see Section 7.2.1), it may well be correct since

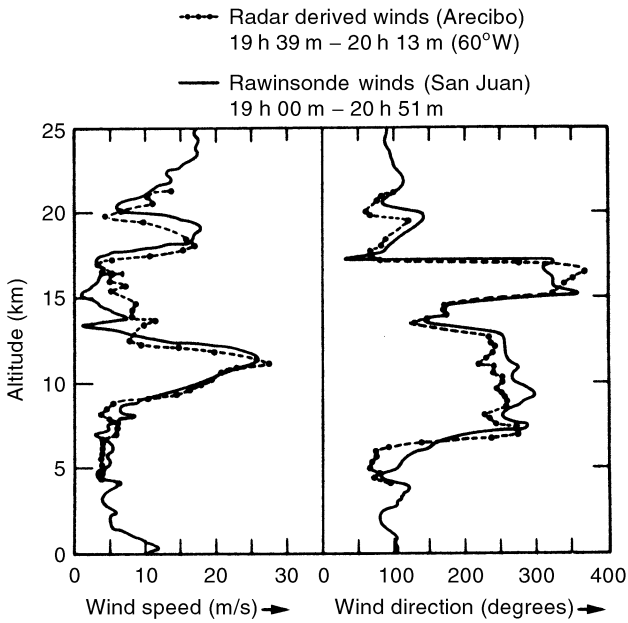

FIGURE 8.2 Comparison of vertical profiles of wind speed and wind direction observed by the Arecibo radar with nearly simultaneous rawinsonde observations from San Juan, Puerto Rico. (From "Tropical winds measured by the Arecibo radar," D.T. Farley *et al.*, *J. Appl. Meteorol.*, **18**: 229, 1979.)

Vincent and Reid (1983) estimated the average wave stress over 3 days of observations.

8.1.3.3 Frequency-Modulated Continuous-Wave Radar

Generally, Doppler radar returns are limited to temperature and humidity inhomogeneities on the scale of meters and to ranges greater than several hundreds of meters above the ground surface. The first restriction is imposed by the radar frequency, and the latter restriction is imposed by the fact that during the transmission of the radar pulse no signal can be received. However, to better understand the dynamics of the planetary boundary layer it is necessary to know the true thickness of thin radar backscatter layers and the processes generating these fine-scale refractive index inhomogeneities. The *FM-CW radar* developed by Richter (1969) makes these observations possible. To eliminate the need for radar pulses which limit the range, a continuous microwave frequency is transmitted and simultaneously received by an identical antenna closeby. In itself, this mode of operation would provide high spatial resolution, but no range information. To get range information, the transmitted frequency is linearly modulated between two frequencies over a time T_M. The received signal will be Doppler shifted by moving scatters, and when the transmitted and received signals are

combined in real time, a sinusoidal beat frequency, f_b, is generated. The time delay, Δt, of the appearance of reflected signal is related to the distance of the scatter by

$$f_b = \frac{F}{T_M}\Delta t = \frac{2F}{c\,T_M}H\,, \tag{8.3}$$

where F is the frequency excursion, c is the speed of propagation, and H is the height of the scatter (assuming the instrument is pointed upward). In the case of multiple returns, a spectrum analysis of the beat frequency allows the different targets to be resolved according to their range, and the amplitudes of the beat frequencies are measures of the reflection coefficients of the targets. Figure 8.3 taken during the CASES-99 field program (Poulos *et al.*, 2001) illustrates the fine wave-like structures that can be revealed by FM-CW radar. The capability of FM-CW radar was enhanced in 1976 when Doppler capability was added (Chadwick *et al.*, 1976; Strauch *et al.*, 1976). This was accomplished by using a digital Fourier transform that preserved the phase and amplitude of spectral density of the radar signal obtained during each sweep. Monitoring the change in phase from sweep to sweep provides the Doppler information needed to estimate radial velocities. Figure 8.4 compares FM-CW Doppler winds with winds observed using a tethered balloon and a rawinsonde. The FM-CW radar is becoming a standard instrument for boundary-layer studies and has proved especially useful in the studies of wave and turbulence in the stable boundary

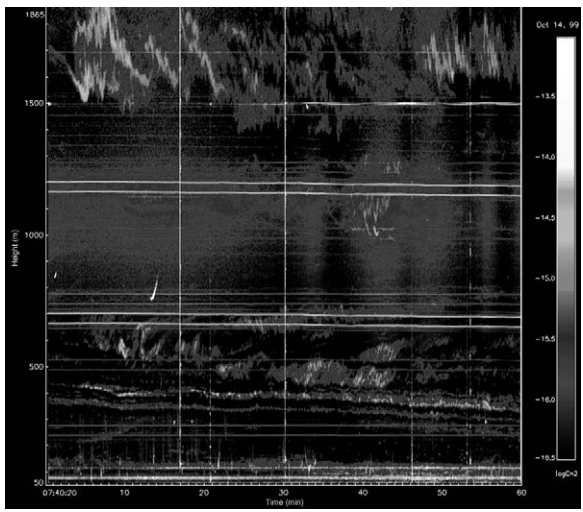

FIGURE 8.3 FM-CW radar images recorded on October 14, 1999. Record begins at 07:40:20 GMT. Kelvin–Helmholtz waves are between 1500 and 1800 m and between 500 and 600 m. (Courtesy of Stephen Frasier, Univ. of Massachusetts, Amherst.)

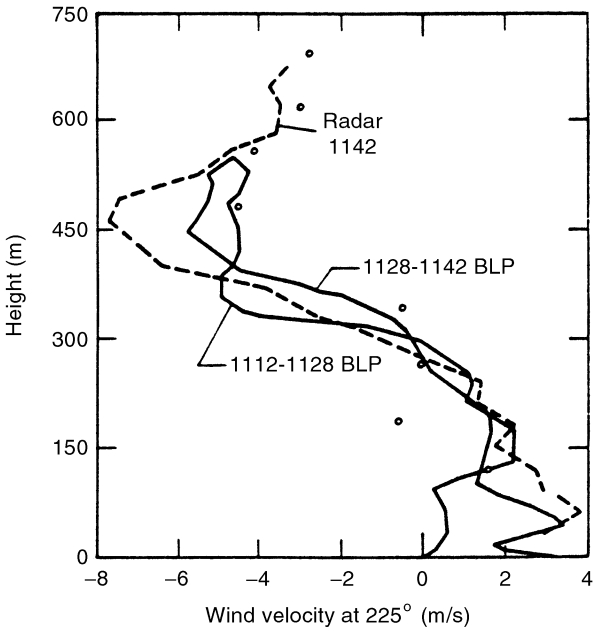

FIGURE 8.4 FM-CW Doppler radar wind speed profile (dashed line) compared with tethered balloon wind profiles (solid lines) and rawinsonde profile (circles). (From "A new radar for measuring winds," R.B. Chadwick *et al.*, *Bull. Am. Meteorol. Soc.*, **57**: 1123, 1976.)

layer (see, for example, Eaton, McLaughlin, and Hines, 1995; De Silva *et al.*, 1996).

8.1.3.4 Sodar

Sodar, which stands for sound detection and ranging, was first described as a research tool for probing the lower atmosphere by Little (1969) and McAllister *et al.* (1969). The historical development of sodar and its principles of operation can be found in Beran, Hooke, and Clifford (1973) and in the reviews by Brown and Hall (1978) and Neff and Coulter (1986). Basically, sodars are like radars, but with sound energy replacing radiofrequency (RF) energy. Little (1969) pointed out that the interactions of sound waves with the lower atmosphere are much stronger than interactions of electromagnetic waves. For example, the change in sonic refractive index for a 1 K fluctuation in temperature is about 1700 N-units, where 1 N-unit equals 1 part in 10^6. For RF wavelengths, the corresponding change in refractive index is about 1 N-unit. For fluctuations in wind speed, the difference is greater; for a 1 m s^{-1} variation in wind speed the change in the sonic refractive index is about 3000 N-units, whereas RF waves are essentially unaffected. Thus, sodar offers a much more sensitive means of observing fine structure and turbulence in the atmospheric boundary layer than radar. An example of this ability is shown in Fig. 1.2.

The dark bands represent sound returns from regions of turbulence and stable stratification. The light regions between the bands are either quiescent or neutrally stratified, *i.e.*, $\partial\theta_0/\partial z = 0$. The small-scale structures of the type shown in Fig. 1.2 have been discussed by Chimonas (1999); they represent complex interaction between waves and turbulence in the stable boundary layer. Emmanuel *et al.* (1972); Hooke, Hall, and Gossard (1973); and Emmanuel (1973) were among the first to use sodar as a means of identifying regions of shear instability in the nocturnal inversion. Merrill (1977) made use of sodar to identify wave instabilities in one of the first comprehensive field studies of waves and turbulence. Since then, sodar has been an integral part of most studies of the boundary layer. Neff and Coulter (1986) presented several examples of these types of studies. The first reported application of Doppler technology to sodar was made by Beran, Little, and Willmarth (1971) who used it to measure vertical velocities in the convective boundary layer. Descriptions of Doppler sodar systems are given by Beran, Hooke, and Clifford (1973) and by Brown and Hall (1978). A discussion of early studies of gravity waves and sodar is given by Beran, Hooke, and Clifford (1973). Since then, the Doppler capabilities have been greatly extended so that routine profiles of the three-dimensional wind field and its accompanying turbulence structure are possible.

8.1.3.5 Lidar

Light detecting and ranging or *lidar* is the optical counterpart of radar. Lidar is the most recent of the remote-sensing techniques, and some aspects of the technology are still under development. Instead of RF pulses, lidars transmit pulses of light and measure its backscatter as a function of time. A discussion of the basics of lidar can be found in Schwiesow (1986). The transmitted light is backscattered by aerosols and molecules depending on the frequency of the light. A lidar system consists basically of a laser; a telescope for transmission and reception; a detector; and, of course, a computer for signal control, signal processing, and data analysis. Because the absorption and scattering of the laser beam is proportional to the density of the absorbers and scatterers, lidars have been often used to remotely measure concentrations of aerosols, trace gases, and atmospheric pollutants. The first reported use of a lidar for observing gravity waves was made by Collis, Fernald, and Alder (1968). They used two pulsed ruby lidars to observe the structure of wave clouds in the lee of the Sierra Nevada mountains in California. Gardner and Shelton (1985) and Gardner and Voelz (1987) developed equations which relate variations of mesospheric sodium (Na) concentrations to gravity waves and used lidar measurements of Na to estimate wave characteristics in the mesosphere. Kwon and Gardner (1990) used airborne lidar measurements of mesospheric Na to estimate not only vertical and horizontal wavelengths, but also intrinsic frequency, phase speed, and propagation direction. Gardner and Taylor (1998) discuss the limits of remotely measuring middle atmosphere gravity wave parameters.

Because the light scatterers move with the mean flow, Doppler techniques can be used to remotely measure wind speeds. However, Eloranta, King, and Weinman (1975) and Sroga, Eloranta, and Barber (1980) demonstrated that three-dimensional boundary-layer flow fields could be measured without the Doppler technique by following the motions of naturally occurring aerosol density inhomogeneities. Examples of the early uses of Doppler lidar for studying winds in the boundary layer can be found in DiMarzio *et al.* (1979), Bilbro *et al.* (1984), and Köpp, Schwiesow, and Werner (1984). One of the first observations of gravity waves with a Doppler lidar was reported by Blumen and Hart (1988). They used an airborne Doppler lidar to study the flow fields in the wake of Mount Shasta in California. Ralph *et al.* (1997) reported on the use of Doppler lidar and other instruments in two studies of trapped gravity waves in the lee of the Rocky Mountains near Boulder, CO. The most recent use of Doppler lidar for gravity wave observations occurred during the CASES-99 field program (Poulos *et al.*, 2001) and is described by Newsom *et al.* (2000). These observations were made with the NOAA/ETL High-Resolution Doppler Lidar (HRDL) which is described in Grund *et al.* (2001). The lidar can achieve 30-m range resolution, a working range of between 2 and 3 km, and a velocity precision of about 0.1 m s^{-1}. Figure 8.5 shows contours of stream-wise velocity as a function or height and horizontal range.

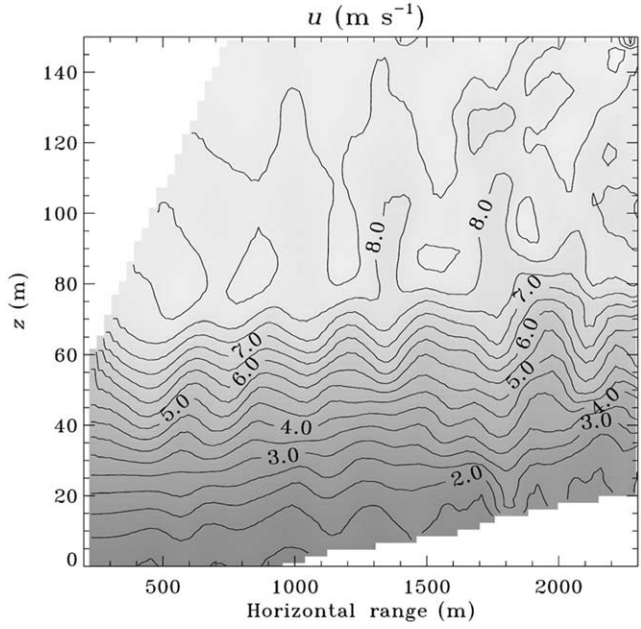

FIGURE 8.5 Sample vertical cross-section wind speed scan taken by the HRDL radar during the CASES-99 field program. Positive wind speeds are away from the radar. (From *14th Symposium on Boundary Layer and Turbulence*, August 7–11, 2000, Aspen, CO, R.K. Newsom *et al.*, *Am. Meteorol. Soc.*, Boston, MA, 2000, p. 363.)

A well-defined wave is seen between 40 and 70 m, and a low-level jet with a maximum velocity of 10 m s^{-1} is seen at a height of about 120 m. Eichinger *et al.* (1999) reported on the development of a scanning Raman water vapor lidar designed for boundary-layer and tropospheric observations. The horizontal range while scanning is about 700 m, and the vertical range can be up to 12 km. Spatial resolutions range from 1.5 m in the near field to 75 m in the far field. Figure 8.6 shows wave activity during the night of October 13–14, 1999, during the CASES-99 field program. While these types of lidars do not give wind speed data directly, their fine spatial resolution is especially useful in estimating wavelengths and regions of wave activity. Also, by observing a wave over successive scans, it is possible to estimate wave speed.

8.2 MULTIPLE STATION OBSERVATIONS

Single-station techniques are generally limited to observations of wave-induced perturbations and their vertical structures. In some cases and with linear theory, wave parameters such as wavelength and phase velocity can be estimated if the waves persists over several cycles with relatively constant amplitude. Also, scanning Doppler lidars may be able to resolve horizontal wavelengths and phase velocities, but this has yet to be demonstrated. For reliable estimates of phase speeds and wavelengths, the disturbance must be detected as it passes over several observing stations. The arrival times of the crests of the disturbance at the stations can be used to estimate phase speeds. If there is a periodicity associated with the disturbance, then wavenumbers and wavelengths can be calculated.

Surface pressure perturbation is the most often used atmospheric variable for tracking gravity waves (see, for example, Herron and Tolstoy, 1969; Stobie, Einaudi, and Uccellini, 1983; Bedard, Canavero, and Einaudi, 1986; Einaudi, Bedard, and Finnigan, 1989; Hauf *et al.*, 1996; Rees *et al.*, 2000). Other atmospheric variables have been used. For example, Kjelaas *et al.* (1974) used a triangular array of sodars to estimate gravity waves characteristics. Observations taken with the sodar array were compared with those obtained with an array of microbarographs. The results from both measurement techniques were comparable when waves were observed by both methods. However, the sodar array was able to detect waves propagating in an elevated inversion above the convective boundary layer, but these waves were not detected by the microbarographs. A similar instance was reported by Nappo, Eckman, and Coulter (1992) who observed a Kelvin–Helmholtz wave at about 300 m AGL in the nighttime boundary layer, but the wave was not seen by a surface array of microbarographs. Eymard and Weill (1979) used a triangular array of Doppler sodars to study gravity waves at two locations in France. Xing-sheng *et al.* (1983) used an optical triangle to calculate wave speeds and directions. The optical anemometers sense path-averaged instantaneous wind speeds, which is perhaps a more robust measure of wave perturbation velocity than observations made at three points.

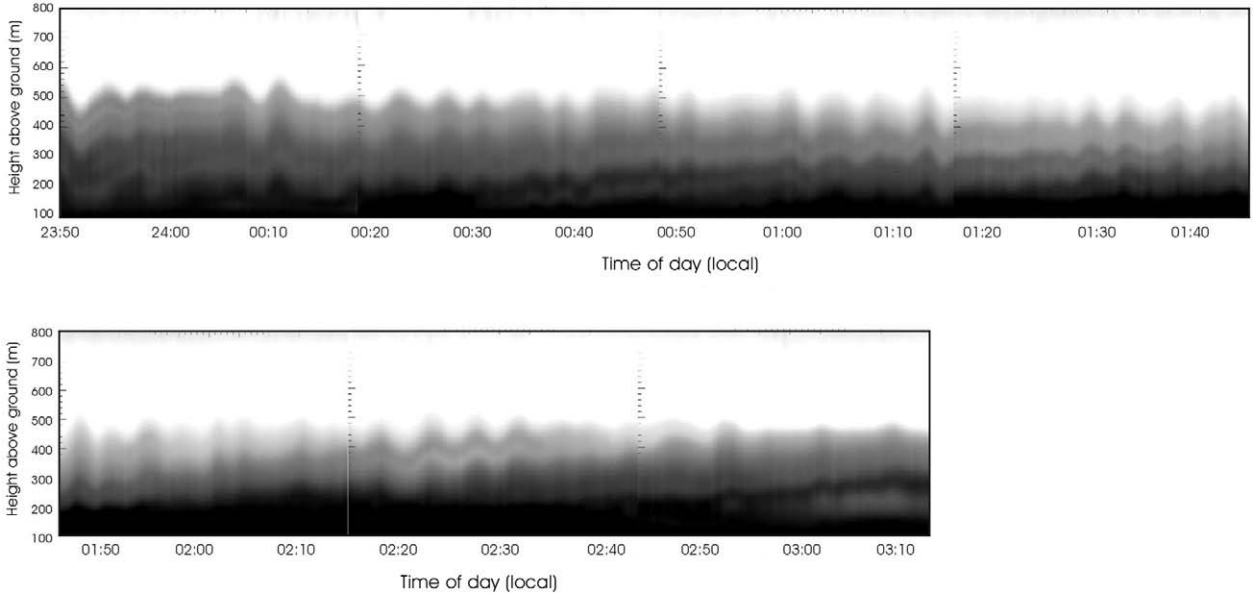

FIGURE 8.6 Boundary layer waves observed by vertically pointed Ramon lidar during the night of October 13–14, 1999, during the CASES-99 field program. Time is CDT. (From "High altitude activity associated with intermittent turbulence in a stable atmosphere," W.E. Eichinger *et al.*, *Boundary-Layer Meteorol.*, submitted, 2001.)

Rees and Mobbs (1988) used time series of wind speed and direction measured at an 8-m height on three meteorological masts at Halley Base, Antarctica. Carter *et al.* (1989) used three vertically directed 50-MHz radar wind profilers spaced between about 5 and 6 km to detect vertical velocities associated with gravity waves during the ALPEX experiment in southern France. They concluded that ". . .monochromatic wave activity is a relatively rare occurrence and that most of the time a wide spectrum of waves influences the vertical velocities in an incoherent fashion." However, the somewhat large horizontal scale of the array may be partly responsible for these incoherent disturbances. As we shall see, if the average separation between stations in the array is large relative to a horizontal wavelength, then aliasing of the wave signal can occur. This can result in an incoherent wave signal.

8.2.1 PRESSURE PERTURBATION MEASUREMENTS

Although several techniques for detecting gravity waves have been tried, monitoring surface pressure is the one most commonly used. Reasons for this are that there are no moving parts, they are relatively cheap to make, and they require little care once in operation. The pressure perturbations associated with most waves will be maximum at the ground surface, and because the background wind speed is generally small at the ground surface, there will be little Doppler shifting of the wave.

Surface pressure perturbations by gravity waves of large amplitude are seldom greater than 1 mb. More typical values range from $\sim$10 to $\sim$100 μb. Because absolute surface pressures are on the order of $\sim$1000 mb, a barograph would require a sensitivity of 1 in 10^4 to detect a 100-μb signal. This sensitivity is beyond most commercial barographs. However, because it is the perturbations and not the absolute values of pressure that are important, one can use an electronic *manometer* to measure the perturbations. Recall that a manometer measures pressure difference. In applications, one measures the pressure difference between a static or slowly varying pressure in a reference chamber and the rapidly varying atmospheric pressure. This will allow the separation of the low-frequency, large-amplitude mean pressure changes from the high-frequency, low-amplitude perturbations. Figure 8.7 illustrates the filtering setup. The differential pressure gauge (the manometer) contains a piezoelectric diaphragm which responds electronically to the strains produced by pressure differences between the reference chamber and the atmosphere. If the reference chamber has a slow leak, then the chamber pressure will slowly adjust to low-frequency atmospheric pressure changes, and the signals of the high-frequency pressure changes will be enhanced. This is a high-pass filter, and the frequencies that are passed are controlled by the size of the leak. We can refer to this type of filter as *mechanical*. However, if the reference chamber is sealed, then all frequencies will be recorded. In this case, the low frequencies must be filtered numerically. We can refer to this type of filter as *digital*.

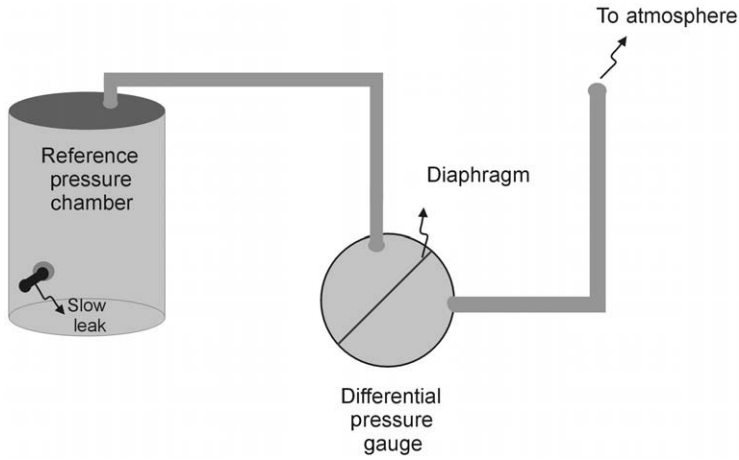

FIGURE 8.7 Schematic of an electronic mechanical filter microbarograph. When the slow leak is sealed, the instrument becomes a digital filter microbarograph.

8.2.1.1 Mechanical Filter Instruments

If there is a leak in the reference chamber, then the pressure, p_c, in the chamber changes according to

$$\frac{dp_c}{dt} = -\alpha \left[(p_c(t) - p_a(t)) \right] , \tag{8.4}$$

where p_a is the atmospheric pressure and α^{-1} is a time constant which is determined by the leak rate. The integration of (8.4) is straightforward if we multiply it by the integrating factor $e^{\alpha t}$ and note that $e^{\alpha t}\, dp_c + \alpha p_c\, e^{\alpha t} dt$ is an exact differential. We can then write (8.4) as

$$d\left[p_c\, e^{\alpha t} \right] = \alpha p_a\, e^{\alpha t} dt . \tag{8.5}$$

Integration of (8.5) gives the result

$$p_c(t) = \alpha \int_0^t p_a(t') e^{-\alpha(t-t')}\, dt' . \tag{8.6}$$

The differential pressure, Δp, at time t is

$$\Delta p(t) = p_a(t) - p_c(t) . \tag{8.7}$$

Using (8.6) in (8.7) gives

$$\Delta p(t) = p_a(t) - \alpha \int_0^t p_a(t')\, e^{-\alpha(t-t')}\, dt' . \tag{8.8}$$

Following, for example, Bendat and Piersol (1971), a linear system which is stable and physically realizable can be represented by

$$y(t) = \int_0^\infty h(\tau)\, x(t-\tau)\, d\tau\,, \tag{8.9}$$

where $h(\tau)$ is a *weighting function* which relates the system output, $y(t)$, to the system input, $x(t)$. Equating (8.9) with (8.8), we see that

$$h(\tau) = \delta(\tau) - \alpha H(\tau)\, e^{-\alpha\tau}\,, \tag{8.10}$$

where $\delta(\tau)$ is the Dirac delta function and $H(\tau)$ is the *Heaviside* function defined by

$$\begin{aligned} H(t-\tau) &= 1 \quad t \geq \tau \\ &= 0 \quad t < \tau\,. \end{aligned} \tag{8.11}$$

The dynamic characteristics of the system are given by the *frequency response function*, $\hat{h}(\nu)$, which is the Fourier transform of the weighting function. The Fourier transform of (8.10) is

$$\hat{h}(\nu) = \frac{\nu^2 + i\alpha\nu}{\alpha^2 + \nu^2}\,, \tag{8.12}$$

where ν is the frequency. It is customary to express the frequency response in polar notation, *i.e.*,

$$\hat{h}(\nu) = G(\nu)\, e^{-i\Phi(\nu)}\,, \tag{8.13}$$

where $G(\nu)$ is the *gain factor* of the system and $\Phi(\nu)$ is the *phase factor* of the system. From (8.12) we see that

$$G(\nu) = \left(\frac{\nu^2}{\alpha^2 + \nu^2}\right)^{1/2} \tag{8.14}$$

and

$$\Phi(\nu) = \tan^{-1}\left(\frac{\alpha}{\nu}\right)\,. \tag{8.15}$$

From (8.14) we see that frequencies less than α are attenuated, while frequencies greater than α are less attenuated. Thus, the leak creates, in effect, a *high-pass filter*. The amplitude of a gravity wave with angular frequency a is reduced by a factor of 0.707, and the phase angle is shifted forward $\pi/4$ degrees. If the period of the wave is 15 min, then the wave phase is shifted forward about 112 s. These changes

in wave amplitude and phase will affect statistics such as cross-correlations as well as the comparisons of pressure measurements with other measurements such a velocity or temperature. Thus, it is necessary that the characteristics of the low-pass filter be known so that the pressure data can be corrected before analysis.

As mentioned above, $1/\alpha$ is a time constant for the reference chamber pressure. This value depends on the frequencies of the wave of interest. For example, Jordan (1972) investigated atmospheric gravity waves generated by several mechanisms such as upper tropospheric winds, jet streams, weather fronts, thunderstorms, *etc*. He selected leak time constants which ranged from 50 to 100 s. Einaudi, Bedard, and Finnigan (1989) examined gravity waves in the planetary boundary layer and used a time constant of 7.5 s. Hauf *et al.* (1996) examined gravity waves on the mesoscale and used a time constant of about 300 s.

8.2.1.2 Digital Filter Instruments

If the pressure reference chamber is sealed, then the differential pressure given by (8.7) is

$$\Delta p(t) = p_a(t) - p_c \,, \tag{8.16}$$

where p_c is now a constant pressure. Such a system does not suffer degradation introduced by a high-pass filter. Indeed, pressure variations on all time scales can be detected if the instrument is operated long enough. Because all frequencies are present in the recorded data, digital filters must be used to isolate and separate desired frequency ranges. However, this enhanced frequency response comes at a cost. One of the most challenging problems is maintaining constant pressure in the reference chamber over the measuring time, which could range from minutes to days. Because the chamber is sealed and has constant volume (neglecting thermal expansion), the gas density is constant at least to first order. Then, from Boyle's law,

$$\frac{\delta p_c}{p_c} = \frac{\delta T_c}{T_c} \,, \tag{8.17}$$

where δp_c is the change in p_c due to a change δT_c in the reference chamber temperature, T_c. For typical values of surface pressure ($\sim$1000 mb) and temperature ($\sim$300 K), a temperature change of 0.01 K results in $\delta p_c = 33$ μb. This is a substantial pressure change and is comparable to the amplitudes of high-frequency gravity waves in the planetary boundary layer. If T_c increases, then p_c increases, and from (8.16) it will appear as if Δp decreases if $p_a(t) > p_c$. But this will be incorrectly interpreted as a decrease in atmospheric pressure. The reverse effect will occur if T_c decreases. If T_c is measured, then it would be possible to correct the data *post facto*. However, at this time it is not possible to measure temperature differences of 0.01 K or smaller. Thus, special care must be given to minimizing reference chamber temperature variations. This can be done by insulating the reference chamber, increasing its thermal inertia, or keeping the reference chamber at

a near-constant temperature. Nappo *et al.* (1991) described a microbarograph system which insulated the reference chamber and used aluminum pellets, which have a high specific heat capacity, to increase thermal inertia in the chamber. Anderson *et al.* (1992) described a microbarograph system which used all three remedies to approach thermal stability. Note that these temperature affects will also affect the mechanical type of microbarograph, but not greatly if the temperature changes are slow. To alleviate these temperature problems, Hauf *et al.* (1996) installed their sensors in a plastic container placed 1.5 m below the ground surface.

Another difficulty with the digital instrument is saturation of the differential pressure gauge. The differential pressure gauge has a limited operating range, say, on the order of a few millibars (Nappo *et al.*, 1991; Anderson *et al.*, 1992). The diurnal changes in atmospheric pressure, moving frontal systems, gust fronts, *etc.* can cause pressure changes of more than a few millibars, and these changes can lead to instrument nonlinearity, saturation, and possible damage. To overcome these possibilities, the reference chamber pressure can be set to ambient pressure by briefly opening the reference chamber to the outside pressure using a solenoid valve. For the Nappo *et al.* (1991) instrument, the "reset" valve is periodically opened; for the Anderson *et al.* (1992) instrument, the valve is opened whenever the differential pressure reaches a predetermined value. Opening the valve sets $p_c = p_a(t_0)$, where t_0 is the time of pressure reset. Thus, (8.16) becomes

$$\Delta p(t) = p_a(t - t_0) - p_a(t_0)\,, \tag{8.18}$$

and the time series $\Delta p(t)$ takes the form of a series of ramp-like structures, as shown in Fig. 8.8. The data shown in Fig. 8.8 were taken on September 1, 2000, at

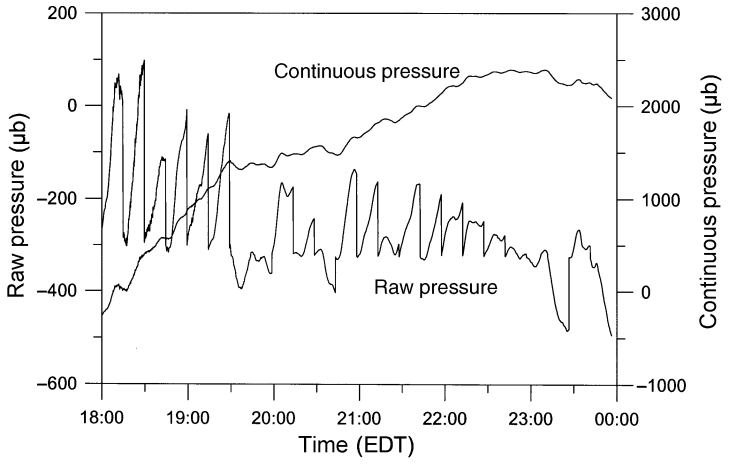

FIGURE 8.8 Time series of raw and postprocessed pressure data observed at Oak Ridge, TN on September 1, 2000.

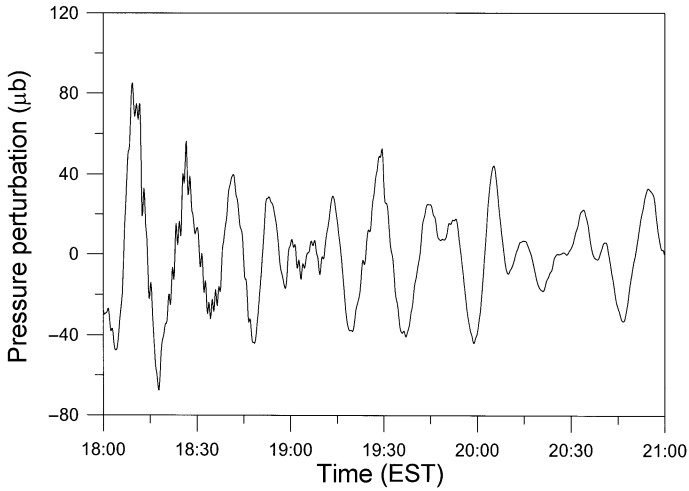

FIGURE 8.9 Pressure perturbations between 18:00 and 21:00 EST observed at Oak Ridge, TN on September 1, 2000. Note the high-frequency activity between 18:00 and 18:45 and again around 19:00. These could be gravity waves or large-scale turbulence eddies from the previous convective period.

Oak Ridge, TN. The reference chamber was set to ambient pressure every 15 min. The differential pressure signal was sampled at 10 Hz, from which 10-s averages were formed and recorded. Postprocessing of the data requires the smooth joining of these ramps to form a continuous time series of differential pressure, also shown in Fig. 8.8. Figure 8.9 shows the pressure perturbations observed between 18:00 and 21:00 EST for the case shown in Fig. 8.8. These data were obtained by bandpass filtering the postprocessed data shown in Fig. 8.8. The filter passed signals with periods between 1 and 30 min.

8.2.1.3 Sampling Arrays

Gravity waves produce coherent periodic disturbances which propagate with a horizontal component of velocity. If the pressure perturbations associated with these waves are observed only at a single point, then all we can learn about the wave is its amplitude and frequency. If we have time series of pressures at two points, then we can estimate the component of the wave vector parallel to the line joining the two locations.[1] However, as illustrated in Fig. 8.10, there is an infinite number of possible wave vectors with components parallel to a line joining two points. For example, let vector AB in Fig. 8.10 be the true wave vector which is directed from station A to station B. However, wave vector AC, with wave fronts indicated by the dashed lines, and wave vector AD, with wave fronts indicated by the solid lines, also have components parallel to wave vector AB. Either of

[1] How these estimates are made will be discussed in the Chapter 9.

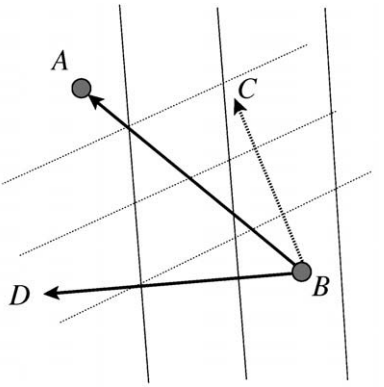

FIGURE 8.10 The apparent wave vector between points A and B is a component of an infinite number of possible wave vectors. Shown in the figure are two possible wave vectors that could have a component along the line joining stations A and B.

these wave vectors could be considered as the true wave vector. Thus, the true wave vector cannot be determined, and consequently, we cannot estimate the true phase speed and wavelength. As we shall see, at least three sensors are necessary to estimate wave characteristics; more sensors increase the accuracy of the estimates. The spatial distribution of the sensors describes an *array* which, in effect, acts like an RF antenna. The *response characteristics* of an antenna determine the range of frequencies and wavelengths of radio waves that can be received. Likewise, the response characteristics of the pressure sampling array determine the range of gravity waves that can be detected.

Figure 8.11 is a schematic of an idealized five-sensor array. Four sensors are placed on the corners of a square with sides 1 km, and one sensor is placed in the center. If the sampling period, *i.e.*, the time between observations, is Δt, and if the greatest distance between the stations is D, then the maximum speed of a disturbance crossing the array that can be detected is

$$c_{max} = \frac{D}{2\Delta t} \,. \tag{8.19}$$

The factor $2\Delta t$ in (8.19) is the *Nyquist period*. It is the reciprocal of the *Nyquist frequency*, which is the highest frequency content of a time series. Disturbances with periods less than $2\Delta t$ will not be detected by the array as a coherent signal. For the idealized array in Fig. 8.11, $D = 1000$ m. If $\Delta t = 10$ s, then $c_{max} = 50$ m s^{-1}. A wave with phase speed greater than c_{max} will be incoherent in the sense that the wave shape observed at each sensor will be different. In this case, the wave energy will appear in waves of lower frequency, a processes known as *aliasing*. The minimum wavelength, λ_{min}, that can be resolved by the array is comparable to the minimum spacing of the sensors. Waves with wavelengths less than the average spacing between station pairs will also suffer an aliasing error,

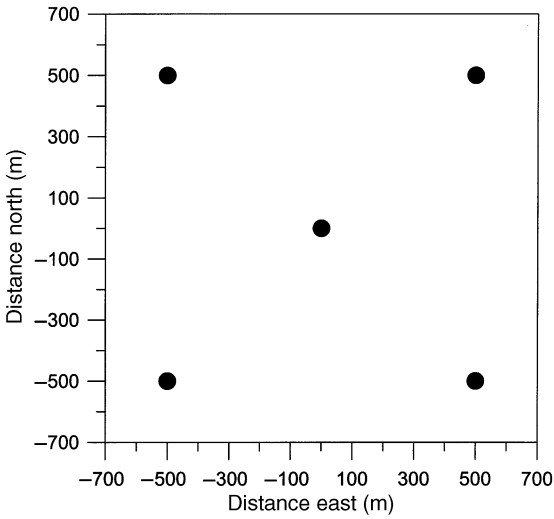

FIGURE 8.11 Idealized five-sensor array for detecting gravity waves.

and their energy will appear in waves with greater wavelengths. For the array illustrated in Fig. 8.11, $\lambda_{min} \approx 700$ m. The maximum resolvable wavenumber is $k_{max} = 2\pi/\lambda_{min}$, and for the array in Fig. 8.12 this is about 0.009 m^{-1}. The maximum detectable wavelength is given by

$$\lambda_{max} = c_{max} T_{max} = \frac{D}{2} \frac{T_{max}}{\Delta t}, \tag{8.20}$$

where we have used (8.19), and T_{max} is the maximum disturbance period that can be detected by the sensors. For the mechanical-filter microbarograph, T_{max} is determined by the filter time constant $1/\alpha$. From (8.14) we see that if the frequency of the wave is equal to α, then the amplitude of the wave is reduced by a factor of 0.707. We can take $T_{max} = 2\pi/\alpha$. If $1/\alpha = 300$ s and $c_{max} = 50$ m s^{-1}, then $\lambda_{max} \approx 90$ km. For the digital-filter microbarograph, λ_{max} is determined by the lowest frequency retained after filtering. If that frequency has a period of 30 min, and if $c_{max} = 50$ m s^{-1}, then λ_{max} is also 90 km.

From the above, we see that the range of gravity waves that can be detected by a sampling array is a function of instrument spacing and sampling frequency. Studies of array design have been made, for example, by Barber (1959), Haubrich (1968), and Asten and Henstridge (1984). As Haubrich (1968) points out, the problem of array design is (1) given N sensors, where should they be placed, and (2) what processing scheme should be applied to the array output. He also states that the solution of a design depends on the intended use of the array. Koch and Golus (1988) used a nested array of measurement systems to observe mesoscale gravity waves. They used an inner array of stations with an average spacing of 7 km and

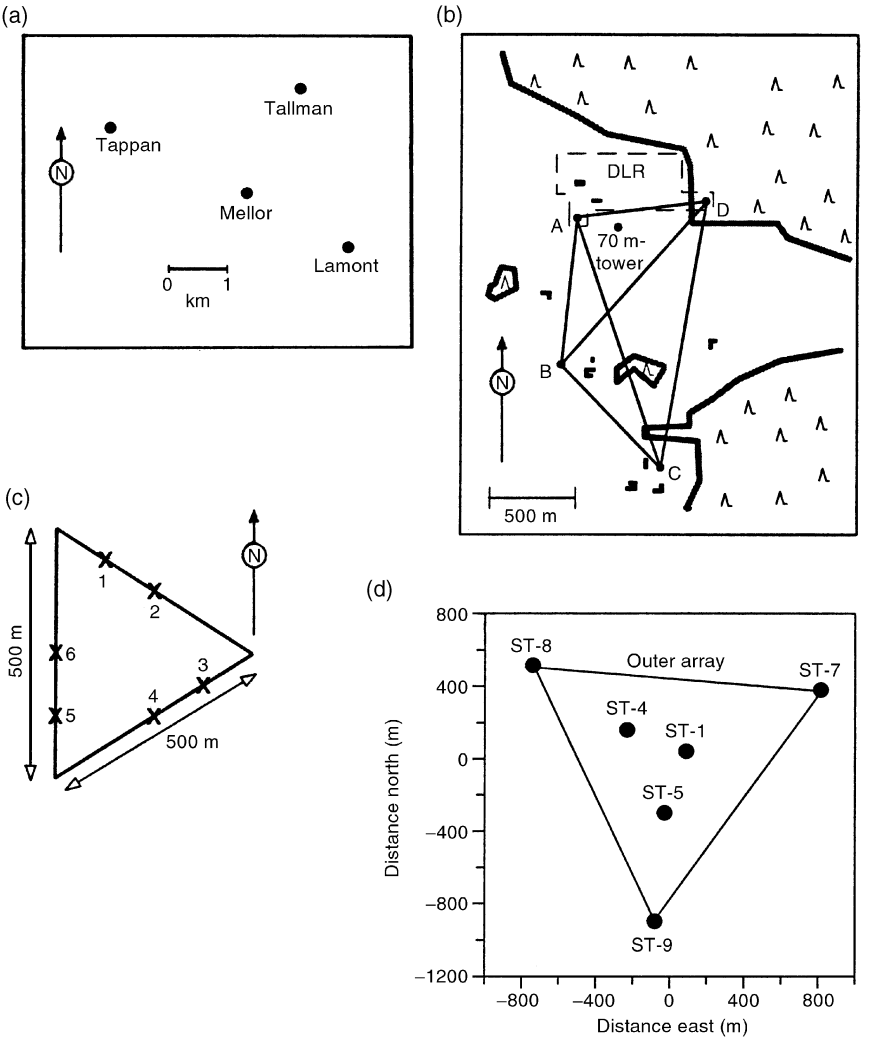

FIGURE 8.12 Microbarograph arrays used by (a) Balachandran (1980), (b) Hauf *et al.* (1996), (c) Rees *et al.* (2000), and (d) Nappo *et al.* (2000).

a courser, regularly spaced array with an average spacing of 20 km. Figure 8.12a shows the array used by Balachandran (1980) to observe thunderstorm-generated gravity waves. Figure 8.12b shows the array used by Hauf *et al.* (1996) to observe gravity waves on the mesoscale. Figure 8.12c shows the array used by Rees *et al.* (2000) to study gravity waves in the stable planetary boundary layer. Figure 8.12d shows the array used by Nappo *et al.* (2000) to study gravity waves in south–central Kansas during the CASES-99 field campaign. It is apparent from Fig. 8.12 that an overall "best" array design may not exist.

8.3 BALLOONS, AIRCRAFT, AIRGLOW, AND SATELLITES

The observation methods described thus far were based on the temporal variations of wave perturbations measured at a fixed location. However, these methods fail when terrain-generated waves are considered. This is because these waves are stationary with respect to the ground. If we wish to study these waves, then we must be able to resolve their spatial structure. We have seen that such a resolution is possible with scanning lidars, but more direct methods are available. In this section, we briefly review these techniques. Nicholls (1973) reviews observational techniques including balloon, aircraft, and satellites used from 1958–1972 to study air flow over mountains.

8.3.1 BALLOONS

If a balloon with neutral lift is released into the atmospheric flow, then it will drift along a line of constant buoyancy. If we track the balloon's motions, then we can estimate the air motion. However, if the balloon volume changes due to heating or cooling, then its buoyancy will change, and it will not be clear what air motions are being followed. If the balloon volume is constant, then the balloon's density is also constant, and the balloon will drift along a surface of constant atmospheric density. The concept of using constant-volume or superpressure balloons was introduced by Angell and Pack (1960). They described the construction of balloons using Mylar film which could withstand superpressures as great as 150 mb. The construction of the balloons required a special heat sealing, and for purposes of economy and reliability, it was desirable that these seals be straight lines. This requirement lead to a tetrahedron shape, and the balloons were called *tetroons*. Because the Mylar film stretches very slightly, the tetroon's volume is nearly constant and, consequently, so is its density. Ideally, once released the tetroon will drift with the wind along a surface of constant atmospheric density. By tracking the tetroon with radar or global positioning system, the wind field along the path of the tetroon can be resolved. However, as discussed by Angell and Pack (1960), there are slight variations in tetroon volume as a function of superpressure, and they give procedures for inflation that account for these variations. These volume variations as well as the finite mass of the tetroon introduce uncertainty in how well the tetroon motion represents the air motion. These issues have been investigated by Angell and Pack (1960, 1962). Booker and Cooper (1965) also investigated superpressure balloons for wind measurements and described balloon shapes other than tetrahedron. Their studies conclude that constant-volume balloons can give accurate information about the movement of air if proper consideration is given to the balloon response to air motion. Vergeiner and Lilly (1970) used constant-volume balloons in their study of lee waves in the Front Range of the Colorado Rocky Mountains. Reynolds (1973) used spherical-shaped, constant-volume balloons to study mountain waves at the White Sands Missile Range. Their results

showed that in wave conditions, the balloons overestimated the wave crests and troughs with an average error of 6%. Nastrom (1989) analyzed the response of superpressure balloons to gravity waves and showed that the response depends on wave period, density and wind amplitudes, and static stability. More recently, Koffi *et al.* (2000) used constant-volume balloons to study mountain lee waves in the Pyrénées Mountains and compared these observations with a mesoscale model. Constant-volume balloons have become an accepted observational tool for mountain waves.

8.3.2 AIRCRAFT

Aircraft have been used as moving platforms for remote sensors (see, for example, Blumen and Hart, 1988; Kwon and Gardner, 1990); however, aircraft have also been used to make *in situ* measurements from which wave parameters can be calculated. The majority of observations have been made over mountains. There are several reasons for this: mountain waves have large amplitudes and can be easily detected; because the waves are stationary, repeated observations of the same wave field are possible; and because the wave fronts tend to be located downwind of the obstacles that generate them, the lee waves are easy to locate. Perhaps the first observations of mountain waves using an aircraft were made by Radok (1954). He proposed repeated flights up- and downwind along a number of tracks. During each flight, the air speed and throttle settings are held constant, corresponding to level flight. Changes in the recorded elevation of the aircraft as well as changes in temperature and pressure are related to vertical velocities associated with the standing waves. Vergeiner and Lilly (1970) used a Beech Queen Air 80 in their study of lee waves off the Colorado Rocky Mountains. The aircraft was equipped with sensors and digital conversion equipment to measure and record temperature, static pressure, air speed, heading, and ground speed using a Doppler navigation system. Most flights were made at constant power settings and pitch angle, and they assumed that the aircraft's vertical velocity was equal to the atmospheric vertical velocity. They estimated the accuracy of this assumption to be about 1 m s^{-1}. Another source of error was uncertainty in the x,y-position of the aircraft, which they estimated to be about ± 2 km. The Colorado Lee Wave Program (Lilly *et al.*, 1971; Lilly and Kennedy, 1973) was an ambitious flight program involving four aircraft: the NCAR DeHavilland Buffalo (turboprop) and three jets, the NCAR Sabreliner, the NOAA B-57B, and an Air Force B-57F stratospheric jet. A primary goal of that program was the evaluation of terrain-induced momentum flux and turbulence generated by breaking gravity waves as described by Lilly (1972). An interesting side result reported by Lilly and Kennedy (1973) was that gustprobe equipment is apparently not necessary for the direct aircraft measurement of wave momentum flux, but an inertial platform or similar stable attitude reference is essential. Smith (1976) used a much less ambitious program, *i.e.*, a lightweight aircraft (Bonanza F33A), to study lee waves generated by the Blue Ridge Mountains in the central Appalachians.

The aircraft had no special meteorological instrumentation other than a laboratory thermometer located outside the cockpit window. Simple as it was, the aircraft had no difficulty in responding to the wave-induced vertical motions of the flow. Comparison of the observations with linear theory and laboratory experiments showed that the linear theory correctly predicted the wavelength, but seriously underpredicted the wave amplitude. Turbulence kinetic energy and waves were measured by Karacostas and Marwitz (1980) using the NCAR Queen Air 304D over Elk Mountain in Wyoming. Brown (1983) used the Hercules and Canberra aircraft of the UK Meteorological Research Flight to investigate mountain waves over the British Isles. As with the previous studies mentioned, Brown (1983) used linear wave theory to calculate wave parameters and momentum fluxes. Gravity waves in the upper atmosphere, between 60 and 140 km, have been analyzed by Fritts, Blanchard, and Cox (1989) and Fritts, Wang, and Blanchard (1993) using density fluctuations measured by high-resolution accelerometers on board the space shuttle during reentries. Aircraft continue to be a primary tool for gravity wave research; recent examples include Moustaoui *et al.* (1999), Leutbecher and Volkert (2000), Lane *et al.* (2000), Poulos *et al.* (2001), and Dörnbrack *et al.* (2001).

8.3.3 AIRGLOW

Airglow is a quasi-steady faint photochemical luminescence occurring in the upper atmosphere between about 80 and 120 km over middle and low latitudes. The near steadiness of airglow distinguishes it from the sporadic aurorae which occur over higher latitudes and at higher elevations. Although the emitted electromagnetic radiation results from photochemical reactions of many atmospheric trace gases, several sources of airglow radiation occur at specific wavelengths, *i.e.*, atomic oxygen at 558 nm (10^{-9} m), sodium at 589 nm, and the hydroxyl radical OH at 600–2000 nm. As examples, the excited OH arises from the reaction (Gardner and Taylor, 1998)

$$\mathrm{H} + \mathrm{O_3} \rightarrow \mathrm{OH^*} + \mathrm{O_2}\,, \tag{8.21}$$

and the sodium emission is based on the Chapman mechanism (Molina, 1983), *i.e.*,

$$\mathrm{Na} + \mathrm{O_3} \rightarrow \mathrm{NaO} + \mathrm{O_2} \tag{8.22}$$

$$\mathrm{NaO} + \mathrm{O} \rightarrow \mathrm{Na^*} + \mathrm{O_2} \tag{8.23}$$

$$\mathrm{Na^*} \rightarrow \mathrm{Na} + h\nu\ (589.3\ \mathrm{nm})\,. \tag{8.24}$$

Each of these emissions occurs at a particular height over a distance of 10–20 km (see, for example, Swenson and Gardner, 1998). Although not visible to the naked eye, the airglow can be photographed under dark skies using high-speed films or charged-coupled device (CCD) imagers. Peterson and Keiffaber (1973) used

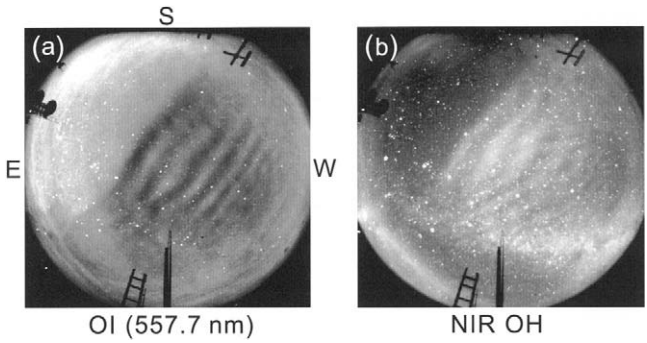

FIGURE 8.13 OH and OI airglow all-sky images from Haleakala, Hawaii on October 10, 1993, 1057 UTC. (From "Spectrometric and imaging measurements of a spectacular gravity wave event observed during the ALOHA-93 campaign," M.J. Taylor, D.N. Turnbull, and R.P. Lowe, *Geophys. Res. Lett.*, **22**: 2850, 1995.)

infrared film and a fast 35-mm camera to make a series of 15-min time exposures of the moonless night sky in New Mexico. The photographs all showed bright cloud-like structures which moved across the sky and varied in brightness. They concluded that the bands were due to varying airglow emission intensity and not intervening atmospheric clouds moving against an otherwise uniform emission background. Assuming a height of 100 km, they calculated speeds of the structures at 20 and 43 m s^{-1}. Because the intensity of the photochemical emission is proportional to the local density and the temperature, variations in intensity can be related to variations in density and temperature. It is now widely accepted that these variations are due to gravity waves (see, for example, Molina, 1983; Hecht *et al.*, 1997; Fritts *et al.*, 1997; and references contained therein). Figure 8.13 shows a striking example of these traveling waves. Indeed, a whole literature exists devoted to gravity waves in the upper atmosphere as revealed by airglow signatures and lidar sensing (see, for example, Swenson and Gardner, 1998). Of particular interest is the number of waves observed to be nearly monochromatic. Gravity waves launched in the troposphere propagate upward in the form of wave packets. Critical levels and wave reflections encountered as the packet moves upward erode the packet until only a small portion of the original wave spectrum exists. The result is a nearly monochromatic wave. Current thinking suggests that some of these waves are ducted modes in upper atmospheric wave guides (see, for example, Munasinghe *et al.*, 1998).

8.3.4 SATELLITES

Almost all analyses of gravity waves using satellite images are limited to wave clouds in the lee of mountains. Some of the first analyses were made, for example, by Döös (1962), Conover (1964), Fritz (1965), and Cohen and Doron (1967). Ernst (1976) analyzed infrared images of low-level mountain waves taken by a

geostationary satellite. He suggested that these data could be used for the early detection and identification of mountain waves and possible episodes of clear air turbulence. Satellite imagery continues to be used in mountain wave research (see, for example, Ralph *et al.*, 1997; Lane *et al.*, 2000; and Leutbecher and Volkert, 2000).

This Page Intentionally Left Blank

9

Data Analyses and Numerical Methods

In the previous chapter we examined some of the tools used to observe gravity waves. In this chapter we examine some of the techniques used to analyze these data and describe a few computer programs for these analyses. We also will describe numerical models of terrain-generated waves and ducted waves. However, before we proceed, we must keep in mind that waves or more accurately "wave-like" disturbances observed in the real atmosphere seldom resemble the waves imagined in the linear theory. This is especially true of waves in the planetary boundary layer where most observations of gravity waves are made. Figure 9.1 shows plots of vertical velocity observed with the University of Wyoming's King-Air B200 research aircraft during the CASES-99 field campaign (Poulos *et al.*, 2001). The wave-like structures and patches of what appears to be turbulence seen in the graphs are often observed in the stable boundary layer. The spatial series shown in Fig. 9.1 extend vertically from about 160 to about 1000 m above the ground surface and cover about a 90-min period. Between about 600 and 800 m we see waves and turbulence, but below 600 m we see mostly waves. The wave field is highly irregular, suggesting the existence of many waves. As pointed out by Finnigan (1988), gravity waves in the boundary layer are mostly nonlinear with time-changing amplitudes and frequencies. It is only when we go far from the disturbing effects of the ground surface that gravity waves take on a more ideal, *i.e.*, linear, structure.

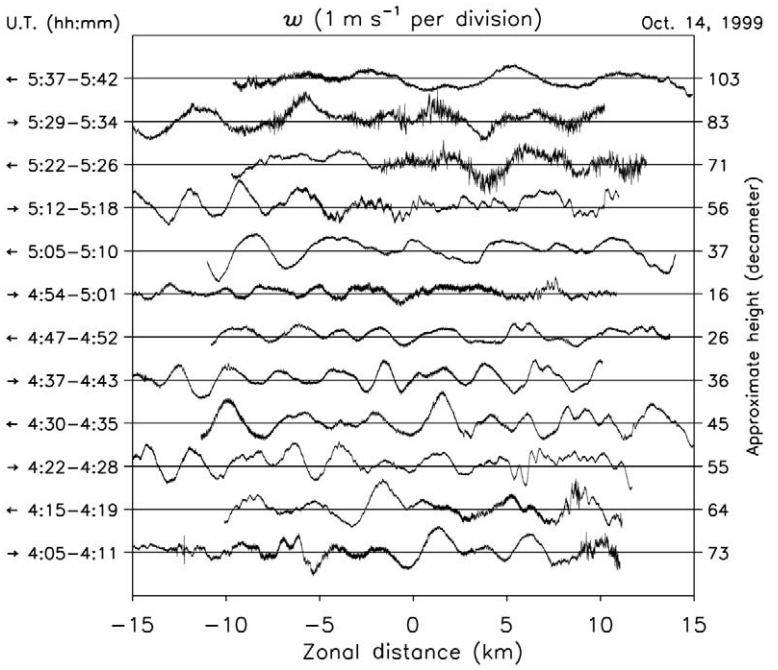

FIGURE 9.1 Vertical velocity recorded by the University of Wyoming King-Air B200 research aircraft on October 14, 1999, during the CASES-99 field campaign. The flights were in the east–west direction at various heights. The arrows on the left indicate the flight direction; the recording times are in universal time.

9.1 DATA ANALYSIS

Waves and turbulence are often observed to exist together, and separating their signals is both necessary and difficult. Classical turbulence theory is based on the simple notion that the flow field can be partitioned into a mean value, u_0, and a turbulence perturbation, u', where

$$u_0 = \frac{1}{2\tau} \int_{t-\tau}^{t+\tau} u(t')\, dt' \tag{9.1}$$

and

$$u'(t) = u(t) - u_0. \tag{9.2}$$

If waves are present in the flow, then depending on the averaging time τ and the frequencies of the waves, the partitioning will put low-frequency wave energy into the mean wind component and high-frequency wave energy into the turbulence. In a sense, the turbulence energy will be *inflated*. One of the important qualities of turbulence is its ability to disperse things such as pollutants, heat, momentum, *etc*.

Atmospheric air quality models rely on turbulence estimates, either measured or parameterized, to calculate the dispersion of atmospheric pollutants. If the turbulence is inflated by waves, then the diffusion will be overestimated, and the air concentrations will be underpredicted by the model. If the waves are not breaking, then the waves will not diffuse material. The waves can move material vertically or horizontally, but this is not a mixing process. Thus, putting wave energy into the turbulence cannot account for greater diffusion. However, as we shall see in this section, separating or isolating waves from observations is not simple, and this implies uncertainty in almost all gravity wave analyses in the boundary layer.

Before data can be analyzed for wave content, we must put the data in a form which approximates the linear theory. This usually requires removing linear trends and mean values and accounting for filtering effects such as attenuations and phase shifts. However, before this is done the data should be broken into blocks or segments of lengths comparable to the frequencies of the waves under consideration. For example, for waves with periods of several minutes, one may wish to break the data into blocks of 1-h lengths, but for waves with periods of hours, one may wish to have blocks with lengths of a day.

9.1.1 PRESSURE–WIND CORRELATION

The polarization equations (2.22)–(2.25) contain the correlations between the wave perturbation quantities. Gossard and Munk (1954) showed how these correlations can be used to determine wave characteristics. In particular, the correlation between pressure and wind perturbations can be used, since these are usually maximum near the ground surface, and can be measured with high precision. This *pressure–wind correlation* is demonstrated in Figs. 9.2 and 9.3. Figure 9.2 shows raw data traces recorded on October 14, 1999 during the CASES-99 field campaign in south-central Kansas (Poulas *et al.*, 2001). The data have been band-passed filtered over a 2–6 minute window. The correlation between the pressure, speed, and direction perturbations is obvious. Figure 9.3 shows the absolute surface pressure, the pressure perturbation, and the perturbation velocity associated with a mesoscale gravity wave event that occurred over the north–central United States on July 11–12, 1981. The wave episode lasted about 8 hours. The wave period had a mean value of 2.5 hours, the wavelength was about 160 km. The phase speed was about 19 m s^{-1}. The coefficient of correlation between p_1 and u_1 in Fig. 9.3 is about 0.95. This is a good illustration of utility and applicability of the linear theory. Gossard and Sweezy (1974) showed that the pressure–wind correlation is a direct measure of the wave signal-to-noise ratio. A strong pressure–wind correlation has been used as supporting evidence for gravity waves, for example, by Bosart and Cussen (1973), Bosart and Sanders (1983), and Koch and Golus (1988).

Gossard and Munk (1954) assumed constant wind speed and Brunt–Väisälä frequency and used (2.22) to get

$$u_1 = \frac{p_1}{\rho_0 (c - u_0)}. \tag{9.3}$$

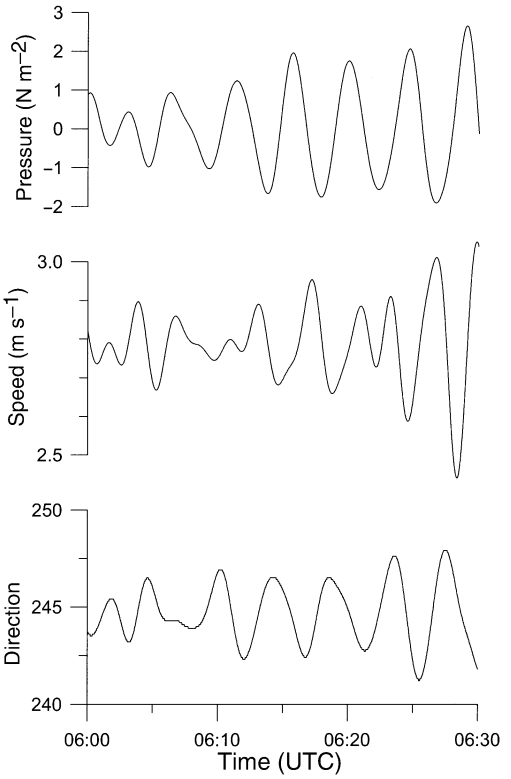

FIGURE 9.2 Band-passed (2–6 minute window) pressure, wind speed, and wind direction observed on October 14, 1999 during the CASES-99 field campaign.

They used (9.3) to define an *impedance relationship*,

$$c_I = c - u_0 = \frac{p_1}{\rho_0 u_1}, \tag{9.4}$$

which could be used to estimate wave characteristics using standard wind and pressure observations if the background wind was assumed constant. In (9.4), c_I is the intrinsic phase speed, and we note that because u_0 is assumed constant, c_I could be evaluated at any elevation. Before we can use (9.4), we must know the direction of wave propagation, and this is generally not known *a priori*. Figure 9.4 illustrates how the wave perturbations to the background horizontal wind can be used to determine the direction of the wave vector. Horizontal wind vectors over several wave cycles are calculated and plotted as shown in Fig. 9.4. The line connecting the extreme wind vectors lies in the direction of the wave vector. The midpoint of this line marks the magnitude and direction of the mean wind vector, and the magnitude of u_1 is equal to one-half of this line. The direction of the wave

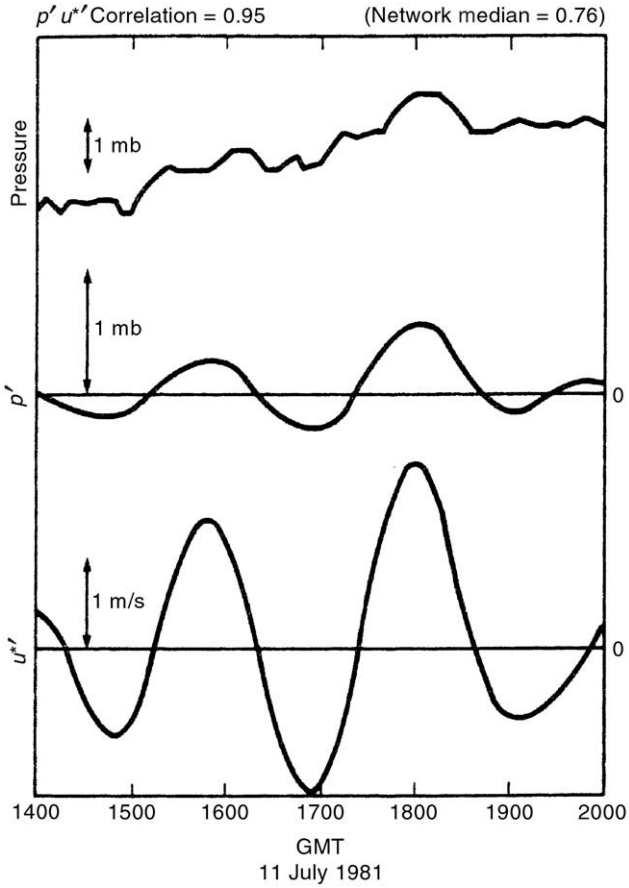

FIGURE 9.3 Time series of pressure (top), perturbation pressure (middle), and perturbation wind speed in the direction of wave propagation (From "A mesoscale gravity wave event observed during CCOPE. Part I: Multiscale statistical analysis of wave characteristics," S.E. Koch and R.E. Golus, *Mon. Weather Rev.*, **116**: 2532, 1988.)

along this line is determined by the location of maximum of p_1, as shown in Fig. 9.4. From the definition of phase velocity (1.18) we see that

$$c_I = c - u_0 = \frac{\Omega}{k} = \frac{\lambda_x}{\tau}, \tag{9.5}$$

where λ_x is the wavelength of the wave and τ is the wave period. Equation (9.5) can be used to estimate λ_x.

Although the pressure–wind correlation technique is straightforward to apply, it has several shortcomings. Turbulence in the surface layer can obscure wave

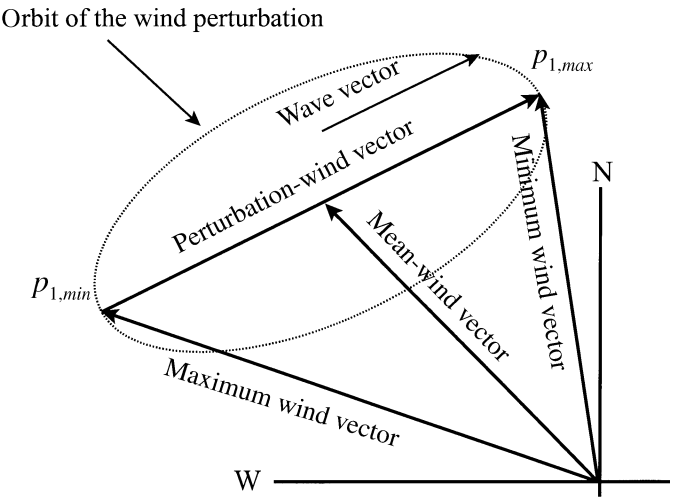

FIGURE 9.4 Mean-wind vector and wave perturbation velocity vector. Total velocity vectors at the extreme points are shown by the dashed vectors. The phase velocity is in the direction of maximum pressure perturbation.

perturbations, and if the background wind speeds are too low there will be uncertainty in the mean wind vectors. It has been assumed that linear wave theory is applicable near the ground surface; however, as discussed by Finnigan (1988), gravity waves in the planetary boundary layer are seldom linear. We have also assumed that the background wind and stratification are constant, but this is also not often the case. Indeed, strong wind shears and vertically changing temperature gradients are often seen near the ground surface. These deviations from ideal flow conditions can result in weak pressure–wind correlations.

9.1.2 LAG ANALYSIS

If a wave moves across an array of meteorological sensors with little change in frequency or wavenumber, then the arrival times of the disturbance at each station can be used to calculate wave characteristics. Consider a wave perturbation of some variable, q, observed at the ground surface or at the same altitude at each station so that we do not consider vertical variations of wave phase. Imagine a wave with constant amplitude and horizontal wave vector, $\vec{\kappa}_h$, observed at stations a and b whose separation is described by the vector $\vec{d}_{ab}$, as illustrated in Fig. 9.5. Let the horizontal wavelength of the wave be ℓ, and let the crests, or any other phase point, of the wave be observed at station a at time t and at station b at time $t + \tau_{ab}$ so that

$$q_a(kx_a + ly_a - \omega t) = q_b[kx_b + ly_b - \omega(t + \tau_{ab})], \tag{9.6}$$

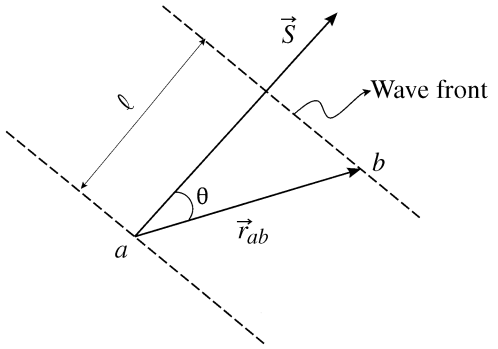

FIGURE 9.5 Wave front observed as it passes from station a to station b in time τ_{ab}. The wavelength of the wave is ℓ.

where k and l are the wavenumbers in the x- and y-directions, respectively. Because the wave does not change shape in moving from a to b, we can write

$$kx_a + ly_a - \omega t = kx_b + ly_b - \omega(t + \tau_{ab}), \tag{9.7}$$

which reduces to

$$k(x_a - x_b) + l(y_a - y_b) = \omega\tau_{ab}. \tag{9.8}$$

The left-hand side of (9.8) is recognized as $\vec{\kappa}_h \cdot \vec{d}_{ab}$, where $\vec{\kappa}_h$ is the horizontal component of the wave vector and $\vec{d}_{ab}$ is the distance vector between stations a and b. We can write (9.8) as

$$\frac{\vec{\kappa}_h}{\omega} \cdot \vec{d}_{ab} = \tau_{ab}. \tag{9.9}$$

From the definitions of phase velocity we see that

$$\frac{\vec{\kappa}_h}{\omega} = \left(\frac{1}{c_x}\right)\hat{x} + \left(\frac{1}{c_y}\right)\hat{y} = \vec{S}. \tag{9.10}$$

The vector $\vec{S}$ is called the *slowness* and has components S_x and S_y. The slowness vector is parallel to the wave vector and has a magnitude of $1/c$. Equation (9.9) now takes the form

$$\vec{S} \cdot \vec{d}_{ab} = \frac{|d_{ab}|}{c}\cos\theta = \frac{\ell}{c} = \tau_{ab}. \tag{9.11}$$

If there is another station, say d, with time lag τ_{ad} between stations a and d, then we have the simultaneous equations

$$S_x(x_a - x_b) + S_y(y_a - y_b) = \tau_{ab} \tag{9.12}$$

$$S_x(x_a - x_d) + S_y(y_a - y_d) = \tau_{ad} \tag{9.13}$$

which can be used to solve for S_x and S_y. Once known, the slowness components can be used to estimate the wave speed, c, and direction, ϕ, from which the wave is coming using

$$c = \frac{1}{\left(S_x^2 + S_y^2\right)^{1/2}} \tag{9.14}$$

$$\phi = \tan^{-1}\left(\frac{S_x}{S_y}\right). \tag{9.15}$$

The wave propagation angle is $\phi + 180$. If the wave frequency is known, then the horizontal wavenumber can also be estimated since $k = \omega/c$.

The use of lags between pairs of stations to estimate wave characteristics requires plotting the wave perturbations at each station and noting the times of passage of a particular crest or trough at each station, as illustrated in Fig. 9.6. This is a time-consuming procedure. An alternative approach to estimating lags was used by Rees and Mobbs (1988). Instead of using graphical data to estimate lag times, they calculated the cross-correlations as functions of lag time using wind speed data between pairs of wind stations in a three-station array. The cross-correlation

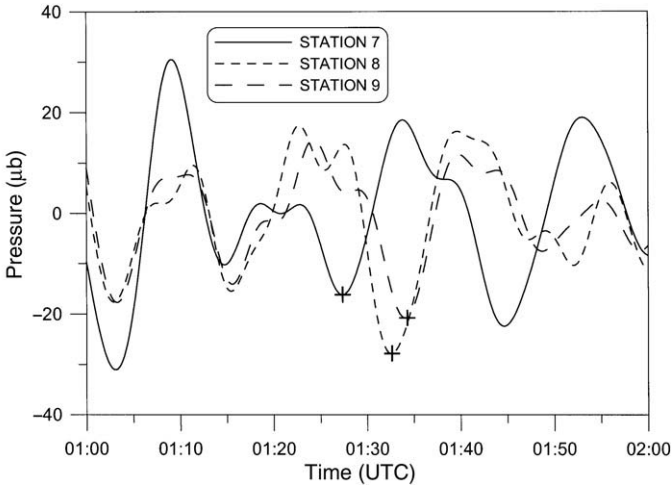

FIGURE 9.6 Pressure perturbations observed on October 18, 1999, during the CASES-99 field study. The crosses mark the times used to calculate wave speed and directions using time-leg analysis.

coefficient is defined as

$$r_{ij}(\tau_{ij}) = \frac{1}{t_2 - t_1}\frac{1}{\sigma_i \sigma_j}\int_{t_1}^{t_2-\tau_{ij}} q_i(t) q_j(t+\tau_{ij})\, dt, \tag{9.16}$$

where σ_i and σ_j are the standard deviations of q_i and q_j, respectively. Rees and Mobbs (1988) assumed that the time lag between stations i and j is that value of τ_{ij} which gives maximum cross-correlation. With three stations, three maximum lags can be estimated, and these can be used to obtain three estimates S_x and S_y. However, they caution that this method is sensitive to changes in wind speed, wave frequency, and wave amplitudes between stations. To check the accuracy of these lag estimates, Rees and Mobbs required that the sum of the two shorter lags equal the longest lag, *i.e.*,

$$|\tau_{ij} + \tau_{jk} - \tau_{ik}| < \epsilon, \tag{9.17}$$

where ϵ is a convergence factor which they take to be 15 s. This consistency check requires that the wave speed be constant along the array.

To illustrate the lag analysis method, consider the pressure perturbations shown in Fig. 9.6. These data were taken on October 18, 1999, during the CASES-99 field campaign. During the night, several short-duration, high-frequency disturbance events were observed to move over the sampling site. The locations of the digital-filter microbarographs operated during the experiment are shown in Fig. 8.12d. Figure 9.6 shows the pressure perturbations observed at the three outer microbarographs during the period 01:00 to 02:00 UTC. These data have been bandpass filtered and represent disturbances with periods between 5 and 25 min. The crosses mark the points which were used to identify the passing of the event at the three stations. The event was observed at Station 7 at 01:27.4, at Station 8 at 01:32.6, and at Station 9 at 01:34.3 (all times are UTC). The lags between the stations were $\tau_{79} = 416$ s, $\tau_{78} = 317$ s, and $\tau_{89} = 99$ s. We see that $|\tau_{78} + \tau_{89} - \tau_{79}| = 0$; the lags check for consistency. Using (9.12) and (9.13) gives $S_x = -0.219$ s m^{-1} and $S_y = 0.172$ s m^{-1}, and we estimate that the disturbance was moving to 231° with a speed of 3.6 m s^{-1}. If we use the time for maximum cross-correlation of pressure for estimating the lags, we get $\tau_{79} = 400$ s, $\tau_{78} = 340$ s, and $\tau_{89} = 70$ s. These values are close to the lags determined graphically, and the resultant speed and direction of the disturbance is estimated to be 3.6 m s^{-1}and 236°, respectively. The two methods give essentially the same results, and this suggests that the disturbance changed little as it crossed the array.

9.1.3 BEAMSTEERING

Rees *et al*. (2000) defined *beamsteering* as "any process that uses data from a spatial array of sensors to determine the direction from which a disturbance

is propagating." The method has been used by Young and Hoyle (1975); Einaudi, Bedard, and Finnigan (1989); Hauf *et al*. (1996); and Rees *et al*. (2000) to determine horizontal wave speeds and directions from surface pressures observed over a sampling array. Discussions of beamsteering techniques are found, for example, in Young and Hoyle (1975), Gossard and Hooke (1975), Asten and Henstridge (1984), and Denholm-Price and Rees (1999). To grasp the technique, imagine a plane wave with constant amplitude traveling horizontally over a sampling array. If it were possible to rotate the sampling array in the horizontal plane until maximum cross-correlation was obtained between all pairs of stations, then that direction would be the direction from which the wave was coming. The phase differences or time lags of the wave at the various sampling stations could then be used to estimate phase speeds. In reality, the "beam" of the array can be steered either through the time, *i.e.*, slowness domain where we seek maximum cross-correlation between pairs of stations, or through the frequency, *i.e.*, wavenumber domain where we seek maximum cross-power spectral density between pairs of stations.

9.1.3.1 Beamsteering in the Slowness Domain

Beamsteering in the slowness domain makes use of the cross-correlation of signals between station pairs. However, now the phase lags between station pairs are varied until maximum cross-correlation is achieved. Consider (9.11) in the form

$$\vec{S} \cdot \vec{d}_{ij} = \tau_{ij}\left(\vec{S}\right). \tag{9.18}$$

With the phase lag now a function of the slowness, and using (9.16), we can write

$$r_{ij}(\tau_{ij}) = \frac{1}{t_2 - t_1} \frac{1}{\sigma_a \sigma_b} \int_{t_1}^{t_2 - \tau_{ij}} q_i(t) q_j\left(t + \vec{S} \cdot \vec{d}_{ij}\right) dt, \tag{9.19}$$

i.e., the cross-correlation is also a function of the slowness vector. Imagine now a *slowness plane* with a horizontal axis S_x and a vertical axis S_y. Each point in this plane defines a slowness vector, and the scalar product of this vector with $\vec{d}_{ij}$ defines a lag, τ_{ij}, which can be used in (9.19) to calculate the cross-correlations between station pairs. Let these cross-correlations be defined as

$$R_{ij}\left(\vec{S}\right) = r_{ij}\left[\tau_{ij}\left(\vec{S}\right)\right]. \tag{9.20}$$

If there are M stations, then at each point in the slowness plane the average cross-correlation among nonrepeated pairs of stations in the array is

$$R(S_x, S_y) = \frac{2}{M(M-1)} \sum_{i=1}^{M-1} \sum_{j=i+1}^{M} R_{ij}\left(\vec{S}\right). \tag{9.21}$$

In practice, (9.21) is evaluated at each point in the slowness plane, and the location of the maximum value of R is taken to be the true slowness vector. Estimates of phase speed and direction are obtained using (9.14) and (9.15), respectively. Note that beamsteering in the slowness plane does not require information regarding the angular frequency of the disturbance being tracked. By implication, we know ω *a priori*. How this frequency is determined is discussed in Section 9.1.4. Because we know ω and the phase speed, the horizontal wavenumber of the disturbance can be obtained from $k = c/\omega$.

The FORTRAN computer program BEAMSTEER.FOR contained in the CD-ROM accompanying this book performs beamsteering in the slowness plane.

9.1.3.2 Beamsteering in the Frequency Domain

When beamsteering in the slowness domain, we know the wave frequency, and we search for the phase speed that leads to maximum cross-correlation. In the frequency domain, beamsteering searches for the horizontal wave vector and wave frequency that lead to maximum *cross-power spectral density* between station pairs. The cross-power spectral density function between stations i and j, $G_{ij}(\omega)$, is obtained by taking the Fourier transform of the cross-correlation function (9.16). $G_{ij}(\omega)$ consists of a real part, $C(\omega)$, called the *co-spectrum* and an imaginary part, $Q(\omega)$, called the *quadrature spectrum*, *i.e.*, $G_{ij} = C + iQ$. The phase relation between the frequencies being analyzed is

$$\tan(\omega\tau) = \frac{Q(\omega)}{C(\omega)}, \tag{9.22}$$

where τ is the time lag between the signals. The cross-spectral magnitude is

$$|G_{ij}(\omega)| = \sqrt{C^2(\omega) + Q^2(\omega)}. \tag{9.23}$$

Using (9.22) and (9.23) we can write

$$C(\omega) = |G_{ij}| \cos(\omega\tau) \tag{9.24}$$

$$Q(\omega) = |G_{ij}| \sin(\omega\tau). \tag{9.25}$$

We can replace τ in (9.24) and (9.25) using (9.9) to get

$$G_{ij}(\omega, \vec{\kappa}) = C + iQ = |G_{ij}(\omega)|\, e^{i\vec{\kappa}\cdot\vec{d}_{ij}}. \tag{9.26}$$

Following Gossard and Hooke (1975), we define an *array power spectrum* as the sum of (9.26) over all the combinations of pairs of sensors in an array of M sensors, *i.e.*,

$$\hat{G}(\omega, \vec{\kappa}) = \sum_{i=1}^{M} \sum_{j=1}^{M} G_{ij}(\omega)\, e^{i\vec{\kappa}\cdot\vec{d}_{ij}}. \tag{9.27}$$

Equation (9.27) is the wavenumber domain counterpart to beamsteering in the slowness domain. Now, one beamsteers in the wavenumber plane over various frequencies to search for that particular pair, ω and $\vec{d}_{ij}$, that gives the maximum value of $\hat{G}$. Because we now know ω and $\vec{\kappa}_H$, we can calculate the slowness components using $S_x = k/\omega$ and $S_y = l/\omega$. Then using (9.14) we can calculate the phase speed.

9.1.3.3 Array Response and Examples

Capon (1969) pointed out that a single monochromatic plane wave of frequency ω_0 and wavenumber $\vec{\kappa}_0$ differs only in phase at each station and, therefore, has a cross-power spectral density of the form

$$G_{ij}(\omega) = \delta(\omega - \omega_0)\, e^{-i\kappa_0 \cdot \vec{d}_{ij}}. \tag{9.28}$$

Using (9.28) in (9.27) gives

$$\hat{G}_{ij}(\omega, \vec{\kappa}) = \delta(\omega - \omega_0) \left| \sum_{j=1}^{M} e^{i(\vec{\kappa} - \vec{\kappa}_0) \cdot \vec{d}_j} \right|^2. \tag{9.29}$$

The function

$$H(\omega, \vec{S}) = \left| \frac{1}{M} \sum_{j=1}^{M} e^{-i\vec{\kappa} \cdot \vec{d}_j} \right|^2 = \left| \frac{1}{M} \sum_{j=1}^{M} e^{-\omega \vec{S} \cdot \vec{d}_j} \right|^2 \tag{9.30}$$

is called the *array response* function (also called the *array transfer* function). The array response function is an important parameter when considering array design. H has a peak value of unity at the origin in either the wavenumber plane, $(k, \ell) = (0, 0)$, or the slowness plane, $(S_x, S_y) = (0, 0)$. The response function is symmetric with respect to reflection through the origin, and it reveals side lobes which are caused by aliasing of wavelengths which are too small to be resolved by the sampling array. Figure 9.7 shows a plot of the response function for the ideal array shown in Fig. 8.11, and Fig. 9.8 shows a plot of the response for the six-station array shown in Fig. 8.12d. In both cases, $\omega = 0.03$ s^{-1}. Side lobes are present, and these indicate the wavenumber or phase speed limits to the beamsteering. The response function plots the sensitivity of the array to a stationary wave. If the wave is moving across the array, then the peak of the response function is moved in the direction from which the wave is coming. This is illustrated in Fig. 9.9, which shows the contours of $R(S_x, S_y)$ resulting from a wave with a wavelength of 10 km coming from 45° with a speed of 20 m s^{-1}across the array shown in Fig. 8.12d. Figure 9.10 shows the $R(S_x, S_y)$ contours for a wave with a 1-km wavelength coming from 45° with a speed of 5 m s^{-1}across the same

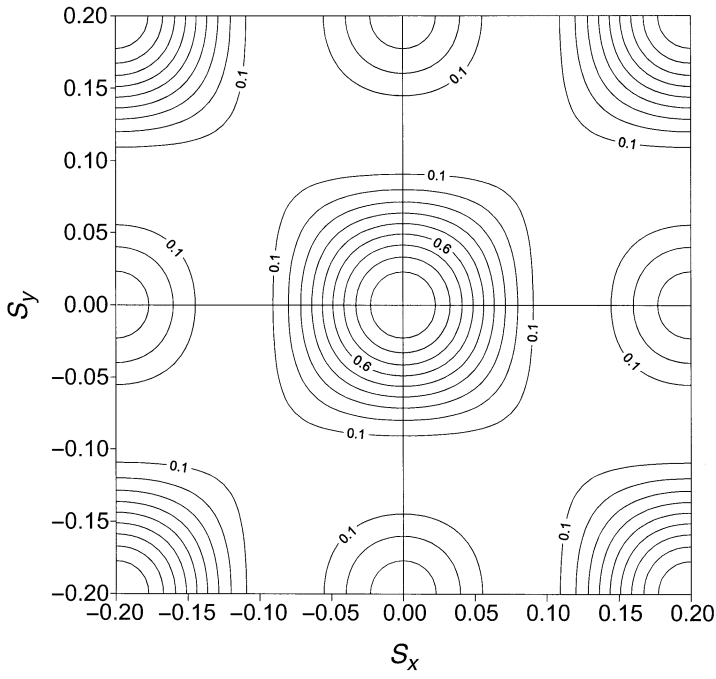

FIGURE 9.7 Array response for the ideal five-sensor array shown in Fig. 8.11.

array as in Fig. 9.9. In this case, the side lobes are quite pronounced. Note that the ranges of the slowness axes in Fig. 9.10 have been doubled relative to those in Fig. 9.9 in order to "see" the maximum cross-correlation. This illustrates one of the fundamental difficulties in beamsteering. In any real application, we will not know *a priori* the wave characteristics, and so we will not be able to adjust the beamsteering parameters in order to achieve maximum sensitivity. In general, one can expect a trial-and-error approach to the problem. Further complications arise when the waves are nonlinear or changing in frequency or amplitude as they move across the sampling array. In these not unusual circumstances one must be prepared to accept a degree of uncertainty in the estimated wave characteristics.

9.1.4 WAVELET ANALYSIS

A time series of a perturbation, say, surface pressure, may consist of several noninteracting waves and turbulence. These waves may be quite different in frequency and wavelength and may be moving in different directions. Only on rare occasions will a single frequency or, more accurately a narrow frequency band, be detected from visual examination of the data. Indeed, in many cases we may not be certain that a wave is present in the data. Beamsteering in the slowness plane

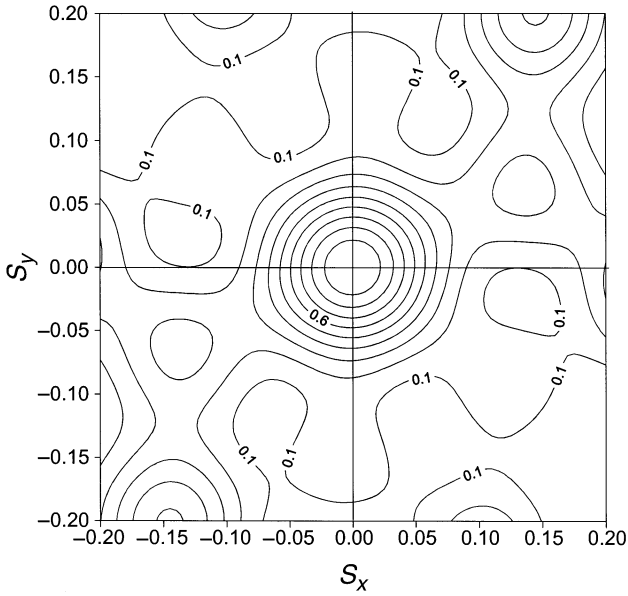

FIGURE 9.8 Array response for the six-sensor array shown in Fig. 8.12d.

requires information on the frequency of the disturbance. Thus, a necessary component of analysis is a means to identify waves and to estimate their frequencies. Spectral techniques have often been used to detect gravity waves in data records (see, for example, Caughey and Readings, 1975; De Baas and Driedonks, 1985; Hunt, Kaimal, and Gaynor, 1985). Spectral methods generally work well when wave amplitude is large and when the wave persists for many cycles. However, small-amplitude waves and waves of short duration can be overlooked by spectral calculations. For example, if a wave persists for 15 min, and if the spectrum is calculated over an hour, then the wave may not be detected. Sometimes two or three waves can exist, each with different but not greatly different frequencies. A spectrum calculation may merge these frequencies into a single broad frequency band, which may have relatively little physical meaning. A short-period wave may sporadically appear for short durations over a few hour's time; however, in a spectrum analysis the wave may appear to have a much longer period. It is clear that spectral techniques may not always be useful in analyzing gravity waves. However, the difficulties just described do not greatly affect the *wavelet analysis* method.

Wavelet transforms which are the bases of the wavelet analysis were formally introduced in the early 1980s. Historical backgrounds and introductions to the formalism can be found, for example, in Combes, Grossman, and Tchamitchian, (1989); Chui (1992); Foufoula-Georgiou and Kumar (1994); Treviño and Andreas (1996); and Torrence and Compo (1998). Examples of wavelet analysis used in

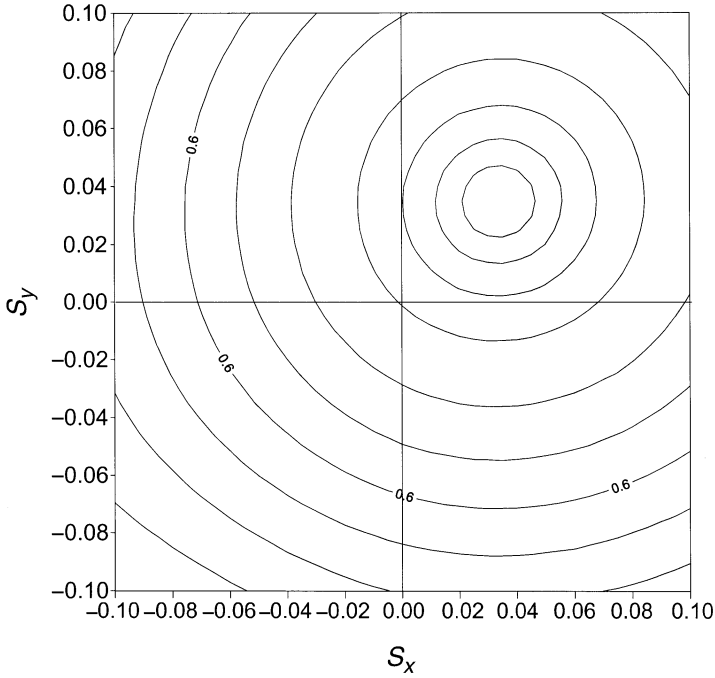

FIGURE 9.9 Contours of cross-correlation in the slowness plane for a wave with a wavelength of 10 km moving at 20 m s^{-1} from 45°.

gravity wave studies are found in Hauf *et al.* (1996); Rees, Staszewski, and Winkler (2001); and Zink and Vincent (2001). Perhaps unwittingly, Herron, Tolstoy, and Kraft (1969) were one of the first to use a wavelet-type approach to data analysis. A description of their technique may be helpful in understanding the nature of the transforms. In an investigation of mesoscale pressure fluctuations, Herron, Tolstoy, and Kraft observed a strong correlation in velocity and direction between gravity waves and the jet stream. Cross-spectral analyses were performed on pairs of microbarograph signals to estimate phase angles and coherences between station pairs. To search the records for intervals of high coherence and to measure motions of the pressure fluctuations, a "moving" cross-spectrum analysis computer program was developed in which a "time window" was moved sequentially across a set of values in overlapping steps. Within each time window, the cross-spectra were calculated between various pairs of signals in the set. The time at the center of the window was assigned to each coherence and phase angle estimate. It is this windowing process that is the basis of the wavelet transformation. By varying the width of the time window, lower frequencies are introduced into the spectrum. Repeated passes through the time series with increasing window size results in a decomposition of the series into time-frequency space. This results in a *localization* in time of the statistics, for example, cross-spectrum or power spectrum.

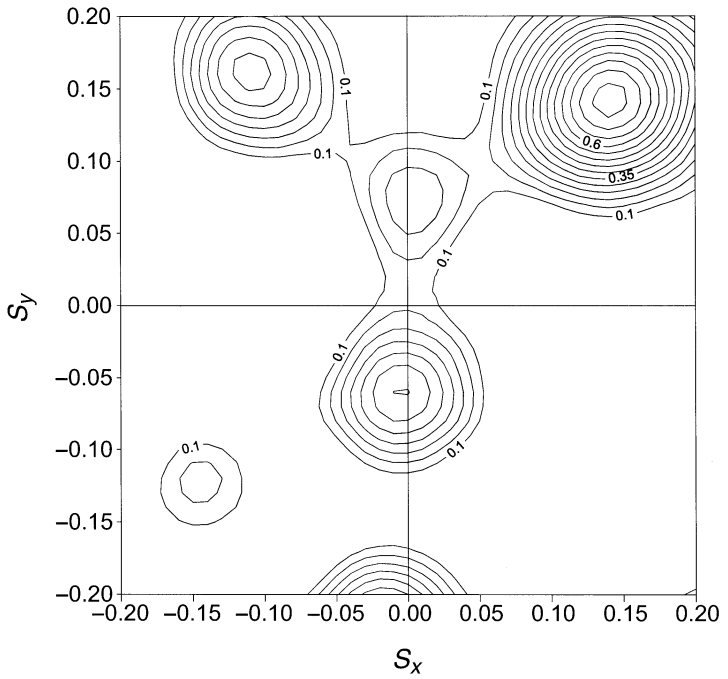

FIGURE 9.10 Contours of cross-correlation in the slowness plane for a wave with a wavelength of 1 km moving at 5 m s^{-1} from 45°.

This contrasts with the *global* view generated by the one-dimensional Fourier transform approach. In the Fourier transform approach, we calculate the total cross-spectrum or power spectrum over the whole time series, but we have no idea how the spectrum varies with time. We can integrate the wavelet energy density over frequency and time to recover the total variance of a time series, but we cannot differentiate a power spectrum with respect to time to see how the spectrum varies with time. This is an example of the utility of the wavelet transform.

We cannot provide here a formal discussion of wavelet analysis. Instead, we present a brief discussion of the technique and present some examples of its use. We also note that computer libraries of mathematical functions such as IDL and MATLAB provide wavelet analysis packages in the same way they provide Fast Fourier Transform packages. Thus, except for special circumstances, it is unnecessary to write wavelet analysis codes. However, as an instruction tool, the FORTRAN program WAVELET.FOR is included in the CD-ROM accompanying this book.

The *wavelet coefficients*, $y(t, a)$, are defined by the continuous wavelet transform of a time series, $x(t)$, as (see, for example, Meneveau, 1991; Farge, 1992)

$$y(t, a) = \int_{-\infty}^{\infty} g_a(t - t')x(t')\,dt', \tag{9.31}$$

where

$$g_a(t) = \frac{1}{a} g\left(\frac{t}{a}\right). \tag{9.32}$$

The basis of the transform is the *mother wavelet* $g(t/a)$, and a is a *dilation* time scale. The function g_a in (9.31) represents a time window of varying width, and the coefficients $y(t, a)$ represent the amplitude of $x(t)$ at dilation a and time t. The Fourier transform of the mother wavelet replaces the time window by a frequency window, *i.e.*,

$$\hat{g}(\omega) = \int_{-\infty}^{\infty} g(t)\, e^{-i\omega t}\, dt. \tag{9.33}$$

The windowing properties are determined by the mother wavelet. We want the window to decay quickly for large time and frequency. The Fourier-transformed window function will have a central frequency ω_c and an effective width σ. Thus, $\hat{g}_a(\omega) = \hat{g}(a\omega)$, with central frequency ω_c/a and effective width σ/a.

We want a window that will give the best resolution of wave-like signals. The window most frequently used is the complex-valued *Morlet* wavelet

$$g(t) = e^{i2\pi t}\, e^{-t^2/2}, \tag{9.34}$$

which represents a sine wave with a Gaussian amplitude. The family of dilated wavelets (9.32) is then

$$g_a(t) = \frac{1}{a} \exp\left(i2\pi \frac{t}{a} - \frac{t^2}{2a^2}\right). \tag{9.35}$$

Figure 9.11 plots the real, *i.e.*, symmetric, part of the Morlet wavelet (9.35) in physical space for dilation values of 1, 2, and 3 s. We see that the amplitude of the window, g_a, decreases with increasing dilation, a, but the window width increases with increasing dilation. The Fourier transform of (9.35) is the window function in frequency space and is given by

$$\hat{g}_a(\omega) = \frac{1}{(2\pi)^2} \exp\left[-\frac{\omega - 2\pi/a}{2/a^2}\right]. \tag{9.36}$$

The center frequency of the window is $\omega_c = 2\pi/a$, and the window width is $\sigma = 1/a$. The oscillation period of the center frequency is $T_a = 2\pi/\omega_c = a$. Note that because the real part of g_a is symmetric, its Fourier transform is real. Figure 9.12 shows plots of $\hat{g}_a(\omega)$ for $a = 1$, 2, and 3 s. The functions g_a behave much like a filtering function in a bandpass filter.

The *wavelet energy density* is defined as

$$W(t, a) = \frac{1}{a^2} y(t, a) y^*(t, a), \tag{9.37}$$

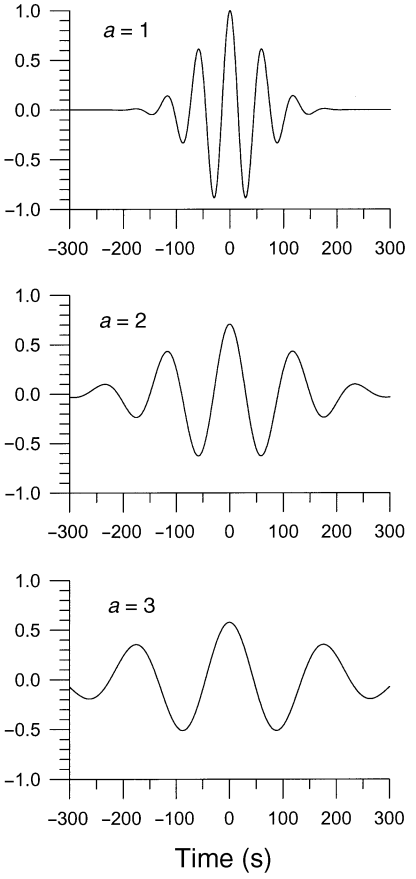

FIGURE 9.11 The Morlet wavelet for various values of the time dilation parameter a.

where * indicates the complex conjugate. A *wavelet analysis diagram* (Hauf *et al.*, 1996) is created by contouring W in either time-frequency space $(t, 1/a)$ or time-period space (t, a). Figure 9.13 shows contours of wavelet energy density calculated from surface pressure data taken on October 14, 1999, during the CASES-99 field campaign (Poulos *et al.*, 2001). Throughout the night of October 14, what appears to have been a ducted gravity wave with period of about 4 min sporadically appeared. Waves with periods centered at about 10 min also appeared. Figure 9.14 plots the filtered pressure data for the period 05:00 to 06:30 UTC. The two frequencies shown in the wavelet analysis diagram between about 05:20 and 05:40 are clearly seen in Fig. 9.14. Similar results can be found in Hauf *et al.* (1996). Recently, Rees, Staszewski, and Winkler (2001) used wavelet transforms to identify periods of wave activity and turbulence. It is expected that the applications of wavelet analysis will continue to

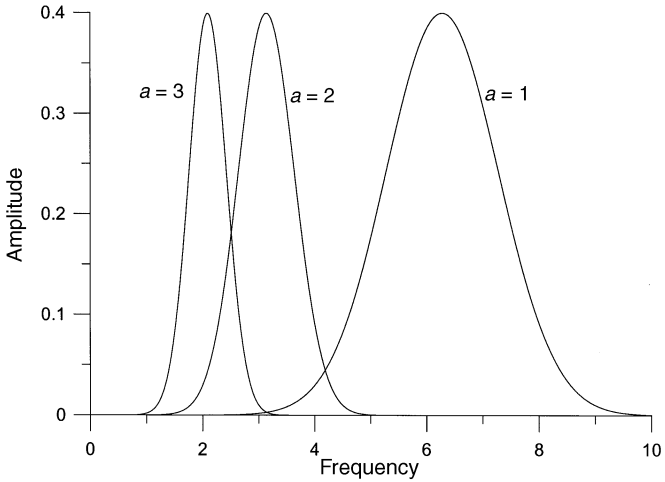

FIGURE 9.12 The Fourier-transformed Morlet wavelet for various values of the time dilation parameter a.

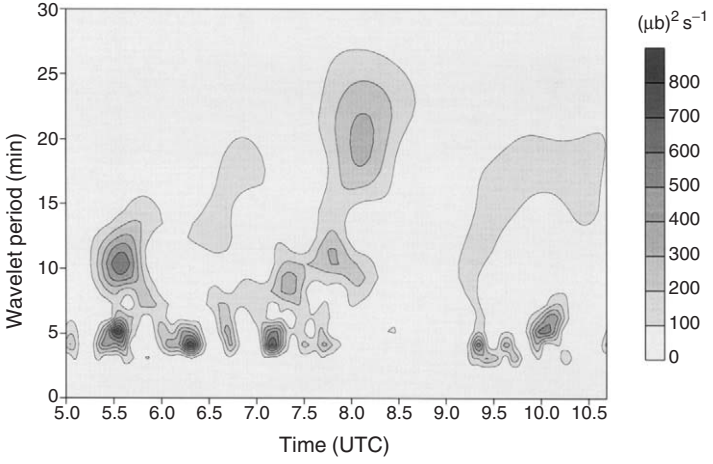

FIGURE 9.13 Wavelet analysis diagram derived from data observed on October 14, 1999, during the CASES-99 field campaign. The contour scale is in $\mu b^2\ s^{-1}$.

expand, especially in the study of waves and turbulence in the stable boundary layer.

9.2 NUMERICAL MODELS

In this section, we describe the linear wave computer models contained in the CD-ROM that accompanies this book. Two problems are considered: terrain-generated gravity waves over a surface corrugation and over an isolated Gaussian

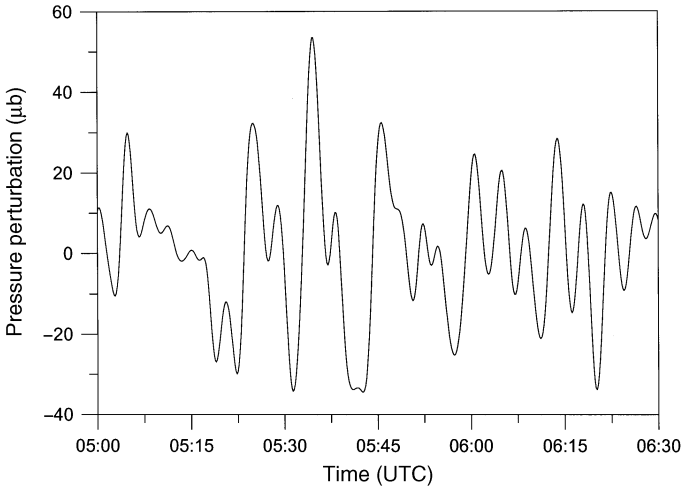

FIGURE 9.14 A sample of the bandpass filtered data used to construct the wavelet analysis diagram shown in Fig. 9.13.

ridge; and wave ducting in a temperature duct and a pure wind duct. In all cases, the computer codes solve the Taylor–Goldstein equation. Recall that if the background wind and temperature fields are constant, then the terrain-generated case can be solved by inspection. However, in such a flow ducting will not occur because wave reflection does not occur. In general, however, we wish to apply the linear theory to real situations, and this requires numerical solutions.

These numerical codes are intended for illustration and should be used as a guide for model development. The programming language is FORTRAN. We realize that more advanced languages exist; however, FORTRAN is a rather transparent code and provides a good basis for advanced model development using higher order languages. Note that in-line graphics are not included in the codes. Many software graphics packages exist, and rather than try to address these it was decided to provide output files which could then be used in graphics packages. Of course, the readers are free and encouraged to modify the codes in any way they wish.

As previously mentioned, the ultimate goal of these codes is to solve the Taylor–Goldstein equation. This is a homogeneous, second-order, partial differential equation with nonconstant coefficients. We use the so-called *extrapolation method* based on the IMSL subroutine DREBS which is a modification of the Bulirsch-Stoer ALGOL procedure DESUB (Bulirsch and Stoer, 1966; Gragg, 1965). While this method is old by today's standards, it is retained in these codes for the simple reason that it works. However, more powerful differential equation solvers are available, and these should be used, especially if computational speed is required. Consider now the differential equation

$$\Phi'' + Q^2(z)\Phi = 0, \tag{9.38}$$

where primes denote vertical derivatives. DREBS solves the system of equations defined by

$$y = \Phi' \tag{9.39}$$

$$\frac{dy}{dz} = -Q^2(z)\Phi. \tag{9.40}$$

Beginning at a boundary point with given values of Φ and Φ', (9.39) and (9.40) are extrapolated vertically (either upward or downward as required) to a prescribed point, say, $z = ztop$. The extrapolation proceeds in vertical steeps of size H. At each step, $Q^2(Z)$ must be evaluated. In the case of the Taylor–Goldstein equation, u_0 and θ_0 must be expressed as continuous differentiable functions of z. The initial step size of the extrapolation is $ztop$. If the equations do not converge at $ztop$ to within a prescribed tolerance, then DREBS halves the step size and repeats the calculation. The process continues until either convergence is reached at $z = ztop$ or the step size becomes less than some prescribed step size. The coefficient $Q^2(z)$ is evaluated in the user-supplied subroutine *FCN*. We shall look at two forms of the background wind and temperature profiles, *i.e.*, analytical expressions and discrete values specified at a finite number of vertical levels. These latter values could be the output values of wind speed and temperature from a forecast model.

9.2.1 TERRAIN-GENERATED GRAVITY WAVE

Regardless of the terrain feature, for example, a two-dimensional surface corrugation, a two-dimensional ridge, or a three-dimensional mountain, the top and bottom boundary conditions are of the same form, *i.e.*, radiation condition at the top of the model and kinematic condition (3.14) at the ground surface. The models differ only in their spatial dimensionality and the Fourier transforms of the surface height. This simplifies the problem. For example, the two-dimensional surface corrugation and the two-dimensional ridge use essentially the same code. In the first case we solve for a single wavenumber, while in the second case we must solve for a series of wavenumbers and then take the inverse Fourier transform to get the perturbation wave field in physical space. For the terrain-generated wave we calculate the perturbation velocities, potential temperature, pressure, and wave stress. As a check, we examine the constancy of the wave stress when wave breaking does not occur. We also consider wave breaking at a critical level. The codes also contain the terrain-height adjustment parameterization discussed in Section 7.2.2.

The Taylor–Goldstein equation (2.29) along with (3.1) takes the form

$$\frac{d^2\hat{w}_n}{dz^2} + \left[\frac{N^2}{u_0^2} - \frac{u_0''}{u_0} - k_n^2\right]\hat{w}_n = 0, \tag{9.41}$$

where we have assumed that the vertical wavelengths are small compared to the adiabatic scale height, H_s, and the subscript n refers to the nth component of the Fourier transform of w_1. We set the top of the model domain at height $z = ZTOP$ and assume that above this height the background wind speed and stratification are constant. This allows us to use the radiation boundary condition at *ZTOP*. The general solution for $z \geq ZTOP$ takes the form

$$\hat{w}_n(k_n, z) = A_n\, e^{im_n(z-ZTOP)} + B_n\, e^{-im_n(z-ZTOP)}. \tag{9.42}$$

where m_n is the constant vertical wavenumber given by

$$m_n = \left[\frac{N^2(ZTOP)}{u_0^2(ZTOP)} - k_n^2\right]^{1/2}. \tag{9.43}$$

If m_n is not real at *ZTOP*, then there is no wave stress associated with that Fourier component. We have seen in Chapter 3 that the A_n solutions in (9.42) correspond to upward-moving wave fronts and downward-moving energy and that the B_n solutions correspond to downward-moving wave fronts and upward-moving energy. Thus, in order to satisfy the radiation boundary condition at $z = ZTOP$, the solution of (9.42) is

$$\hat{w}_n(k_n, ZTOP) = B_n(k_n), \tag{9.44}$$

and the vertical derivative at *ZTOP* is

$$\frac{d\hat{w}_n}{dz} = -im_n\, B_n(k_n). \tag{9.45}$$

From (3.47), the bottom boundary condition is

$$\hat{w}_n(kn, 0) = ik_n u_0(0)\hat{h}(k_n), \tag{9.46}$$

where $\hat{h}$ is the Fourier transform of the terrain height. If we introduce the shape factor $\Phi(k_n, z)$ defined by (3.50), *i.e.*,

$$\hat{w}_n = \hat{w}_n(k_n, 0)\frac{\Phi(k_n, z)}{\Phi(k_n, 0)}, \tag{9.47}$$

then below *ZTOP* the Taylor–Goldstein equation has the form

$$\frac{d^2\Phi}{dz^2} + \left[\frac{N^2}{u_0^2} - \frac{u_0''}{u_0} - k_n^2\right]\Phi = 0, \tag{9.48}$$

with the upper boundary condition $\Phi(k_n, ZTOP) = 1$. We also see that $B_n(k_n) = \hat{w}_n(k_n, 0)/\Phi(k_n, 0)$.

Below *ZTOP*, we must account for upward and downward (reflected) waves, and this is done by choosing the Φ complex, *i.e.*, $\Phi = \Phi_r + i\Phi_i$. We must solve (9.48) for the real and imaginary parts of Φ. We begin the integrations at $z = ZTOP$, where

$$\Phi_R + i\Phi_I = 1 \tag{9.49}$$

$$\Phi'_R + i\Phi'_I = -im_n, \tag{9.50}$$

and hence

$$\Phi_R = 1 \tag{9.51}$$

$$\Phi_I = 0 \tag{9.52}$$

$$\Phi'_R = 0 \tag{9.53}$$

$$\Phi'_I = -m_n. \tag{9.54}$$

The vertical structure of the mountain wave field is obtained by solving (9.48) at a number of vertical levels. We simplify the model by using equal spacing between the model levels; however, the spacings do not have to be equal. Before the integrations begin, the background wind is checked for critical levels, *i.e.*, where $u_0 = 0$. The models assume complete wave absorption at a critical level, and so only the lowest critical level is considered. Subroutine CRLEV carries the solutions over the critical level, as discussed in Chapter 5. Subroutine WINDXZ calculates the wave perturbation quantities in physical space, checks for wave breaking, and accounts for wave saturation using the terrain-height adjustment scheme. If a critical level exists, then the wave stress is decreased linearly from the first wave-breaking level to the critical level.

As previously mentioned, two types of background wind and temperature profiles are possible: continuous analytical expressions and discrete values defined at the model levels. Because subroutine DREBS must evaluate $Q^2 = (N^2/u_0^2) - (u_0''/u_0) - k_n^2$ at any height, analytical expressions for wind speed and temperature are desirable. However, in many applications we know the background wind speeds and temperatures only at discrete points. An example is the output from a weather forecast model. It may be possible to make these data continuous by either fitting the points to a polynomial expression or using splines. A simple approach is to join these points with straight lines so that within each model layer u_0 varies linearly with z and N is constant. However, this procedure will result in discontinuities in u_0' at the model levels, and this can lead to discontinuities in pressure across the model levels. At each model level, the dynamic and kinematic boundary conditions must hold. Recall from Section 4.1, that the dynamic boundary condition requires continuity in pressure across the

boundary, and the kinematic boundary condition requires continuity in vertical velocity across the boundary. Using (2.22), (2.24), and (3.50) and noting that for mountain waves $\Omega = -u_0 k_n$, we write for Φ_r

$$u_0 \frac{d\Phi_r}{dz} - \Phi_r \frac{du_0}{dz} = ik\frac{\tilde{p}}{\rho_0}. \tag{9.55}$$

At each model level J, we apply (9.55) above and below J and require that $\tilde{p}_{J+1} = \tilde{p}_{J-1}$ and $\Phi_{J+1} = \Phi_{J-1}$. Noting that u_0 is continuous at J, we get

$$\Phi'_{r,J} = \Phi'_{r,J+1} - \frac{u'_{0,J+1} - u'_{0,J-1}}{u_{0,J}} \Phi_{r,J+1}, \tag{9.56}$$

where $u'_{0,J+1}$ and $u'_{0,J-1}$ are the background wind shears in the upper and lower layers, respectively, and $\Phi'_{r,J+1}$ and $\Phi_{r,J+1}$ are calculated by DREBS extrapolation in the upper layer to level J. A similar calculation is made for Φ_1.

Computer codes are given for four cases: a surface corrugation and a Gaussian-shaped ridge each with continuous or discrete background wind speed profiles. For all cases, the wind profile is described by the hyperbolic-tangent function,

$$u_0(z) = -0.5(UB + UT) + 0.5(UB - UT)\tanh\left(\frac{z - ZI}{ZS}\right), \tag{9.57}$$

where *UB* is the wind speed at the bottom of the model, *UT* is the wind speed at the top of the model, ZI is the height of the inflection point of the profile, and ZS is a vertical scale height. The speed changes from *UB* to *UT* in a vertical distance of about $4ZS$. For simplicity, the thermal stratification in each model is constant so that the Brunt–Väisälä frequency is constant; however, provision is made in the codes for nonconstant temperature gradients, *i.e.*, height-varying Brunt–Väisälä frequency. The codes *CORRUGATION_C.FOR* and *RIDGE_C.FOR* simulate the surface corrugation and surface ridge, respectively, with continuous background wind profiles. *CORRUGATION_D.FOR* and *RIDGE_D.FOR* consider the case of discrete background wind profiles. The input data are contained in the files *CORRUGATION_INPUT.DAT* and *RIDGE_INPUT.DAT*. Output files, for example, *CORRUGATION_C_UWTP.DAT*, contain the wave perturbation fields in physical space. These data can be used to generate isopleths, calculate energy flux, *etc*. Output files, for example, *CORRUGATION_C_OUTPUT.DAT*, contain the vertical profiles of background wind speed and wave stress. Of course, these output quantities can be modified as the reader wishes.

9.2.2 DUCTED GRAVITY WAVES

We have seen in Chapter 4 that wave ducting is an eigenvalue problem. For a given flow, only those waves associated with a family of wavenumbers and associated frequencies will be ducted. This is because ducting requires wave reflections from vertical boundaries, and wave reflection is a function of stratification, wind speed, phase speed, and wavenumber. Most commonly, one of the boundaries is the ground surface, and the other is an elevated layer of sharp change in stratification or wind speed or even both. However, elevated ducting regions above the ground surface are also possible when there are velocity jets.

The numerical solution of the ducting problem involves the search for waves with eigenvalues (k, c), which are solutions to the Taylor–Goldstein equation and which satisfy the boundary conditions. At the ground surface, we require $\hat{w} = 0$. At the top boundary of the model, the ducted wave must be evanescent because the wave must not transport energy out of the model domain. In this case, the wave energy is confined below the top boundary. Unlike the terrain-generated wave, we do not consider upward- and downward-propagating waves. Instead, we seek a horizontally propagating wave with node points at the ground surface and some upper reflecting height. Thus, we take Φ to be real. We do not consider critical levels. If a critical level exists, and if the Richardson number is greater than 0.25, then the wave will be absorbed. If instead the Richardson number is less than 0.25, then unstable modes will develop, and these codes are not designed to search for unstable modes. In either case, a critical level will result in no ducting. The modes we consider are stable. As in the previous section, the Taylor–Goldstein equation is solved using the DREBS extrapolation technique. However, because we cannot determine wave amplitudes and because there is neither stress nor upward-propagating energy associated with ducted waves, we need not calculate the wave field at various vertical levels. This greatly simplifies the problem, especially if we have analytical expressions for the background wind and temperature profiles. Above $z = ZTOP$, the background wind and stratification is assumed constant so that

$$\Phi = A\, e^{q(z-ZTOP)} + B\, e^{-q(z-ZTOP)}, \tag{9.58}$$

where

$$q^2 = k^2 - \frac{N^2(ZTOP)}{(c - u_0(ZTOP))^2}. \tag{9.59}$$

The solution is obtained by finding the eigenvalues k and c that result in $A \to 0$ at $ZTOP$. At the top boundary, (9.58) and its first derivative take the form

$$\Phi = A + B \tag{9.60}$$

$$\frac{d\Phi}{dz} = qA - qB. \tag{9.61}$$

Solving (9.60) and (9.61) for A and setting this result to zero gives

$$GROW = \Phi + \frac{1}{q}\frac{d\Phi}{dz} = 0. \tag{9.62}$$

We begin with a relatively large wavenumber and an initial phase speed. Because we do not consider critical levels, the minimum phase speed must be greater than the maximum background wind speed, *i.e.*, $c_{min} > u_{0,max}$. At *ZTOP* from (9.59) we require $k > N(ZTOP)/(c - u_0(ZTOP))$ so that the maximum phase velocity is $c_{max} = N(ZTOP)/k + u_0(ZTOP)$. The phase speeds of the ducted waves must lie between c_{min} and c_{max}. The extrapolation solution of the Taylor–Goldstein equation begins at the ground surface where $\Phi = 0$; and $d\Phi/dz$ is set to one, and $c = c_{min}$. At *ZTOP*, the value of *GROW* is calculated using (9.62), and the values of c and *GROW* are stored in a file. The calculation is repeated, but now with a slightly greater phase speed, $c_{min} + \Delta c$. Again c and *GROW* are stored. The procedure continues until we have run through the range of phase speeds. Examination of the stored output values shows that every so often *GROW* changes sign between adjacent values of c. This indicates a passage of *GROW* through zero and the presence of a ducted mode. We assume that the first zero crossing corresponds to the fundamental mode, c_0. The second crossing corresponds to the first harmonic mode, c_1, *etc*. However, we will need to refine these estimates of phase speed if we

TABLE 9.1 Mode Scans for a Pure Temperature Duct

	First scan		Second scan	
Fundamental mode	$c = 4.272$	$GROW = 9.362$	$c = 4.2386$	$GROW = 0.050$
	$c = 4.250$	$GROW = 3.281$	$c = 4.2385$	$GROW = 0.020$
	$c = 4.228$	$GROW = -2.715$	$c = 4.2383$	$GROW = -0.010$
	$c = 4.207$	$GROW = -8.622$	$c = 4.2382$	$GROW = -0.040$
First harmonic	$c = 2.761$	$GROW = -11.503$	$c = 2.7243$	$GROW = -0.039$
	$c = 2.739$	$GROW = -4.599$	$c = 2.7241$	$GROW = -0.004$
	$c = 2.717$	$GROW = 2.369$	$c = 2.7240$	$GROW = 0.031$
	$c = 2.695$	$GROW = 9.378$	$c = 2.7239$	$GROW = 0.066$
Second harmonic	$c = 1.906$	$GROW = 13.571$	$c = 1.8811$	$GROW = 0.100$
	$c = 1.884$	$GROW = 1.754$	$c = 1.8810$	$GROW = 0.040$
	$c = 1.862$	$GROW = -10.295$	$c = 1.8809$	$GROW = -0.020$
	$c = 1.840$	$GROW = -22.427$	$c = 1.8808$	$GROW = -0.080$
Third harmonic	$c = 1.446$	$GROW = -30.862$	$c = 1.4107$	$GROW = -0.109$
	$c = 1.424$	$GROW = -12.085$	$c = 1.4106$	$GROW = -0.010$
	$c = 1.402$	$GROW = 7.626$	$c = 1.4105$	$GROW = 0.090$
	$c = 1.380$	$GROW = 27.587$	$c = 1.4104$	$GROW = 0.189$

Note: c = phase speed; *grow* = amplitude of exponentially growing wave component at top of model.

are to locate the true eigenvalue of c. To do this, we repeat the mode scan, but now with c_{min} and c_{max} set equal to the phase speeds on either side of the sign change of *GROW*. This second scan is usually sufficient to find the value of c that results in an acceptably small absolute value of *GROW*. Table 9.1 lists the results for the first and second scans for modes in a pure temperature duct calculated with program *TEMP_DUCT_SCAN.FOR*. For this case, the ducting region extends from the ground surface to 300 m. The Brunt–Väisälä frequency is 0.055 s^{-1} below 300 m and zero above. There is no background wind. At this point, we know only pairs of eigenvalues corresponding to the ducting modes. However, each mode has a family of eigenvalues such as those plotted in Fig. 4.11. To generate these curves we must increment the wavenumber value and scan the phase speeds for wave ducting, *i.e.*, where *GROW* $\rightarrow$ 0. The program *TEMP_DUCT_MODES.FOR* performs these calculations for the pure temperature duct. These calculations begin with the first eigenvalues for a given mode, and the computer program must be executed for each mode. However, the interested reader could construct a code to do all these calculations in one run. *TEMP_DUCT_MODES.FOR* also calculates the horizontal group velocity and the frequency associated with each wavenumber.

The wind duct is treated in the programs *WIND_DUCT_SCAN.FOR*, which scans for the neutral modes, and *WIND_DUCT_MODES.FOR*, which calculates the wavenumber and phase speed eigenvalues, the group velocities, and the wave frequencies. These codes use the background wind and temperature profiles given in (4.74) and (4.75), and Fig. 4.14 shows an example result. These codes are essentially the same as the temperature duct codes, except that now there is a wind component.

This Page Intentionally Left Blank

Appendix A

The Hydrostatic Atmosphere

A.1 THE HYDROSTATIC APPROXIMATION

Vertical motions of the atmosphere tend to be small except within relatively small horizontal regions of convection, for example, thermal plumes, cumulus clouds, thunderstorms, hurricanes, *etc.* This suggests that there is a balance between the upward-directed pressure force and the weight of the atmosphere. Consider an elemental volume of atmosphere with unit cross-section, height δz, and density ρ. The weight of the volume is $g\rho\delta z$, and this force is directed downward. The net pressure force acting on the volume is the difference between the pressures at the top and the bottom of the volume. Let this difference be δp. The balance between the pressure and gravity forces gives

$$\delta p = -\rho g \delta z. \tag{A.1}$$

In the limit of small δz, (A.1) becomes

$$\frac{\partial p}{\partial z} = -\rho g, \tag{A.2}$$

which is generally referred to as the *hydrostatic equation*.

A.2 THE SCALE HEIGHT OF THE ISOTHERMAL ATMOSPHERE

Using the equation of state for an ideal gas in (A.2) leads to

$$\frac{1}{\rho}\frac{\partial \rho}{\partial z} + \frac{1}{T}\frac{\partial T}{\partial z} = -\frac{g}{RT}, \tag{A.3}$$

where R is the universal gas constant for dry air and T is the temperature. For many applications, we can replace the atmospheric temperature by an average value, T_A. Then integrating (A.3) gives

$$\rho(z) = \rho_s e^{-gz/RT_A}, \tag{A.4}$$

where ρ_s is the atmospheric density at the ground surface. We define the isothermal scale height of the atmosphere as $H_s = RT_A/g$. For the standard atmosphere, $H_s = 8$ km.

A.3 ADIABATIC LAPSE RATE

An adiabatic process within a system is one in which there is neither loss nor gain of heat within the system. Then the first law of thermodynamics becomes

$$dq = c_p\, dT - \alpha\, dp = 0, \tag{A.5}$$

where c_p is the specific heat capacity at constant pressure and $\alpha = 1/\rho = RT/P$ is the specific volume. Using the hydrostatic equation (A.2) in (A.5) leads to

$$c_p\, dT + g\, dz = 0. \tag{A.6}$$

We define the adiabatic lapse rate, Γ, as

$$\Gamma = -\frac{dT}{dz} = \frac{g}{c_p} \approx 0.0098 \text{ K m}^{-1}. \tag{A.7}$$

A.4 POTENTIAL TEMPERATURE

The potential temperature is defined as the temperature an air parcel would have if it were expanded or compressed adiabatically from its existing pressure to a pressure of 1000 mb or 100 hPa. From (A.5), using the definition of specific volume, we get

$$\frac{c_p}{R}\frac{dT}{T} = \frac{dP}{P}. \tag{A.8}$$

Integration of (A.8) from $P = 1000$ mb where the temperature is θ to pressure P where the temperature is T gives

$$\frac{c_p}{R} \ln\left(\frac{T}{\theta}\right) = \ln\left(\frac{P}{1000}\right). \tag{A.9}$$

Then the potential temperature is

$$\theta = T\left(\frac{1000}{P}\right)^{R/c_p}, \tag{A.10}$$

where $(R/c_p) = 0.286$.

A.5 BOUSSINESQ RELATIONS

We can develop (1.66) by first taking the logarithmic differential of the potential temperature (A.10) with respect to z to get

$$\frac{1}{\theta}\frac{d\theta}{dz} = \frac{1}{T}\frac{dT}{dz} - \frac{R}{pc_p}\frac{dp}{dz}. \tag{A.11}$$

The equation of state for the atmosphere is well approximated by the ideal gas law,

$$p = \rho RT. \tag{A.12}$$

Taking the vertical derivative of (A.12) with respect to z and dividing this result by p, one gets

$$\frac{1}{T}\frac{dT}{dz} = \frac{1}{p}\frac{dp}{dz} - \frac{1}{\rho}\frac{d\rho}{dz}. \tag{A.13}$$

Substitution of (A.13) into (A.11) leads to

$$\frac{1}{\theta} = \frac{1}{\rho}\left[\left(\frac{\rho}{p}\frac{c_v}{c_p}\right)\frac{dp}{dz} - \frac{T\rho}{dz}\right]. \tag{A.14}$$

The speed of sound is $c_s^2 = (c_p/c_v)(p/\rho)$. Thus, we can write (A.14) as

$$\frac{1}{\theta}\frac{d\theta}{dz} = \frac{1}{\rho}\left[\frac{1}{c_s^2}\frac{dp}{dz} - \frac{d\rho}{dz}\right]. \tag{A.15}$$

Because rates of motion of the atmosphere and gravity waves are generally much less than the speed of sound, (A.15) reduces to

$$\frac{1}{\theta}\frac{d\theta}{dz} = -\frac{1}{\rho}\frac{d\rho}{dz}. \tag{A.16}$$

Equation (1.67) follows from (A.16) if we identify $d\theta$ with perturbation θ_1 and $d\rho$ with perturbation ρ_1.

A.6 THE GEOSTROPHIC WIND

The equations of motion on a rotating Earth are (Holton, 1992)

$$\frac{du}{dt} - \frac{uv\tan\Phi}{a} + \frac{uw}{a} = -\frac{1}{\rho}\frac{\partial p}{\partial x} + 2\Omega_E v\sin\Phi - 2\Omega_E\cos\Phi + F_x \tag{A.17}$$

$$\frac{dv}{dt} + \frac{u^2\tan\Phi}{a} + \frac{vw}{a} = -\frac{1}{\rho}\frac{\partial p}{\partial y} - 2\Omega_E\sin\Phi + F_y \tag{A.18}$$

$$\frac{dw}{dt} - \frac{u^2+v^2}{a} = -\frac{1}{\rho}\frac{\partial p}{\partial z} - g + 2\Omega_E u\cos\Phi + F_z, \tag{A.19}$$

where

$$+\frac{d}{dt} = \frac{\partial}{\partial t} + u\frac{\partial}{\partial x} + v\frac{\partial}{\partial y} + w\frac{\partial}{\partial z} \tag{A.20}$$

is the total derivative; a is the mean radius of the Earth; Ω_E is the angular velocity of the Earth; and F_x, F_y, and F_z are friction forces in the x-, y-, and z-directions, respectively. The terms involving $1/a$ are due to the effects of the Earth's curvature. The terms involving Ω_E represent the apparent forces due to the Earth's rotation. These are the *Coriolis forces*. The Coriolis force acts perpendicular to the velocity vector; thus, it can change the direction of motion, but not the magnitude. In the Northern Hemisphere, bodies moving horizontally are deflected to the right. In the Southern Hemisphere (where the angular velocity vector is negative), the motion is directed to the left. Holton (1992) scales (A.17)–(A.19) using

1. $U \sim 10$ m s^{-1}: horizontal velocity scale
2. $W \sim 1$ cm s^{-1}: vertical velocity scale
3. $L \sim 10^6$ m: length scale
4. $D \sim 10^4$ m: depth scale
5. $\Delta P/\rho \sim 10^3$ m^2 s^{-2}: horizontal pressure fluctuation scale
6. $L/U \sim 10^5$ s: time scale

TABLE A.1 Scale Analysis of the Horizontal Momentum Equations

	A	B	C	D	E	F
x-component momentum equation	$\frac{du}{dt}$	$-2\Omega v \sin\phi$	$+2\Omega w \cos\phi$	$+\frac{uw}{a}$	$-\frac{uv\tan\phi}{a}$	$=-\frac{1}{\rho}\frac{\partial p}{\partial x}$
y-component momentum equation	$\frac{dv}{dt}$	$+2\Omega u \sin\phi$		$+\frac{vw}{a}$	$+\frac{u^2\tan\phi}{a}$	$=-\frac{1}{\rho}\frac{\partial p}{\partial y}$
Scales of individual terms	$\frac{U^2}{L}$	$f_0 U$	$f_0 W$	$\frac{UW}{a}$	$\frac{U^2}{a}$	$\frac{\Delta P}{\rho L}$
Magnitudes of the terms (m s^{-2})	10^{-4}	10^{-3}	10^{-6}	10^{-8}	10^{-5}	10^{-3}

Table A.1 taken from Holton (1992) shows the scaled magnitudes of the terms in (A.17)–(A.19), where

$$f_0 = 2\Omega_E \sin 45^\circ = 2\Omega_E \cos 45^\circ. \tag{A.21}$$

Retaining only the greatest terms in Table A.1 gives

$$fu = -\frac{1}{\rho}\frac{\partial p}{\partial x} \tag{A.22}$$

$$fv = \frac{1}{\rho}\frac{\partial p}{\partial y}. \tag{A.23}$$

The horizontal components of the *geostrophic wind* are defined as

$$u_g = -\frac{1}{f\rho}\frac{\partial p}{\partial x} \tag{A.24}$$

$$v_g = \frac{1}{f\rho}\frac{\partial p}{\partial y}. \tag{A.25}$$

The geostrophic wind represents the balance between the pressure gradient force and the Coriolis force. In the Northern Hemisphere, this balance results in a wind blowing parallel to lines of constant pressure with low pressure to the left.

A.7 THE ECKMAN WIND SPIRAL

In the planetary boundary layer, time scales for variations of the wind range from several minutes to an hour or so. Thus, to first order, and using Table A.1,

the mean winds in the boundary layer can be represented by

$$-fv = -\frac{1}{\rho}\frac{\partial p}{\partial x} + \frac{\partial}{\partial z}\left(\frac{\tau_x}{\rho}\right) \tag{A.26}$$

$$fu = -\frac{1}{\rho}\frac{\partial p}{\partial y} + \frac{\partial}{\partial z}\left(\frac{\tau_y}{\rho}\right), \tag{A.27}$$

where τ_x and τ_y are the turbulence stress terms in the x- and y-directions, respectively. Representing the turbulence stresses with a constant *eddy diffusivity* K gives, for example, $\tau_x = \rho K \partial u/\partial z$. Using this in (A.26) and (A.27) along with the definitions of u_g and v_g gives

$$K\frac{\partial^2 u}{\partial z^2} + f(v - v_g) = 0 \tag{A.28}$$

$$K\frac{\partial^2 v}{\partial z^2} - f(u - u_g) = 0. \tag{A.29}$$

Equations (A.28) and (A.29) show that the height-varying departure of the local wind from its geostrophic value is due to the turbulence stress. Physically, the stress reduces the wind speed, and this reduces the Coriolis force. However, the pressure gradient force is unchanged, and an imbalance between the forces results. Now, because the pressure gradient force is greater than the Coriolis force, the wind takes on a component directed down the pressure gradient. Now let us assume that at $z = 0$, $u = 0$ and $v = 0$, and at some upper boundary $u \to u_g$ and $v \to v_g$. For simplicity, we assume that $v_g = 0$. We can then write

$$K\frac{\partial^2}{\partial z^2}(u - u_g) + fv = 0 \tag{A.30}$$

$$K\frac{\partial^2}{\partial z^2}v - f(u - u_g) = 0. \tag{A.31}$$

If we now multiply (A.31) by $i = \sqrt{-1}$ and add this result to (A.30), we get

$$\frac{\partial^2}{\partial z^2}[(u - u_g) + iv] - \frac{if}{K}[(u - u_g) + iv] = 0. \tag{A.32}$$

The general solution of (A.32) is

$$(u - u_g) + iv = Ae^{\sqrt{if/K}z} + Be^{-\sqrt{if/K}z}. \tag{A.33}$$

For bounded solutions we take $A = 0$, and to satisfy the boundary condition at $z = 0$ we set $B = -u_g$. Using the identity $i = e^{i\pi/2}$, it follows that $\sqrt{i} = (1 + i)/\sqrt{2}$. Thus, we can write (A.33) as

$$u + iv = u_g\left(1 - e^{-\gamma(1+i)z}\right), \tag{A.34}$$

where $\gamma = \sqrt{f/2K}$. Separating (A.34) into real and imaginary parts gives the equations of the Ekman spiral:

$$u = u_g(1 - e^{-\gamma z})\cos(\gamma z) \tag{A.35}$$

$$v = u_g e^{-\gamma z}\sin(\gamma z). \tag{A.36}$$

When $z = \pi/\gamma$, the wind becomes parallel to the isobars. The depth of the Ekman, π/γ, is usually associated with the depth of the planetary boundary layer.

This Page Intentionally Left Blank

Appendix B

Computer Codes and Data on CD-ROM

B.1 INTRODUCTION

There are ten FORTRAN 77 computer codes and six ASCII data files contained in the CD-ROM accompanying this book. These codes and data are included as learning aides rather than operational software. The reader is encouraged to experiment with these codes, and use them as a guide to further model development. For example, the linear wave models are two-dimensional; expanding them to the three-dimensional case is straightforward but not necessarily easy. It is recognized that FORTRAN 77 is, perhaps, an arcane language; readers may wish to rewrite these codes in more modern languages such as FORTRAN 90/95, C, C^{++}, Visual Basic, *etc*. The numerical techniques used in these codes are described in Chapter 9. In this appendix, these codes and data sets are briefly described for quick reference. The codes themselves are also documented. The FORTRAN codes have been successfully compiled on several PC and workstation compilers. The user of these codes should make sure that the Read Only property of the files is negated.

B.2 FORTRAN CODES

B.2.1 BEAMSTEER.FOR

Beamsteering and slowness are described in Chapter 9. Beamsteering is an analysis technique used to estimate the horizontal phase velocity and wavelength of a gravity wave. The method uses time series of observations taken from a horizontal array of sensors. Although surface pressure perturbations are often used in analysis of gravity wave characteristics, any wave-perturbation quantity such as horizontal wind speed, vertical wind speed, or temperature can be used. Beamsteering in the slowness domain makes use of the cross-correlation of signals between station pairs in an array of at least three measuring stations. The phase lag between a pair of stations is the scalar product of the slowness vector and the radius vector between the stations. Although the radius vectors are fixed, the components of the slowness vectors can be varied in the slowness plane, and this causes changes in the phase lags between pairs of stations. The phase lags between all pairs of stations are systematically varied until maximum cross-correlation is achieved over the whole sampling array. In BEAMSTEER.FOR, the specified horizontal coordinates used are for the six-station surface pressure sampling array used in the CASES-99 field campaign. These coordinates are relative to the 55 m CASES-99 tower which was in the middle of the array. If this code is used for another application, then these coordinates and the number of stations must be changed accordingly.

Two "synthetic" data files are provided for executing BEAMSTEER.FOR, and these are described in Section B.3. The sampling rate of these data is 1 s. The beamsteering calculations extend over some time interval. In the current code, ISTART and ISTOP are set at 100 s and 1000 s respectively. Different start and stop values should be tried, and the results examined. The wave amplitudes in these synthetic data are constant. In reality, this seldom happens.

B.2.2 CORRUGATION_C.FOR AND CORRUGATION_D.FOR

These codes calculate the two-dimensional wave field and wave stress over one cycle of a surface corrugation with amplitude HEIGHT and horizontal wavelength LX. This is done by solving the Taylor–Goldstein equation for the single wavenumber that defines the corrugation. Both codes use a hyperbolic-tangent wind speed profile and a constant thermal stratification; however, other wind speed and temperature profiles can be used with only slight code modifications. CORRUGATION_C.FOR uses a continuous wind speed profile given by an analytical expression. CORRUGATION_D.FOR uses discrete values of wind speed and temperature specified at each vertical level of the model. Both codes allow for critical levels. A critical level can be created by giving the variables UB and UT opposite signs in the input file. For example, if $UB > 0$ and $UT < 0$, then a

critical level will exist. Care must be given in assigning these values so that a critical level does not lie on a computational level. If this happens, then DREBS will not converge. Note also, that these mountain wave codes will have computational "problems" is the Richardson number at the critical level is less than or equal to 1/4. CORRUGATION_D.FOR can be used for discrete wind speed and temperature observations, say from a sounding or the output of an atmospheric flow model. Input data for these codes are given in the file CORRUGATION_INPUT.DAT. Model outputs are written to files CORRUGATION_C(or D)_OUTPUT.DAT and CORRUGATION_C(or D)_UWTP.DAT. The first output file contains information about the model run and vertical profiles of background wind speed and wave stress. The second output file contains the two-dimensional (vertical and horizontal) wave field perturbations of horizontal and vertical wind speed, temperature and pressure.

B.2.3 RIDGE_C.FOR AND RIDGE_D.FOR

RIDGE_C.FOR and RIDGE_D.FOR are similar to CORRUGATION_C.FOR and CORRUGATION_D.FOR except that instead of a surface corrugation there is now an isolated ridge. Because of this, the Taylor–Goldstein equation must be solved for a spectrum of wavenumbers rather than a single wavenumber. The ridge shape is Gaussian with a maximum height labeled HEIGHT and width-scale XSIG. The horizontal domain size is given by XSCALE, which should be large compared to the width scale of the ridge, XSIG. If this is not the case, then errors will be introduced in the inverse Fourier transform. These and other values are contained in the file RIDGE_INPUT.DAT. The output files are identical to those for the surface corrugation codes.

B.2.4 TEMP_DUCT_SCAN.FOR AND TEMP_DUCT_MODES.FOR

The code TEMP_DUCT_SCAN.FOR searches for trapped or ducted gravity waves in a temperature duct, *i.e.*, calm background winds. The temperature ducting region extends from the ground surface to 300 m, and is characterized by a constant thermal stratification. Above the ducting region the stratification is neutral, *i.e.*, the Brunt–Väisälä frequency is zero. Beginning with a fixed wavenumber and an initial guess for the phase speed, the Taylor–Goldstein equation is solved for waves that have zero vertical velocity at the ground surface and exponentially decreasing wave amplitude above the ducting region. The phase speeds range between CMIN and CMAX which are determined by the requirement that the gravity wave must be internal in the ducting region. The upper boundary condition requires that the amplitude of the exponentially growing wave be zero or very small at the top boundary which is taken to be the top of the ducting region. A shooting technique is used to find the resonant wave. Starting with the initial phase speed,

the Taylor–Goldstein equation is integrated from the ground surface upward. If the upper boundary condition is not satisfied, then the phase speed is slightly increased, and the calculation is repeated. The process continues until the sign of the amplitude of the growing wave at the top boundary changes between two successive trial phase speeds. These successive speeds become the new values for CMAX and CMIN, and the above procedure is repeated. With each new pair of CMAX and CMIN values, the amplitude of the growing wave decreases. Usually, by the third iteration the amplitude is sufficiently small. In the first iteration, several zero-crossings of the amplitude of the growing wave will be seen. If the wavenumber is sufficiently large, the first zero corresponds to the fundamental mode; the second zero corresponds to the first harmonic, *etc*.

Each wave mode possesses a series of eigenvalues corresponding to discrete pairs of wavenumber and phase speed values which are solutions to the Taylor–Goldstein equation. These eigenvalues are calculated in the program TEMP_DUCT_MODES.FOR. The calculations begin with the first eigenvalue pair. The wavenumber is incrementally decreased, and a series of phase speeds are tried until the upper boundary condition is satisfied. The wavenumber is again decreased, and the above process is repeated. The output from this code is written to file TP_MODES.DAT, and contains the values of wavenumber, phase speed, group velocity, and wave frequency.

B.2.5 WIND_DUCT_SCAN.FOR AND WIND_DUCT_MODES.FOR

These codes are similar to those described in Section B.2.4, but now a background wind with a velocity jet is present. In these codes, analytical expressions for a low level jet and an accompanying temperature profile are used. However, aside from this the wind duct codes operate the same way as the temperature duct codes. Care must be taken so that the minimum phase speed is greater than the maximum background wind speed. If the condition is not met, then a critical level will be introduced, and the calculation will fail.

B.2.6 WAVELET.FOR

The program WAVELET.FOR performs a wavelet analysis on a time series of data. The wavelet function is the Morlet wavelet which is a Gaussian-damped sine wave. The analysis is based on the Fast Fourier Transform (FFT), and so the input data must be 2^n or greater in size where n is an integer. The input data are contained in the file P-291.DAT, which is described in Section B.3. The output is written to file WAVELET_OUTPUT.DAT. Each line of the output file contains time (fraction of dat UTC), wavelet period (minutes), and wavelet energy density. These data must be contoured in order to see the time-wavelet-window distribution of wavelet energy density.

B.3 SYNTHETIC WAVE DATA

Two synthetic wave data sets are provided for testing the beamsteering code. These data simulate the pressure perturbations observed by a six-sensor array of microbarographs. The presumed sampling rate is 1 Hz, and the sampling time is 1 hour. The wavelength is 1000 m, and the wave is coming from 45E. In one case the speed is 5 m s^{-1}, and in the other it is 20 m s^{-1}.

B.4 SAMPLE PRESSURE DATA

The ASCII file T-291.DAT contains the raw pressure perturbation data recorded from 6 microbarographs on October 19, 1999 during the CASES-99 field campaign in south central Kansas. The pressure data consists of 1-s averages formed from 10 Hz samples. The times are in fractions of a day UTC. Thus, a time of 0.250 corresponds to 06:00, *etc*. The microbarographs were of the differential type, and every 15 min the reference chamber was opened for 5 s to allow the pressure difference to go to zero. This zero setting procedure results in a series of ramps, each ramp being 15 min long. In order to get a useful data set, these ramps have to be connected to form a continuous time series. This has been done, and these data appear in the file P-291.DAT. These data, however, contain all the pressure variations over the day including the diurnal changes and slowly-varying temperature effects. Thus, it is necessary to filter these data over some frequency range in order to derive a useful data set. The (x, y) locations of the pressure sensors relative to the CASES tower are, in meters, Station 1 (90.6, 42.3); Station 4 (−229.4, 160.6); Station 5 (−26.1, −298.8); Station 7 (815.7, 380.4); Station 8 (−737.2, 516.2); Station 9 (−78.4, −896.6).

B.5 CONTACT

The reader can contact the author at:

nappo@atdd.noaa.gov

or

cjnappo1@comcast.net

This Page Intentionally Left Blank

BIBLIOGRAPHY

Alexander, M. J. and Vincent, R. A. Gravity waves in the tropical lower stratosphere: A model study of seasonal and interannual variability. *J. Geophys. Res.* **105**:17,983–17,994, 2000.

Alexander, M. J., Holton, J. R., and Durran, D. R. The gravity wave response above deep convection in a squall line simulation. *J. Atmos. Sci.* **52**:2212–2226, 1995.

Alexander, M. J., Beres, J. H., and Pfister, L. Tropical stratospheric gravity wave activity and relationship to clouds. *J. Geophys. Res.* **105**:22,299–22,309, 2000.

Allen, S. J. and Vincent, R. A. Gravity-wave activity in the lower atmosphere: Seasonal and latitudinal variations. *J. Geophys. Res.* **100**:1327–1350, 1995.

Anderson, P. S., Mobbs, S. D., King, J. C., McConnell, I., and Rees, J. M. A microbarograph for internal gravity wave studies in Antarctica. *Antarct. Sci.* **4(2)**:241–248, 1992.

Angell, J. K. and Pack, D. H. Analysis of some preliminary low-level constant level balloon (tetroon) flights. *Mon. Weather Rev.* **88**:235–248, 1960.

Angell, J. K. and Pack, D. H. Analysis of low-level constant volume balloon (tetroon) flights from Wallops Island. *J. Atmos. Sci.* **19**:87–98, 1962.

Asten, M. W. and Henstridge, J. D. Array estimators and the use of microseisms for reconnaissance of sedimentry basins. *Geophysics* **49**:1828–1837, 1984.

Baines, P. G. *Topographic Effects in Stratified Flows*, 1995. New York: Cambridge Univ. Press.

Baines, P. G. and Palmer, T. N. Rational for a new physically based parameterization of sub-grid scale orographic effects. Technical Report, Tech. Memo. 169, 1990. European Center for Medium-Range Weather Forecasts.

Baker, R. D., Schuberrt, G., and Jones, P. W. Convectively generated internal gravity waves in the lower atmosphere of Venus. Part I: No wind shear. *J. Atmos. Sci.* **57**:184–215, 2000.

Balachandran, N. K. Gravity waves from thunderstorms. *Mon. Weather Rev.* **108**:804–816, 1980.

Barber, N. S. Design of "optimum" arrays for direction finding. *Electron. Radio Eng.* **36**:222–232, 1959.

Bedard, A. J., Canavero, F., and Einaudi, F. Atmospheric gravity waves and aircraft turbulence encounters. *J. Atmos. Sci.* **43**:2838–2844, 1986.

Beer, T. *Atmospheric Waves*, 1974. New York: Wiley.

Bendat, J. S. and Piersol, A. G. *Randon Data: Analysis and Measurement Procedures*, 1971. New York: Wiley-Interscience.

Bender, C. M. and Orzag, S. A. *Advanced Mathematical Methods for Scientists and Engineers*, 1999. New York: Springer-Verlag.

Beran, D. W., Little, C. G., and Willmarth, B. C. Acoustic Doppler measurements of vertical velocities in the atmosphere. *Nature* **230**:160–162, 1971.

Beran, D. W., Hooke, W. H., and Clifford, S. F. Acoustic echo-sounding techniques and their application to gravity-wave, turbulence, and stability studies. *Boundary-Layer Meteorol.* **4**:133–153, 1973.

Bilbro, J., Fichtl, G., Fitzjarrald, D., Krause, M., and Lee, R. Airborne Doppler lidar wind field measurements. *Bull. Am. Meteorol. Soc.* **65**:348–359, 1984.

Blumen, W. and Hart, J. E. Airborne Doppler lidar wind field measurements of waves in the lee of Mount Shasta. *J. Atmos. Sci.* **45**:1571–1583, 1988.

Blumen, W. and McGregor, C. D. Wave drag by three-dimensional mountain lee-waves in nonplanar shear flow. *Tellus* **28**:287–298, 1976.

Booker, D. R. and Cooper, L. W. Superpressure balloons for weather research. *J. Appl. Meteorol.* **4**:122–129, 1965.

Booker, J. R. and Bretherton, F. P. The critical level for internal gravity waves in a shear flow. *J. Fluid Mech.* **27**:513–539, 1967.

Bosart, L. F. and Cussen, J. P. Gravity wave phenomena accompanying east coast cyclogenesis. *Mon. Weather Rev.* **101**:446–454, 1973.

Bosart, L. F. and Sanders, F. Mesoscale structure in the megalopolitan snowstorm of 11–12 January 1983: Part III: A large-amplitude gravity wave. *J. Atmos. Sci.* **43**:924–939, 1983.

Bretherton, F. P. The propagation of groups of internal gravity waves in a shear flow. *Q. J. R. Meteorol. Soc.* **92**:466–480, 1966.

Bretherton, F. P. Waves and turbulence in stably stratified fluids. *Radio Sci.* **4**:1279–1287, 1969.

Brown, E. H. and Hall, F. F. Advances in atmospheric acoustics. *Rev. Geophys. Space Phys.* **16**:47–110, 1978.

Brown, R. A. Aircraft measurements of mountain waves and their associated momentum flux over the British Isles. *Q. J. R. Meteorol. Soc.* **109**:849–865, 1983.

Brown, R. A. Longitudinal instabilities and secondary flow in the planetary boundary layer: A review. *Rev. Geophys. Space Phys.* **18**:683–697, 1980.

Bulirsch, R. and Stoer, J. Numerical treatment of ordinary differential equations by extrapolation methods. *Numerisch Mathematik* **8(1)**:1–13, 1966.

Capon, J. High resolution frequency-wavenumber analysis. *Proc. Inst. Electr. Electron. Eng.* **58**:760–770, 1969.

Carter, D. A., Balsley, B. B., Ecklund, W. L., Gauge, K. S., Riddle, A. C., Garello, R., and Crochet, M. Investigations of internal gravity waves using three vertically directed closely spaced wind profilers. *J. Geophys. Res.* **94**:8633–8642, 1989.

Caughey, S. J. and Readings, C. J. An observation of waves and turbulence in the Earth's boundary layer. *Boundary-Layer Meteorol.* **9**:279–296, 1975.

Chadwick, R. B. and Gossard, E. E. Radar probing and measurement of the planetary boundary layer: Part I. Scattering from refractive index irregularities. In *Probing the Atmospheric Boundary Layer*, D. H. Lenschow, ed., pp. 163–182, 1986. Boston, MA: Am. Meteorological Soc.

Chadwick, R. B., Moran, K. P., Strauch, R. G., Morrison, G. E., and Campbell, W. C. A new radar for measuring winds. *Bull. Am. Meteorol. Soc.* **57**:1120–1125, 1976.

Chandrasekhar, S. *Hydrodynamic and Hydromagnetic Stability*, 1961. Oxford: Clarendon.

Chimonas, G. The stability of a coupled wave-turbulence system in a parallel shear flow. *Boundary-Layer Meteorol.* **2**:444–452, 1972.

Chimonas, G. Surface drag instabilities in the atmospheric boundary layer. *J. Atmos. Sci.* **50**:1914–1924, 1993.

Chimonas, G. Jeffrey's drag instability applied to waves in the lower atmosphere: Linear and non-linear growth rates. *J. Atmos. Sci.* **51**:3758–3775, 1994.

Chimonas, G. Steps, waves and turbulence in the stably stratified planetary boundary layer. *Boundary-Layer Meteorol.* **90**:397–421, 1999.

Chimonas, G. and Hines, C. O. Doppler ducting of atmospheric gravity waves. *J. Geophys. Res.* **91**:1219–1230, 1986.

Chimonas, G. and Nappo, C. J. A thunderstorm bow wave. *J. Atmos. Sci.* **44**:533–541, 1987.

Chimonas, G. and Nappo, C. J. Wave drag in the planetary boundary layer over complex terrain. *Boundary-Layer Meteorol.* **47**:217–232, 1989.

Chui, C. K. *An Introduction to Wavelets*, 1992. San Diego: Academic Press.

Chun, H.-Y. and Baik, J.-J. Momentum flux by thermally induced internal gravity waves and its approximation for large-scale models. *J. Atmos. Sci.* **55**:3299–3310, 1998.

Chun, H.-Y., Song, I.-S., and Baik, J.-J. Some aspects of internal gravity waves in the multicell-type connvection system. *Meteorol. Atmos. Phys.* **69**:205–222, 1999.

Chun, H.-Y., Song, M.-D., Kim, J.-W., and Baik, J.-J. Effects of gravity wave drag induced by cumulus convection on the atmospheric general circulation. *J. Atmos. Sci.* **58**:302–319, 2001.

Clark, T. L. and Peltier, W. R. On the evolution and stability of finite amplitude mountain waves. *J. Atmos. Sci.* **34**:1715–1730, 1977.

Cohen, A. and Doron, E. Mountain lee waves in the Middle East: Theoretical calculations compared with satellite pictures. *J. Appl. Meteorol.* **6**:669–673, 1967.

Collis, R. T. H., Fernald, F. G., and Alder, J. E. Lidar observations of Sierra-wave conditions. *J. Appl. Meteorol.* **7**:227–233, 1968.

Combes, J. M., Grossman, A., and Tchamitchian, P. *Wavelets*, 1989. Berlin/New York: Springer-Verlag.

Conover, J. H. Lee-wave clouds photographed from an aircraft and a satellite. *Weather* **19**:79–92, 1964.

Corby, G. A. A preliminary study of atmospheric waves using radiosonde data. *Q. J. R. Meteorol. Soc.* **83**:49–60, 1957.

De Baas, A. F. and Driedonks, G. M. Internal gravity waves in the stably stratified boundary layer. *Boundary-Layer Meteorol.* **31**:303–323, 1985.

de la Torre, A. and Alexander, P. The interpretation of wavelengths and periods as measured from atmospheric balloons. *J. Appl. Meteorol.* **34**:2747–2754, 1995.

De Silva, I. P. D., Fernando, H. J. S., Eaton, F., and Hebert, D. Evolution of Kelvin–Helmholtz billows in nature and laboratory. *Earth Planet. Sci. Lett.* **143**:217–231, 1996.

Denholm-Price, J. C. W. and Rees, J. M. Detecting waves using an array of sensors. *Mon. Weather Rev.* **127**:57–69, 1999.

DiMarzio, C., Harris, C., Bilbro, J. W., Weaver, E. A., Burnham, D. C., and Hallock, J. N. Pulsed laser Doppler measurements of wind shear. *Bull. Am. Meteorol. Soc.* **60**:1061–1066, 1979.

Döös, B. R. Theoretical analysis of lee wave clouds observed by TYROS I. *Tellus* **14**:301–309, 1962.

Doran, J. C., Fast, J. D., and Horel, J. The VTMX 2000 campaign. *Bull. Am. Meteorol. Soc.* **83**:537–551, 2001.

Dörnbrack, A. Turbulent mixing by breaking gravity waves. *J. Fluid Mech.* **375**:113–142, 1998.

Dörnbrack, A., Birner, T., Fix, A., Flentje, H., Meister, A., Schmid, H., Browell, E., and Mahoney, M. J. Evidence for inertia-gravity waves forming polar stratospheric clouds over Scandinavia. *J. Geophys. Res.* submitted, 2001.

Dörnbrack, A. and Nappo, C. J. A note on the application of linear wave theory at a critical level. *Boundary-Layer Meteorol.* **82**:399–416, 1997.

Doviak, R. J. and Ge, R. An atmospheric solitary gust observed with a Doppler radar, a tall tower and a surface network. *J. Atmos. Sci.* **41**:2559–2573, 1984.

Durran, D. R. Another look at downslope windstorms. Part I: The development of analogs to supercritical flow in an infiniely deep, continuously stratified fluid. *J. Atmos. Sci.* **43**:2527–2543, 1986.

Eaton, F. D., McLaughlin, S. A., and Hines, J. R. A new frequency-modulated continuous wave radar for studying planetary boundary layer morphology. *Radio Sci.* **30**:75–88, 1995.

Eckart, C. *Hydrodynamics of Oceans and Atmospheres*, 1960. New York: Pergamon Press.

Eichinger, W. E., Cooper, D. I., Forman, P. R., Griegos, J., Osborn, M. A., Richter, D., Tellier, L. L., and Thornton, R. The development of a scanning Raman water vapor lidar for boundary layer and tropospheric observations. *J. Atmos. Oceanic. Technol.* **11(2)**:1753–1766, 1999.

Eichinger, W. E., Eichinger, H. L., Cooper, D. I., Krieger, J., and Carlson, E. High altitude activity associated with intermittent turbulence in a stable atmosphere. *Boundary-Layer Meteorol.* submitted, 2001.

Einaudi, F. and Finnigan, J. J. The interaction between an internal gravity wave and the planetary boundary layer. Part I: The linear analysis. *Q. J. R. Meteorol. Soc.* **107**:793–806, 1981.

Einaudi, F. and Finnigan, J. J. Wave-turbulence dynamics in the stably stratified boundary layer. *J. Atmos. Sci.* **50**:1841–1864, 1993.

Einaudi, F. and Hines, C. O. WKB approximation in application to acoustic-gravity waves. *Can. J. Phys.* **48**:1458–1471, 1970.

Einaudi, F., Bedard, A. J., and Finnigan, J. J. A climatology of gravity waves and other coherent disturbances at the Boulder atmospheric observatory during March–April 1984. *J. Atmos. Sci.* **46**:303–329, 1989.

Eliassen, A. and Palm, E. On the transfer of energy in stationary waves. *Geofys. Publ.* **22**:1–23, 1960.

Eloranta, E. W., King, J. M., and Weinman, J. A. The determination of wind speed in the boundary layer by monostatic lidar. *J. Appl. Meteorol.* **14**:1485–1489, 1975.

Emmanuel, C. B. Richardson number profiles through shear instability wave regions observed in the lower planetary boundary layer. *Boundary-Layer Meteorol.* **5**:19–27, 1973.

Emmanuel, C. B., Bean, B. R., McAllister, L. G., and Pollard, J. R. Observations of Helmholtz waves in the lower atmosphere with an acoustic sounder. *J. Atmos. Sci.* **29**:886–892, 1972.

Ernst, J. A. SMS-1 nighttime infrared imagery of low level mountain waves. *Mon. Weather Rev.* **104**:207–209, 1976.

Etling, D. and Raasch, S. Numerical simulation of vortex roll development during a cold air outbreak. *Dyn. Atmos. Oceans* **10**:277–290, 1987.

Eymard, L. and Weill, A. A study of gravity waves in the planetary boundary layer by acoustic sounding. *Boundary-Layer Meteorol.* **17**:231–245, 1979.

Farge, M. Wavelet transforms and their applications to turbulence. *Annu. Rev. Fluid Mech.* **24**:359–457, 1992.

Farley, D. T., Balsley, B. B., Swartz, W. E., and Hoz, C. L. Tropical winds measured by the Arecibo radar. *J. Appl. Meteorol.* **18**:227–230, 1979.

Finnigan, J. J. Kinetic energy transfer between internal gravity waves and turbulence. *J. Atmos. Sci.* **45**:486–505, 1988.

Finnigan, J. J. and Einaudi, F. The interaction of an internal gravity wave and the planetary boundary layer. II: Effects of the wave on the turbulence structure. *Q. J. R. Meteorol. Soc.* **107**:807–832, 1981.

Finnigan, J. J., Einaudi, F., and Fua, D. The interaction between an internal gravity wave and turbulence in a stably-stratified nocturnal boundary layer. *J. Atmos. Sci.* **41**:2409–2436, 1984.

Foufoula-Georgiou, E. and Kumar, P. *Wavelets in Geophysics*, 1994. San Diego: Academic Press.

Fovell, R., Durran, D., and Holton, J. R. Numerical simulations of convectively generated stratospheric gravity waves. *J. Atmos. Sci.* **49**:1427–1442, 1992.

Fritts, D. C. Gravity wave saturation in the middle atmosphere. A review of theory and observations. *Rev. Geophys. Space Phys.* **22**:275–308, 1984.

Fritts, D. C. and Dunkerton, T. J. A quasi-linear study of gravity wave saturation and self acceleration. *J. Atmos. Sci.* **41**:3272–3289, 1984.

Fritts, D. C. and Geller, M. A. Viscous stabilization of gravity critical level flows. *J. Atmos. Sci.* **33**:2276–2284, 1976.

Fritts, D. C. and Isler, J. R. Mean motions and tidal and two-day structure and variability in the mesosphere and lower thermosphere over Hawaii. *J. Atmos. Sci.* **51**:2145–2164, 1994.

Fritts, D. C. and Nastrom, G. D. Sources of mesoscale variability of gravity waves. Part II: Frontal, convective, and jet stream excitation. *J. Atmos. Sci.* **49**:111–127, 1992.

Fritts, D. C., Blanchard, R. C., and Coy, L. Gravity wave structure between 60 and 90 km inferred from space shuttle reentry. *J. Atmos. Sci.* **46**:423–434, 1989.

Fritts, D. C., Wang, D.-Y., and Blanchard, R. C. Gravity wave and tidal structures between 60 and 140 km inferred from space shuttle reentry data. *J. Atmos. Sci.* **50**:837–849, 1993.

Fritts, D. C., Isler, J. R., Hecht, J. H., Waletscheid, R. L., and Andreassen, O. Wave breaking signatures in sodium densities and OH nightglow. 2. Simulation of wave and instability structures. *J. Geophys. Res.* **102**:6669–6684, 1997.

Fritz, S. The significance of mountain lee waves as seen from satellite pictures. *J. Appl. Meteorol.* **4**:31–37, 1965.

Fua, D., Chimonas, G., Einaudi, F., and Zeman, O. An analysis of wave-turbulence interaction. *J. Atmos. Sci.* **39**:2450–2463, 1982.

Gardner, C. S. and Gardner, N. F. Measurement distortion in aircraft, space shuttle, and balloon observations of atmospheric density and temperature perturbation spectra. *J. Geophys. Res.* **98**:1023–1033, 1993.

Gardner, C. S. and Shelton, J. D. Density response of neutral atmospheric layers to gravity wave perturbations. *J. Geophys. Res.* **90**:1745–1754, 1985.

Gardner, C. S. and Taylor, M. J. Observational limits for lidar, radar, and airglow imager measurements of gravity wave parameters. *J. Geophys. Res.* **103**:6427–6437, 1998.

Gardner, C. S. and Voelz, D. G. Lidar studies of the nighttime sodium layer over Urbana, Illinois. *J. Geophys. Res.* **92**:4673–4694, 1987.

Garratt, J. R. *The Atmospheric Boundary Layer*, 1992. Cambridge, UK: Cambridge Univ. Press.

Gauge, K. S. and Balsley, B. B. Doppler radar probing of the clear atmosphere. *Bull. Am. Meteorol. Soc.* **59**:1074–1093, 1978.

Gill, A. E. *Atmosphere-Ocean Dynamics*, 1982. San Diego: Academic Press.

Goldstein, S. On the stability of superposed streams of fluids of different densities. *Proc. R. Soc. London A*, **132**:524–548, 1931.

Gossard, E. E. Vertical flux of energy into the lower ionsophere from internal gravity waves generated in the troposphere. *J. Geophys. Res.* **67**:745–758, 1962.

Gossard, E. E. and Hooke, W. H. *Waves in the Atmosphere*, 1975. Amsterdam/New York: Elsevier.

Gossard, E. E. and Munk, W. On gravity waves in the atmosphere. *J. Meteorol.* **11**:259–269, 1954.

Gossard, E. E. and Sweezy, W. B. Dispersion and spectra of gravity waves in the atmosphere. *J. Atmos. Sci.* **31**:1540–1548, 1974.

Gragg, W. E. On extrapolation algorithms for ordinary initial value problems. *SIAM J. Numerical Anal.* **Series B**:384–403, 1965.

Grasso, L. D. The differentiation between grid spacing and resolution and their applications to numerical modeling. *Bull. Am. Meteorol. Soc.* **81**:579–580, 2000.

Grisogono, B. Dissipation of waves in the atmospheric boundary layer. *J. Atmos. Sci.* **51**:1237–1243, 1994.

Grisogono, B., Pryor, S. C., and Keislar, R. E. Mountain wave drag over double bell-shaped orography. *Q. J. R. Meteorol. Soc.* **119**:199–206, 1993.

Grund, C. L., Banta, R. M., George, J. L., Howell, J. N., Post, M. J., Richter, R. A., and Weickmann, A. M. High-resolution Doppler lidar for boundary layer and cloud research. *J. Atmos. Oceanic Technol.* **18**:376–393, 2001.

Guest, F. M., Reeder, M. J., Marks, C. J., and Karoly, D. J. Inertia-gravity waves observed in the lower stratosphere over Macquarie Island. *J. Atmos. Sci.* **57**:737–752, 2000.

Haubrich, R. A. Array design. *Bull. Seismol. Soc. Am.* **58**:977–991, 1968.

Hauf, T., Finke, U., Neisser, J., Bull, G., and Stangenberg, J.-G. A ground-based network for atmospheric pressure fluctuations. *J. Atmos. Oceanic Technol.* **13**:1001–1023, 1996.

Hazel, P. The effect of viscosity and heat conduction on internal gravity waves at a critical level. *J. Fluid Mech.* **30**:775–784, 1967.

Hecht, J. H., Waltersheid, R. L., Fritts, D. C., Isler, J. R., Senft, D. C., Gardner, C. S., and Franke, S. J. Wave breaking signatures in OH airglow and sodium densities and temperatures. 1. Airglow imaging, Na lidar, and MF radar observations. *J. Geophys. Res.* **102**:6655–6668, 1997.

Herron, T. J. and Tolstoy, I. Tracking jet stream winds from ground level pressure sensors. *J. Atmos. Sci.* **26**:266–269, 1969.

Herron, T. J., Tolstoy, I., and Kraft, D. W. Atmospheric pressure background fluctuations in the mesoscale range. *J. Geophys. Res.* **74**:1321–1329, 1969.

Hicks, J. J. and Angell, J. K. Radar observations of breaking gravity waves in the visually clear atmosphere. *J. Appl. Meteorol.* **7**:114–121, 1968.

Hines, C. O. Hydromagnetic resonance in ionospheric waves. *J. Atmos. Terr. Phys.* **7**:14–30, 1955.

Hines, C. O. Internal atmospheric gravity waves at ionospheric heights. *Can. J. Phys.* **38**:1441–1481, 1960.

Hines, C. O. The upper atmosphere in motion. *Q. J. R. Meteorol. Soc.* **89**:1–42, 1963.

Hines, C. O. Atmospheric gravity waves: A new toy for the wave theorist. *Radio Sci.* **69D**:375–380, 1965.

Hines, C. O. Tidal oscillations, shorter period gravity waves and shear waves. *Meteorol. Monogr.* **9**:114–121, 1968.

Hines, C. O. Generalization of the Richardson criterion for the onset of atmospheric turbulence. *Q. J. R. Meteorol. Soc.* **97**:429–439, 1971.

Hines, C. O. *The Upper Atmosphere in Motion*, 1974. Washington, DC: Am. Geophys. Union.

Hines, C. O. A modeling of atmospheric gravity waves and wave drag generated by isotropic and anisotropic terrain. *J. Atmos. Sci.* **45**:309–322, 1988.

Hines, C. O. Earlier days of gravity waves revisited. *Pure Appl. Geophys.* **130**:151–170, 1989a.

Hines, C. O. Tropopasual mountain waves over Arecibo: A case study. *J. Atmos. Sci.* **46**:476–488, 1989b.

Hodges, R. R. Generation of turbulence in the upper atmosphere by internal gravity waves. *J. Geophys. Res.* **72**:3455–3458, 1967.

Hodges, R. R. Eddy diffusion coefficients due to instabilities in internal gravity waves. *J. Geophys. Res.* **74**:4087–4090, 1969.

Holton, J. R. The role of gravity wave induced drag and diffusion in the momentum budget of the mesosphere. *J. Atmos. Sci.* **39**:791–799, 1982.

Holton, J. R. *An Introduction to Dynamic Meteorology*, 1992. New York: Academic Press.

Holton, J. R. and Lindzen, R. S. An updated theory for the quasi-biennial cycle of the tropical stratosphere. *J. Atmos. Sci.* **29**:1076–1080.

Hooke, W. F., Hall, F. F., and Gossard, E. E. Observed generation of an atmospheric gravity wave by shear instability in the mean flow of the planetary boundary layer. *Boundary-Layer Meteorol.* **5**:29–42, 1973.

Howard, L. N. Note on a paper of John W. Miles. *J. Fluid Mech.* **10**:509–512, 1961.

Hunt, J. C. R., Kaimal, J. C., and Gaynor, J. E. Some observations of turbulence structure in stable layers. *Q. J. R. Meteorol. Soc.* **111**:793–815, 1985.

Hussain, A. K. M. F. and Reynolds, W. C. The mechanics of an organized wave in a turbulent shear flow. *J. Fluid Mech.* **54**:241–258, 1972.

Jefferys, H. The flow of water in an inclined channel of rectangular cross section. *Phil. Mag.* **49**:793–807, 1925.

Jordan, A. R. Atmospheric gravity waves from winds and storms. *J. Atmos. Sci.* **29**:445–456, 1972.

Karacostas, T. S. and Marwitz, J. D. Turbulent kinetic energy budgets over mountainous terrain. *J. Appl. Meteorol.* **19**:163–174, 1980.

Kim, J. and Mahrt, L. Momentum transport by gravity waves. *J. Atmos. Sci.* **49**:735–748, 1992.

Kjelaas, A. G., Beran, D. W., Hooke, W. H., and Bean, B. R. Waves observed in the planetary boundary layer using an array of acoustic sounders. *J. Atmos. Sci.* **31**:2040–2045, 1974.

Koch, S. E. and Golus, R. E. A mesoscale gravity wave event observed during CCOPE. Part I: Multiscale statistical analysis of wave characteristics. *Mon. Weather Rev.* **116**:2527–2544, 1988.

Koffi, E. N., Georgelin, M., Benech, B., and Richard, E. Trapped lee waves observed during PYREX by constant volume balloons: Comparison with Meso-NH simulations. *J. Atmos. Sci.* **57**:2007–2021, 2000.

Köpp, F., Schwiesow, R. L., and Werner, C. Remote measurements of boundary-layer wind profiles using a CW Doppler lidar. *J. Clim. Appl. Meteorol.* **23**:148–154, 1984.

Kropfli, R. A. Radar probing and measurement of the planetary boundary layer: Part II. Scattering from particulates. In *Probing the Atmospheric Boundary Layer*, D. H. Lenschow, ed., pp. 183–199, 1986. Boston, MA: Am. Meteorol. Soc.

Kwon, K. H. and Gardner, C. S. Airborne sodium lidar measurements of gravity wave intrinsic parameters. *J. Geophys. Res.* **95**:20,457–20,467, 1990.

Lalas, D. P. and Einaudi, F. Tropospheric gravity waves: Their detection by and influence on rawinsonde balloon data. *Q. J. R. Meteorol. Soc.* **106**:855–864, 1980.

Lane, T. P., Reeder, M. J., Morton, B. R., and Clark, T. L. Observations and numerical modelling of mountain waves over the Southern Alps. *Q. J. R. Meteorol. Soc.* **126**:2765–2788, 2000.

Laprise, J. P. R. An assessment of the WKBJ approximation to the vertical structure of linear mountain waves: Implications for gravity-wave drag parameterizations. *J. Atmos. Sci.* **50**:1469–1487, 1993.

Lee, X. and Barr, A. G. Climatology of gravity waves in a forest. *Q. J. R. Meteorol. Soc.* **124**:1403–1419, 1998.

Lee, X., Neumann, H. H., Hartog, G. D., Fuentes, J. D., Black, T. A., Yang, P. C., and Blanken, P. D. Observation of gravity waves in a boreal forest. *Boundary-Layer Meteorol.* **84**:383–398, 1997.

Leutbecher, M. and Volkert, H. The propagation of mountain waves into the stratosphere: Quantitative evaluation of three-dimensional simulations. *J. Atmos. Sci.* **57**:3090–3108, 2000.

Lighthill, M. J. *Waves in Fluids*, 1978. Cambridge, UK: Cambridge Univ. Press.

Lilly, D. K. Wave momentum flux-a GARP problem. *Bull. Am. Meteorol. Soc.* **53**:17–23, 1972.

Lilly, D. K. A severe downslope windstorm and aircraft turbulence event induced by a mountain wave. *J. Atmos. Sci.* **35**:59–77, 1978.

Lilly, D. K. and Kennedy, P. J. Observations of a stationary mountain wave and its associated momentum flux and energy dissipation. *J. Atmos. Sci.* **30**:1135–1152, 1973.

Lilly, D. K. and Zipser, E. J. The front range windstorm of 11 January 1972—a meteorological narrative. *Weatherwise* **25**:56–63, 1972.

Lilly, D. K., Pann, Y., Kennedy, P., and Tootenhoofd, W. Data catalog for the 1970 Colorado Lee Wave Observational Program. Technical Report, Tech. Note NT/STR-72, 1971, Boulder, CO: National Center for Atmospheric Research.

Lin, Y.-L. and Chun, H.-Y. Effects of diabatic cooling in a shear flow with a critical level. *J. Atmos. Sci.* **48**:2476–2491, 1991.

Lindzen, R. S. Thermally driven diurnal tide in the atmosphere. *Q. J. R. Meteorol. Soc.* **93**:18–42, 1967.

Lindzen, R. S. Turbulence and stress owing to gravity wave and tidal breakdown. *J. Geophys. Res.* **86**:9707–9714, 1981.

Lindzen, R. S. Supersaturation of vertically propagating internal gravity waves. *J. Atmos. Sci.* **45**:705–711, 1987.

Lindzen, R. S. and Holton, J. R. A theory of the quasi-biennial oscillation. *J. Atmos. Sci.* **25**:1095–1107, 1968.

Little, C. G. Acoustic methods for the remote probing of the lower atmosphere. *Proc. IEEE* **57**:571–578, 1969.

Lott, F. and Miller, M. J. A new subgrid-scale orographic drag parameterization: Its formulation and testing. *Q. J. R. Meteorol. Soc.* **123**:101–127, 1997.

Ludlum, F. H. Characteristics of billow clouds and their relation to clear-air turbulence. *Q. J. R. Meteorol. Soc.* **93**:419–435, 1967.

Mahrt, L. Vertical structure and turbulence in the very stable boundary layer. *J. Atmos. Sci.* **42**:2333–2349, 1985.

Manson, H. A. Gravity wave horizontal and vertical wavelengths: An update of measurements in the mesosphere region (∼80–100 km). *J. Atmos. Sci.* **47**:2765–2773, 1990.

Martyn, D. F. Cellular atmospheric waves in the ionosphere and troposphere. *Proc. R. Soc. A*, **201**:216–234, 1950.

Mason, P. J. and Sykes, R. I. A two-dimensional numerical study of horizontal roll vortices in an inversion capped planetary boundary layer. *Q. J. R. Meteorol. Soc.* **108**:801–823, 1982.

Mastrantonio, G., Einaudi, F., and Fua, D. Generation of gravity waves by jet streams in the atmosphere. *J. Atmos. Sci.* **33**:1730–1738, 1976.

McAllister, L. G., Pollard, J. R., Mahoney, A. R., and Shaw, P. J. R. Acoustic sounding: A new approach to the study of atmospheric structure. *Proc. IEEE* **57**:597–587, 1969.

McFarlane, N. A. The effect of orographically excited gravity wave drag on the general circulation of the lower stratosphere and troposphere. *J. Atmos. Sci.* **44**:1775–1800, 1987.

McMintyre, M. E. On the "wave momentum" myth. *J. Fluid Mech.* **106**:331–347, 1981.

Meneveau, C. Analysis of turbulence in the orthonormal wavelet representation. *J. Fluid Mech.* **232**:469–520, 1991.

Merrill, J. T. Observational and theoretical study of shear instability in the airflow near the ground. *J. Atmos. Sci.* **34**:911–921, 1977.

Miles, J. W. On the stability of heterogeneous shear flows. *J. Fluid Mech.* **10**:496–508, 1961.

Miller, M. J., Palmer, T. N., and Swinbank, R. Parameterization and influence of subgrid-scale orography in general circulation and numerical weather prediction models. *Meteorol. Atmos. Phys.* **40**:84–109, 1989.

Molina, A. Sodium nightglow and gravity waves. *J. Atmos. Sci.* **40**:2444–2450, 1983.

Monserrat, S. and Thorpe, A. J. Use of ducting theory in an observed case of gravity waves. *J. Atmos. Sci.* **53**:1724–1736, 1996.

Moustaoui, M., Teitelbaum, H., van Velthoven, P. F. J., and Kelder, H. Analysis of gravity waves during the POLINAT experiment and some consequences of stratospheric-tropospheric exchange. *J. Atmos. Sci.* **56**:1019–1030, 1999.

Munasinghe, G., Hur, H., Huang, T. Y., Bhattachryya, A., and Tuan, T. F. Application of the dispersion formula to long- and short-period gravity waves: Comparisons with ALOHA-93 data and an analytical model. *J. Geophys. Res.* **103**:6467–6481, 1998.

Nappo, C. J. and Chimonas, G. Wave exchange between the ground surface and a boundary-layer critical level. *J. Atmos. Sci.* **49**:1075–1091, 1992.

Nappo, C. J. and Johansson, P.-E. Summary of the Lövånger international workshop on turbulence and diffusion in the stable planetary boundary layer. *Boundary-Layer Meteorol.* **90**:345–374, 1999.

Nappo, C. J. and Physick, W. Gravity wave stress parameterization in a mesoscale sea breeze model. In *11th Conference on Air Pollution Meteorology with the A&WMA, 9–14 January, Long Beach, CA*, pp. 263–268, 2000. Boston, MA: Am. Meteorol. Soc.

Nappo, C. J., Crawford, T. L., Eckman, R. M., and Auble, D. L. A high-precision sensitive electronic microbarograph network. In *7th Symposium on Meteorological Observations and Instrumentation*, pp. j179–j181, 1991. Boston, MA: Am. Meteorol. Soc.

Nappo, C. J., Eckman, R. M., and Coulter, C. L. An episode of wave-generated turbulence in the stable boundary layer. In *Tenth Symposium on Turbulence and Diffusion*, pp. 118–122, 1992. Boston, MA: Am. Meteorol. Soc.

Nappo, C. J., Auble, D. L., Dumas, E., Cuxart, J., Morales, G., Yague, C., and Terradellas, E. Coherent pressure disturbances during CASES-99. In *14th Symposium on Boundary Layer and Turbulence, 7–11 August, Aspen CO*, pp. 366–368, 2000. Boston, MA: Am. Meteorol. Soc.

Nastrom, G. D. The response of supperpressure balloons to gravity waves. *J. Appl. Meteorol.* **19**:1013–1019, 1989.

Nastrom, G. D., Balsley, B. B., and Carter, D. A. Mean meriodinal winds in the mid- and high latitude summer mesosphere. *Geophys. Res. Lett.* **9**:139, 1982.

Neff, W. D. and Coulter, R. L. Acoustic remote sensing. In *Probing the Atmospheric Boundary Layer*, D. H. Lenschow, ed., pp. 201–239, 1986. Boston, MA: Am. Meteorol. Soc.

Newsom, R. K., Banta, R. M., Otten, J., Eberhard, W. L., and Lundquist, J. K. Doppler lidar observations on internal gravity waves, shear instability and turbulence during CASES-99. In *14th Symposium on Boundary Layer and Turbulence, August 7–11, 2000, Aspen, CO*, pp. 362–365, 2000. Boston, MA: Am. Meteorol. Soc.

Nicholls, J. M. The airflow over mountains, research 1958–1972. Technical Report, Tech. Note. No. 127, 1973. Geneva: World Meteorological Organization.

Ottersten, H., Hardy, K. R., and Little, C. G. Radar and sodar probing of waves and turbulence in statically stable clear-air layers. *Boundary-Layer Meteorol.* **4**:47–89, 1973.

Palm, E. Multiple-layer mountain wave models with constant stability and shear. Technical Report, Sci. Rep., 3, Contract No. AF 19(604)-728, 1955. Air Force Cambridge Research Center, Cambridge, MA.

Palmer, T. N., Shutts, G. J., and Swinbank, R. Alleviation of a systematic westerly bias in general circulation and numerical weather prediction through an orographic gravity wave drag parameterization. *Q. J. R. Meteorol. Soc.* **112**:1001–1040, 1986.

Pedlosky, J. *Geophysical Fluid Dynamics*, 1979. New York: Springer-Verlag.

Peltier, W. R. and Calrk, T. L. The evolution and stability of finite amplitude mountain waves. Part II. Surface wave drag and severe downslope windstorms. *J. Atmos. Sci.* **36**:1498–1529, 1979.

Peterson, A. W. and Keiffaber, L. M. Infrared photography of OH airglow structures. *Nature* **242**:321–322, 1973.

Phillips, O. O. *The Dynamics of the Upper Ocean*, 1977. Cambridge, UK: Cambridge Univ. Press.

Piani, C., Durran, D., Alexander, M. J., and Holton, J. R. The propagation of a gravity-inertia wave in a positively sheared flow. *J. Atmos. Sci.* **57**:3689–3702, 2000.

Pielke, R. A. *Mesoscale Meteorological Modeling*, 1984. San Diego: Academic Press.

Pierce, A. D. and Coroniti, S. C. A mechanism for the generation of acoustic-gravity waves during thunderstorm formation. *Nature* **210**:1209–1210, 1960.

Pitteway, M. L. and Hines, C. O. The reflection and ducting of atmospheric acoustic-gravity waves. *Can. J. Phys.* **43**:2222–2243, 1965.

Poulos, G. S., Blumen, W., Fritts, D. C., Lundquist, J. K., Sun, J., Burns, S. P., Nappo, C., Banta, R., Newsom, R., Cuxart, J., Terradellas, E., Balsley, B., and Jensen, M. CASES-99: A comprehensive investigation of the stable nocturnal boundary layer. ??? *Bull. Am. Meteorol. Soc.* **83**:555–581, 2001.

Queney, P. The problem of air flow over mountains: A summary of theoretical studies. *Bull. Am. Meteorol. Soc.* **29**:16–26, 1948.

Radok, U. A procedure for studying mountain effects at low levels. *Bull. Am. Meteorol. Soc.* **35**:412–416, 1954.

Ralph, F. M., Neiman, P. J., Keller, T. L., Levinson, D., and Fedor, L. Observations, simulations, and analysis of nonstationary trapped lee waves. *J. Atmos. Sci.* **54**:1308–1333, 1997.

Rayleigh, J. W. S. *The Theory of Sound, Vol. II*, 1945. New York: Dover.

Rees, J. M. and Mobbs, D. D. Studies of internal gravity waves at Hally Station, Antarctica, using wind observations. *Q. J. R. Meteorol. Soc.* **114**:939–966, 1988.

Rees, J. M., Denholm-Price, J. C. W., King, J. C., and Anderson, P. S. A climatological study of internal gravity waves in the atmospheric boundary layer overlying the Brunt ice shelf, Antarctica. *J. Atmos. Sci.* **57**:511–526, 2000.

Rees, J. M., Staszewski, W. J., and Winkler, J. R. Case study of a wave event in the stable atmospheric boundary layer overlying an Antartic ice shelf using orthogonal wavelet transform. *Dyn. Atmos. Oceans* **34**:245–261, 2001.

Reid, S. J. An observational study of lee waves using radiosonde data. *Tellus*. **24**:593–596, 1972.

Reynolds, R. D. Supperpressure balloons as isentropic/isopycnic tracers. *J. Appl. Meteorol.* **12**:369–373, 1973.

Reynolds, W. C. and Hussain, A. K. M. F. The mechanics of an organized wave in turbulent shear flow. Part 3. Theoretical models and comparisons with experiments. *J. Fluid Mech.* **54**:263–288, 1972.

Richter, J. H. High resolution tropospheric radar sounding. *Radio Sci.* **4**:1261–1268, 1969.

Rosenhead, L. The formation of vortices from a surface discontinuity. *Proc. R. Soc. London A*, **143**:170–192, 1931.

Rottman, J. W. and Einaudi, F. Solitary waves in the atmosphere. *J. Atmos. Sci.* **50**:2116–2136, 1993.

Rottman, J. W. and Smith, R. B. A laboratory model of severe downslope winds. *Tellus*. **41A**:401–415, 1989.

Sawyer, J. S. The introduction of the effects of topography into methods of numerical forecasting. *Q. J. R. Meteorol. Soc.* **85**:31–43, 1959.

Schoeberl, M. R. A model of stationary gravity wave breakdown with convective adjustment. *J. Atmos. Sci.* **45**:980–992, 1988.

Schwiesow, R. L. Lidar measurements of boundary-layer variables. In *Probing the Atmospheric Boundary Layer*, D. H. Lenschow, ed., pp. 139–162, 1986. Boston, MA: Am. Meteorol. Soc.

Scorer, R. S. Theory of waves in the lee of mountains. *Q. J. R. Meteorol. Soc.* **75**:41–56, 1949.

Scorer, R. S. *Environmental Aerodynamics*, 1978. New York: Wiley.

Shutts, G. J., Kitchen, M., and Hoare, P. H. A large amplitude gravity wave in the lower stratosphere detected by radiosonde. *Q. J. R. Meteorol. Soc.* **114**:579–594, 1988.

Shutts, G. J., Healey, P., and Mobbs, S. D. A multiple sounding technique for the study of gravity waves. *Q. J. R. Meteorol. Soc.* **120**:59–79, 1994.

Smith, R. B. The generation of lee waves by the Blue Ridge. *J. Atmos. Sci.* **33**:507–519, 1976.

Smith, R. B. The steepening of hydrostatic mountain waves. *J. Atmos. Sci.* **34**:1634–1654, 1977.

Smith, R. B. The influence of mountains on the atmosphere. *Adv. Geophys.* **21**:87–230, 1979.

Smith, R. B. Linear theory of stratified hydrostatic flow past an isolated mountain. *Tellus* **32**:348–364, 1980.

Smith, R. B. On severe downslope winds. *J. Atmos. Sci.* **42**:2597–2603, 1985.

Smith, R. B. and Lin, Y.-L. The addition of heat to a stratified airstream with application to the dynamics of orographic rain. *Q. J. R. Meteorol. Soc.* **108**:353–378, 1982.

Spiegel, E. A. and Veronis, G. On the Boussinesq approximation for a compressible fluid. *Astrophys. J.* **131**:442–447, 1960.

Sroga, J. T., Eloranta, E. W., and Barber, T. Lidar measurements of wind velocity profiles in the boundary layer. *J. Appl. Meteorol.* **19**:598–605, 1980.

Stern, W. F. and Pierrehumbert, R. T. The impact of an orographic gravity wave drag parameterization on extended range predicitons with a GCM. In *Eighth Conference on Numerical Weather Prediction*, pp. 745–750, 1988. Boston MA: Am. Meteorol. Soc.

Stewart, R. W. Turbulence and waves in a stratified atmosphere. *Radio Sci.* **4**:1269–1278, 1969.

Stobie, J. G., Einaudi, F., and Uccellini, L. W. A case study of gravity waves—convective storms interactions: 9 May 1997. *J. Atmos. Sci.* **40**:2804–2830, 1983.

Strauch, R. G., Campbell, W. C., Chadwick, R. B., and Moran, K. P. Microwave FM-CW radar for boundary layer probing. *Geophys. Res. Lett.* **3**:193–196, 1976.

Stull, R. B. *An Introduction to Boundary Layer Meteorology*, 1988. Dordrecht, The Netherlands: Kluwer Academic.

Sutton, O. G. *Micrometeorology*, 1953. New York: McGraw-Hill.

Swenson, G. R. and Gardner, C. S. Analytical models for the response of the mesospheric OH^* and Na layers to atmospheric gravity waves. *J. Geophys. Res.* **103**:6271–6294, 1998.

Taylor, G. I. Effect of variation in density on the stability of superposed streams of fluid. *Proc. R. Soc. London A*, **201**:499–523, 1931.

Taylor, M. J., Turnbull, D. N., and Lowe, R. P. Spectrometric and imaging measurements of a spectacular gravity wave event observed during the ALOHA-93 campaign. *Geophys. Res. Lett.* **22**:2848–2852, 1995.

Thorpe, S. A. An experimental study of critical levels. *J. Fluid Mech.* **32**:693–704, 1981.

Thorpe, S. A. On the reflection of a train of finite-amplitude internal waves from a uniform slope. *J. Fluid Mech.* **178**:279–302, 1987.

Tolstoy, I. The theory of waves in stratified fluids including the effects of gravity wave rotation. *Rev. Mod. Phys.* **35(1)**:207–230, 1963.

Torrence, C. T. and Compo, G. P. A practical guide to wavelet analysis. *Bull. Am. Meteorol. Soc.* **79**:61–78, 1998.

Treviño, G. and Andreas, E. L. On wavelet analysis of nonstationary turbulence. *Boundary-Layer Meteorol.* **81**:271–288, 1996.

Turner, J. S. *Buoyancy Effects in Fluids*, 1973. Cambridge, UK: Cambridge Univ. Press.

Uccellini, L. W. A case study of apparent gravity wave initiation of severe convective storms. *Mon. Weather Rev.* **103**:497–513, 1975.

Uccellini, L. W. and Kock, S. E. The synoptic setting and possible energy sources for mesoscale wave disturbances. *Mon. Weather Rev.* **115**:721–729, 1987.

Vergeiner, I. and Lilly, D. K. The dynamic structure of lee wave flow as obtained from balloon and air plane observations. *Mon. Weather Rev.* **98**:220–238, 1970.

Vincent, R. A. and Alexander, M. J. Gravity waves in the tropical lower troposphere: An observational study of seasonal and interannual variability. *J. Geophys. Res.* **105**:17,971–17,982, 2000.

Vincent, R. A. and Reid, I. M. HF Dopplar measurements of mesocale gravity wave momentum fluxes. *J. Atmos. Sci.* **40**:1321–1333, 1983.

Vincent, R. A., Allen, S. J., and Eckermann, S. D. Gravity wave parameters in the lower stratosphere. In *Gravity Wave Processes: Their Parameterization in Global Climate Models*, pp. 7–25, 1997. Berlin/New York: Springer-Verlag.

Wunsch, C. On the propagation of internal waves on a slope. *Deep Sea Res.* **18**:588–591, 1968.

Xing-sheng, L., Nai-ping, L., Gaynor, J. E., and Kaimal, J. C. A method for measuring the phase speed and azimuth of gravity waves in the boundary layer using an optical triangle. In *Studies of Nocturnal Stable Layers at BAO*, pp. 93–107, 1983. Boulder, CO: National Atmospheric and Oceanic Administration, NOAA/ERL.

Xue, M., Droegemeier, K. K., Wong, V., Shapiro, A., and Brewster, K. ARPS version 4.0 User's Guide. Technical Report, 1995. Univ. of Oklahoma: Center for Analysis and Prediction of Storms.

Young, J. M. and Hoyle, W. A. Computer programs for multidimensional spectra array processing. Technical Report, NOAA Technical Report ERL 345-WPL 43, 1975. U.S. Dept. of Commerce, National Oceanic and Atmospheric Administration, Boulder, CO.

Zamora, R. L. Richardson number computations in the planetary boundary layer. In *Studies of Nocturnal Stable Layers at BAO*, pp. 109–129, 1983. Boulder, CO: National Atmospheric and Oceanic Administration, NOAA/ERL.

Zink, F. and Vincent, R. A. Wavelet analysis of stratospheric gravity wave packets over Macquarie Island. I. Wave parameters. *J. Geophys. Res.* **106**:10,275–10,298, 2001.

This Page Intentionally Left Blank

INDEX

International Geophysics Series

EDITED BY

RENATA DMOWSKA
Division of Applied Science
Harvard University
Cambridge, Massachusetts

JAMES R. HOLTON
Department of Atmospheric Sciences
University of Washington
Seattle, Washington

H. THOMAS ROSSBY
Graduate School of Oceanography
University of Rhode Island
Narragansett, Rhode Island

Volume 26 KUO-NAN LIOU. An Introduction to Atmospheric Radiation. 1980

Volume 27 DAVID H. MILLER. Energy at the Surface of the Earth: An Introduction to the Energetics of Ecosystems. 1981

Volume 28 HELMUT G. LANDSBERG. The Urban Climate. 1991

Volume 29 M. I. BUDKYO. The Earth's Climate: Past and Future. 1982*

Volume 30 ADRIAN E. GILL. Atmosphere-Ocean Dynamics. 1982

Volume 31 PAOLO LANZANO. Deformations of an Elastic Earth. 1982*

Volume 32 RONALD T. MERRILL AND MICHAEL W. MCELHINNY. The Earth's Magnetic Field: Its History, Origin, and Planetary Perspective. 1983

Volume 33 JOHN S. LEWIS AND RONALD G. PRINN. Planets and Their Atmospheres: Origin and Evolution. 1983

Volume 34 ROLF MEISSNER. The Continental Crust: A Geophysical Approach. 1986

Volume 35 M. U. SAGITOV, B. BODKI, V. S. NAZARENKO, AND KH. G. TADZHIDINOV. Lunar Gravimetry. 1986

Volume 36 JOSEPH W. CHAMBERLAIN AND DONALD M. HUNTEN. Theory of Planetary Atmospheres, 2nd Edition. 1987

Volume 37 J. A. JACOBS. The Earth's Core, 2nd Edition. 1987

Volume 38 J. R. APEL. Principles of Ocean Physics. 1987

Volume 39 MARTIN A. UMAN. The Lightning Discharge. 1987

Volume 40 DAVID G. ANDREWS, JAMES R. HOLTON, AND CONWAY B. LEOVY. Middle Atmosphere Dynamics. 1987

Volume 41 PETER WARNECK. Chemistry of the Natural Atmosphere. 1988

Volume 42 S. PAL ARYA. Introduction to Micrometeorology. 1988

Volume 43 MICHAEL C. KELLEY. The Earth's Ionosphere. 1989

Volume 44 WILLIAM R. COTTON AND RICHARD A. ANTHES. Storm and Cloud Dynamics. 1989

Volume 45 WILLIAM MENKE. Geophysical Data Analysis: Discrete Inverse Theory, Revised Edition. 1989

Volume 46 S. GEORGE PHILANDER. El Niño, La Niña, and the Southern Oscillation. 1990

Volume 47 ROBERT A. BROWN. Fluid Mechanics of the Atmosphere. 1991

Volume 48 JAMES R. HOLTON. An Introduction to Dynamic Meteorology, Third Edition. 1992

Volume 49 ALEXANDER A. KAUFMAN. Geophysical Field Theory and Method.
Part A: Gravitational, Electric, and Magnetic Fields. 1992
Part B: Electromagnetic Fields I. 1994
Part C: Electromagnetic Fields II. 1994

Volume 50 SAMUEL S. BUTCHER, GORDON H. ORIANS, ROBERT J. CHARLSON, AND GORDON V. WOLFE. Global Biogeochemical Cycles. 1992

Volume 51 BRIAN EVANS AND TENG-FONG WONG. Fault Mechanics and Transport Properties of Rocks. 1992

Volume 52 ROBERT E. HUFFMAN. Atmospheric Ultraviolet Remote Sensing. 1992

Volume 53 ROBERT A. HOUZE, JR. Cloud Dynamics. 1993

Volume 54 PETER V. HOBBS. Aerosol-Cloud-Climate Interactions. 1993

Volume 55 S. J. GIBOWICZ AND A. KIJKO. An Introduction to Mining Seismology. 1993

Volume 56 DENNIS L. HARTMANN. Global Physical Climatology. 1994

Volume 57 MICHAEL P. RYAN. Magmatic Systems. 1994

Volume 58 THORNE LAY AND TERRY C. WALLACE. Modern Global Seismology. 1995

Volume 59 DANIEL S. WILKS. Statistical Methods in the Atmospheric Sciences. 1995

Volume 60 FREDERIK NEBEKER. Calculating the Weather. 1995

Volume 61 MURRY L. SALBY. Fundamentals of Atmospheric Physics. 1996

Volume 62 JAMES P. MCCALPIN. Paleoseismology. 1996

Volume 63 RONALD T. MERRILL, MICHAEL W. MCELHINNY, AND PHILLIP L. MCFADDEN. The Magnetic Field of the Earth: Paleomagnetism, the Core, and the Deep Mantle. 1996

Volume 64 NEIL D. OPDYKE AND JAMES E. T. CHANNELL. Magnetic Stratigraphy. 1996

Volume 65 JUDITH A. CURRY AND PETER J. WEBSTER. Thermodynamics of Atmospheres and Oceans. 1998

Volume 66 LAKSHMI H. KANTHA AND CAROL ANNE CLAYSON. Numerical Models of Oceans and Oceanic Processes. 2000

Volume 67 LAKSHMI H. KANTHA AND CAROL ANNE CLAYSON. Small Scale Processes in Geophysical Fluid Flows. 2000

Volume 68 RAYMOND S. BRADLEY. Paleoclimatology, Second Edition. 1999

Volume 69 LEE-LUENG FU AND ANNY CAZANAVE. Satellite Altimetry and Earth Sciences: A Handbook of Techniques and Applications. 2000

Volume 70 DAVID A. RANDALL. General Circulation Model Development: Past, Present, and Future. 2000

Volume 71 PETER WARNECK. Chemistry of the Natural Atmosphere, Second Edition. 2000

Volume 72 MICHAEL C. JACOBSON, ROBERT J. CHARLESON, HENNING RODHE, AND GORDON H. ORIANS. Earth System Science: From Biogeochemical Cycles to Global Change. 2000

Volume 73 MICHAEL W. MCELHINNY AND PHILLIP L. MCFADDEN. Paleomagnetism: Continents and Oceans. 2000

Volume 74 ANDREW E. DESSLER. The Chemistry and Physics of Stratospheric Ozone. 2000

Volume 75 BRUCE DOUGLAS, MICHAEL KEARNEY, AND STEPHEN LEATHERMAN. Sea Level Rise: History and Consequences. 2000

Volume 76 ROMAN TEISSEYRE AND EUGENIUSZ MAJEWSKI. Earthquake Thermodynamics and Phase Transformations in the Interior. 2001

Volume 77 GEROLD SIEDLER, JOHN CHURCH, AND JOHN GOULD. Ocean Circulation and Climate: Observing and Modelling the Global Ocean. 2001

Volume 78 ROGER A. PIELKE SR. Mesoscale Meteorological Modeling, 2nd Edition. 2001

Volume 79 S. PAL ARYA. Introduction to Micrometeorology. 2001

Volume 80 BARRY SALTZMAN. Dynamical Paleoclimatology: Generalized Theory of Global Climate Change. 2002

Volume 81A WILLIAM H. K. LEE, HIROO KANAMORI, PAUL JENNINGS, AND CARL KISSLINGER. International Handbook of Earthquake and Engineering Seismology, Part A. 2002[NYP]

Volume 81B WILLIAM H. K. LEE, HIROO KANAMORI, PAUL JENNINGS, AND CARL KISSLINGER. International Handbook of Earthquake and Engineering Seismology, Part B. 2002[NYP]

Volume 82 GORDON G. SHEPHERD. Spectral Imaging of the Atmosphere. 2002[NYP]

Volume 83 ROBERT P. PEARCE. Meteorology at the Millennium. 2001

Volume 84 KUO-NAN LIOU. An Introduction to Atmospheric Radiation, 2nd Ed. 2002[NYP]

Volume 85 CARMEN J. NAPPO. An Introduction to Atmospheric Gravity Waves. 2002[NYP]

*Out of print.
[NYP]Not yet published.